県立広島大学
Prefectural University of Hiroshima

Polymer and Biochar Composite Engineering and Its Application

In partial fulfilment of the conditions for the award of the degree PhD in Biological System Science

2131003

Endar Hidayat

Graduate School of Comprehensive Scientific Research
Program in Biological System Science
Prefectural University of Hiroshima
2024

TABLE OF CONTENTS

ABSTRACT

Industrial effluents, especially from the chemical industry sectors like textiles, printing, food processing, pharmaceuticals, and paints, contribute significantly to global water pollution. The main pollutants include dyes (such as Congo Red, Acid Black 1, and Indigo Carmine), heavy metals, phenols, and nutrients like nitrogen and phosphorus, which lead to soil contamination. To address these environmental issues, we employed polymer and biochar as fundamental materials. Initially, our focus was on removing dyes from water using polymer and biochar composites through adsorption methods.

1. Composites of hydrogel beads made from sodium alginate and cetyltrimethylammonium bromide were found to remove congo red dye at a capacity of 153.24 mg/g.
2. Porous sodium alginate/poly (acrylic acid) composites achieved a 95.43% removal rate for acid black 1 dye under conditions of pH 8.9, a 90-minute contact period, and a temperature of 45 °C.
3. The effectiveness of unactivated and activated coffee husk biochar for adsorbing indigo carmine dye from water was studied under room temperature conditions using HNO_3 and $NaHCO_3$, with results showing that chemical activation increased adsorption capacity.

In addition, to combat challenges like water scarcity and soil degradation including salinity, heavy metals, and glyphosate contamination, which adversely impact food production. We developed hydrogel beads and biochar composites derived from sodium alginate and coffee husk. The hydrogel bead composites demonstrated an ability to retain up to 30% more water in soil compared to untreated soil, significantly enhancing soil nutrients and reducing heavy metals like iron and arsenic by 89.6% and 87.81%, respectively. Furthermore, we designed hydrogel bead composites containing struvite ($MgNH_4PO_4 \cdot 6H_2O$) for use as slow-release fertilizers to improve salt-affected soils. These materials effectively released Mg, P, and N-NH_4 ($P<0.05$) and successfully reduced soil salinity to normal levels while boosting soil nutrient content.

Additionally, we synthesized MgO-biochar composites for the removal of glyphosate. Findings showed that higher temperatures resulted in an increased specific surface area (BET-SSA) and total pore volume while decreasing the average pore diameter. Glyphosate removal reached up to 50.42% after a week of soil incubation. The addition of biochar-MgO to the soil increased the pH and significantly raised ($P<0.05$) electrical conductivity (EC) and exchangeable cation contents (Mg, Ca, and Na).

Finally, to further improve the functionality of these materials, we developed:

1. Porous biochar through in-situ techniques using a combination of materials, including ZrO, chitosan, and Fe_3O_4, to remove NH_4, PO_4, and phenol from water via adsorption.
2. Hydrogel bead composites with and without oleic acid as slow-release NH_4 fertilizers for use in mitigating soil acidity.

The application of biochar demonstrated that this combination could enhance the simultaneous removal of NH_4, P, and phenol. Additionally, the inclusion of oleic acid led to greater porosity, an increased swelling rate, and reduced NH_4 release, indicating a potential role in controlling NH_4 ion release from the polymer matrix. Soil CO_2 release studies revealed that hydrogel bead-oleic acid composites had lower CO_2 emissions compared to those without oleic acid, suggesting their potential in reducing CO_2 emissions. Both studies highlight the potential of these materials in addressing soil acidity.

LIST OF TABLES

LIST OF FIGURES

Chapter 1: Background

1.1 Motivation

The study of materials has always been essential for significant societal advancements and technological progress across various fields. With the rapid growth of manufacturing industries and increasing societal demands, there is a growing need for advanced materials to create innovative products. The limitations of traditional materials have become apparent due to rising demands and the optimization of industrial techniques, leading to the development of advanced materials (Yashas Gowda et al., 2018). Recently, polymer and biochar matrices have largely replaced traditional materials because of their advantages over conventional options. Polymer and biochar have emerged as the fastest-growing and most widely used composite materials due to their unique properties and versatile applications, including environmental and agricultural uses. The aim of this dissertation is the remediation of water and soil pollutants to promote sustainable soil health. The problem statement and an overview of the dissertation are illustrated in Figures 1 and 2, respectively.

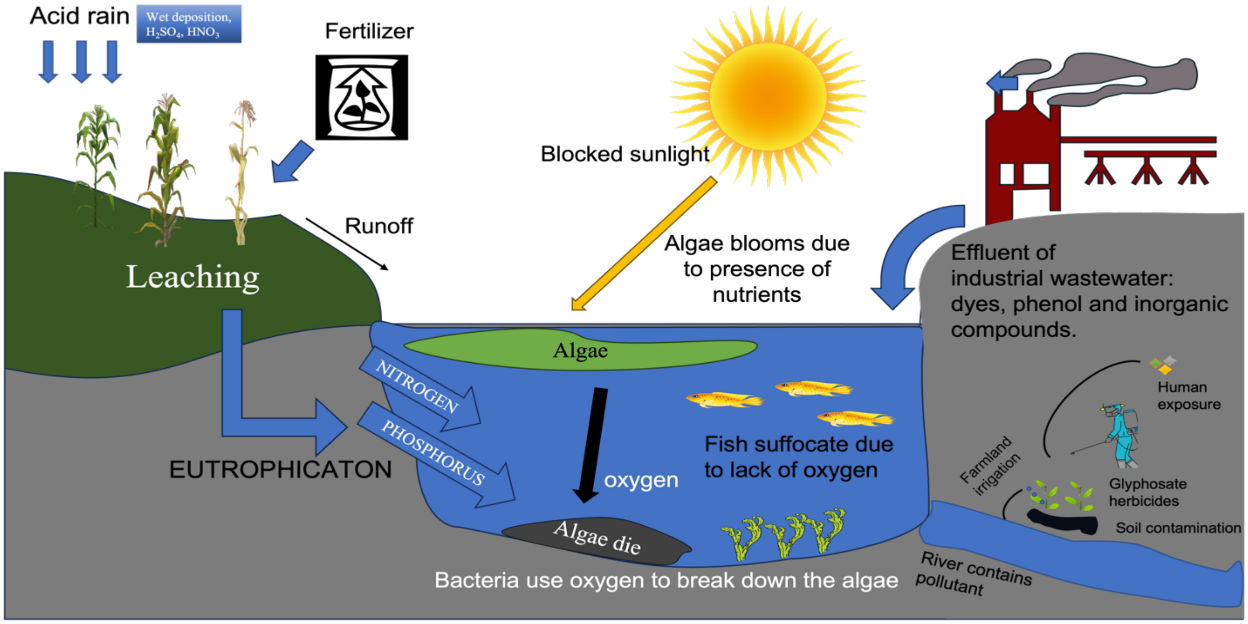

Figure. 1. Illustration of problem statements

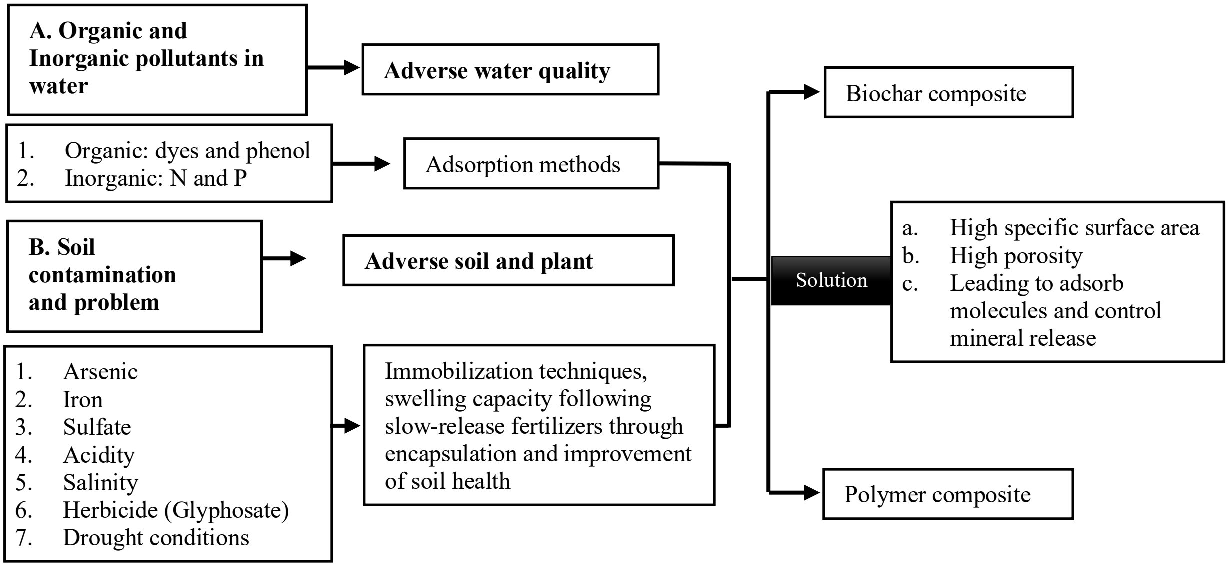

Figure. 2. Overview of dissertation regarding problem statements

1.2 Organization of chapters

The end of the first chapter contains a review of the most recent published literature relevant to polymers and biochar as materials for wastewater treatment, soil immobilization, and amelioration.

The second chapter focuses on the fabrication of polymers as hydrogel beads derived from sodium alginate and biochar composites. The goal of this study was to optimize methods for dye removal by adsorption from aqueous solutions. Scanning electron microscopy (SEM) and Fourier transform infrared spectroscopy (FTIR) were used to visualize and characterize functional groups before and after adsorption. Additionally, adsorption isotherms, kinetics, and thermodynamics were calculated to understand the adsorption mechanisms. This research has been published in Desalination and Wastewater Treatment (2024, 319, 100407 and 2024, 318, 100313) and accepted as a book chapter by Elsevier (ISBN: 9780443298776).

The third chapter presents a study that developed materials to immobilize salinity, heavy metals, and glyphosate contamination while improving soil health. Soil incubation techniques were used to determine the effects of samples on the immobilization rate. The chapter explores the extent to which hydrogel beads and biochar composites are related to sample properties and their interactions with soil contamination. This research has been published in the Arabian Journal of Chemistry (2024, 17(9), 105877) and Case Studies in Chemical and Environmental Engineering (2024, 9, 100642, 1-8).

The fourth chapter develops materials from the previous chapters. We developed (1) porous biochar composites via an in-situ technique to remove NH_4, P, and phenol from water through adsorption, and (2) hydrogel bead composites with oleic acid as slow-release NH_4 fertilizers and their application in soil acidity amelioration. This technique demonstrated multifunctionality in remediating water pollutants and enhancing soil acidity properties. This research has been published in Environmental Technology (2024, 1-20).

The fifth chapter describes the general conclusions from the combined studies on polymers as hydrogel beads and biochar, and outlines future work to be done in the area of polymer and biochar characterization and engineering.

1.3 Recent literature review

1.3.1 Dyes contamination and sources

Water contamination resulting from the improper disposal of wastewater by textile industries is a major global concern. The textile sector plays a significant role in both the global economy and environmental pollution in many countries (Al-Tohamy et al., 2022). Annually, around 70 million tons of synthetic dyes are produced worldwide, with textile industries consuming over 10,000 tons of these dyes (Chandanshive et al., 2020). Dyes are classified based on their origin, structure, and usage (Akpomie & Conradie, 2020). The most commonly used synthetic dyes in the textile industry include azo, direct, reactive, mordant, acid, basic, disperse, and sulfide dyes (Figure 3). Some textile factories treat their wastewater to decompose the free azo dyes before discharging it into the environment, while others release untreated industrial effluents directly into water bodies, posing significant ecotoxicological threats and harmful effects on living organisms (Figure 1). In developing countries, it is common for farmers to irrigate their agricultural lands with wastewater containing untreated industrial effluents, which adversely affects soil quality and crop germination rates (Sojobi & Zayed, 2022).

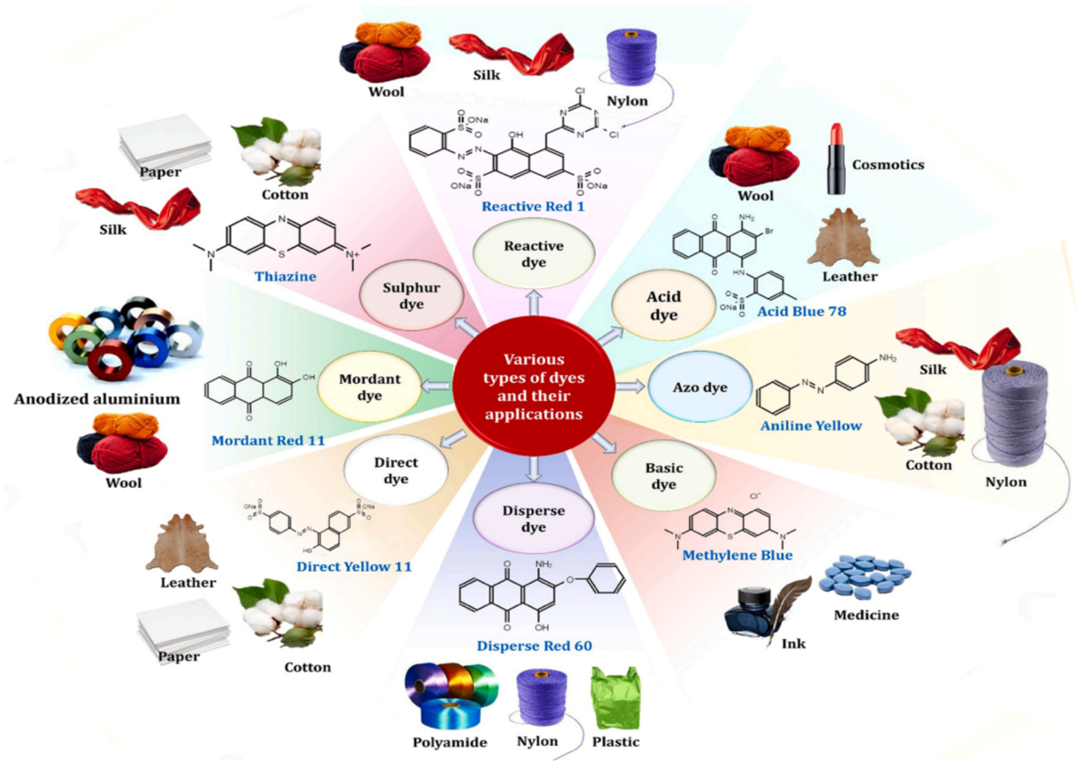

Figure. 3. Various type of dyes and its possible applications (Al-Tohamy et al., 2022)

Although water covers more than 71% of the Earth's surface, the scarcity of pure, high-quality drinking water remains one of humanity's most urgent challenges. The demand for clean drinking water is rapidly increasing, with agriculture, industry, and households consuming 70%, 19%, and 11% of available water, respectively (Gupta et al., 2015). The textile industry significantly contributes to the degradation of water quality, leading to long-term environmental pollution. Human activities have adversely affected natural habitats by introducing pollutants into both land and water ecosystems (Soni et al., 2021). This pollution results in considerable ecological impacts, such as changes in aquatic ecosystems and a reduction in photosynthesis among aquatic plants (M. D. Khan et al., 2015). Additionally, wastewater from the textile industry can cause allergies, dermatitis, skin irritations, cancers, and genetic mutations in humans, while also degrading water quality by altering its odor and color, making it toxic (Sarvajith et al., 2018). The presence of high concentrations of textile dyes in water depletes oxygen levels, blocks sunlight, and disrupts the biological activities of aquatic plants and animals (Ghaedi et al., 2015).

1.3.2 Polymer for wastewater treatment

The recent rapid expansion of industries has resulted in significant environmental challenges. Effluents from various sectors, including paint, metal plating, food, pharmaceuticals, and battery manufacturing, often contain heavy metal ions, dyes, and organic materials that are directly discharged into water bodies, leading to pollution. When these pollutants exceed permissible levels, they pose serious risks to humans and other terrestrial and aquatic life. They infiltrate and accumulate in organisms through food chains (Fu & Wang, 2011). To address and purify contaminated water, several methods are used, including chemical precipitation, ion exchange, biological processes, membrane separation, reverse osmosis, coagulation and flocculation, catalysis, photodegradation, and adsorption. Among these, adsorption is regarded as an economical, efficient, and environmentally friendly approach for wastewater treatment (Rehman et al., 2019).

The adsorption process can be categorized into chemisorption and physisorption. Chemisorption, or chemical adsorption, involves the creation of a chemical bond between the adsorbate and the adsorbent, making it an irreversible process. On the other hand, physisorption, or physical adsorption, occurs through physical interactions like hydrogen bonding, van der Waals forces, and hydrophobic interactions between the adsorbate and adsorbent, and it is a reversible process (Cruz et al., 2018). Key factors influencing the adsorption efficiency of hydrogels include conditions such as pH, ionic strength, the dosage of both adsorbate and adsorbent, contact time, and temperature. Optimizing these factors is essential, particularly when scaling up the adsorption process.

Hydrogels are three-dimensional, cross-linked, and flexible polymer networks that contain hydrophilic groups such as hydroxyl, carboxyl, and amide, allowing them to swell in water (Cruz et al., 2018). This swelling capability is reversible and highly sensitive to environmental conditions, which is why hydrogels are often termed intelligent or smart materials. Sodium alginate, a bio-based polymer, can be used to form hydrogels. It is a linear copolymer consisting of β-D-mannuronic acid (M) and α-L-guluronic acid (G) residues, connected through 1,4-glycosidic bonds. These residues can either form homopolymers made of a single type of monosaccharide or heteropolymer blocks that contain both types (H. Guo et al., 2023). Alginates are natural polysaccharides produced by bacteria or extracted from brown algae, comprising β-D-mannuronate (M blocks) and α-L-guluronate (G blocks) linked by 1→4 bonds (Figure 4). These bonds alternate between mannuronate-guluronate structures and guluronate-mannuronate dyads (Da Costa et al., 2024).

The versatility of sodium alginate is evident in its ability to undergo chemical modifications, making it adaptable to specific treatment conditions. It is particularly effective as an adsorbent in water treatment, thanks to its unique capacity to form gels in the presence of calcium ions, creating hydrogel matrices that enhance adsorption (Duru Kamacı & Kamacı, 2024). However, its linear structure (H. Guo et al., 2023) limits the effectiveness of using sodium alginate alone in complex water environments. When employed for pollution remediation, sodium alginate encounters challenges such as poor mechanical strength, low structural stability, and inadequate heat resistance (Ates et al., 2020). To address these issues, modifying sodium alginate with synthetic polymers like poly (acrylic acid) and surfactants such as cetyltrimethylammonium bromide (CTAB) offers a promising solution to improve its mechanical strength and stability.

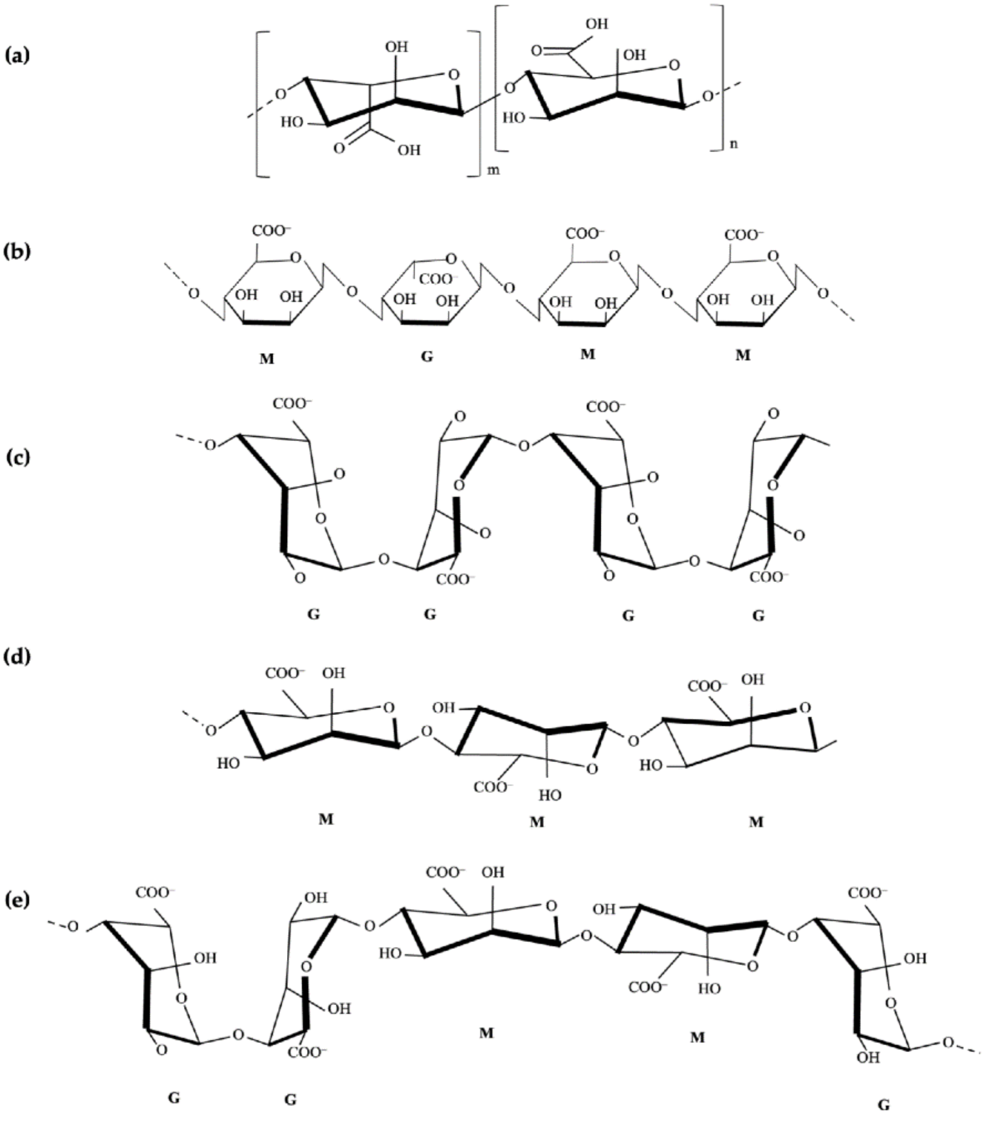

Figure. 4. Sodium alginate structure (a). Chain segment structure of alginate (MGMM) (b). Blocks of acid groups in grouping (guluronicz) GG (c), (mannuronic) MM (d), and GGMMG (e). (Bustos-Terrones, 2024).

1.3.2.1 Poly (acrylic acid)

Polyacrylic acid (PAA) is a polymer formed through the polymerization of acrylic acid monomers. PAA can produce hydrogels with varying properties through covalent and physical cross-linking, as well as hydrogen bond formation (Zhao et al., 2017). The high concentration of carboxyl groups in PAA enhances the water absorption capacity of its hydrogels. Additionally, the sensitivity of these carboxyl groups to pH and ionic strength affects the swelling ratio of PAA hydrogels. PAA hydrogels can also evolve into smart hydrogels that are useful in wastewater treatment and agricultural applications.

1.3.2.2 Cetyltrimethylammonium bromide

Cetyltrimethylammonium bromide (CTAB) is a cationic quaternary ammonium surfactant commonly used as an emulsifying agent because of its ability to form micelles in aqueous solutions. CTAB can emulsify two immiscible liquids by interacting with both the hydrophilic and hydrophobic components of the liquids. As an amphiphilic compound, CTAB reduces surface and interfacial tension between two phases. Furthermore, CTAB is recognized for its properties in dispersion, suspension, solubilization, and transport (Mohyaldinn et al., 2023), making it ideal for mixing or interacting with other solutions like sodium alginate.

1.3.3 Biochar for wastewater treatment

Biochar is a porous carbon-rich material produced through the thermochemical decomposition of biomass feedstock in a low-oxygen environment. The biomass feedstock can include various organic waste materials, such as crop residues, forest residues, wood chips, algae, sewage sludge, manures, and organic municipal solid wastes (Xiong et al., 2019). The selection of feedstock is influenced by factors like availability, cost, energy content, and the desired properties of the biochar, resulting in differences in composition, porosity, and reactivity among biochars derived from different feedstocks (Wan Mahari et al., 2022).

Biochar can be produced through methods such as pyrolysis, gasification, and hydrothermal carbonization. Pyrolysis, the most commonly used method, involves heating biomass in the absence of oxygen, breaking down the organic matter into char. The properties of the resulting biochar are greatly influenced by the temperature and heating rate, with higher temperatures typically leading to increased carbon content and enhanced stability (Yek et al., 2021). Gasification entails the controlled combustion of biomass to produce syngas, which can then be further processed into biochar. Hydrothermal carbonization converts biomass into biochar by using high temperatures and pressures in the presence of water (Mishra & Mohanty, 2022), each method offers distinct advantages and produces biochar with unique characteristics (Okiemute Akpasi et al., 2023).

Biochar is increasingly being utilized in water and wastewater treatment. Its large surface area, high pore volume, rich organic carbon content, mineral components, and diverse functional groups give biochar a notable ability to adsorb both organic and inorganic contaminants from aqueous solutions (Ahmad et al., 2014). However, a significant challenge with biochar use is its reusability and regeneration after adsorption, which can potentially result in secondary pollution (Ambaye et al., 2021). To mitigate this issue, biochar has been modified with iron oxide nanoparticles, a technique that has been shown to be effective in regeneration without causing secondary pollution, thereby ensuring environmental safety (El-Naggar et al., 2022). Various chemical methods, including acid and base treatments, metal salt or oxidizing agent modifications, and carbonaceous material enhancements, have been used to improve the properties of biochar specifically for wastewater treatment applications (El-Naggar et al., 2022).

1.3.4 Polymer as soil conditioner

The increasing global demand for water, combined with the impacts of climate change, is exerting significant pressure on water resources, leading to shortages in arid, semi-arid, and other regions worldwide. Additionally, sectors such as urban development, industry, and agriculture, which together consume more than two-thirds of the world's freshwater, are competing for the limited water supply (Oladosu et al., 2019). Abiotic stresses like temperature extremes, acidity, salinity, heavy metals, and drought heavily affect agricultural productivity, and these challenges are expected to intensify with urbanization and land degradation. As irrigation water becomes scarcer, there is a global emphasis on adopting agricultural practices that improve water use efficiency. One of the most crucial factors influencing crop growth and yield is the ability of plants to survive under water stress, which can be mitigated through irrigation. Therefore, it is essential to research and develop new materials for water management and sustainability. In light of water scarcity and the growing emphasis on environmental conservation, there is significant interest in exploring biodegradable hydrogels for commercial agricultural applications (Oladosu et al., 2022).

Water-absorbing polymers, commonly known as hydrogels, were first introduced for agricultural use in the 1980s (Oladosu et al., 2022). Hydrogels are crosslinked, hydrophilic polymers capable of absorbing large amounts of water, up to a hundred times their dry weight, without dissolving, and they release that water when subjected to mechanical pressure (Ahmed, 2015). In arid regions, hydrogels improve soil water retention by gradually releasing the absorbed water into the soil, earning them the name superabsorbent polymers (SAPs). With the increasing focus on environmental conservation, manufacturers of hydrogels are now prioritizing the development of biodegradable superabsorbents. Recent research has concentrated on creating ecofriendly absorbent materials derived from renewable resources, as opposed to using synthetic, petroleum-based hydrogels (Mali et al., 2018).

Alginate and poly(acrylic acid) are examples of natural polymers that can form hydrogels. Traditionally, synthetic polymers used for hydrogel production have been synthesized through chemical polymerization processes. A hydrogel is composed of networks of polymer chains linked together on a macroscopic scale, resulting in a single large molecule or a gel-like substance with physical properties that are neither fully solid nor completely liquid. The terms "gel" and "hydrogel" are often used interchangeably. These materials display interesting relaxation behaviors due to their semi-solid, semi-liquid nature, characteristics that are not present in purely solid or liquid states. Hydrogels can undergo significant volume changes in response to external stimuli, such as electric fields, pH shifts, solvent quality, and temperature variations (Neethu et al., 2018). However, concerns about their potential toxicity, particularly in agricultural or human-related applications, have led to hydrogels being considered potential soil pollutants (Ben Ammar et al., 2020).

As soil conditioners, hydrogels can be combined with fertilizers to control nutrient release and enhance soil water retention, functioning as agents for slow-release fertilizers (Pourjavadi et al., 2012; Ramli, 2019). This combination has the potential to improve plant nutrition, reduce the environmental impact associated with conventional fertilizers, and minimize both evaporation losses and the frequency of irrigation (R. Liang et al., 2009).

1.3.5 Biochar as soil conditioner

The imperative to develop more sustainable agricultural systems and bolster weak rural economies necessitates significant changes in agricultural management. Soil degradation, which includes reduced fertility and increased erosion, poses a major global agricultural concern

(Jianping, 1999). Prolonged soil cultivation can lead to degradation characterized by acidification, depletion of soil organic matter, and severe erosion (De Meyer et al., 2011). Furthermore, the decline in soil organic matter diminishes soil aggregate stability (Annabi et al., 2011). Hence, it is crucial to remediate degraded soils using simple and sustainable methods.

Manures and composts contain pathogens, heavy metals, and pharmaceuticals, potentially causing long-term contamination of farmland. Additionally, they can release ammonia and methane, exacerbating global warming and leading to significant nutrient pollution in groundwater and streams. Biochar, being a renewable resource with economic and environmental benefits, holds promise for managing soil fertility (Ding et al., 2016).

Biochar typically contains carbon, nitrogen, hydrogen, and various minor nutrient elements such as K, Ca, Na, and Mg (H. Zhang et al., 2015). Generally, carbon content increases with higher pyrolysis temperatures (300 to 800 °C), while nitrogen and hydrogen contents decrease. Biochar has been shown to enhance soil chemical, physical, and microbial properties. Studies indicate that integrating biochar with soils can improve soil structure, increase porosity, reduce bulk density, enhance aggregation, and improve water retention (Baiamonte et al., 2015). Moreover, biochar can increase soil electrical conductivity by 124.6%, decrease soil acidity by 31.9% (Oguntunde et al., 2004), and raise cation exchange capacity by 20% (Laird et al., 2010).

1.3.5.1 Soil contamination

Soil contamination is a major environmental issue. It can arise in numerous ways, with various substances acting as pollutants, which can be either natural or synthetic chemicals resulting from environmental changes or human activities. These pollutants infiltrate the soil, occupying the pores around soil particles, or are retained through chemical adsorption. Since both soil and contaminants are mostly inert, they tend to remain in soil pores or as liquid on soil particles due to capillary forces. Changes in the chemistry of subsurface soil fluids and their environmental interactions affect their characteristics and behavior. It's well established that changes in pore fluid chemistry significantly influence soil strength properties. The sensitivity of soil to contaminants depends on factors such as the local environment, mineral structure, particle bonding qualities, particle size, ion exchange capacities, and other variables (Singh et al., 2009). Examples of soil contamination include pollution in sanitary landfill soils and acidic pollutants in river and groundwater.

1.3.5.2 Soil heavy metals contamination

Soil contamination by heavy metals has emerged as a global environmental concern, drawing considerable public attention due to the growing worries about the safety of agricultural products (Hu et al., 2017). Across the globe, there are 5 million contaminated sites spanning 500 million hectares, where soils are polluted with various heavy metals or metalloids, and the concentrations in these soils surpass geo-baseline or regulatory standards (Liu et al., 2018). The global economic impact of heavy metal pollution in soils is estimated to exceed US$10 billion annually (Wuana & Okieimen, 2011).

Heavy metals enter the agroecosystem through both natural processes and human activities. Numerous studies suggest that natural sources of heavy metals in the environment are generally less impactful compared to those arising from human activities (Dixit et al., 2015). Some soils naturally contain high levels of heavy metals inherited from parent material, which can negatively affect plants and organisms. Human activities such as fossil fuel burning (Muradoglu et al., 2015), pesticide application (Ogunlade & Agbeniyi, 2011), mining and smelting (Chen et al., 2015), sewage irrigation (Sun et al., 2013), municipal waste disposal (I. Khan & Ghani, 2016), and fertilizer use (Atafar et al., 2010) significantly contribute to the increased levels of heavy metals in agricultural soils (Li et al., 2019).

1.3.5.3 Soil acidity contamination

Soil acidification is a gradual, natural process associated with soil weathering, but it can be accelerated by human activities such as intensive agriculture (Bolan et al., 2022). In agricultural soils, the continuous application of nitrogen (N) and sulfur (S) fertilizers leads to higher concentrations of H^+ ions, which can negatively impact plant growth, soil properties, and microbial activity (Fageria & Nascente, 2014). Elevated levels of H^+ ions increase the mobility and solubility of toxic metals like Al and Mn, which can impair plant growth and development and pose health risks to humans when these metals enter the food chain (Briffa et al., 2020). Additionally, soil acidity reduces the availability of essential nutrients such as phosphorus (P), molybdenum (Mo), calcium (Ca), and magnesium (Mg), further hindering plant growth and development (Briffa et al., 2020). Although soil acidification naturally occurs through processes like mineral weathering and rainfall, the extensive use of nitrogen fertilizers, acid rain, and industrial emissions are the primary factors contributing to the global increase in soil acidification (J. H. Guo et al., 2010).

Soil pH plays a crucial role in plant health by affecting nutrient uptake. In acidic soils, plants are exposed to three primary toxicities from H^+, Mn, and Al ions, which inhibit root growth, cell division, and nutrient absorption, while also disrupting the cytoskeleton (Kaur et al., 2019). Al toxicity often manifests as phosphorus deficiency, with symptoms such as dark green leaves, stunted growth, delayed maturity, and purpling of stems, leaves, and veins (Kaur et al., 2019). While Mn is an essential nutrient, it becomes toxic in excess and is the second most significant toxin in acidic soils (Sumner et al., 1991). Low soil pH also inhibits root growth due to the influx of H^+ ions, which causes membrane depolarization and disrupts cytoplasmic acidity (Babourina et al., 2001). Elevated H^+ levels also damage root tissues, significantly reducing growth and development (Msimbira & Smith, 2020).

Soil acidification increases the concentration of toxic metals like Fe and Al, leading to higher phosphorus (P) retention in the soil through adsorption and precipitation, which ultimately hinders plant growth (Ng et al., 2022). Acidic conditions also worsen the deficiency of base cations such as Ca and Mg by promoting the leaching of exchangeable forms of these nutrients (Maathuis, 2009). Although low soil pH may not significantly impact zinc (Zn) availability for plants, it does elevate Mn levels, which can be detrimental to crops, as many plants are sensitive to high Mn concentrations (Alejandro et al., 2020). Generally, Fe has low solubility in acidified soils (Zhu et al., 2021), making redox reactions essential for dissolving Fe to meet plant requirements (Jin et al., 2014). Additionally, soil acidity can increase the availability of other elements, further influencing plant growth (Sá & Ernani, 2016).

1.3.5.4 Soil salinity contamination

Soil salinity is a significant stressor that hampers plant growth by disrupting various plant processes, including morphological, physiological, biochemical, and molecular functions (Imran et al., 2022). Annually, 1-2% of cultivated soils worldwide are lost to salinity, and approximately 23% of arable land (800 million hectares) is affected by salt, posing a serious threat to food production (Alqahtani et al., 2019). By 2050, it is estimated that 50% of arable land will be salt-affected due to rising groundwater levels with high salt concentrations, poor irrigation and drainage systems, and the excessive use of chemical fertilizers (Raza et al., 2023). Salinity stress leads to substantial yield losses, with potential reductions of up to 65% in many cultivated regions (Nawaz et al., 2022). Under saline conditions, plants experience reduced germination, stunted seedling growth, and lower yields, along with disruptions in physiological and molecular processes

(Hassan et al., 2023). Salinity also triggers the production of reactive oxygen species (ROS), which damage proteins, DNA, and lipids, while also increasing the loss of essential osmolytes (Kamran et al., 2019). Additionally, salinity stress affects plant growth and development by causing ionic and osmotic stress (K. Liang et al., 2022). Ionic toxicity from salinity increases the concentration of harmful ions and reduces essential nutrients like Ca, and K (Akhtar et al., 2015). Osmotic stress due to salinity decreases soil water availability by lowering soil water potential, which limits nutrient and water uptake and reduces the photosynthetic rate, thereby inhibiting plant growth (Hussain et al., 2019; W. Zhang et al., 2023).

The main causes of global soil salinity include factors like low rainfall, high evaporation rates, climate change, increasing global temperatures, the movement of saline groundwater, and salt deposition from oceans (Tavakoli Kivi & Bailey, 2017). Recently, these issues have been intensified by rapid industrialization and economic growth. Moreover, intensive agricultural practices, such as improper irrigation, overuse of fertilizers, and pesticide application, are contributing to the rising levels of soil salinity around the world (Bello, 2021). Among these human-induced factors, the excessive use of salts combined with inadequate drainage systems is the primary reason for rising water tables and the accumulation of salts on the soil surface (Tavakoli Kivi & Bailey, 2017). This not only hinders plant growth but also poses serious risks to soil health. For example, salinity stress can reduce nutrient availability, destabilize organic matter, and lower the soil’s redox potential (Rengasamy, 2010). Research shows that soil salinity decreases organic matter content, water-holding capacity, infiltration rates, and disrupts the stability of soil aggregates (Gonçalo Filho et al., 2019). High levels of sodium in the soil lead to salt stress, which depletes soil fertility and creates osmotic potential that can cause cell death due to reduced water uptake (Ahanger et al., 2018). Excess sodium also leads to plant wilting (Assaha et al., 2017), and negatively impacts soil microbial activity, microbial populations, enzyme activity, and biomass production (M. Zhang et al., 2019). Additionally, soil salinity reduces carbon fixation, disrupts nutrient cycling, lowers porosity, and weakens plant growth and vigor (Almeida et al., 2017). The excessive absorption of toxic ions also harms plant growth by reducing the availability of water and essential nutrients such as N, P, K, Ca, Mg, Fe, and Zn (A. Khan et al., 2019).

References

Ahanger, M. A., Alyemeni, M. N., Wijaya, L., Alamri, S. A., Alam, P., Ashraf, M., & Ahmad, P. (2018). Potential of exogenously sourced kinetin in protecting Solanum lycopersicum from NaCl-induced oxidative stress through up-regulation of the antioxidant system, ascorbate-glutathione cycle and glyoxalase system. *PLOS ONE*, *13*(9), e0202175. https://doi.org/10.1371/journal.pone.0202175

Ahmad, M., Rajapaksha, A. U., Lim, J. E., Zhang, M., Bolan, N., Mohan, D., Vithanage, M., Lee, S. S., & Ok, Y. S. (2014). Biochar as a sorbent for contaminant management in soil and water: A review. *Chemosphere*, *99*, 19–33. https://doi.org/10.1016/j.chemosphere.2013.10.071

Ahmed, E. M. (2015). Hydrogel: Preparation, characterization, and applications: A review. *Journal of Advanced Research*, *6*(2), 105–121. https://doi.org/10.1016/j.jare.2013.07.006

Akhtar, S. S., Andersen, M. N., & Liu, F. (2015). Residual effects of biochar on improving growth, physiology and yield of wheat under salt stress. *Agricultural Water Management*, *158*, 61–68. https://doi.org/10.1016/j.agwat.2015.04.010

Akpomie, K. G., & Conradie, J. (2020). Advances in application of cotton-based adsorbents for heavy metals trapping, surface modifications and future perspectives. *Ecotoxicology and Environmental Safety*, *201*, 110825. https://doi.org/10.1016/j.ecoenv.2020.110825

Alejandro, S., Höller, S., Meier, B., & Peiter, E. (2020). Manganese in Plants: From Acquisition to Subcellular Allocation. *Frontiers in Plant Science*, *11*. https://doi.org/10.3389/fpls.2020.00300

Almeida, D. M., Oliveira, M. M., & Saibo, N. J. M. (2017). Regulation of Na+ and K+ homeostasis in plants: towards improved salt stress tolerance in crop plants. *Genetics and Molecular Biology*, *40*(1 suppl 1), 326–345. https://doi.org/10.1590/1678-4685-gmb-2016-0106

Alqahtani, M., Roy, S. J., & Tester, M. (2019). Increasing Salinity Tolerance of Crops. In *Encyclopedia of Sustainability Science and Technology* (pp. 1–24). Springer New York. https://doi.org/10.1007/978-1-4939-2493-6_429-3

Al-Tohamy, R., Ali, S. S., Li, F., Okasha, K. M., Mahmoud, Y. A.-G., Elsamahy, T., Jiao, H., Fu, Y., & Sun, J. (2022). A critical review on the treatment of dye-containing wastewater: Ecotoxicological and health concerns of textile dyes and possible remediation approaches for environmental safety. *Ecotoxicology and Environmental Safety*, *231*, 113160. https://doi.org/10.1016/j.ecoenv.2021.113160

Ambaye, T. G., Vaccari, M., van Hullebusch, E. D., Amrane, A., & Rtimi, S. (2021). Mechanisms and adsorption capacities of biochar for the removal of organic and inorganic pollutants from industrial wastewater. *International Journal of Environmental Science and Technology*, *18*(10), 3273–3294. https://doi.org/10.1007/s13762-020-03060-w

Annabi, M., Le Bissonnais, Y., Le Villio-Poitrenaud, M., & Houot, S. (2011). Improvement of soil aggregate stability by repeated applications of organic amendments to a cultivated silty loam soil. *Agriculture, Ecosystems & Environment*, *144*(1), 382–389. https://doi.org/10.1016/j.agee.2011.07.005

Assaha, D. V. M., Ueda, A., Saneoka, H., Al-Yahyai, R., & Yaish, M. W. (2017). The Role of Na+ and K+ Transporters in Salt Stress Adaptation in Glycophytes. *Frontiers in Physiology*, *8*. https://doi.org/10.3389/fphys.2017.00509

Atafar, Z., Mesdaghinia, A., Nouri, J., Homaee, M., Yunesian, M., Ahmadimoghaddam, M., & Mahvi, A. H. (2010). Effect of fertilizer application on soil heavy metal concentration. *Environmental Monitoring and Assessment*, *160*(1–4), 83–89. https://doi.org/10.1007/s10661-008-0659-x

Ates, B., Koytepe, S., Ulu, A., Gurses, C., & Thakur, V. K. (2020). Chemistry, Structures, and Advanced Applications of Nanocomposites from Biorenewable Resources. *Chemical Reviews*, *120*(17), 9304–9362. https://doi.org/10.1021/acs.chemrev.9b00553

Babourina, O., Hawkins, B., Lew, R. R., Newman, I., & Shabala, S. (2001). K+ transport by Arabidopsis root hairs at low pH. *Functional Plant Biology*, *28*(7), 637. https://doi.org/10.1071/PP01018

Baiamonte, G., De Pasquale, C., Marsala, V., Cimò, G., Alonzo, G., Crescimanno, G., & Conte, P. (2015). Structure alteration of a sandy-clay soil by biochar amendments. *Journal of Soils and Sediments*, *15*(4), 816–824. https://doi.org/10.1007/s11368-014-0960-y

Bello, S. K. (2021). An Overview of the Morphological, Genetic and Metabolic Mechanisms Regulating Phosphorus Efficiency Via Root Traits in Soybean. *Journal of Soil Science and Plant Nutrition*, *21*(2), 1013–1029. https://doi.org/10.1007/s42729-021-00418-y

Ben Ammar, N. E., Barbouche, M., & Hamzaoui, A. H. (2020). Historical view of hydrogel characterization. In *Hydrogels Based on Natural Polymers* (pp. 459–479). Elsevier. https://doi.org/10.1016/B978-0-12-816421-1.00017-3

Bolan, N., Hoang, S. A., Beiyuan, J., Gupta, S., Hou, D., Karakoti, A., Joseph, S., Jung, S., Kim, K.-H., Kirkham, M. B., Kua, H. W., Kumar, M., Kwon, E. E., Ok, Y. S., Perera, V., Rinklebe, J., Shaheen, S. M., Sarkar, B., Sarmah, A. K., … Van Zwieten, L. (2022). Multifunctional applications of biochar beyond carbon storage. *International Materials Reviews*, *67*(2), 150–200. https://doi.org/10.1080/09506608.2021.1922047

Briffa, J., Sinagra, E., & Blundell, R. (2020). Heavy metal pollution in the environment and their toxicological effects on humans. *Heliyon*, *6*(9), e04691. https://doi.org/10.1016/j.heliyon.2020.e04691

Bustos-Terrones, Y. A. (2024). A Review of the Strategic Use of Sodium Alginate Polymer in the Immobilization of Microorganisms for Water Recycling. *Polymers*, *16*(6), 788. https://doi.org/10.3390/polym16060788

Chandanshive, V., Kadam, S., Rane, N., Jeon, B.-H., Jadhav, J., & Govindwar, S. (2020). In situ textile wastewater treatment in high rate transpiration system furrows planted with aquatic macrophytes and floating phytobeds. *Chemosphere*, *252*, 126513. https://doi.org/10.1016/j.chemosphere.2020.126513

Chen, Z., Zhao, Y., Fan, L., Xing, L., & Yang, Y. (2015). Cadmium (Cd) Localization in Tissues of Cotton (Gossypium hirsutum L.), and Its Phytoremediation Potential for Cd-Contaminated Soils. *Bulletin of Environmental Contamination and Toxicology*, *95*(6), 784–789. https://doi.org/10.1007/s00128-015-1662-x

Cruz, H., Luckman, P., Seviour, T., Verstraete, W., Laycock, B., & Pikaar, I. (2018). Rapid removal of ammonium from domestic wastewater using polymer hydrogels. *Scientific Reports*, *8*(1), 2912. https://doi.org/10.1038/s41598-018-21204-4

Da Costa, R., Ghobril, C., Perrin, P., & Sanson, N. (2024). Adsorption of sodium alginate on calcium carbonate microparticles: Effect of molar mass and composition. *Colloids and Surfaces A: Physicochemical and Engineering Aspects*, *682*, 132782. https://doi.org/10.1016/j.colsurfa.2023.132782

De Meyer, A., Poesen, J., Isabirye, M., Deckers, J., & Raes, D. (2011). Soil erosion rates in tropical villages: A case study from Lake Victoria Basin, Uganda. *CATENA*, *84*(3), 89–98. https://doi.org/10.1016/j.catena.2010.10.001

Ding, Y., Liu, Y., Liu, S., Li, Z., Tan, X., Huang, X., Zeng, G., Zhou, L., & Zheng, B. (2016). Biochar to improve soil fertility. A review. *Agronomy for Sustainable Development*, *36*(2), 36. https://doi.org/10.1007/s13593-016-0372-z

Dixit, R., Wasiullah, Malaviya, D., Pandiyan, K., Singh, U., Sahu, A., Shukla, R., Singh, B., Rai, J., Sharma, P., Lade, H., & Paul, D. (2015). Bioremediation of Heavy Metals from Soil and Aquatic Environment: An Overview of Principles and Criteria of Fundamental Processes. *Sustainability*, *7*(2), 2189–2212. https://doi.org/10.3390/su7022189

Duru Kamacı, U., & Kamacı, M. (2024). Hydrogel beads based on sodium alginate and quince seed nanoparticles for the adsorption of methylene blue. *Inorganic Chemistry Communications*, *160*, 111919. https://doi.org/10.1016/j.inoche.2023.111919

El-Naggar, A., Mosa, A., Ahmed, N., Niazi, N. K., Yousaf, B., Sarkar, B., Rinklebe, J., Cai, Y., & Chang, S. X. (2022). Modified and pristine biochars for remediation of chromium contamination in soil and aquatic systems. *Chemosphere*, *303*, 134942. https://doi.org/10.1016/j.chemosphere.2022.134942

Fageria, N. K., & Nascente, A. S. (2014). *Management of Soil Acidity of South American Soils for Sustainable Crop Production* (pp. 221–275). https://doi.org/10.1016/B978-0-12-802139-2.00006-8

Fu, F., & Wang, Q. (2011). Removal of heavy metal ions from wastewaters: A review. *Journal of Environmental Management*, *92*(3), 407–418. https://doi.org/10.1016/j.jenvman.2010.11.011

Ghaedi, M., Hajjati, S., Mahmudi, Z., Tyagi, I., Agarwal, S., Maity, A., & Gupta, V. K. (2015). Modeling of competitive ultrasonic assisted removal of the dyes – Methylene blue and Safranin-O using Fe3O4 nanoparticles. *Chemical Engineering Journal*, *268*, 28–37. https://doi.org/10.1016/j.cej.2014.12.090

Gonçalo Filho, F., da Silva Dias, N., Suddarth, S. R. P., Ferreira, J. F. S., Anderson, R. G., dos Santos Fernandes, C., de Lira, R. B., Neto, M. F., & Cosme, C. R. (2019). Reclaiming Tropical Saline-Sodic Soils with Gypsum and Cow Manure. *Water*, *12*(1), 57. https://doi.org/10.3390/w12010057

Guo, H., Qin, Q., Chang, J.-S., & Lee, D.-J. (2023). Modified alginate materials for wastewater treatment: Application prospects. *Bioresource Technology*, *387*, 129639. https://doi.org/10.1016/j.biortech.2023.129639

Guo, J. H., Liu, X. J., Zhang, Y., Shen, J. L., Han, W. X., Zhang, W. F., Christie, P., Goulding, K. W. T., Vitousek, P. M., & Zhang, F. S. (2010). Significant Acidification in Major Chinese Croplands. *Science*, *327*(5968), 1008–1010. https://doi.org/10.1126/science.1182570

Gupta, V., Garg, S., Capalash, N., Gupta, N., & Sharma, P. (2015). Production of thermo-alkali-stable laccase and xylanase by co-culturing of Bacillus sp. and B. halodurans for biobleaching of kraft pulp and deinking of waste paper. *Bioprocess and Biosystems Engineering*, *38*(5), 947–956. https://doi.org/10.1007/s00449-014-1340-0

Hassan, M. U., Nawaz, M., Shah, A. N., Raza, A., Barbanti, L., Skalicky, M., Hashem, M., Brestic, M., Pandey, S., Alamri, S., Mostafa, Y. S., Sabagh, A. E. L., & Qari, S. H. (2023). Trehalose: A Key Player in Plant Growth Regulation and Tolerance to Abiotic Stresses. *Journal of Plant Growth Regulation*, *42*(8), 4935–4957. https://doi.org/10.1007/s00344-022-10851-7

Hu, B., Chen, S., Hu, J., Xia, F., Xu, J., Li, Y., & Shi, Z. (2017). Application of portable XRF and VNIR sensors for rapid assessment of soil heavy metal pollution. *PLOS ONE*, *12*(2), e0172438. https://doi.org/10.1371/journal.pone.0172438

Hussain, S., Shaukat, M., Ashraf, M., Zhu, C., Jin, Q., & Zhang, J. (2019). Salinity Stress in Arid and Semi-Arid Climates: Effects and Management in Field Crops. In *Climate Change and Agriculture*. IntechOpen. https://doi.org/10.5772/intechopen.87982

Imran, S., Sarker, P., Hoque, Md. N., Paul, N. C., Mahamud, Md. A., Chakrobortty, J., Tahjib-Ul-Arif, Md., Latef, A. A. H. A., Hasanuzzaman, M., & Rhaman, M. S. (2022). Biochar actions for the mitigation of plant abiotic stress. *Crop & Pasture Science*, *74*(2), 6–20. https://doi.org/10.1071/CP21486

Jianping, Z. (1999). Soil erosion in Guizhou province of China: a case study in Bijie prefecture. *Soil Use and Management*, *15*(1), 68–70. https://doi.org/10.1111/j.1475-2743.1999.tb00067.x

Jin, C. W., Ye, Y. Q., & Zheng, S. J. (2014). An underground tale: contribution of microbial activity to plant iron acquisition via ecological processes. *Annals of Botany*, *113*(1), 7–18. https://doi.org/10.1093/aob/mct249

Kamran, M., Parveen, A., Ahmar, S., Malik, Z., Hussain, S., Chattha, M. S., Saleem, M. H., Adil, M., Heidari, P., & Chen, J.-T. (2019). An Overview of Hazardous Impacts of Soil Salinity in Crops, Tolerance Mechanisms, and Amelioration through Selenium Supplementation. *International Journal of Molecular Sciences*, *21*(1), 148. https://doi.org/10.3390/ijms21010148

Kaur, C., Selvakumar, G., & Ganeshamurthy, A. N. (2019). *Acid Tolerant Microbial Inoculants: A Requisite for Successful Crop Production in Acidic Soils* (pp. 235–247). https://doi.org/10.1007/978-981-32-9664-0_10

Khan, A., Khan, A. L., Muneer, S., Kim, Y.-H., Al-Rawahi, A., & Al-Harrasi, A. (2019). Silicon and Salinity: Crosstalk in Crop-Mediated Stress Tolerance Mechanisms. *Frontiers in Plant Science*, *10*. https://doi.org/10.3389/fpls.2019.01429

Khan, I., & Ghani, A. (2016). Comparative Analysis of Heavy Metal Profile of Brassica campestris (L.) and Raphanus sativus (L.) Irrigated with Municipal Waste Water of Sargodha City. *Journal of Clinical Toxicology*, *6*(3). https://doi.org/10.4172/2161-0495.1000307

Khan, M. D., Abdulateif, H., Ismail, I. M., Sabir, S., & Khan, M. Z. (2015). Bioelectricity Generation and Bioremediation of an Azo-Dye in a Microbial Fuel Cell Coupled Activated Sludge Process. *PLOS ONE*, *10*(10), e0138448. https://doi.org/10.1371/journal.pone.0138448

Laird, D. A., Fleming, P., Davis, D. D., Horton, R., Wang, B., & Karlen, D. L. (2010). Impact of biochar amendments on the quality of a typical Midwestern agricultural soil. *Geoderma*, *158*(3–4), 443–449. https://doi.org/10.1016/j.geoderma.2010.05.013

Li, C., Zhou, K., Qin, W., Tian, C., Qi, M., Yan, X., & Han, W. (2019). A Review on Heavy Metals Contamination in Soil: Effects, Sources, and Remediation Techniques. *Soil and Sediment*

Contamination: An International Journal, *28*(4), 380–394. https://doi.org/10.1080/15320383.2019.1592108

Liang, K., Peng, X., & Liu, F. (2022). Physiological response of Miscanthus genotypes to salinity stress under elevated CO2. *GCB Bioenergy*, *14*(7), 858–874. https://doi.org/10.1111/gcbb.12948

Liang, R., Yuan, H., Xi, G., & Zhou, Q. (2009). Synthesis of wheat straw-g-poly(acrylic acid) superabsorbent composites and release of urea from it. *Carbohydrate Polymers*, *77*(2), 181–187. https://doi.org/10.1016/j.carbpol.2008.12.018

Liu, L., Li, W., Song, W., & Guo, M. (2018). Remediation techniques for heavy metal-contaminated soils: Principles and applicability. *Science of The Total Environment*, *633*, 206–219. https://doi.org/10.1016/j.scitotenv.2018.03.161

Maathuis, F. J. (2009). Physiological functions of mineral macronutrients. *Current Opinion in Plant Biology*, *12*(3), 250–258. https://doi.org/10.1016/j.pbi.2009.04.003

Mali, K. K., Dhawale, S. C., Dias, R. J., Dhane, N. S., & Ghorpade, V. S. (2018). Citric Acid Crosslinked Carboxymethyl Cellulose-based Composite Hydrogel Films for Drug Delivery. *Indian Journal of Pharmaceutical Sciences*, *80*(4). https://doi.org/10.4172/pharmaceutical-sciences.1000405

Mishra, R. K., & Mohanty, K. (2022). Pyrolysis of low-value waste sawdust over low-cost catalysts: physicochemical characterization of pyrolytic oil and value-added biochar. *Biofuel Research Journal*, *9*(4), 1736–1749. https://doi.org/10.18331/BRJ2022.9.4.4

Mohyaldinn, M. E., Alakbari, F. S., Bin Azman Nor, A. N. A., & Hassan, A. M. (2023). Stability, Rheological Behavior, and pH Responsiveness of CTAB/HCl Acidic Emulsion:

Experimental Investigation. *ACS Omega*, *8*(25), 22428–22439. https://doi.org/10.1021/acsomega.2c08243

Msimbira, L. A., & Smith, D. L. (2020). The Roles of Plant Growth Promoting Microbes in Enhancing Plant Tolerance to Acidity and Alkalinity Stresses. *Frontiers in Sustainable Food Systems*, *4*. https://doi.org/10.3389/fsufs.2020.00106

Muradoglu, F., Gundogdu, M., Ercisli, S., Encu, T., Balta, F., Jaafar, H. Z., & Zia-Ul-Haq, M. (2015). Cadmium toxicity affects chlorophyll a and b content, antioxidant enzyme activities and mineral nutrient accumulation in strawberry. *Biological Research*, *48*(1), 11. https://doi.org/10.1186/s40659-015-0001-3

Nawaz, M., Hassan, M. U., Chattha, M. U., Mahmood, A., Shah, A. N., Hashem, M., Alamri, S., Batool, M., Rasheed, A., Thabit, M. A., Alhaithloul, H. A. S., & Qari, S. H. (2022). Trehalose: a promising osmo-protectant against salinity stress—physiological and molecular mechanisms and future prospective. *Molecular Biology Reports*, *49*(12), 11255–11271. https://doi.org/10.1007/s11033-022-07681-x

Neethu, T. M., Dubey, P. K., & Kaswala, A. R. (2018). Prospects and Applications of Hydrogel Technology in Agriculture. *International Journal of Current Microbiology and Applied Sciences*, *7*(05), 3155–3162. https://doi.org/10.20546/ijcmas.2018.705.369

Ng, J. F., Ahmed, O. H., Jalloh, M. B., Omar, L., Kwan, Y. M., Musah, A. A., & Poong, K. H. (2022). Soil Nutrient Retention and pH Buffering Capacity Are Enhanced by Calciprill and Sodium Silicate. *Agronomy*, *12*(1), 219. https://doi.org/10.3390/agronomy12010219

Ogunlade, M. O., & Agbeniyi, S. O. (2011). Impact of pesticides use on heavy metals pollution in cocoa soils of Cross-River State, Nigeria. *African Journal of Agricultural Research*, *6*(16), 3725–3728. https://doi.org/10.5897/AJAR10.541

Oguntunde, P. G., Fosu, M., Ajayi, A. E., & van de Giesen, N. (2004). Effects of charcoal production on maize yield, chemical properties and texture of soil. *Biology and Fertility of Soils*, *39*(4), 295–299. https://doi.org/10.1007/s00374-003-0707-1

Okiemute Akpasi, S., Michael Smarte Anekwe, I., Adedeji, J., & Lewis Kiambi, S. (2023). Biochar Development as a Catalyst and Its Application. In *Biochar - Productive Technologies, Properties and Applications*. IntechOpen. https://doi.org/10.5772/intechopen.105439

Oladosu, Y., Rafii, M. Y., Arolu, F., Chukwu, S. C., Salisu, M. A., Fagbohun, I. K., Muftaudeen, T. K., Swaray, S., & Haliru, B. S. (2022). Superabsorbent Polymer Hydrogels for Sustainable Agriculture: A Review. *Horticulturae*, *8*(7), 605. https://doi.org/10.3390/horticulturae8070605

Oladosu, Y., Rafii, M. Y., Samuel, C., Fatai, A., Magaji, U., Kareem, I., Kamarudin, Z. S., Muhammad, I., & Kolapo, K. (2019). Drought Resistance in Rice from Conventional to Molecular Breeding: A Review. *International Journal of Molecular Sciences*, *20*(14), 3519. https://doi.org/10.3390/ijms20143519

Pourjavadi, A., Doulabi, M., Soleyman, R., Sharif, S., & Eghtesadi, S. A. (2012). Synthesis and characterization of a novel (salep phosphate)-based hydrogel as a carrier matrix for fertilizer release. *Reactive and Functional Polymers*, *72*(10), 667–672. https://doi.org/10.1016/j.reactfunctpolym.2012.06.010

Ramli, R. A. (2019). Slow release fertilizer hydrogels: a review. *Polymer Chemistry*, *10*(45), 6073–6090. https://doi.org/10.1039/C9PY01036J

Raza, A., Tabassum, J., Fakhar, A. Z., Sharif, R., Chen, H., Zhang, C., Ju, L., Fotopoulos, V., Siddique, K. H. M., Singh, R. K., Zhuang, W., & Varshney, R. K. (2023). Smart reprograming of plants against salinity stress using modern biotechnological tools. *Critical*

Reviews in Biotechnology, *43*(7), 1035–1062. https://doi.org/10.1080/07388551.2022.2093695

Rehman, T. U., Shah, L. A., Khan, M., Irfan, M., & Khattak, N. S. (2019). Zwitterionic superabsorbent polymer hydrogels for efficient and selective removal of organic dyes. *RSC Advances*, *9*(32), 18565–18577. https://doi.org/10.1039/C9RA02488C

Rengasamy, P. (2010). Soil processes affecting crop production in salt-affected soils. *Functional Plant Biology*, *37*(7), 613. https://doi.org/10.1071/FP09249

Sá, A. A. de, & Ernani, P. R. (2016). Boron Leaching Decreases withIncreases on Soil pH. *Revista Brasileira de Ciência Do Solo*, *40*(0). https://doi.org/10.1590/18069657rbcs20150008

Sarvajith, M., Reddy, G. K. K., & Nancharaiah, Y. V. (2018). Textile dye biodecolourization and ammonium removal over nitrite in aerobic granular sludge sequencing batch reactors. *Journal of Hazardous Materials*, *342*, 536–543. https://doi.org/10.1016/j.jhazmat.2017.08.064

Singh, S. K., Srivastava, R. K., & John, S. (2009). Studies on soil contamination due to used motor oil and its remediation. *Canadian Geotechnical Journal*, *46*(9), 1077–1083. https://doi.org/10.1139/T09-047

Sojobi, A. O., & Zayed, T. (2022). Impact of sewer overflow on public health: A comprehensive scientometric analysis and systematic review. *Environmental Research*, *203*, 111609. https://doi.org/10.1016/j.envres.2021.111609

Soni, V., Keswani, K., Bhatt, U., Kumar, D., & Singh, H. (2021). In vitro propagation and analysis of mixotrophic potential to improve survival rate of Dolichandra unguis-cati under ex vitro conditions. *Heliyon*, *7*(2), e06101. https://doi.org/10.1016/j.heliyon.2021.e06101

Sumner, M. E., Fey, M. V., & Noble, A. D. (1991). Nutrient Status and Toxicity Problems in Acid Soils. In *Soil Acidity* (pp. 149–182). Springer Berlin Heidelberg. https://doi.org/10.1007/978-3-642-74442-6_7

Sun, W. H., Jiang, Y. X., & Li, X. (2013). Research of the Evaluation on Heavy-Metal Pollution in Rice by Sewage Irrigation. *Applied Mechanics and Materials*, *295–298*, 1594–1599. https://doi.org/10.4028/www.scientific.net/AMM.295-298.1594

Tavakoli Kivi, S., & Bailey, R. T. (2017). Modeling sulfur cycling and sulfate reactive transport in an agricultural groundwater system. *Agricultural Water Management*, *185*, 78–92. https://doi.org/10.1016/j.agwat.2017.02.002

Wan Mahari, W. A., Waiho, K., Azwar, E., Fazhan, H., Peng, W., Ishak, S. D., Tabatabaei, M., Yek, P. N. Y., Almomani, F., Aghbashlo, M., & Lam, S. S. (2022). A state-of-the-art review on producing engineered biochar from shellfish waste and its application in aquaculture wastewater treatment. *Chemosphere*, *288*, 132559. https://doi.org/10.1016/j.chemosphere.2021.132559

Wuana, R. A., & Okieimen, F. E. (2011). Heavy Metals in Contaminated Soils: A Review of Sources, Chemistry, Risks and Best Available Strategies for Remediation. *ISRN Ecology*, *2011*, 1–20. https://doi.org/10.5402/2011/402647

Xiong, X., Yu, I. K. M., Tsang, D. C. W., Bolan, N. S., Sik Ok, Y., Igalavithana, A. D., Kirkham, M. B., Kim, K.-H., & Vikrant, K. (2019). Value-added chemicals from food supply chain wastes: State-of-the-art review and future prospects. *Chemical Engineering Journal*, *375*, 121983. https://doi.org/10.1016/j.cej.2019.121983

Yashas Gowda, T. G., Sanjay, M. R., Subrahmanya Bhat, K., Madhu, P., Senthamaraikannan, P., & Yogesha, B. (2018). Polymer matrix-natural fiber composites: An overview. *Cogent Engineering*, *5*(1), 1446667. https://doi.org/10.1080/23311916.2018.1446667

Yek, P. N. Y., Cheng, Y. W., Liew, R. K., Wan Mahari, W. A., Ong, H. C., Chen, W.-H., Peng, W., Park, Y.-K., Sonne, C., Kong, S. H., Tabatabaei, M., Aghbashlo, M., & Lam, S. S. (2021). Progress in the torrefaction technology for upgrading oil palm wastes to energy-dense biochar: A review. *Renewable and Sustainable Energy Reviews*, *151*, 111645. https://doi.org/10.1016/j.rser.2021.111645

Zhang, H., Voroney, R. P., & Price, G. W. (2015). Effects of temperature and processing conditions on biochar chemical properties and their influence on soil C and N transformations. *Soil Biology and Biochemistry*, *83*, 19–28. https://doi.org/10.1016/j.soilbio.2015.01.006

Zhang, M., Muhammad, R., Zhang, L., Xia, H., Cong, M., & Jiang, C. (2019). Investigating the effect of biochar and fertilizer on the composition and function of bacteria in red soil. *Applied Soil Ecology*, *139*, 107–116. https://doi.org/10.1016/j.apsoil.2019.03.021

Zhang, W., Wei, J., Guo, L., Fang, H., Liu, X., Liang, K., Niu, W., Liu, F., & Siddique, K. H. M. (2023). Effects of Two Biochar Types on Mitigating Drought and Salt Stress in Tomato Seedlings. *Agronomy*, *13*(4), 1039. https://doi.org/10.3390/agronomy13041039

Zhao, L., Huang, J., Zhang, Y., Wang, T., Sun, W., & Tong, Z. (2017). Programmable and Bidirectional Bending of Soft Actuators Based on Janus Structure with Sticky Tough PAA-Clay Hydrogel. *ACS Applied Materials & Interfaces*, *9*(13), 11866–11873. https://doi.org/10.1021/acsami.7b00138

Zhu, K., Hopwood, M. J., Groenenberg, J. E., Engel, A., Achterberg, E. P., & Gledhill, M. (2021). Influence of pH and Dissolved Organic Matter on Iron Speciation and Apparent Iron Solubility in the Peruvian Shelf and Slope Region. *Environmental Science & Technology*, *55*(13), 9372–9383. https://doi.org/10.1021/acs.est.1c02477

Chapter 2: Performance of hydrogel beads and biochar composites toward dyes adsorption from aqueous solution

2.1 Introduction

The continued expansion of the industrial sector inevitably leads to various environmental problems, due to the usage of enormous amounts of chemicals (Karimifard & Alavi Moghaddam, 2018). In particular, the availability of safe water is one of the most serious global challenges owing to the limited access to freshwater. Rivers are important sources of drinking water and also help maintain diverse aquatic ecosystems that provide food sources for humans and animals. Rivers are an important component of Earth's landforms and carry nutrients to the oceans by flowing water from sedimentary areas. However, they have been considered sites for dumping undesirable materials and chemicals by careless people and businesses. The primary threat to water security is the unmitigated release of pollutants of diverse origins directly into aquatic ecosystems without sufficient treatment (Wong et al., 2020). Organic dyes, which are commonly used to color clothing, are pollutants that need to be treated for environmental protection. In particular, azo dyes, identified by the presence of azo (-N=N-) groups, are toxic, carcinogenic, and mutagenic to organisms.

Several traditional chemical, physical, and biological techniques have been shown to effectively eliminate azo dye pollutants. However, concerns persist regarding their operational expenses, removal efficacy, and the potential creation of secondary pollutants (Piaskowski et al., 2018). Amongst all the efficient removal method, adsorption has emerged as a successful strategy for removing azo dyes from water. This method is not only economically viable, but also boasts a remarkable retention efficiency while avoiding the generation of secondary pollution (Liang et al., 2020; Srivatsav et al., 2020). In this regard, different types of materials have been explored as potential adsorbent which are classified into two types: porous and non-porous. Examples of nonporous adsorbents include barium sulfate and graphite soot (Wiśniewska et al., 2017) whereas porous adsorbents such as metal-organic frameworks (MOF) (Au, 2020) and polymer-coated MCM-41 (Torabinejad et al., 2017) have been utilized for the adsorption of synthetic dyes. However, better adsorbent qualities, such as fast adsorption and superior mechanical strength for repeated use, are still required.

Hydrogel beads are three-dimensional, crosslinked polymer networks capable of absorbing and retaining large volumes of water or aqueous solutions (Baigorria et al., 2020). Their tuneable properties, such as porosity, swelling behaviour, and surface chemistry, make them highly suitable for various applications, including water purification (Chen et al., 2022). By integrating specific functional groups or additives, hydrogel beads can be tailored to selectively adsorb target pollutants, such as dyes. Among the materials used in hydrogel bead synthesis, sodium alginate derived from brown algae, stands out as a biocompatible, renewable, and economically viable option (Frent et al., 2022; Hidayat, Sarbani, Lahiri, et al., 2024; Tang et al., 2018). Calcium cations are frequently employed in crosslinking sodium alginate, leading to ion exchange and the formation of Ca alginate hydrogel. Furthermore, its molecular structure contains numerous hydroxyl (-OH) and carboxyl (-COOH) groups, making it an environmentally friendly choice for variety of dye molecules productivity (Merakchi et al., 2019; Thakur & Arotiba, 2018).

On the other hand, biochar has appeared as one of the potentially effective adsorbents in recent years owing to its low cost, environmental friendliness, abundance, and carbon-rich nature. Biochar was created by pyrolysis in the temperature range between 500-800 °C under oxygen-limited conditions (Chatterjee et al., 2020). Owing to its highly porous structure and large surface area, it is ideal for adsorption applications (Lita et al., 2023). Several studies have successfully used biochar from biomass, including the brown seaweed *Turbinaria conoides* (Vijayaraghavan & Ashokkumar, 2019), *Cocos nucifera* shell (Saravanan et al., 2020), mycelia biomass from *Exserohilum rostratum* NMS1.5 (Hidayat, Khaekhum, et al., 2022), agriculture waste (Moharm et al., 2022), sewage sludge (Jellali et al., 2022), and cattle manure (Zhu et al., 2018).

Moreover, it is noteworthy that coffee is a very profitable commodity globally, ranking second only to petroleum in terms of revenue (Campos-Vega et al., 2015). By 2021/2022, it amounted to 2.4 billion kilograms of global coffee production (Silveira Junior et al., 2023). Coffee processing produces by-products, one of which is coffee husk. The total quantity of coffee husk produced is estimated to be 0.3 billion tons, calculated by considering that 6% of coffee husk is generated by 48% of coffee plants (Hidayat et al., 2021). Typically, this coffee husk is discarded after coffee processing by producers, which could pose an environmental risk if not appropriately managed. Thus, these materials have the potential to be viable alternatives as biochar. The chemical activation of biochar adsorbents is necessary to increase the adsorption capacity. This can be successfully attained by reinforcing the functional groups and increasing the surface area and the adsorption capacity (Tran et al., 2021). Several chemicals, such as potassium hydroxide (KOH), peroxymonosulfate, sodium hydroxide (NaOH), aluminium chloride ($AlCl_3$), and phosphoric acid (H_3PO_4), have been used to remove water pollutants, including Methylene blue (Tran et al., 2021), Tetracycline (H. Liu et al., 2021), Ciprofloxacin (Sun et al., 2016), Methyl orange (B. Zhang et al., 2020), Rhodamine B (Ouyang et al., 2023), and Reactive black 5 (Tsoutsa et al., 2023). However, these studies used a hydrothermal approach at temperatures above 100 °C to activate biochar, which requires much energy. Thus, activation at room temperature (25-30 ºC) is a practical technique for enhancing the number of adsorbent surface sites, as well as improve the adsorption capacity, and as a novel material.

In this chapter, we would like to evaluate the feasibility of using hydrogel bead derived from sodium alginate and biochar from coffee husk for dyes adsorption. It is expected that this research could address the lack of comprehensive studies on the properties, characterization, and application of both hydrogel bead and biochar composite as adsorbent.

2.2 Material and method

2.2.1 Materials

Congo red dye (CR), Acid Black 1 dye (AB1), and Indigo Carmine (IC), calcium chloride ($CaCl_2$), Ferric Chloride ($FeCl_3$), hydrochloric acid (HCl) and sodium hydroxide (NaOH) were supplied from Kanto Chemical Co. Inc., Japan. Sodium alginate (SA) and Cetyltrimethylammonium bromide (CTAB) were purchased from Wako Chemical Industries, Osaka, Japan. Poly (acrylic acid) (MW: 100,000) was purchased from Scientific Polymer Products, INC, New York.

2.2.2 Sample preparation

2.2.2.1 Performance of hydrogel beads composites derived from sodium alginate-cetyltrimethylammonium bromide toward congo red dye adsorption from aqueous solution

Preparation of hydrogel beads was done by mixing 20 mL of 1 wt.% SA solution and 2 mL of CTAB aqueous solution with difference concentration: 0.1 wt.%, 1 wt.% and 3 wt.%, referred as SC1, SC2 and SC3, respectively. After the solution was put into bottle flasks, it was shaken for 30 minutes at ambient temperature using a rotary shaker (Rotator RT-50). The solution was then gradually injected into 4 wt.% $CaCl_2$ aqueous solution by using a 10 mL syringe. Next, the sample was allowed to cure for a full night in order to produce hydrogel beads. Afterward, the beads were allowed to dry in an oven for 24 hours at 60 °C after being cleaned with ethanol and deionized water (DI).

2.2.2.2. Porous sodium alginate/poly (acrylic acid) composites cross-linked with $FeCl_3$ for acid black 1 dye removal from aqueous solution

The SA/PAA-Fe adsorbents were synthesized using the following procedure. A mixture containing 6 mL of aqueous SA solution with 1 wt% concentration, 6 mL of aqueous PAA solution (5 wt%), 1 mL of 3M NaOH solution, and 1 mL of distilled water was prepared in a bottle flask. The mixture was then stirred with a magnetic stirrer for one hour at room temperature. The mixture was introduced dropwise into a 10 wt% aqueous $FeCl_3$ solution using a syringe. After 90 min, the SA/PAA-Fe was then washed using ethanol and distilled water and then dried at 60 °C for 24 h. The collected adsorbent was pulverized using a mortar and sieved to ≤ 425 μm for further experiments.

2.2.2.3 Performance of unactivated and activated coffee husk biochar under room temperature using HNO_3 and $NaHCO_3$ for indigo carmine dye adsorption from water

2.2.3 Adsorption experiments

A series of experiments were executed to examine the impacts of several factors, such as initial pH, dyes concentration, and adsorption duration, on the elimination of dyes. Batch adsorption trials were performed by submerging the sample in 50 mL of dyes solution. The remaining concentration of dyes after the experiment was analyzed using a UV-Vis spectrophotometer (JASCO V-530) at a wavelength of 562, 621, and 612 nm for congo red, acid black 1, and indigo carmine, respectively. The formulas utilized for computing the removal percentage (Removal, %) (Eq. 1) and adsorption equilibrium quantity (q_e, mg/g) (Eq. 2) are outlined below.

$$\text{Removal }\% = \frac{C_i - C_e}{C_i} \times 100 \tag{1}$$

$$q_e = \frac{C_i - C_e}{W} \times V \tag{2}$$

where *Removal* % represents the efficiency of removal, with C_i and C_e denoting the initial and equilibrium concentrations of dyes (mg/L), respectively. q_e stands for the adsorption capacity at equilibrium of the adsorbent (mg/g), while W signifies the quantity of adsorbent (g), and V indicates the volume of the dyes solution (L).

2.2.4 Determination of carboxyl groups

A technique of conductometric titration was utilized to quantify the carboxyl (COOH) group of the hydrogel beads (H. Yang et al., 2012). To achieve homogenous distribution, the dried hydrogel bead was incorporated with 2.5 mL of 20 mM NaCl solution for 30 min. Then, HCl was added into the mixture until the pH to achieve pH 3.0. Afterward, the mixture solution then incrementally adjusted to pH of 11.0 using a NaOH solution. The content of COOH group inside the hydrogel beads was assessed using the following Eq. (3).

$$\text{Carboxyl group content, COOH (mmol/g)} = \frac{V_{NaOH} \times M_{NaOH}}{W_d} \tag{3}$$

where V_{NaOH} (mL) is the NaOH volume needed to deprotonate COOH groups. M_{NaOH} (mol/L) is the concentration of NaOH, while W_d (g) represents the initial weight of dry hydrogel beads.

2.2.5 Swelling properties

The swelling properties of the hydrogel composites were assessed using DI by performing the experiment using batch shaker for 24 h at room temperature. The percentage of swelling was estimated by applying the Eq. (4).

$$\text{Swelling, \%} = \frac{W_s - W_d}{W_d} \times 100 \tag{4}$$

where W_s and W_d represent the weights of swollen hydrogel beads and dried hydrogel beads, respectively.

2.2.6 Analytical measurements

FTIR spectra were acquired utilizing a Thermo Scientific Nicolet iS10 instrument (Thermo Fisher Scientific Inc., Waltham, MA, USA) both prior to and after CR adsorption. The morphology of adsorbent were observed via scanning electron microscopy (SEM) (Miniscope TM3000, Hitachi-hitech, Tokyo, Japan). The pH_{zpc} value, indicative of the neutral surface charge was determined. Dried hydrogel beads were immersed with 10 mM NaCl with different pH between 2 and 10, then mixed for 24 h under room temperature. The pH_{zpc} calculated using the equation: $\Delta pH = pH\text{-final} - pH\text{-initial}$ (Hidayat, Yoshino, et al., 2022).

2.3 Results and discussion

2.3.1 Performance of hydrogel beads composites derived from sodium alginate-cetyltrimethylammonium bromide toward congo red dye adsorption from aqueous solution

2.3.1.1 Characterization of hydrogel beads

The morphology of hydrogel beads before and after CR adsorption acquired using Scanning electron microscopy (SEM) is presented in Figure. 5. According to Figure. 5, all samples exhibit a rough and wrinkle surface before adsorption experiment. The SC3 sample which contains the highest percentage of CTAB (3 wt.%) has a rougher surface with multiple crystal-like shapes on its surface. After CR adsorption process, all of the samples showed changes on their morphology by becoming slightly smooth. It can be observed that there is a pore present on the surface of SC1 sample after adsorption.

Table 1. Characteristics of hydrogel bead

Sample	Swelling (%)	COOH (mmol/g)
SC1	49.67 ± 5.84	0.40 ± 0.06
SC2	96.50 ± 0.98	0.38 ± 0.03
SC3	162.28 ± 8.92	0.28 ± 0.06

Table 1 depicts the swelling percentage and the carboxyl groups content present in the hydrogel beads. The swelling percentage data demonstrate that higher CTAB concentration led to increase in swelling percentage. This is probably due to CTAB molecules that are amphiphilic, meaning they have both hydrophilic and hydrophobic parts. When CTAB concentration is high, the hydrophilic parts of the molecules may interact more strongly with the polymer chains, making the hydrogel beads more hydrophilic overall. This increased hydrophilicity can increase the affinity of the hydrogel towards water, thereby increasing swelling percentage.

Likewise, increase CTAB concentrations may lead to a decline in the COOH content of the hydrogel bead composite. This could be attributed to the competitive binding of CTAB, which competes for available binding sites on the alginate polymer chains. As CTAB molecules bind to these chains, they may occupy sites that would otherwise be utilized by Ca ions for cross-linking the alginate molecules. This competition for binding sites ultimately reduces the overall cross-linking density of the hydrogel beads, subsequently decreasing the COOH content.

The FTIR spectra of the hydrogel bead before and after CR adsorption are depicted in Figure. 6. The peak in the range of 3200 cm^{-1} to 3500 cm^{-1} corresponds to OH groups (Modrzejewska, 2013a). A new peak emerged after CR adsorption in the range of 2849 cm^{-1} to 2920 cm^{-1}, attributed to methylene group (Aslam & Javed, 2023). Another peak at approximately 1590 cm^{-1}, assigned to the stretching of $–COO^{-}$ (Patel et al., 2021; Qurrat-Ul-Ain et al., 2019), and a peak at around 1023 cm^{-1} representing the C-O stretching vibrations (Merakchi et al., 2019). IR analysis suggest that intermolecular forces involving the functional components of hydrogel beads and CR dye molecules likely contribute to dye adsorption, alongside with electrostatic attraction. Possible mechanisms of CR dye adsorption onto hydrogel bead composite as shown in Figure. 13.

2.3.1.2 Initial pH effect analysis

The pH level of solution influences both the charged state of the CR and the charge surface of the hydrogel bead (Naushad et al., 2017). Figure. 8a illustrates the adsorption behaviour of CR as the pH of the CR solution varies. The removal percentage initially increases, and then decreases within the pH range of 2 to 9. The graph shows that pH 2 provides optimal condition for SC1, SC2 and SC3, resulting in an optimum removal percentage of 70.75%, 78.55% and 77.47%, respectively. Figure. 8b show the surface charges of the hydrogel bead. The data revealed that the samples, namely, SC1, SC2 and SC3 exhibited negative charges below pH_{zpc} values of 4.2, 2.6 and 4.0, respectively, while CR dye exhibits a positive charge under acidic conditions due to protonation. This observation indicates that the electrostatic attraction between the hydrogel beads and CR dye. A comparable outcomes of CR adsorption onto CTAB modified pumice (Shayesteh et al., 2016) and tea waste (Foroughi-dahr et al., 2015) have been reported.

The adsorption of CR onto hydrogel beads was examined by adjusting the initial CR concentration in the range of 5 to 40 mg/L. This experiment was conducted for 30 min, at pH 4 for SC1, SC2 and SC3, respectively, and an adsorbent dosage of 10 mg/50 mL. The results demonstrated that increasing the CR concentration to 40 mg/L resulted in enhanced CR adsorption capacity in the hydrogel beads for all samples (Figure. 9). As the initial CR concentration increases, a greater concentration gradient is established between the CR solution and the hydrogel bead surface. This amplifies the driving force for adsorption, thereby attracting and capturing more CR dye molecules onto the hydrogel bead material.

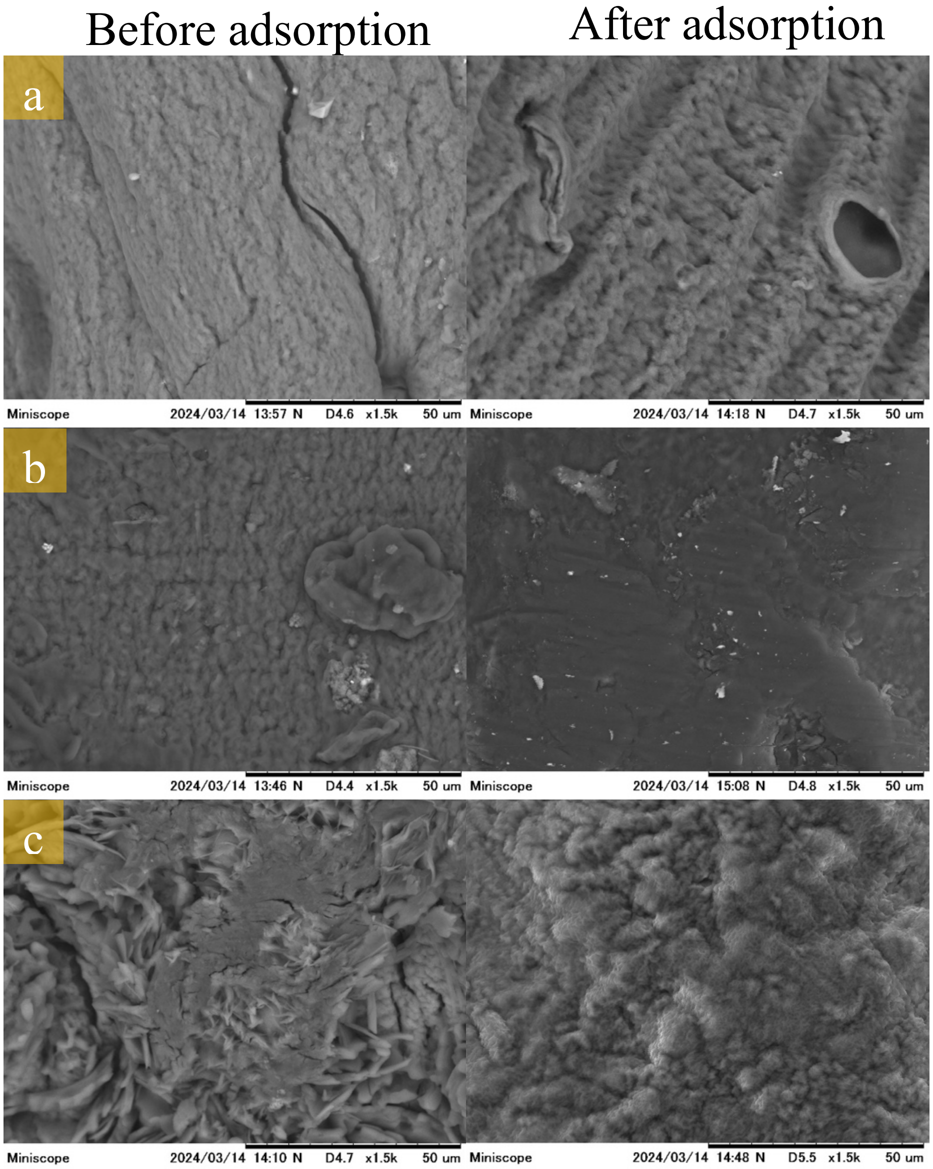

Figure. 5. SEM morphology of hydrogel beads (a) SC1 (b) SC2 (c) SC3.

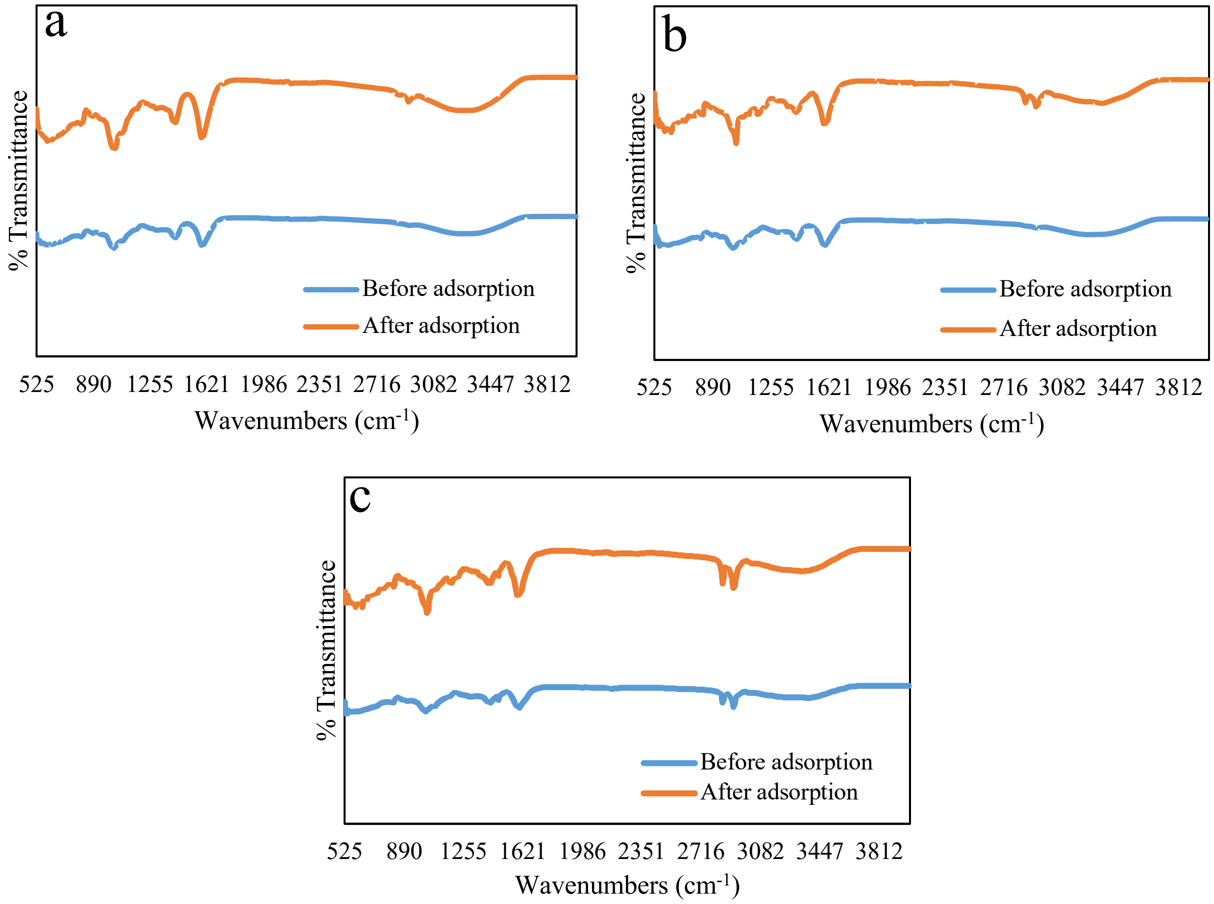

Figure. 6. FTIR spectra of hydrogel bead before and after CR adsorption. (a) SC1 (b) SC2 (c) SC3.

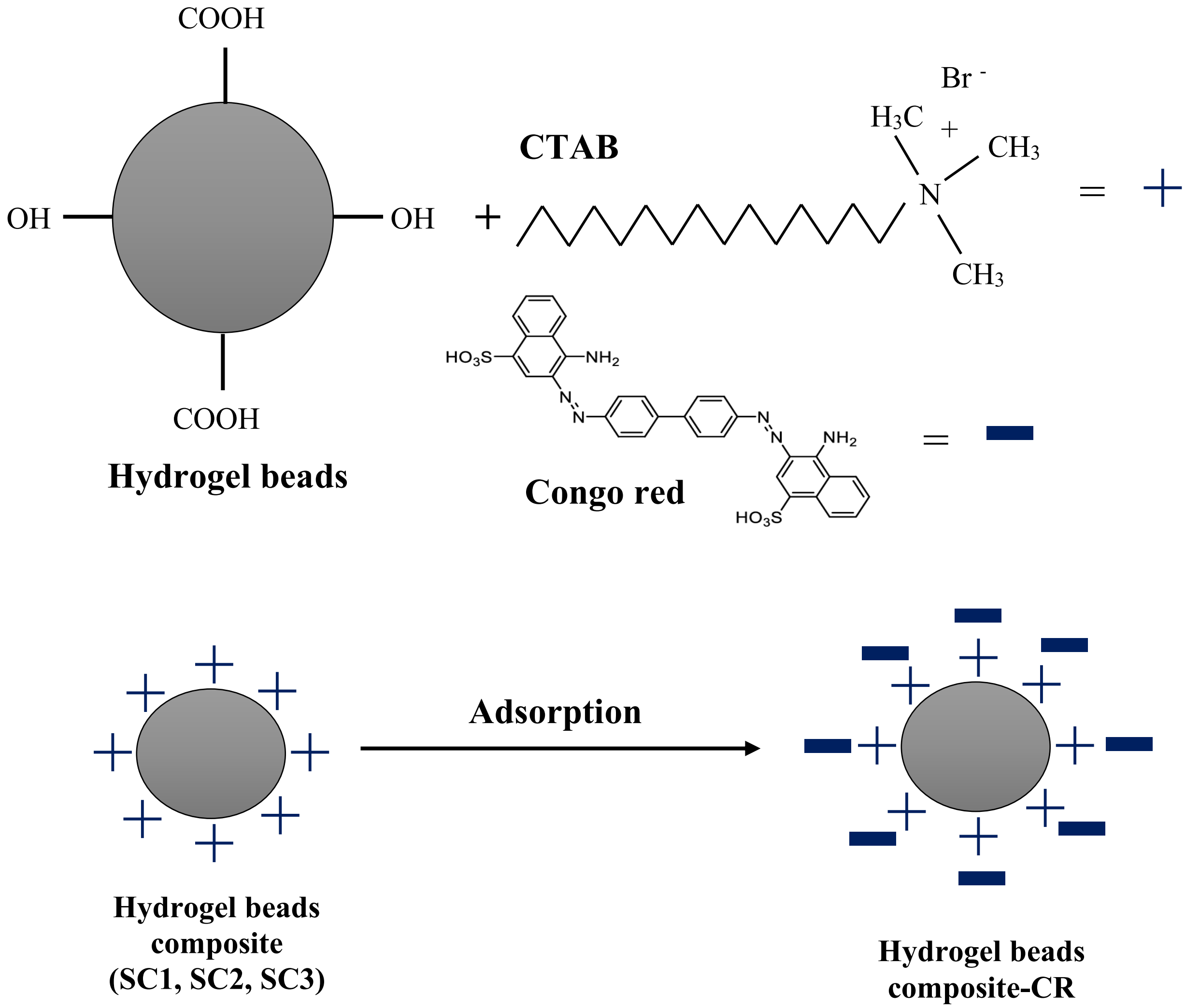

Figure. 7. Proposed mechanisms of CR adsorption.

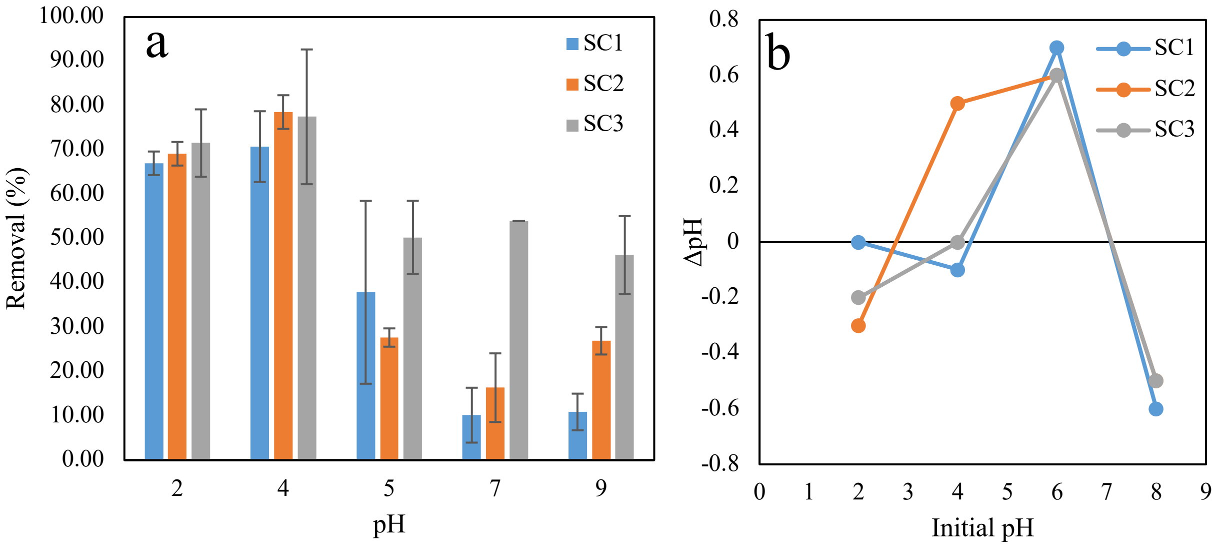

Figure. 8. (a) Effect of pH versus removal percentage (b) surface charge of hydrogel beads.

2.3.1.3 Initial concentration effect analysis

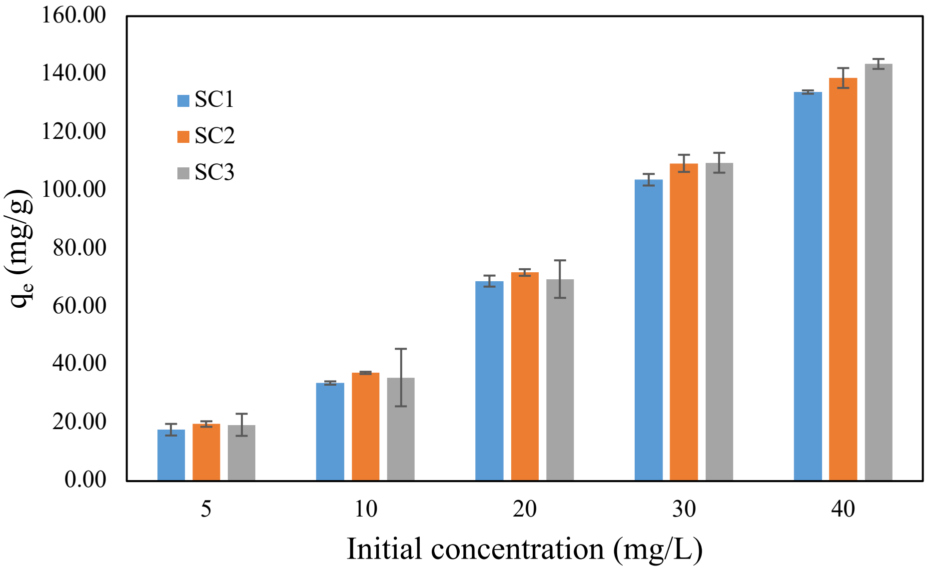

Figure. 9. Effect of initial CR concentration versus adsorption capacity. Initial pH 4 for SC1, SC2 and SC3.

2.3.1.4 Adsorption isotherm analysis

The adsorption isotherm helps to clarify the relation between the adsorbent hydrogel bead and CR dye, thereby enhancing our comprehension of the adsorption process. In this study, we utilized Langmuir (Eq. 5) and Freundlich (Eq. 6) models to evaluate the data derived from the adsorption experiments. Table 2 presents the linear regression coefficient (R^2) values obtained from Figure. 7, along with additional characteristics of the adsorption isotherms. The result observed show that Freundlich model suit the adsorption data compared to the Langmuir model across all samples, as indicated by the higher R^2 values. The 1/n values showed indicate a favourable adsorption process as the value being less than 1. These results suggest that a multilayer-like adsorption occurred at the adsorption sites of hydrogel beads.

$$C_e/q_e = \left(\frac{C_e}{q_{max}}\right)+1/(K_L q_{max}) \tag{5}$$

$$\ln q_e = \ln K_F + \frac{1}{n} \ln C_e \tag{6}$$

In this context, q_e (mg/g) represents the adsorption capacity, C_e (mg/L) denotes the equilibrium concentration, q_{max} (mg/g) signifies the maximum adsorption capacity, R_L indicates a coefficient reflecting the stronger of adsorption, K_L (L/mg) and K_F (mg/g) represent the equilibrium constants of adsorption, and *1/n* signifies the adsorption intensity.

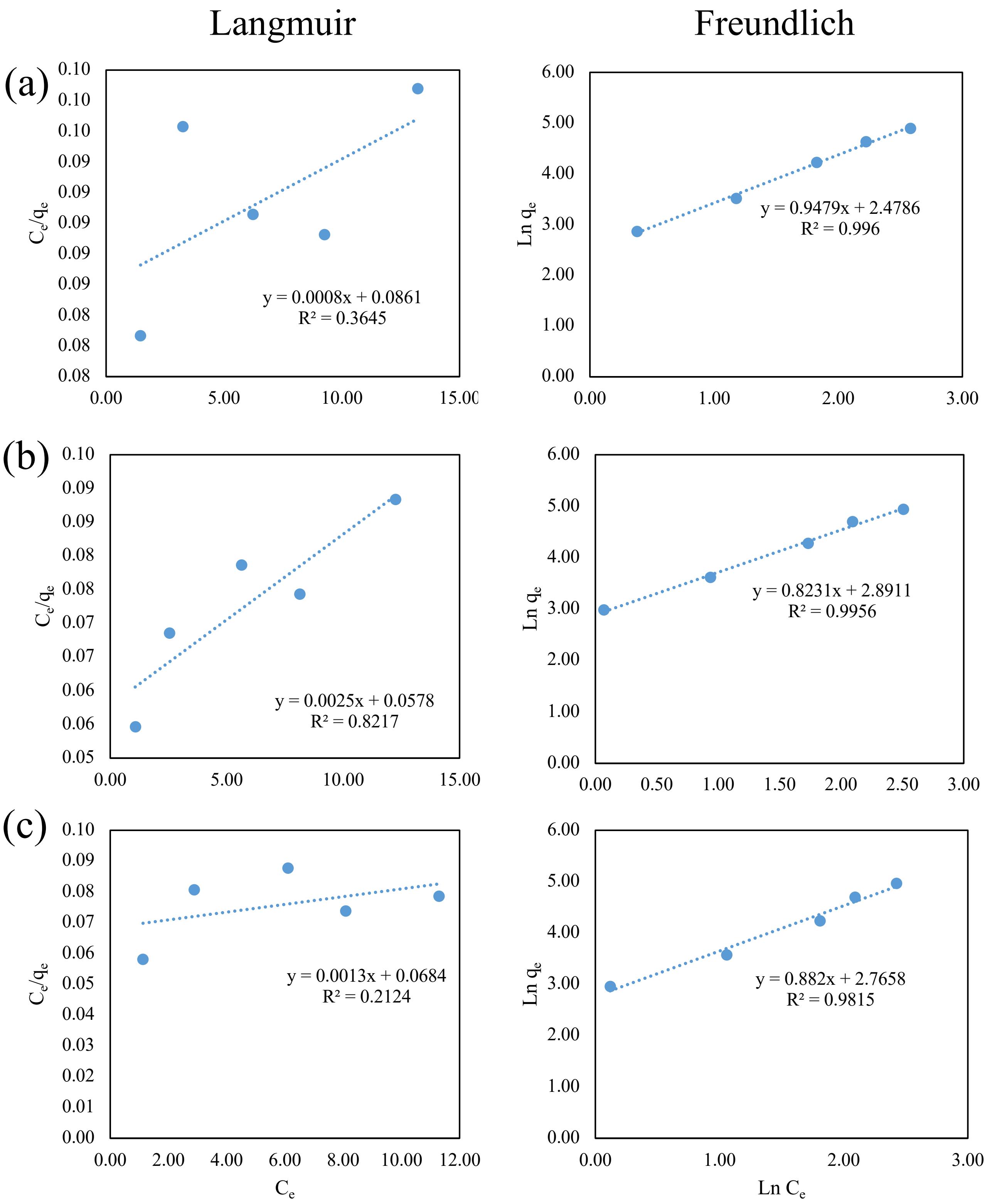

Figure. 10. Isotherm model of CR adsorption (a) SC1 (b) SC2 (c) SC3.

2.3.1.5 Adsorption kinetic analysis

An adsorption kinetic model serves as a mathematical framework employed to depict the pace of adsorption progression as time elapses. These models are designed to elucidate the underlying mechanisms and dynamics of adsorption phenomena by quantifying alterations in the concentration of the adsorbate (CR dye) within the adsorbent (hydrogel bead) over time. The impact of varying adsorption durations (30-1440 min) on the adsorption of CR using hydrogel bead at a concentration of 40 mg/L is shown in Figure. 11. The observations indicate that the adsorption of CR fluctuated over a period of 1440 minutes for all hydrogel bead samples. This evidenced that a higher concentration of CTAB in the hydrogel beads resulted in an increased adsorption capacity for the CR dye. This suggests that the swelling rate and COOH group content (Table 1) affect the adsorption of CR dye. Ultimately, equilibrium was reached after 1440 minutes, with adsorption capacity of 141.08 mg/g, 144.50 mg/g, and 153.24 mg/g for SC1, SC2, and SC3, respectively.

The kinetic data provided significant insights on the adsorption process. The data collected from the CR adsorption on the hydrogels were examined using kinetic models: the first-order in Eq. (7) and second order models in Eq. (8).

Table 2. Isotherm model parameters for adsorption CR dye.

Isotherm models	Parameters	Sample		
		SC1	SC2	SC3
Langmuir	R^2	0.3645	0.8217	0.2124
Freundlich		0.996	0.9956	0.9815
Freundlich	K_f (g/mg min^{-1})^n	301.0243	778.2555	583.2367
	1/n	0.9479	0.8231	0.8820

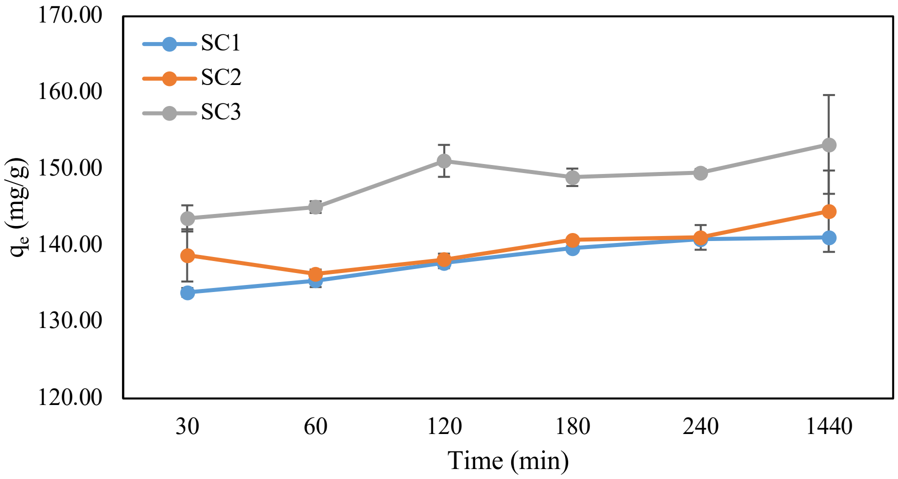

Figure. 11. Effect of contact time versus adsorption capacity. Initial pH: 4, Initial CR concentration: 40 mg/L.

$$\log(q_e - q_t) = \log q_e - K_1 t \tag{7}$$

$$t/q_t = 1/(K_2 q_e^2) + t/q_e \tag{8}$$

where K_1 (min^{-1}) is the rate constant of the pseudo-first-order model and t (min) is the time. K_2 is the constant rate of pseudo-second-order models.

Table 3. Kinetic model parameters for adsorption CR dye.

Kinetic models	Parameters	Sample		
		SC1	SC2	SC3
First-order	R^2	0.1528	0.882	0.6605
Second-order		1	1	1
Second-order	q_e (mg/g)	140.8451	144.9275	153.8462
	K_2 (g/mg min^{-1})	0.0034	0.0015	0.0016

Figure. 12 and Table 3 show the linear correlation coefficients and kinetic variables for CR adsorption. The first-order kinetic model obtained a significantly lower R^2 value than the second-order kinetic model for all hydrogel bead samples. Thus, the adsorption process is regulated by chemisorption. The finding was corresponded with previous studies conducted by K(Hidayat, Mohamad Sarbani, et al., 2023a; Sami et al., 2018) who used CS/ZL/ZrO/Fe_3O_4 and chitosan polyacrylamide hydrogels for phosphate and CR adsorption, respectively.

2.3.1.6 Regeneration of CR dye adsorption

Studying the regeneration of CR dye adsorption is crucial for comprehending the adsorbent's efficacy in capturing CR molecules repeatedly. In the analysis of hydrogel bead regeneration, a combination of acetone and DI water was employed to cleanse the CR dye from the adsorbent surface. Figure. 10 illustrates the reusability of this hydrogel for up to three cycles. The findings indicate that SC1 exhibited fluctuating trends of increase and decrease, whereas SC2 displayed a consistent decrease. Conversely, SC3 demonstrated a stable performance in adsorption capacity. From this, it can be inferred that the concentration of CTAB has an impact on CR dye adsorption.

2.3.1.7 Comparison between SC1, SC2, SC3 and other adsorbents to remove CR dye

To evaluate the efficacy of this adsorbent, it is notable to compare the adsorption capacity (q_e) of the SC1, SC2, and SC3 adsorbents towards the anionic CR dye, with those of previously published adsorbents, as shown in Table 4. Of all the adsorbents reported in the literature, it can be certainly differentiated that SC1, SC2, and SC3 show the greatest q_e for CR dye adsorption.

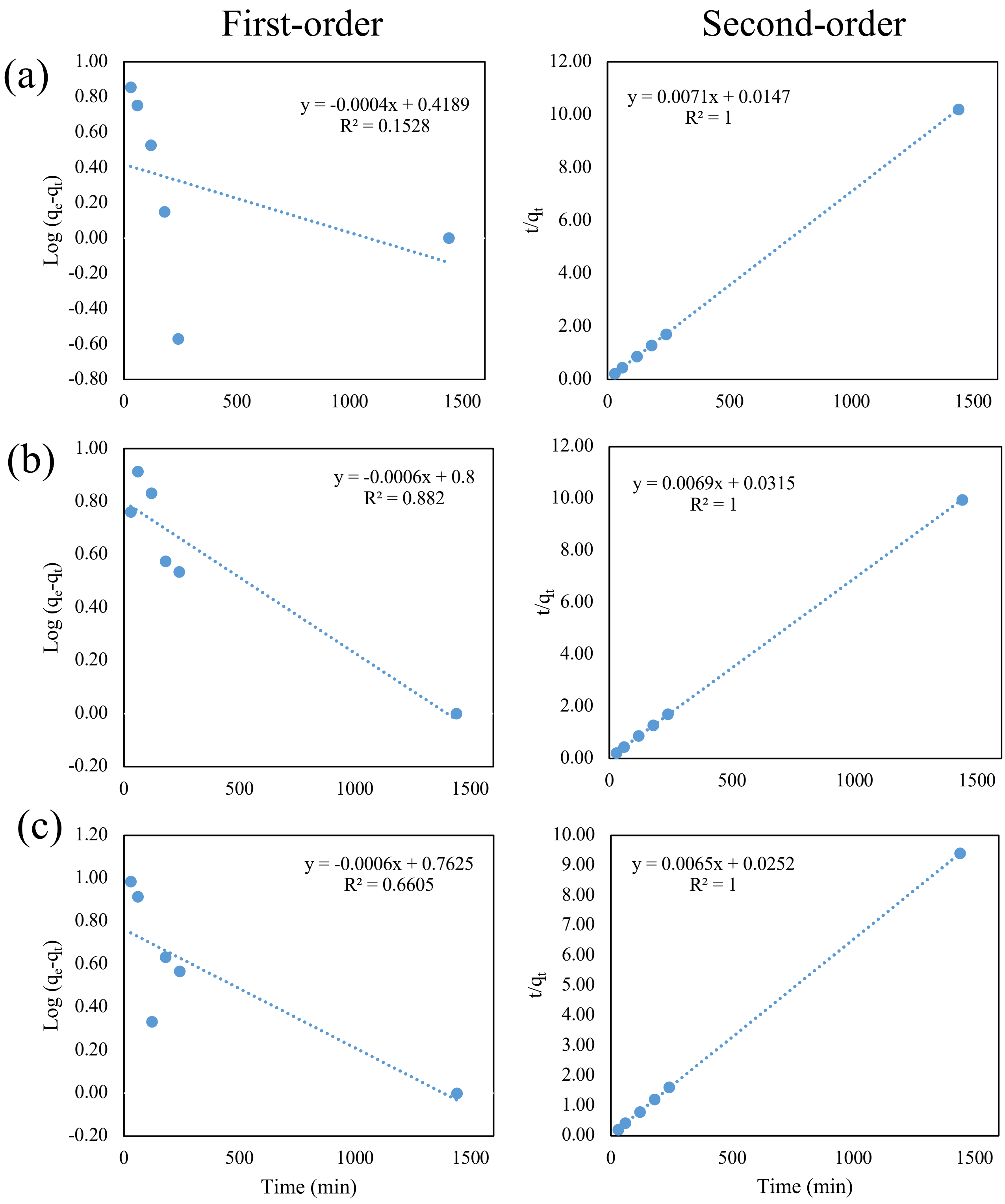

Figure. 12. Kinetic model of CR adsorption. (a) SC1 (b) SC2 (c) SC3.

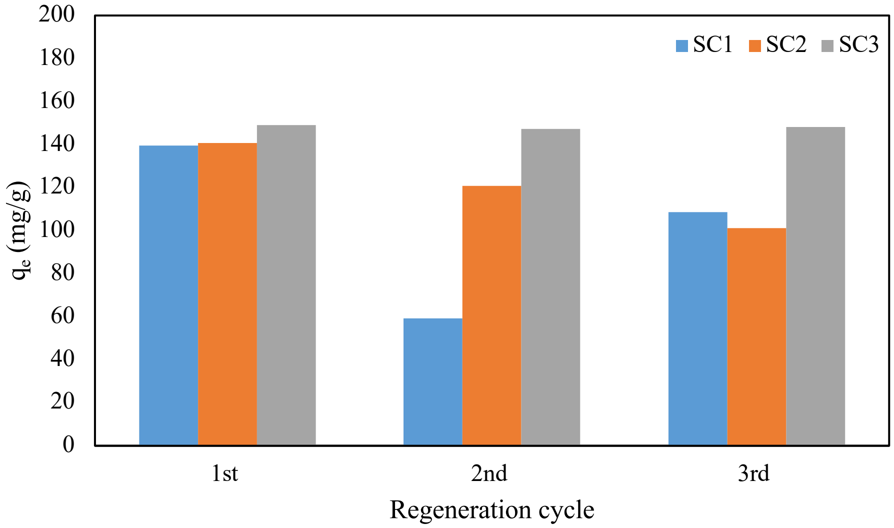

Figure. 13. Regeneration of CR adsorption.

Table 4. Comparison adsorbents for CR adsorption.

Adsorbent	q_e (mg/g)	Reference
Fly ash	22.12	(Harja et al., 2022)
$ZnCr_2O_4$ oxide	44.03	(Gao et al., 2021)
$MgCr_2O_4$ oxide	43.59	(Gao et al., 2021)
$CoCr_2O_4$	28.71	(Gao et al., 2021)
2Clph-BU-Cs	93.46	(Alharbi et al., 2023)
CS-DE@CA	23.28	(D. Zhao & Shen, 2023)
DE@CA	38.84	(D. Zhao & Shen, 2023)
Na_2SiO_3-CTAB	73.04	(Fadimatou et al., 2024)
SC1	141.08	This study
SC2	144.50	This study
SC3	153.24	This study

2.3.2 Porous sodium alginate/poly (acrylic acid) composites cross-linked with FeCl$_3$ for acid black 1 dye removal from aqueous solution

2.3.2.1 Characterization of SA/PAA-Fe

Figure. 14a. displays the N_2 adsorption/desorption isotherms and Table 5 summarizes the Brunauer-Emmett-Teller (BET) specific surface area (S_{BET}), total pore volume (V_{total}), and pore size (D_{meso}) of the adsorbent. The adsorbent exhibited a mesoporous structure with a size of 19.1 nm. However, it possessed only a small specific surface area and total pore volume of 1.6 m^2 g^{-1} and 0.008 cm^3 g^{-1}, respectively. X-ray diffraction (XRD) spectra of the SA/PAA-Fe adsorbent is shown in Figure. 14b. The XRD peaks at 2θ = 7.00° and 16.01° suggest that SA/PAA-Fe was amorphous, which might be explained by the major components of SA and PAA. Moreover, the diffraction peaks seen at 2θ = 41.16°, 47.91°, 70.08°, 89.35°, 108.60°, and 130.34° may be attributed to Halite (JCPDS 01-076-3452), which may be slightly contaminated on the collection process of SA/PAA-Fe.

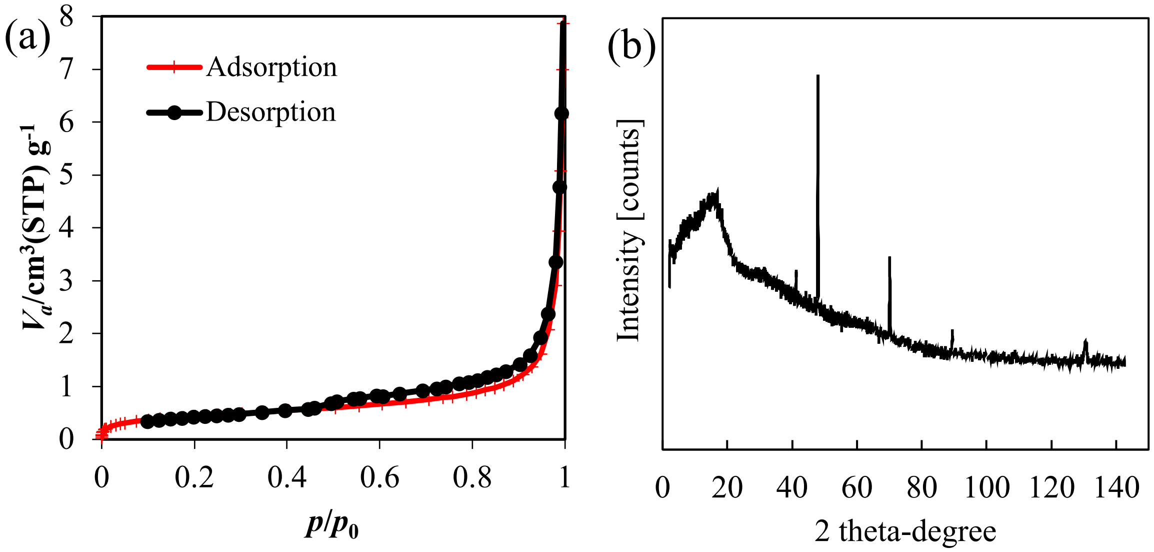

Figure. 14. (a) N_2 adsorption/desorption of SA/PAA-Fe (b) XRD spectra of SA/PAA-Fe.

The morphology of SA/PAA-Fe before and after AB1 adsorption was obtained by using scanning electron microscopy (SEM) is presented in Figure. 15. The surface of the adsorbent was rough before adsorption, and became flat and smooth after AB1 adsorption. Table 6 presents the weight percentage (wt%) of the element from EDS data. The analysis revealed that the synthesized SA/PAA-Fe compound consisted of carbon (C), oxygen (O), iron (Fe), chloride (Cl), and sodium (Na). Moreover, the detection of sulfur (S) and nitrogen (N) components after AB1 adsorption suggests that AB1 molecules were captured at the surface of the SA/PAA-Fe adsorbent.

Table 5. Characteristics of SA/PAA-Fe.

Adsorbent	S_{BET} [m^2 g^{-1}]	V_{total} [cm^3 g^{-1}]	D_{meso} [nm]
SA/PAA-Fe	1.6	0.008	19.1

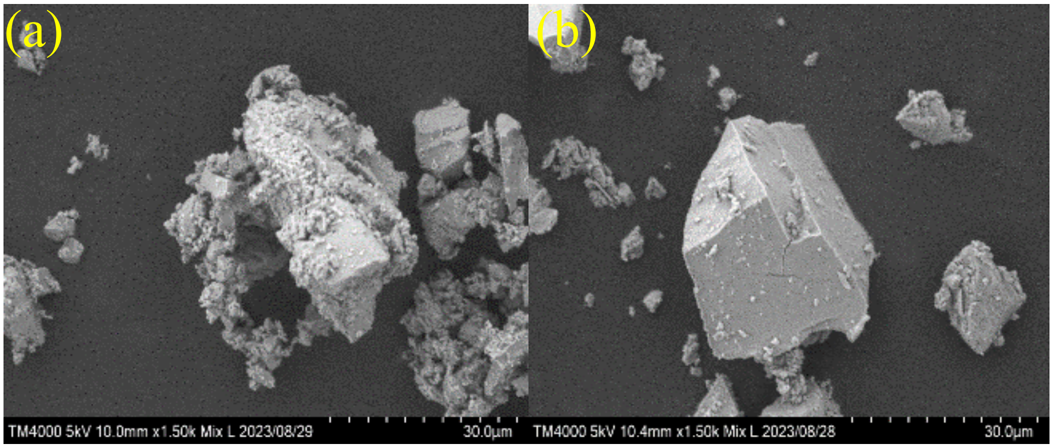

Figure. 15. SEM images (a) before and (b) after the adsorption of AB1.

Table 6. EDS data of SA/PAA-Fe before and after adsorption.

Parameters (wt%)	Before adsorption	After adsorption
C	48.94	49.54
O	19.95	18.62
Fe	21.27	28.85
Cl	8.97	0.68
Na	0.87	0.15
S		0.12
N		2.05

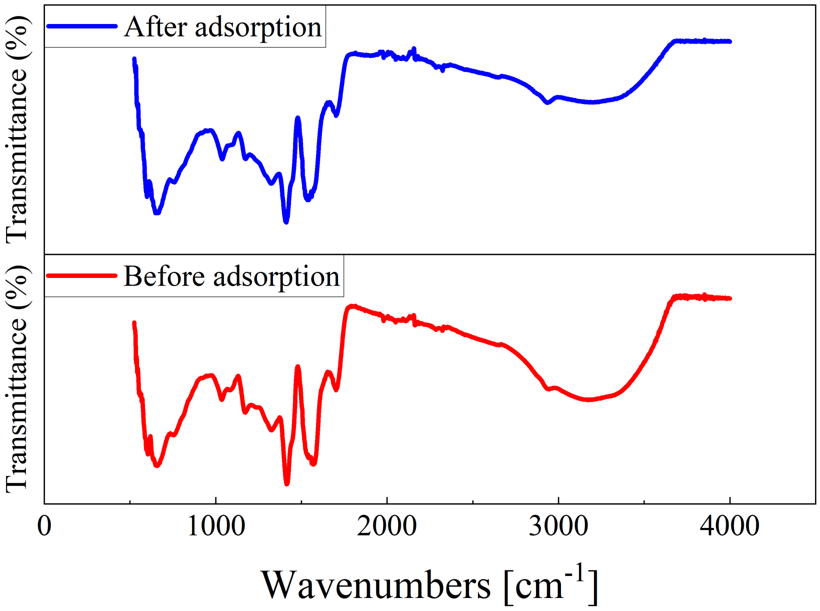

Figure. 16. FTIR spectra of SA/PAA-Fe before and after AB1 adsorption.

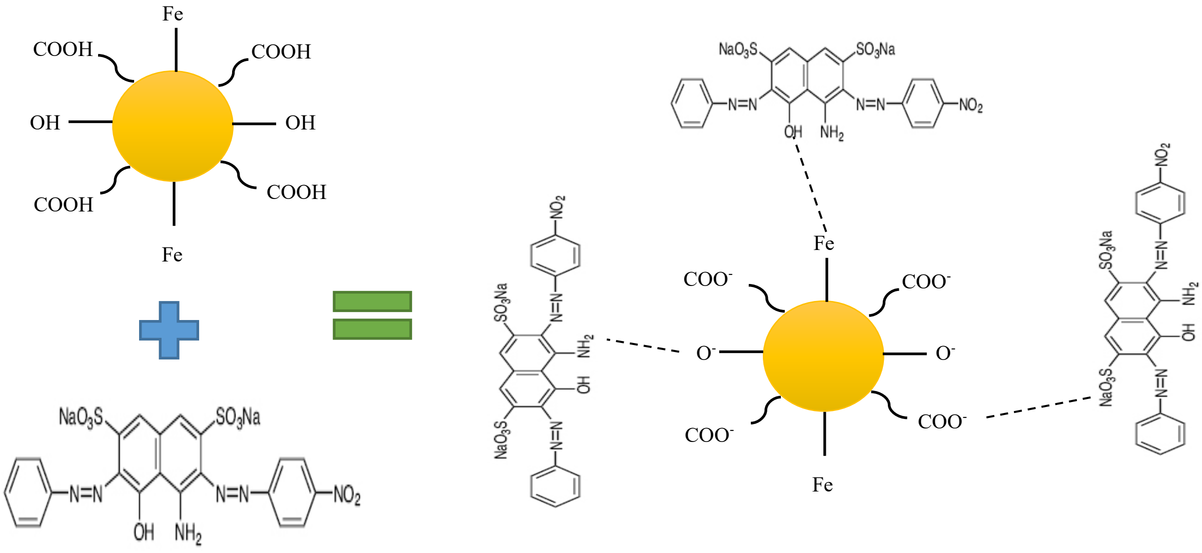

Figure. 17. Proposed AB1 adsorption mechanisms.

The FT-IR spectra of the adsorbent and the AB1-loaded adsorbent are shown in Figure. 16. The peak decrease after AB1 adsorption from 3170 cm^{-1} to 2936 cm^{-1} is expected to be due to the functional groups that engage in the process of adsorption through the interactions of intermolecular bonds, such as van der Waals and (-OH) bonding interactions (Modrzejewska, 2013b). The peak at 1701 cm^{-1} was assigned to C=O. A decrease in the peak intensity was detected at 1570 cm^{-1} to 1541 cm^{-1}, which was assigned to the stretching of –COO^{-} (Qurrat-ul-Ain et al., 2019). The peak at 1172 cm^{-1} represents the C-O bond. A shifted peak occurred from 656 cm^{-1} to 648 cm^{-1} and 604 cm^{-1} to 599 cm$^{-1,}$ corresponding to Fe-O. While most of the peaks were consistent after adsorption, some were shifted to lower wavenumbers, indicating the influence of stronger intermolecular interactions between SA/PAA-Fe and the AB1 dye. According to the IR analysis, both electrostatic attraction and intermolecular interactions connecting the functional compositions of SA/PAA-Fe and AB1 dye molecules likely contribute to dye adsorption. The proposed mechanism of AB1 adsorption onto SA/PAA-Fe is shown in Figure. 17.

2.3.2.2 Initial pH effect and surface charge of adsorbent (pH_{zpc})

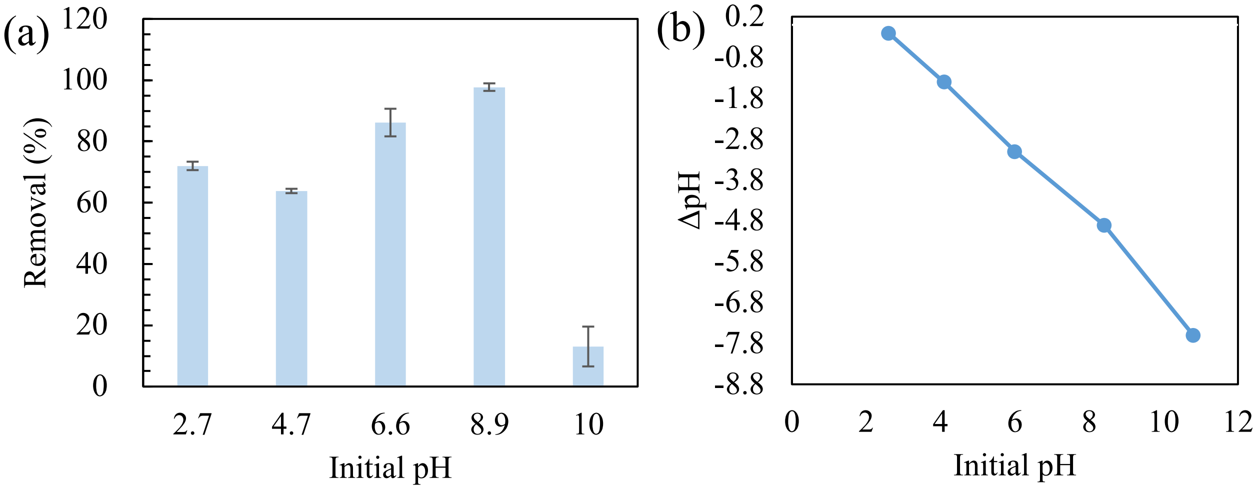

Figure. 18. (a) Initial pH effect versus removal percentage (b) Surface charge (pH_{zpc}) of SA/PAA-Fe.

The pH of the adsorption system influences the ionization of the adsorbates and surface charge of the adsorbent material (Naushad et al., 2017). Figure. 18a. shows the adsorption of AB1 when the pH of the AB1 solution was changed. The percentage of removal decreased and then increased within this pH range (2.7 to 10). A pH of 8.9 was optimal for adsorption, resulted in a removal percentage of 97.7%. Figure. 18b. shows that the adsorbent exhibited a negative surface charge, whereas AB1 had a positive charge under alkaline conditions. This finding demonstrates that the electrostatic connection of the SA/PAA-Fe and AB1 dyes has a greater impact than the pH of the solution.

2.3.2.3 Effect of initial concentration

The adsorption removal of AB1 on SA/PAA-Fe was studied by varying the initial AB1 concentration in the range of 10 to 50 mg/L. The adsorption experiment was performed under a contact period of 30 min, pH of 8.9, adsorbent amount of 0.05 g/50 mL, and temperature of 25 °C. Increasing the AB1 concentration to 50 mg/L reduced the AB1 removal percentage on the

SA/PAA-Fe surface (Figure. 19). The adsorbed amount of AB1 was calculated to be 10–21 mg/L, which is almost independent of the initial concentration of AB1. This is because of the presence of excess AB1 molecules, which are much larger than the number of available sites of SA/PAA-Fe for adsorption.

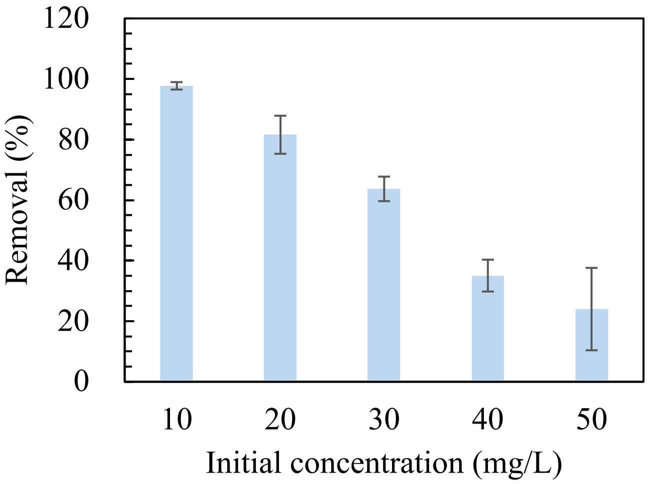

Figure. 19. Effect of the initial AB1 dye concentration on the removal percentage.

2.3.2.4 Effect of adsorbent dosage

To assess the impact of the quantity of adsorbent used in the adsorption of AB1, several quantities of SA/PAA-Fe were introduced, ranging from 0.05 to 0.5 g, in a 50 mL solution. The research were conducted using an initial AB1 concentration of 50 mg/L adjusted to pH 8.9 at 25 °C. Figure. 20 shows the effects of adsorbent quantity on AB1 adsorption. Increasing the adsorbent dosage can increased the removal percentage from 24.0% to 77.8%. This could be ascribed to the increase in the SA/PAA–Fe active sites, leading to an enhanced removal percentage due to the adsorption-desorption equilibrium. On the other hand, the adsorption capacity of SA/PAA–Fe decreased (12.00 to 3.89 mg/g), as the adsorbent dosage increase. This is because of the reduced availability of active adsorbent sites caused by the accumulation and overlapping of the adsorbent particles (Zeydouni et al., 2019). This study matches the findings of (Hidayat, Harada, et al., 2022), in which a zeolite/chitosan hydrogel was used to remove Acid Red 88.

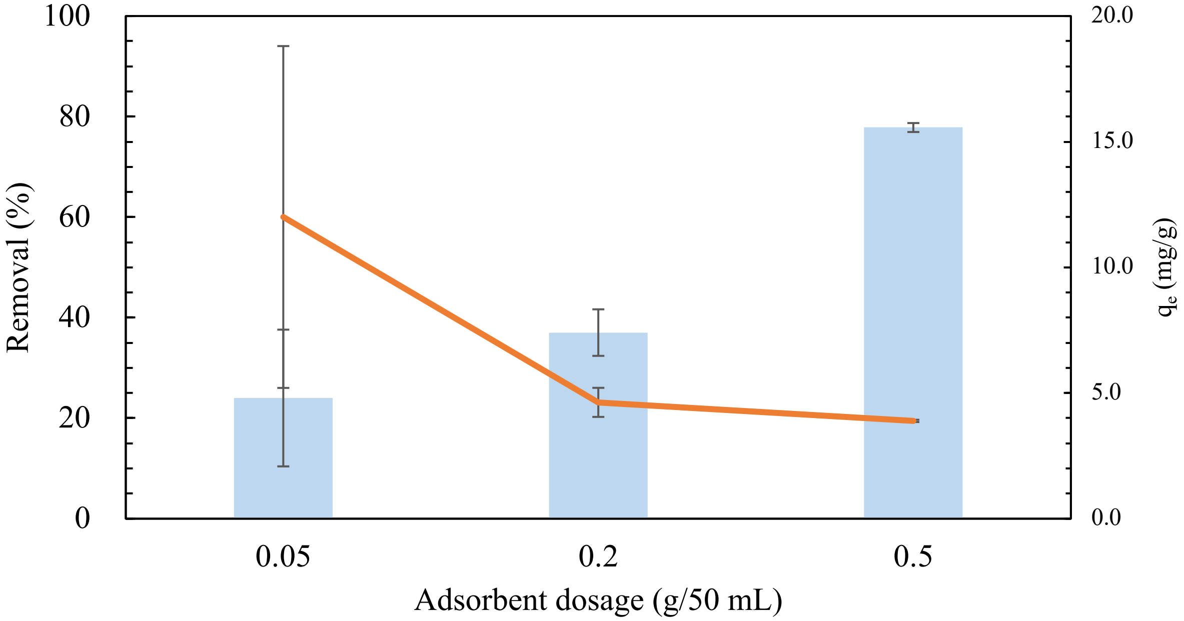

Figure. 20. Effect of adsorbent dosage on removal percentage and adsorption capacity of AB1.

2.3.2.5 Adsorption isotherm analysis

The adsorption isotherms were analysed by applying the Langmuir in Eq. (9) and Freundlich in Eq. (11) models to the adsorption experimental data. Table 7 depicts the value of the linear regression coefficient (R^2) obtained from Figure. 21. in conjunction with the additional adsorption isotherm characteristics. The Langmuir model fits the AB1 dye adsorption data better than the Freundlich model, as evidenced by the higher R^2 values. The R_L and *1/n* values are <1. Therefore, the adsorption process using this indicator was verified to be favorable. These findings suggest that adsorption process occurred in a monolayer condition at the adsorption sites on the surface of SA/PAA-Fe.

$$C_e/q_e = \left(\frac{C_e}{q_{max}}\right)+1/(K_L q_{max}) \tag{9}$$

$$R_L = \left(\frac{1}{1+bC_o}\right) \tag{10}$$

$$\ln q_e = \ln K_F + \frac{1}{n} \ln C_e \tag{11}$$

where *q* (mg/g) is the adsorption capacity, C_e (mg/L) is the equilibrium concentration, q_{max} (mg/g) is the maximum adsorption capacity, C_0 (mg/L) is the initial concentration, R_L is a greater coefficient indicating a stronger adsorption capacity, $R_L > 1$ (unfavorable), $R_L = 1$ (linear), and $0 < R_L$ (favorable). K_L (L/mg) and K_F (mg/g) are the equilibrium constants of adsorption and $1/n$ is the adsorption intensity.

2.3.2.6 Effect of contact time and kinetic experiment studies

The effect of adsorption durations (30-90 min) towards the adsorption of AB1 using SA/PAA-Fe at a dye concentration of 50 mg/L and adsorbent concentration of 0.5 g/50 mL of adsorbent is shown in Figure. 22. The original pH was maintained and the adsorption data are shown in Figure. 15. Observations indicate that the removal percentage declined between 30 and 45 min but then significantly increased at 60 min. It eventually reached equilibrium after 90 min, with 84.1% dye removal and an adsorption capacity of 4.20 mg/g.

Table 7. Isotherm model for adsorption AB1 onto SA/PAA-Fe.

Isotherm models	Parameters	Value
Langmuir	q_{max} (mg/g)	12.0952
	K_L (L/mg)	7.3905
	R^2	0.9841
	R_L	0.0014
Freundlich	K_F (g/mg min^{-1})^n	331.8751
	1/n	0.0597
	R^2	0.2210

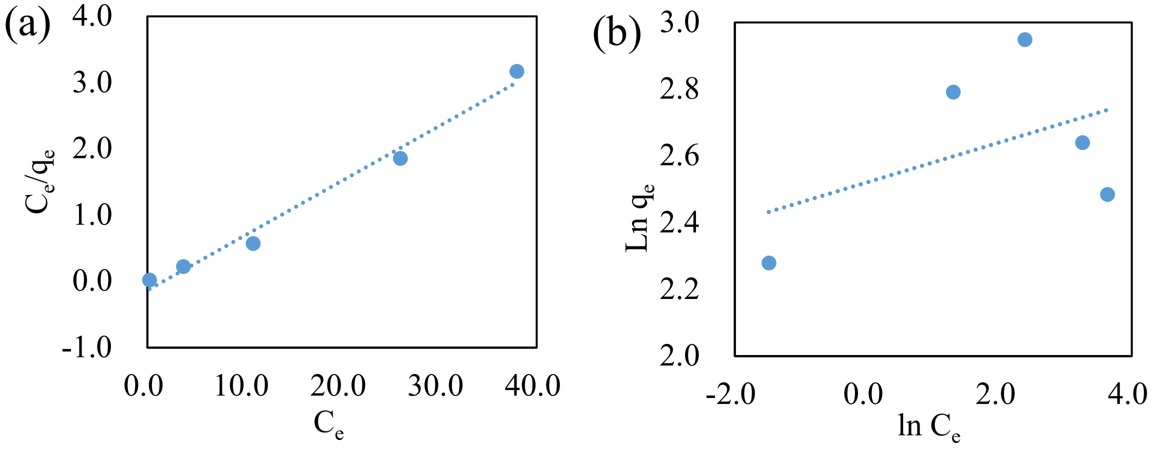

Figure. 21. Adsorption isotherms of AB1 analyzed by (a) Langmuir (b) Freundlich models.

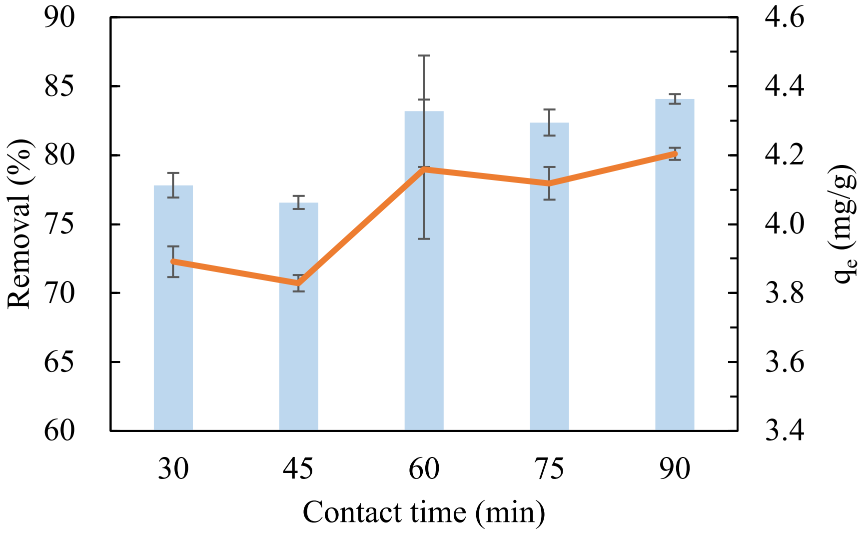

Figure. 22. Removal percentage and adsorption capacity of AB1 vs. contact time (min).

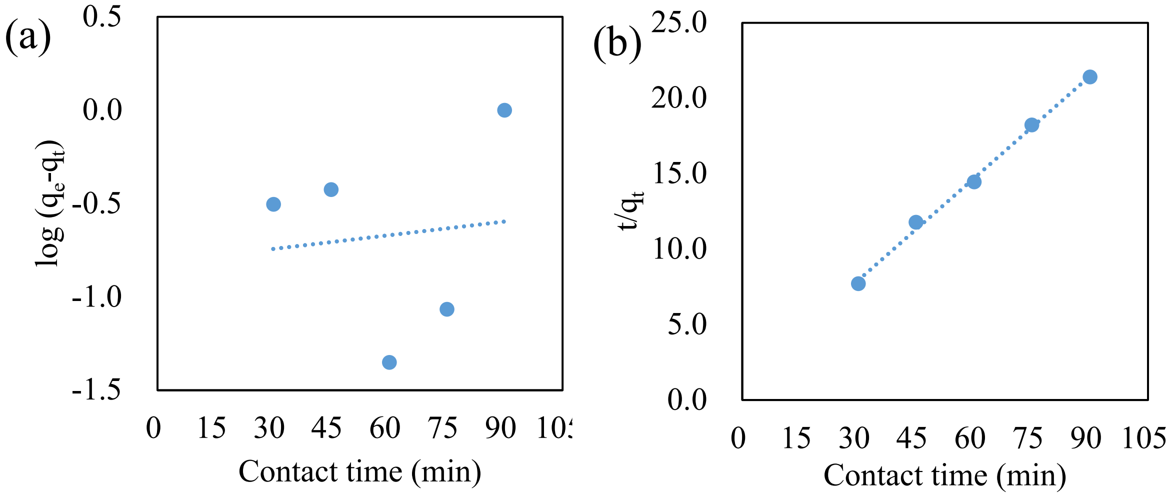

Figure. 23. Adsorption kinetics were analyzed using pseudo-first-order (a) and pseudo-second-order (b) curves.

Table 8. Kinetic model parameters for adsorption AB1 onto SA/PAA-Fe.

Kinetic models	Parameters	Value
	q_e (mg/g)	2.2628
Pseudo-first-order	K_1 (min^{-1})	0.00004
	R^2	0.0116
	q_e (mg/g)	4.4307
Pseudo-second-order	K_2 (g/mg min^{-1})	0.04391
	R^2	0.9971

The results from kinetic models provided valuable insights into the adsorption process. The data obtained from the AB1 adsorption on the SA/PAA-Fe surface were evaluated using two kinetic models: the pseudo-first-order model in Eq. (12) and pseudo-second order in Eq. (13).

$$\log (q_e - q_t) = \log q_e - k_1 t \tag{12}$$

$$t/q_t = 1/(k_2 q_e^2) + t/q_e \tag{13}$$

where k_1 (min^{-1}) is the rate constant of the pseudo-first-order model and t (min) is the time. Linear plots of log t against log (q_e-q_t) and t against t/q_t were used to determine k_1 and k_2 from the slope of the linear plots of the pseudo-first-order and pseudo-second-order models, respectively.

The kinetic variables and linear correlation coefficients for AB1 adsorption are displayed in Figure. 23. and Table 8. The R^2 value of the pseudo-second-order kinetic model ($R^2 = 0.9971$) was much higher compared to the pseudo-first-order kinetic model ($R^2 = 0.0116$), demonstrated that the adsorption process is regulated by chemisorption. The findings were related with previous works conducted by (Hidayat et al., 2023b; Lita et al., 2023; Mohamad Sarbani et al., 2023), who utilize CS/ZL/ZrO/Fe_3O_4 for phosphate adsorption, Coffee husk biochar-Fe_3O_4 for glyphosate adsorption and carboxyl methyl cellulose-chitosan magnetite for Cr (VI) and Pb (II) adsorption, respectively.

2.3.2.7 Adsorption thermodynamic study

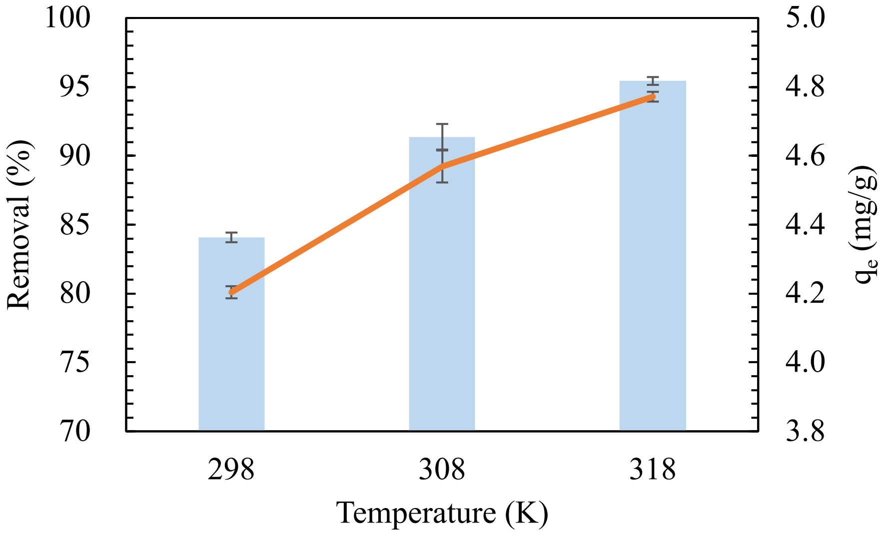

Figure. 24. Effect of temperature on AB1 adsorption onto SA/PAA-Fe

In the adsorption of AB1, the impact of certain variables, such as temperature has been investigated at temperatures of 298, 308, and 318 K. Figure. 24 demonstrates that higher temperatures can enhance the removal percentage and adsorption capacity from 84.08 to 95.43 % and 4.20 to 4.77 mg/g, respectively. The adsorption capacity increased, which may be due to the enhanced interaction between SA and PAA, leading to the formation of more active adsorption sites at high temperatures, leading to an increase in the adsorption amount.

The following Gibbs` and Van`t Hoff equations were used to visually derive the thermodynamic parameters (ΔG^o, ΔH^o and ΔS^o):

$$\Delta G° = -RT\ln K \tag{14}$$

$$\Delta G° = \Delta H° - T\Delta S° \tag{15}$$

$$\ln K = \frac{\Delta S°}{R} - \frac{\Delta H°}{RT} \tag{16}$$

Where K is the equilibrium constant, R (J.mol $^{-1}$ K $^{-1}$) is the gas constant, T (K) is the temperature, $\Delta G°$ is the Gibbs free energy (kJ mol $^{-1}$), $\Delta S°$ is the entropy (kJ mol $^{-1}$), and $\Delta H°$ is the enthalpy (kJ mol $^{-1}$). $\Delta H°$ and $\Delta S°$ were obtained from the slope and intercept of the plot of ln$K$ versus 1/T.

Table 9. Thermodynamic parameters of AB1 adsorption onto SA/PAA/Fe.

Temp (K)	K	ΔG^o (kJ.mol^{-1})	ΔH^o (kJ.mol^{-1})	ΔS^o (kJ.mol^{-1} K^{-1})	R^2
298	0.528	1.583	54.157	176.390	0.9999
308	1.060	-0.149			
318	2.088	-1.947			

The effect of temperature on the adsorption of AB1 on the Van`t Hoff diagram is illustrated in Figure. 25. Table 9 presents a list of plot parameters. The Gibbs free energy ($\Delta G°$)

value at 308 and 318 K are negative, which corresponds with the thermodynamic constants shown in Table 9 and is consistent with the Δ*S* °value (ΔS > 0 = spontaneous process). The positive ΔH° values indicate an endothermic adsorption process (Cordova Estrada et al., 2021). This endothermic condition in the adsorption process has also been demonstrated in several previous studies on the adsorption of RB5 dye onto powdered banana peel (Munagapati et al., 2018), and heavy metal adsorption onto FCPNC (El-Sabbagh et al., 2023).

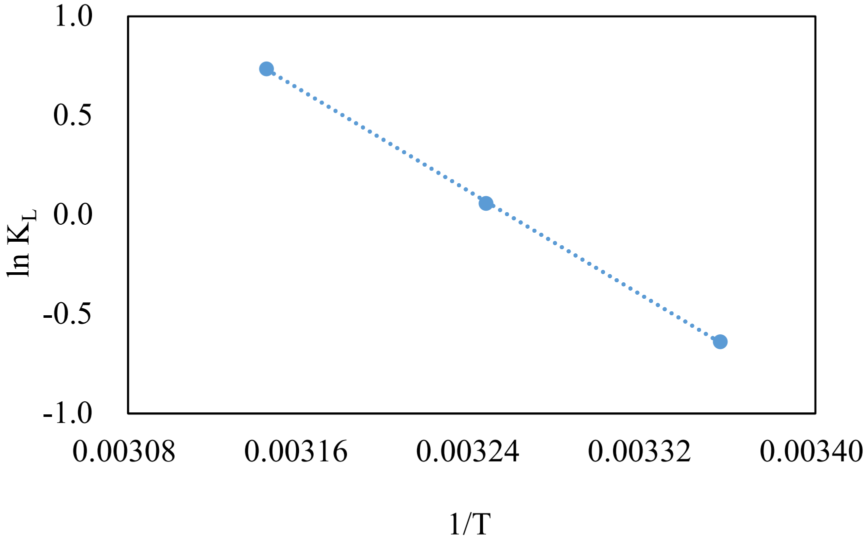

Figure. 25. Thermodynamic adsorption of AB1 onto SA/PAA-Fe.

2.2.3 Performance of unactivated and activated coffee husk biochar under room temperature using HNO_3 and $NaHCO_3$ for indigo carmine dye adsorption from water

2.2.3.1 Characterization

Figure. 26 shows a 3D picture of CH-B, which shows that the adsorbent has many porous internal structures that are beneficial for the adsorption of IC molecules from water. Figure. 27 shows the images of the scanning electron micrographs for each adsorbent. Figure 27(a) depicts the surface of CH-B, which was wrinkled, porous, and uneven. In contrast, the surface properties of CH-B-HNO_3 changed dramatically, resulting in a much more uneven and rough surface as well as pores (Figure. 27(b)). While, after activation with $NaHCO_3$, the surface is similar to CH-B-

HNO_3 and slightly rough (Figure. 27(c)). It can be presumed that the activating chemicals influence the surface of biochar. During further experiment, the adsorbent’s surface becomes smoother after IC adsorption, which indicated that IC dye molecules trapped to the adsorbent surfaces.

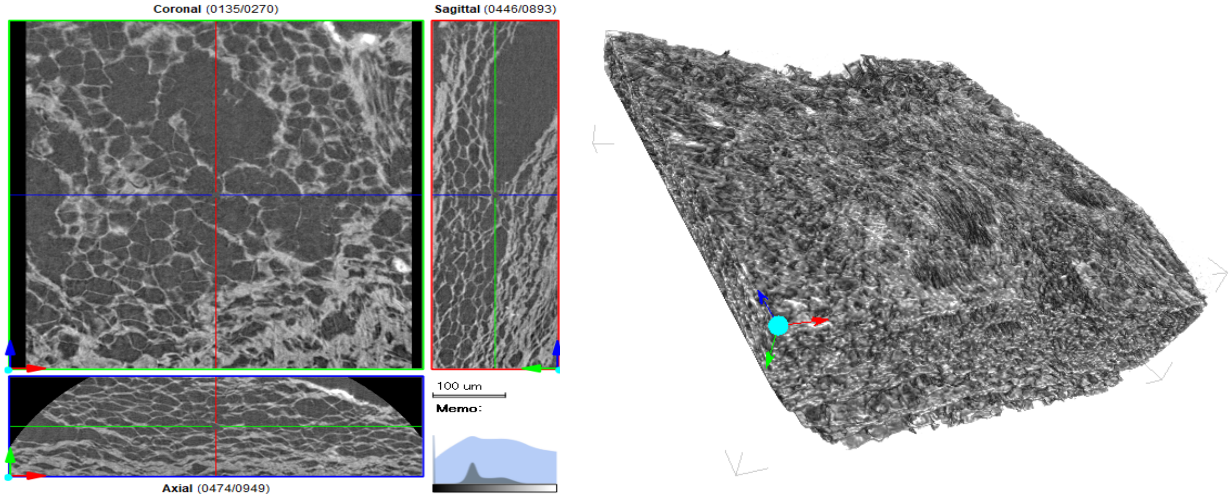

Figure. 26. 3D picture morphology of CH-B.

Figure. 28 demonstrates the FTIR spectra for IC adsorption (before and after). The O-H stretching peak overlapped with the N-H groups from 3000 to 3800 cm^{-1} (T. Yang et al., 2020). Moreover, many peaks appeared in this region after IC adsorption for all adsorbents, indicating a strong interaction between the IC and the adsorbent. The peak at 2353 cm^{-1} from CH-B decreased to 2161 cm^{-1} and 2322 cm^{-1} for CH-B-HNO_3 and CH-B-$NaHCO_3$, respectively, which were assigned to C=C stretching vibrations (Md Salim et al., 2021). While a new peak appeared for CH-B-HNO_3 at 1694 cm^{-1} is associated with the –COOH groups (Barroso-Bogeat et al., 2019). The peak at 1557 cm^{-1} from CH-B shifted to 1574, 1557, 1538, and 1506 cm^{-1} and 1567, 1557, 1538, and 1506 cm^{-1} for CH-B-HNO_3 and CH-B-$NaHCO_3$, respectively, which were ascribed to C=C/C=O stretching (Shamsuddin & Munajat, 2023). The existence of these peaks after chemical activation could improve the hydrophilicity of the biochar surface, leading to an active surface charge of the biochar, thus enhancing its ability to absorb IC dye (Wang et al., 2020). The peaks at 1042 shifted to 1138 and 1035 cm^{-1} for CH-B, CH-B-HNO_3, and CH-B-$NaHCO_3$, respectively, which were attributed to C-O-C. Many peaks also appeared after IC adsorption for CH-B-HNO_3 and CH-B-$NaHCO_3$ between 1000 and 650 cm^{-1}, in contrast to CH-B, which was assigned to C-H bending (Md Salim et al., 2021). These results indicate that CH-B-HNO_3 and CH-B-$NaHCO_3$ were more efficient IC adsorption compared than CH-B.

2.2.3.2 Initial pH effect and surface charge of adsorbent (pH_{zpc})

In the adsorption process, the initial pH of adsorbate is a significant influence because it can alter the physicochemical features of the adsorbent’s surface, as well as the speciation of the adsorbate in the solution (S. Zhang et al., 2021). Figure. 29 shows the variation in the adsorption capacity of the adsorbents under pH ranging from 2.2 to 10.2. It can be clearly observed that the best condition was obtained at pH 2.2 for IC adsorption for all adsorbents. Moreover, the adsorption capacity increased by 87.3% and 90.4% for CH-B-HNO_3 and CH-B-$NaHCO_3$, respectively, compared with the CH-B (without activation). The surface charges of the adsorbents are presented in Figure. 30. The data revealed that the adsorbents, namely, CH-B, CH-B-HNO_3, and CH-B-$NaHCO_3$, exhibited positive charges below pH_{zpc} values of 10.1, 2.3, and 8.9, respectively. pH_{zpc} is the pH where the adsorbent's surface charge becomes neutral. Owing to the presence of sulfuric groups in the molecular structure of the IC dye which comprises a negative charge, an electrostatic interactions may occur between the dye and the adsorbent material (Sánchez-Rodríguez et al., 2015)

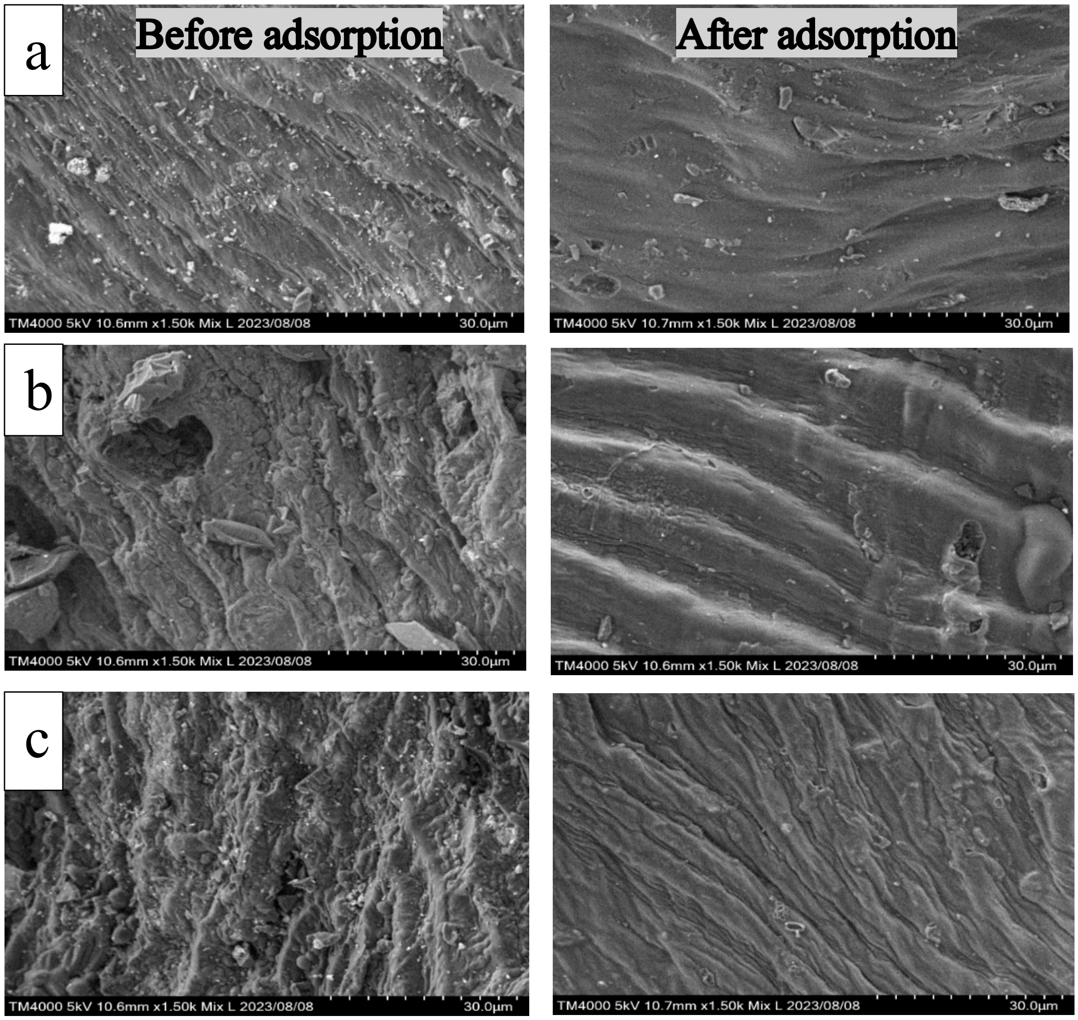

Figure. 27. SEM morphology of adsorbents (a) CH-B (b) CH-B-HNO_3 (c) CH-B-$NaHCO_3$.

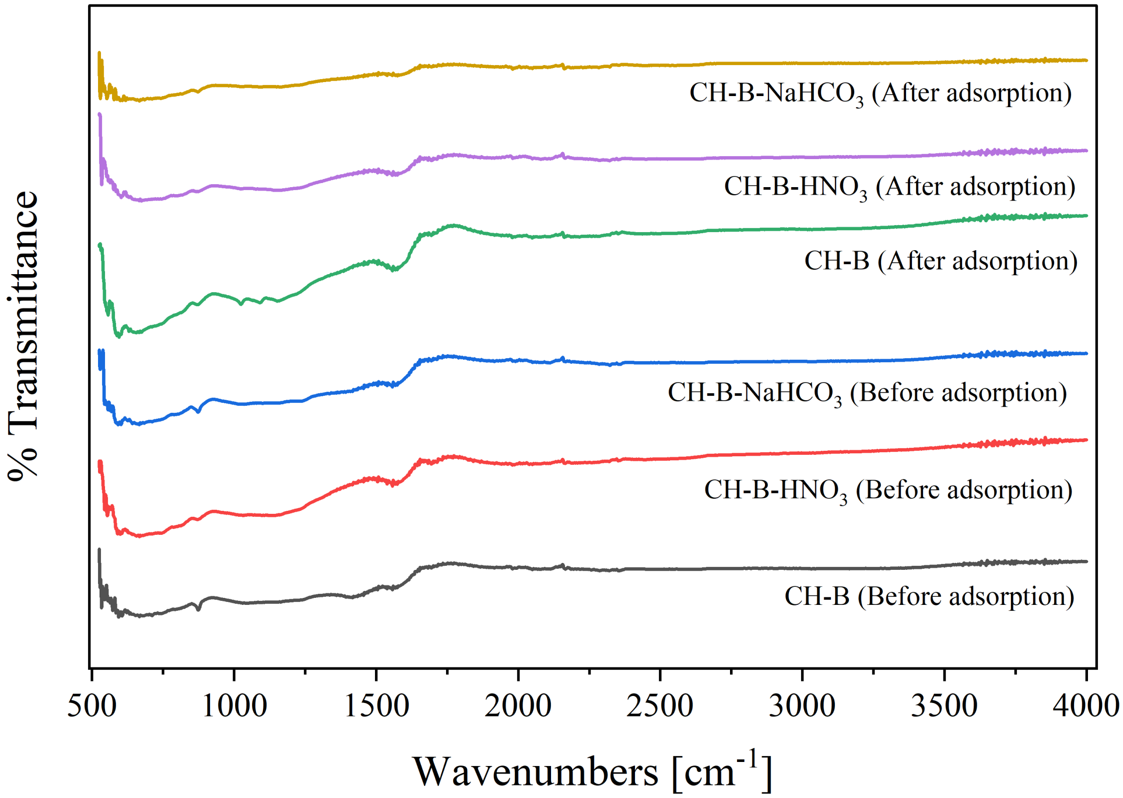

Figure. 28. FTIR spectra of adsorbent before and after IC adsorption.

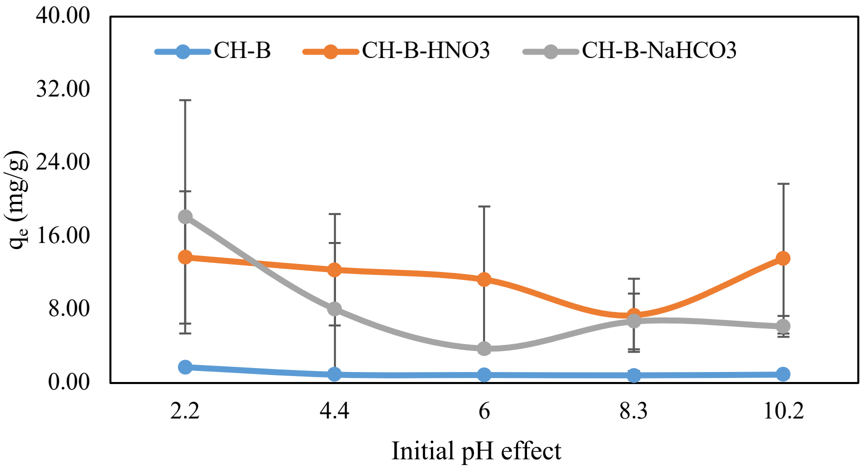

Figure. 29. Initial pH effect versus adsorption capacity (q_e). (IC concentration: 10 mg/L, contact time: 30 min, experiments were conducted under room temperature).

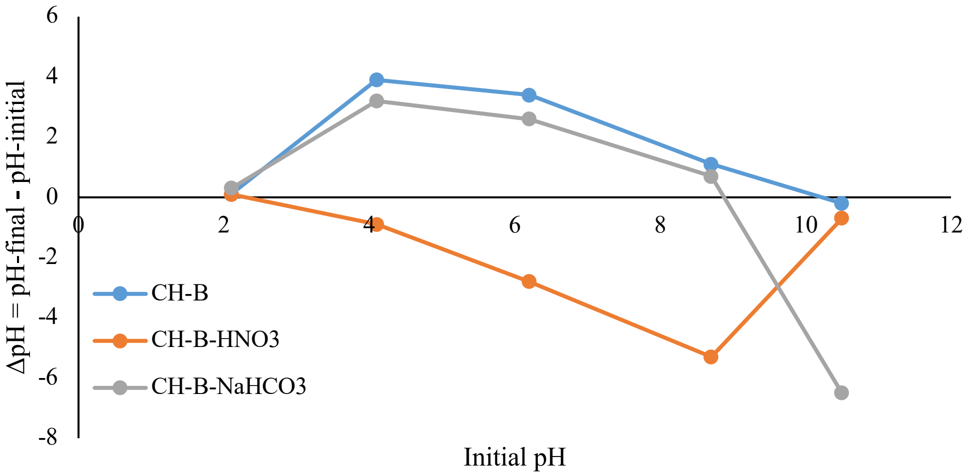

Figure. 30. pH_{zpc} of the adsorbent.

2.2.3.3 Initial IC concentration effect and isotherm studies

An adsorption isotherm is required to evaluate the functionalities of an adsorbent and the reaction between the adsorbate (IC) and the adsorbent (biochar). The contact time for CH-B was 1020 min, while that for CH-B-HNO_3 and CH-B-$NaHCO_3$ was 90 min because the isotherm data followed the kinetic equilibrium results. Figure. 31 shows an increase in the adsorption capacity when the IC dye concentration increases. The highest of adsorption capacity was observed in CH-B-$NaHCO_3$, followed by CH-B-HNO_3, and CH-B with values of 24.11 mg/g, 19.49 mg/g, and 7.11 mg/g, respectively. The low concentration of IC dye has resulted in less concentration gradient and therefore produces insufficient force to propel the dye molecule toward overcoming the transfer barrier between the biochar and the IC molecules. Consequently, the IC molecules unable to fully occupy the sites of adsorbent surface. However, when the initial amount of IC dye rose, the equivalent driving force provided by the concentration gradient also increased, providing a greater boost to the adsorbate (IC). Thus, more dye molecules will transfer and trap onto the adsorbent surface and resulted in an increase in the adsorption capacity.

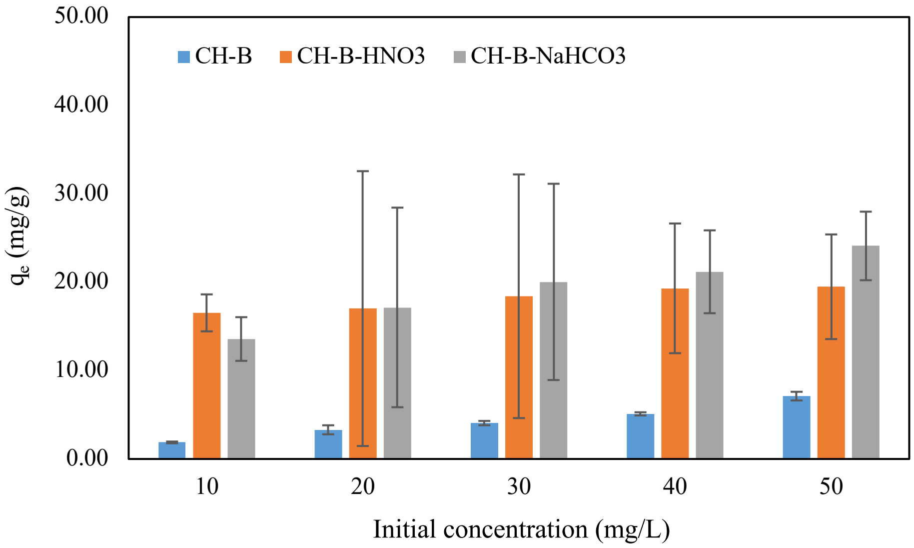

Figure. 31. Initial IC dye concentration effect onto adsorbent. (pH: 2.2, contact time for CH-B: 1020 min, for CH-B-HNO_3 and CH-B-$NaHCO_3$: 90 min, experiment was conducted under room temperature).

Langmuir and Freundlich isotherm models were employed to construct an effective adsorption system. The Langmuir model explains homogenous surfaces as well as monolayer sorption. The Freundlich model assumes a heterogeneous multilayer sorption. Figures. 32 and 33 show fitting diagrams for the Langmuir and Freundlich isotherm models, respectively. The results for the corresponding parameters are calculated as shown in Table 10. The Freundlich model's linear correlation coefficient (R^2) provided a better fit for CH-B and CH-B-$NaHCO_3$. The Langmuir model was ideally fitted to the CH-B-HNO_3. The models for the adsorption process were determined based on their strong linear correlation (R^2) values. More importantly, the values of R_L and 1/n were smaller than one for all adsorbents. Thus, this indicator provide confirmation that the adsorption process was favourable.

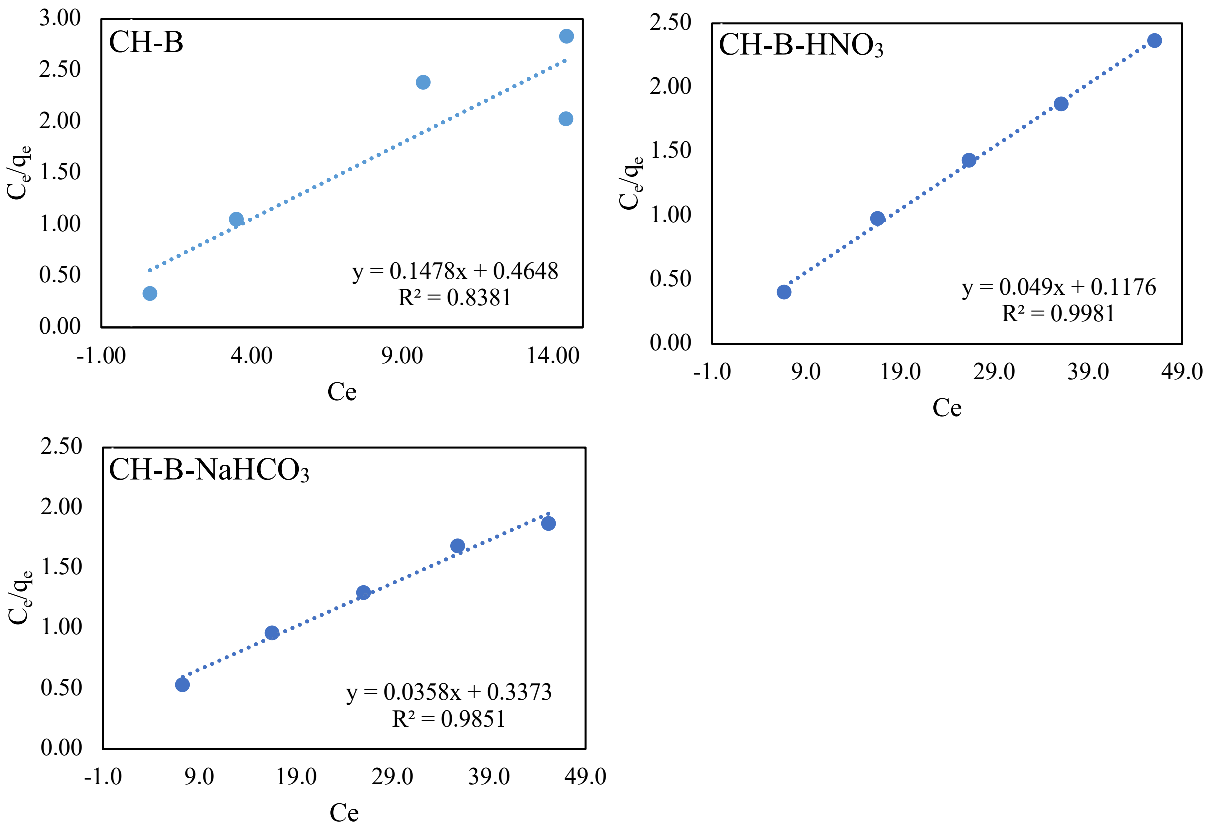

Figure. 32. Langmuir isotherm model for IC adsorption. (pH: 2.2, contact time for CH-B: 1020 min, for CH-B-HNO_3 and CH-B-$NaHCO_3$: 90 min, experiments were conducted under room temperature).

Table 10. Isotherm model for adsorption IC onto adsorbent

Isotherm	Parameters	Adsorbent		
		CH-B	CH-B-HNO_3	CH-B-$NaHCO_3$
Langmuir	q_{max} (mg/g)	6.7681	20.4126	27.9668
	K_L (L/mg)	2.1514	8.5026	2.9649
	R^2	0.8381	0.9981	0.9851
	R_L	0.0046	0.0012	0.0034
Freundlich	K_f (g/mg min^{-1})^n	5.8905	408.5193	99.5091
	1/n	0.3541	0.0926	0.3040
	R^2	0.9007	0.9079	0.9900

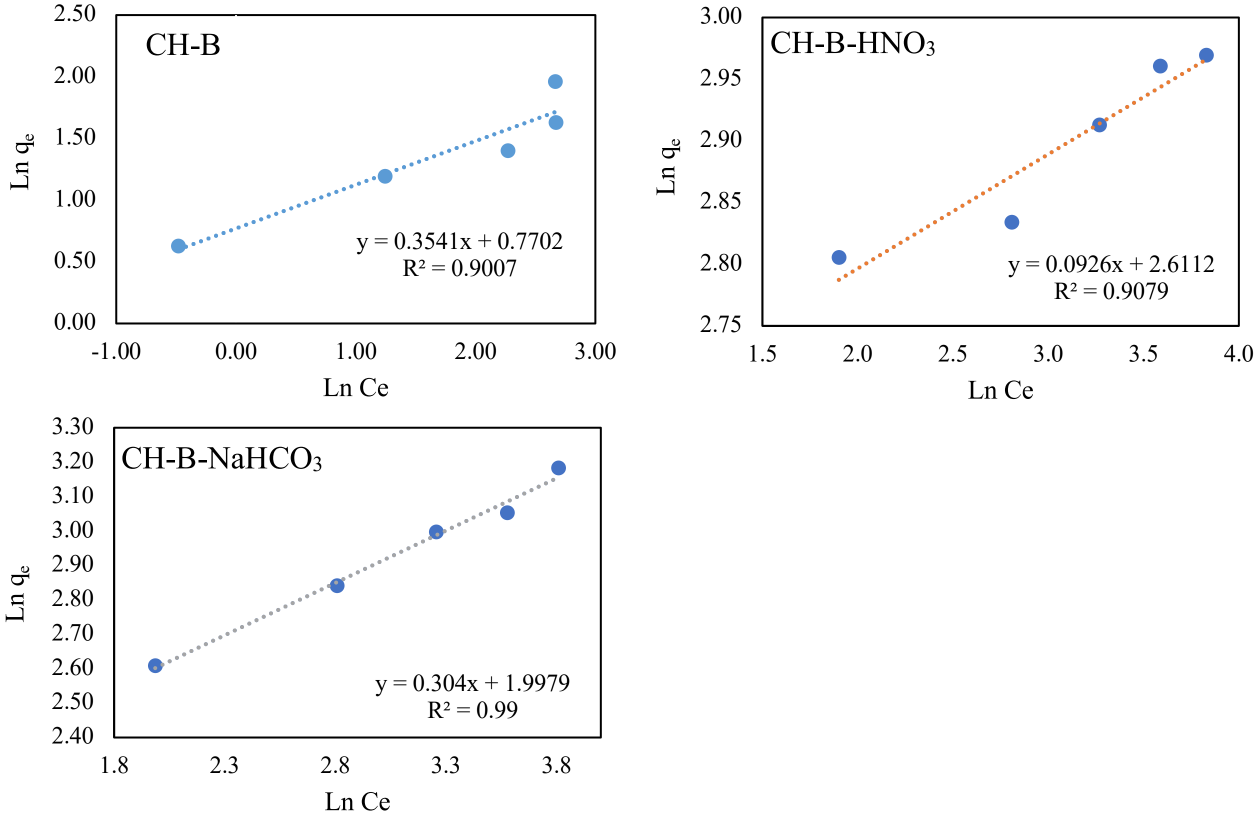

Figure. 33. Freundlich isotherm model for IC adsorption. (pH: 2.2, contact time for CH-B: 1020 min, for CH-B-HNO_3 and CH-B-$NaHCO_3$: 90 min, experiments were conducted under room temperature).

2.2.3.4 Equilibrium time effect and kinetic studies

The phrase "equilibrium time" refers to the shortest period of time necessary for adsorbents to achieve saturation and adsorption equilibrium, and is a critical indicator that displays the efficiency of adsorbent. Figure. 34 displays the findings regarding the way contact time influence the quantity of IC dye adsorbed. The IC dye quickly adsorbed onto CH-B-$NaHCO_3$ and CH-B-HNO_3, reaching equilibrium within 90 min. Both of these materials have adsorption capacity of 24.1 and mg/g 19.5 mg/g, respectively. In contrast, CH-B required 1020 min to reach equilibrium with an adsorption capacity of 7.1 mg/g. This is understandable because the activation of biochar enhanced the adsorption sites on the surface, consequently producing a greater adsorption capacity. Furthermore, the adsorption capacity was slow and fast up to 1020 min. The amount of available adsorption sites either decreased or increased throughout the experiment, resulting in either strong or weak concentrations that were able to overcome the resistance against mass transfer and settle on the surface of adsorbent.

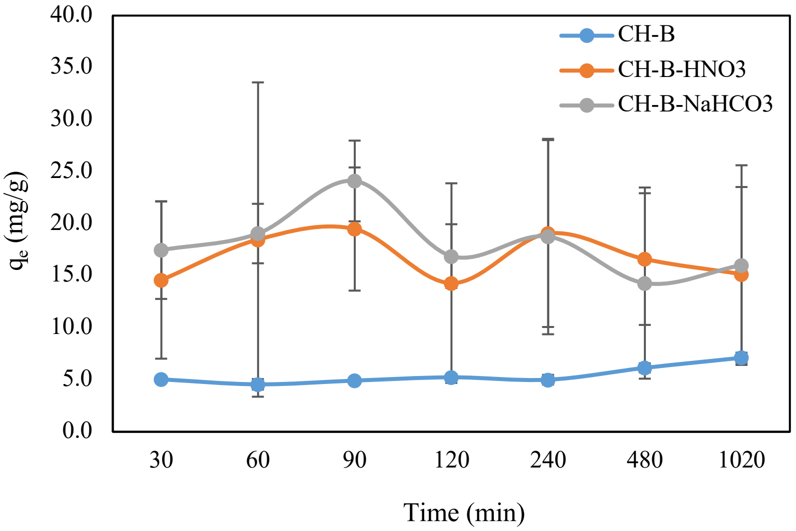

Figure. 34. Contact time for IC dye adsorption. (pH: 2.2, IC concentration: 50 mg/L, experiments were conducted under room temperature).

The fitted kinetic data for the P-F-O and P-S-O responses are presented in Figures. 35 and 36, respectively. The P-S-O model generated the most appropriate calculations of the experimental kinetic data for the adsorption capacity of all adsorbents. Table 11 lists the parameters derived by applying the kinetic models to the data of our research. The R^2 parameter with the highest value in Table 11 confirmed that the P-S-O kinetic model could be the best to characterize the adsorption process in this study. This model suggests that the IC dye adsorption onto the surfaces of the adsorbents CH-B, CH-B-HNO_3, and CH-B-$NaHCO_3$ is a chemisorption process. Surface exchange mechanisms connect the dye molecules to the adsorbent during this process.

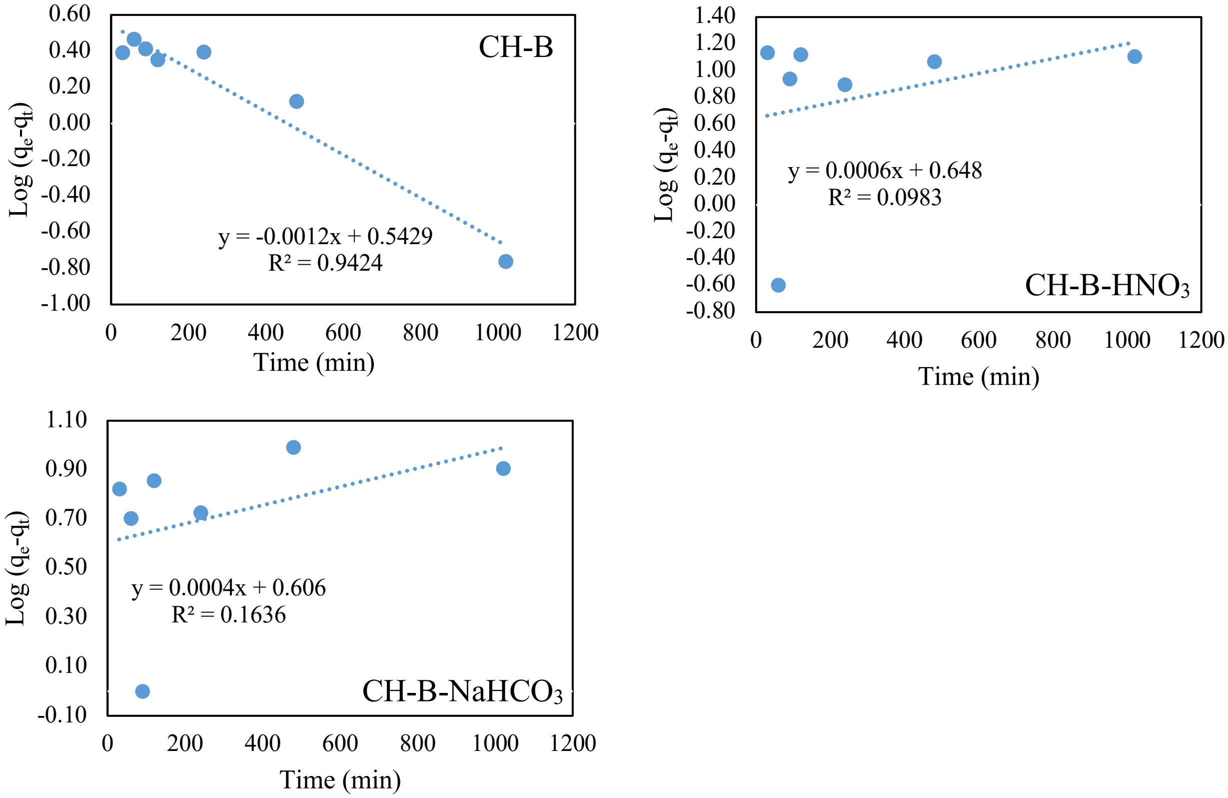

Figure. 35. P-F-O kinetic model for IC dye adsorption. (pH: 2.2, IC concentration: 50 mg/L, experiments were conducted under room temperature).

Table 11. Kinetic model parameters for adsorption IC dye.

Kinetics	Parameters	Adsorbent		
		CH-B	CH-B-HNO_3	CH-B-$NaHCO_3$
P-F-O	q_e (mg/g)	1.7210	1.9117	1.8331
	K_1 (min $^{-1}$)	0.00000118	0.0000067	0.00000044
	R^2	0.9424	0.0983	0.1636
P-S-O	q_e (mg/g)	52.7390	230.2657	241.8678
	K_2 (g/mg min^{-1})	0.00267	0.00411	0.00537
	R^2	0.9904	0.9962	0.9940

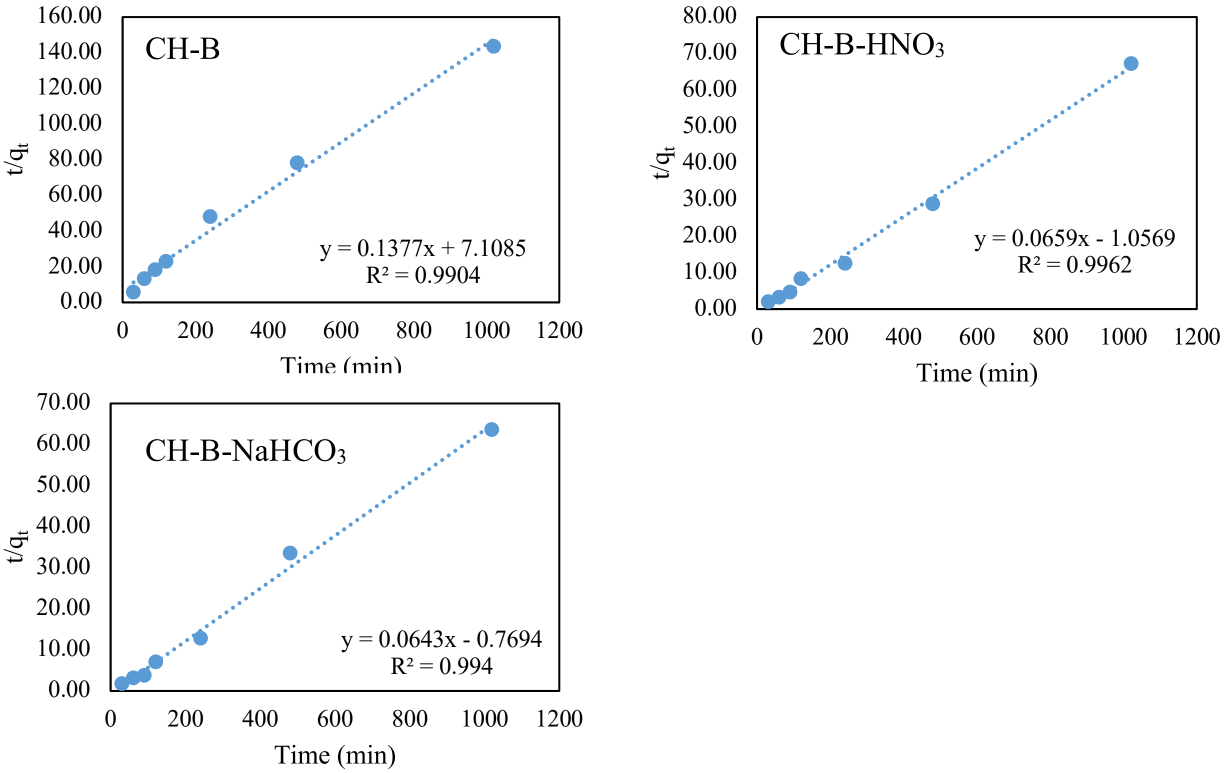

Figure. 36. P-S-O kinetic model for IC dye adsorption. (pH: 2.2, IC concentration: 50 mg/L, experiments were conducted under room temperature).

Table 12 presents a comparative analysis of the adsorption capacity described in published research on IC removal. These findings suggest that CH-B, CH-B-HNO_3, and CH-B-$NaHCO_3$ had higher adsorption capacity than fly ash, zeolite ZM, and calcium hydroxide. This indicates that all the adsorbents used in this study were effective for IC removal from water.

Table 12. Various adsorbent for IC dye removal from water

Adsorbents	Qe (mg/g)	Conditions	Initial IC concentration (mg/L)	References
Fly ash	1.48	Room temperature	14.7	(De Carvalho et al., 2011)
Zeolite ZM	1.23	Room temperature	11.0	(De Carvalho et al., 2011)
nWTRs	172.4	45 ºC	500	(El-Kammah et al., 2022)
WTR	30.86	45 ºC	500	(El-Kammah et al., 2022)
Composite Nanofibers (PAN/Fe_3O_4-MPA)	154.5	Room temperature	20	(Yazdi et al., 2018)
Calcium hydroxide	0.95	Room temperature	50	(Ramesh et al., 2017)
CH-B	7.1	Room temperature	50	This study
CH-B-HNO_3	19.5	Room temperature	50	This study
CH-B-$NaHCO_3$	24.1	Room temperature	50	This study

2.4 Conclusion

2.4.1 Hydrogel beads derived from SA-CTAB crosslinked $CaCl_2$ for congo red dye adsorption

This research uncovered the remarkable effectiveness of the hydrogel beads composite in removing CR from aqueous solutions. Factors influencing the sorption process of CR dye included CTAB concentrations (0.1 wt.%, 1 wt.%, and 3 wt.%, referred to as SC1, SC2, and SC3, respectively), pH levels, initial CR concentration, and duration. The results demonstrated that increasing CTAB concentration led to increased swelling percentage and decreased carboxyl group. Impressively, the adsorption capacity for CR were measured at 141.08 mg/g, 144.50 mg/g and 153.24 mg/g for SC1, SC2 and SC3, respectively. Isotherm and kinetic models were fitted Freundlich and pseudo-second-order models. These results strongly suggest a complex adsorption mechanism characterized by multilayer formations and chemical interactions.

2.4.2 Porous SA-PAA crosslinked $FeCl_3$ for acid black 1 dye adsorption

This investigation revealed the exceptional efficacy of SA/PAA-Fe in eliminating AB1 from aqueous solution. Several factors such as dosage of adosrbent, pH, initial concentration, and temperature were identified as influential parameters for the sorption of AB1. The adsorption capacity of AB1 was 4.77 mg/g, and the removal percentage was 95.43%. Langmuir and pseudo-second-order models were used on this study to obtain information on the isotherms and kinetics of the adsorption process. These findings suggest that the adsorption process is a monolayer and involves chemical adsorption. Thermodynamic analyses (ΔG°, ΔH°, and ΔS°) demonstrated that the adsorption process of AB1 was endothermic and spontaneous.

2.4.3 Performance of unactivated and activated coffee husk biochar under room temperature using HNO_3 and $NaHCO_3$ for indigo carmine dye adsorption from water

Indigo carmine (IC) dye pollution in water has become a serious environmental hazard owing to the rising industrialization worldwide. Therefore, scientists must prioritize developing effective methods and materials to address these challenges as soon as possible. In this study, an adsorption technique was used to remove IC from water. Coffee husk biochar in unactivated (CH-B) and activated with HNO_3 (CH-B-HNO_3) and $NaHCO_3$ (CH-B-$NaHCO_3$) were prepared as adsorbent. The results show that pH 2.2 is the best condition for all adsorbents. The equilibrium time for CH-B-HNO_3 and CH-B-$NaHCO_3$ was within 90 min, whereas that for CH-B was 1020 min. The adsorption capacity was increased by 63.59% and 70.53% for CH-B- HNO_3 and CH-B-$NaHCO_3$, respectively. The Freundlich isotherm model was fitted for CH-B and CH-B-$NaHCO_3$, whereas the Langmuir isotherm model was fitted for CH-B-HNO_3. P-S-O kinetic models were fitted for all adsorbents. This indicates that the adsorption process was chemisorption. These studies indicate that activating HNO_3 and $NaHCO_3$ is effective in increasing the adsorption capacity for IC removal from water.

References:

Ahmad, R., & Kumar, R. (2010). Adsorptive removal of congo red dye from aqueous solution using bael shell carbon. *Applied Surface Science*, *257*(5), 1628–1633. https://doi.org/10.1016/j.apsusc.2010.08.111

Alharbi, R. A., Alminderej, F. M., Al-Harby, N. F., Elmehbad, N. Y., & Mohamed, N. A. (2023). Preparation and Characterization of a New Bis-Uracil Chitosan-Based Hydrogel as Efficient Adsorbent for Removal of Anionic Congo Red Dye. *Polymers*, *15*(6), 1529. https://doi.org/10.3390/polym15061529

Aljeboree, A. M., & Alkaim, A. F. (2024). Studying removal of anionic dye by prepared highly adsorbent surface hydrogel nanocomposite as an applicable for aqueous solution. *Scientific Reports*, *14*(1), 9102. https://doi.org/10.1038/s41598-024-59545-y

Aslam, U., & Javed, T. (2023). Potential of Citrus limetta peel powder (CLPP) for adsorption of hazardous Congo red dye from wastewater. *Water Practice & Technology*, *18*(5), 1051–1073. https://doi.org/10.2166/wpt.2023.068

Baigorria, E., Cano, L. A., Sanchez, L. M., Alvarez, V. A., & Ollier, R. P. (2020). Bentonite-composite polyvinyl alcohol/alginate hydrogel beads: Preparation, characterization and their use as arsenic removal devices. *Environmental Nanotechnology, Monitoring and Management*, *14*. https://doi.org/10.1016/j.enmm.2020.100364

Barroso-Bogeat, A., Alexandre-Franco, M., Fernández-González, C., & Gómez-Serrano, V. (2019). Activated carbon surface chemistry: Changes upon impregnation with Al(III), Fe(III) and Zn(II)-metal oxide catalyst precursors from NO3− aqueous solutions. *Arabian Journal of Chemistry*, *12*(8), 3963–3976. https://doi.org/10.1016/j.arabjc.2016.02.018

Campos-Vega, R., Loarca-Piña, G., Vergara-Castañeda, H. A., & Dave Oomah, B. (2015). Spent coffee grounds: A review on current research and future prospects. In *Trends in Food Science and Technology* (Vol. 45, Issue 1, pp. 24–36). Elsevier Ltd. https://doi.org/10.1016/j.tifs.2015.04.012

Chatterjee, R., Sajjadi, B., Chen, W. Y., Mattern, D. L., Hammer, N., Raman, V., & Dorris, A. (2020). Effect of Pyrolysis Temperature on PhysicoChemical Properties and Acoustic-Based Amination of Biochar for Efficient CO2 Adsorption. *Frontiers in Energy Research*, *8*. https://doi.org/10.3389/fenrg.2020.00085

Chawla, S., Uppal, H., Yadav, M., Bahadur, N., & Singh, N. (2017). Zinc peroxide nanomaterial as an adsorbent for removal of Congo red dye from waste water. *Ecotoxicology and Environmental Safety*, *135*, 68–74. https://doi.org/10.1016/j.ecoenv.2016.09.017

Chen, T., Liu, H., Gao, J., Hu, G., Zhao, Y., Tang, X., & Han, X. (2022). Efficient Removal of Methylene Blue by Bio-Based Sodium Alginate/Lignin Composite Hydrogel Beads. *Polymers*, *14*(14). https://doi.org/10.3390/polym14142917

Cordova Estrada, A. K., Cordova Lozano, F., & Lara Díaz, R. A. (2021). Thermodynamics and Kinetic Studies for the Adsorption Process of Methyl Orange by Magnetic Activated Carbons. *Air, Soil and Water Research*, *14*. https://doi.org/10.1177/11786221211013336

De Carvalho, T. E. M., Fungaro, D. A., Magdalena, C. P., & Cunico, P. (2011). Adsorption of indigo carmine from aqueous solution using coal fly ash and zeolite from fly ash. *Journal of Radioanalytical and Nuclear Chemistry*, *289*(2), 617–626. https://doi.org/10.1007/s10967-011-1125-8

El-Kammah, M., Elkhatib, E., Gouveia, S., Cameselle, C., & Aboukila, E. (2022). Cost-effective ecofriendly nanoparticles for rapid and efficient indigo carmine dye removal from wastewater: Adsorption equilibrium, kinetics and mechanism. *Environmental Technology and Innovation*, *28*. https://doi.org/10.1016/j.eti.2022.102595

El-Sabbagh, S. M., Mira, H. I., Desouky, O. A., Hussien, S. S., Elgohary, D. M., Ali, A. O., & El Naggar, A. M. A. (2023). Synthesis of fungal chitosan–polystyrene modified by nanoparticles of binary metals for the removal of heavy metals from waste aqueous media. *RSC Advances*, *13*(42), 29735–29748. https://doi.org/10.1039/D3RA04451C

Fadimatou, N. M., Fotsing, P. N., Mandjewil, A., Siewe, J. M., Vieillard, J., Dotto, G. L., Woumfo, E. D., & Ngueagni, P. T. (2024). Cetyltrimethylammonium bromide (CTAB) functionalization of sodium silicate from rice husks ash for Naphthol Green B and Congo Red adsorption. *Emergent Materials*. https://doi.org/10.1007/s42247-024-00655-8

Foroughi-dahr, M., Abolghasemi, H., Esmaieli, M., Nazari, G., & Rasem, B. (2015). Experimental study on the adsorptive behavior of Congo red in cationic surfactant-modified tea waste. *Process Safety and Environmental Protection*, *95*, 226–236. https://doi.org/10.1016/j.psep.2015.03.005

Frent, O. D., Vicas, L. G., Duteanu, N., Morgovan, C. M., Jurca, T., Pallag, A., Muresan, M. E., Filip, S. M., Lucaciu, R. L., & Marian, E. (2022). Sodium Alginate—Natural

Microencapsulation Material of Polymeric Microparticles. In *International Journal of Molecular Sciences* (Vol. 23, Issue 20). MDPI. https://doi.org/10.3390/ijms232012108

Gao, H. J., Wang, S. F., Fang, L. M., Sun, G. A., Chen, X. P., Tang, S. N., Yang, H., Sun, G. Z., & Li, D. F. (2021). Nanostructured spinel-type M(M = Mg, Co, Zn)Cr2O4 oxides: novel adsorbents for aqueous Congo red removal. *Materials Today Chemistry*, *22*, 100593. https://doi.org/10.1016/j.mtchem.2021.100593

Harja, M., Buema, G., & Bucur, D. (2022). Recent advances in removal of Congo Red dye by adsorption using an industrial waste. *Scientific Reports*, *12*(1), 6087. https://doi.org/10.1038/s41598-022-10093-3

Hidayat, E., Halem, H. I. A., Mitoma, Y., & Harada, H. (2021). Recovery of Biomass Incinerated as Struvite-K Precipitates Followed Aluminium Removal. *Green and Sustainable Chemistry*, *11*(03), 96–106. https://doi.org/10.4236/gsc.2021.113009

Hidayat, E., Harada, H., Mitoma, Y., Yonemura, S., & Halem, H. I. A. (2022). Rapid Removal of Acid Red 88 by Zeolite/Chitosan Hydrogel in Aqueous Solution. *Polymers*, *14*(5). https://doi.org/10.3390/polym14050893

Hidayat, E., Khaekhum, S., Yonemura, S., Mitoma, Y., & Harada, H. (2022). Biosorption of Eriochrome Black T Using Exserohilum rostratum NMS1.5 Mycelia Biomass. *J*, *5*(4), 427–434. https://doi.org/10.3390/j5040029

Hidayat, E., Mohamad Sarbani, N. M. B., Yonemura, S., Mitoma, Y., & Harada, H. (2023a). Application of Box–Behnken Design to Optimize Phosphate Adsorption Conditions from Water onto Novel Adsorbent CS-ZL/ZrO/Fe3O4: Characterization, Equilibrium, Isotherm, Kinetic, and Desorption Studies. *International Journal of Molecular Sciences*, *24*(11). https://doi.org/10.3390/ijms24119754

Hidayat, E., Mohamad Sarbani, N. M. B., Yonemura, S., Mitoma, Y., & Harada, H. (2023b). Application of Box–Behnken Design to Optimize Phosphate Adsorption Conditions from Water onto Novel Adsorbent CS-ZL/ZrO/Fe3O4: Characterization, Equilibrium, Isotherm, Kinetic, and Desorption Studies. *International Journal of Molecular Sciences*, *24*(11). https://doi.org/10.3390/ijms24119754

Hidayat, E., Sarbani, N. M. M., Lahiri, S. K., Samitsu, S., Yonemura, S., Mitoma, Y., & Harada, H. (2024). Effects of sodium alginate-poly(acrylic acid) cross-linked hydrogel beads on soil conditioner in the absence and presence of phosphate and carbonate ions. *Case Studies in Chemical and Environmental Engineering*, *9*, 100642. https://doi.org/10.1016/j.cscee.2024.100642

Hidayat, E., Yoshino, T., Yonemura, S., Mitoma, Y., & Harada, H. (2022). Synthesis, Adsorption Isotherm and Kinetic Study of Alkaline- Treated Zeolite/Chitosan/Fe3+ Composites for Nitrate Removal from Aqueous Solution—Anion and Dye Effects. *Gels*, *8*(12). https://doi.org/10.3390/gels8120782

Jellali, S., Azzaz, A. A., Al-Harrasi, M., Charabi, Y., Al-Sabahi, J. N., Al-Raeesi, A., Usman, M., Al Nasiri, N., Al-Abri, M., & Jeguirim, M. (2022). Conversion of Industrial Sludge into Activated Biochar for Effective Cationic Dye Removal: Characterization and Adsorption Properties Assessment. *Water (Switzerland)*, *14*(14). https://doi.org/10.3390/w14142206

Karimifard, S., & Alavi Moghaddam, M. R. (2018). Application of response surface methodology in physicochemical removal of dyes from wastewater: A critical review. In *Science of the Total Environment* (Vols. 640–641, pp. 772–797). Elsevier B.V. https://doi.org/10.1016/j.scitotenv.2018.05.355

Lal Maurya, K., Swain, G., Kumar Sonwani, R., Verma, A., & Sharan Singh, R. (2022). Biodegradation of Congo red dye using polyurethane foam-based biocarrier combined with activated carbon and sodium alginate: Batch and continuous study. *Bioresource Technology*, *351*, 126999. https://doi.org/10.1016/j.biortech.2022.126999

Li, Y., Meas, A., Shan, S., Yang, R., & Gai, X. (2016). Production and optimization of bamboo hydrochars for adsorption of Congo red and 2-naphthol. *Bioresource Technology*, *207*, 379–386. https://doi.org/10.1016/j.biortech.2016.02.012

Liang, C., Ren, J., El Hankari, S., & Huo, J. (2020). Aqueous Synthesis of a Mesoporous Zr-Based Coordination Polymer for Removal of Organic Dyes. *ACS Omega*, *5*(1), 603–609. https://doi.org/10.1021/acsomega.9b03192

Lita, A. L., Hidayat, E., Mohamad Sarbani, N. M., Harada, H., Yonemura, S., Mitoma, Y., Herviyanti, & Gusmini. (2023). Glyphosate Removal from Water Using Biochar Based Coffee Husk Loaded Fe3O4. *Water*, *15*(16), 2945. https://doi.org/10.3390/w15162945

Liu, H., Xu, G., & Li, G. (2021). Preparation of porous biochar based on pharmaceutical sludge activated by NaOH and its application in the adsorption of tetracycline. *Journal of Colloid and Interface Science*, *587*, 271–278. https://doi.org/10.1016/j.jcis.2020.12.014

Liu, J., Wang, N., Zhang, H., & Baeyens, J. (2019). Adsorption of Congo red dye on FexCo3-xO4 nanoparticles. *Journal of Environmental Management*, *238*, 473–483. https://doi.org/10.1016/j.jenvman.2019.03.009

Md Salim, R., Asik, J., & Sarjadi, M. S. (2021). Chemical functional groups of extractives, cellulose and lignin extracted from native Leucaena leucocephala bark. *Wood Science and Technology*, *55*(2), 295–313. https://doi.org/10.1007/s00226-020-01258-2

Merakchi, A., Bettayeb, S., Drouiche, N., Adour, L., & Lounici, H. (2019). Cross-linking and modification of sodium alginate biopolymer for dye removal in aqueous solution. *Polymer Bulletin*, *76*(7), 3535–3554. https://doi.org/10.1007/s00289-018-2557-x

Modrzejewska, Z. (2013a). Sorption mechanism of copper in chitosan hydrogel. *Reactive and Functional Polymers*, *73*(5), 719–729. https://doi.org/10.1016/j.reactfunctpolym.2013.02.014

Modrzejewska, Z. (2013b). Sorption mechanism of copper in chitosan hydrogel. *Reactive and Functional Polymers*, *73*(5), 719–729. https://doi.org/10.1016/j.reactfunctpolym.2013.02.014

Mohamad Sarbani, N. M., Hidayat, E., Naito, K., Mitoma, Y., & Harada, H. (2023). Cr (VI) and Pb (II) Removal Using Crosslinking Magnetite-Carboxymethyl Cellulose-Chitosan Hydrogel Beads. *Gels*, *9*(8), 612. https://doi.org/10.3390/gels9080612

Moharm, A. E., El Naeem, G. A., Soliman, H. M. A., Abd-Elhamid, A. I., El-Bardan, A. A., Kassem, T. S., Nayl, A. A., & Bräse, S. (2022). Fabrication and Characterization of Effective Biochar Biosorbent Derived from Agricultural Waste to Remove Cationic Dyes from Wastewater. *Polymers*, *14*(13). https://doi.org/10.3390/polym14132587

Mokeddem, A., Benykhlef, S., Bendaoudi, A. A., Boudouaia, N., Mahmoudi, H., Bengharez, Z., Topel, S. D., & Topel, Ö. (2023). Sodium Alginate-Based Composite Films for Effective Removal of Congo Red and Coralene Dark Red 2B Dyes: Kinetic, Isotherm and Thermodynamic Analysis. *Water*, *15*(9), 1709. https://doi.org/10.3390/w15091709

Munagapati, V. S., Yarramuthi, V., Kim, Y., Lee, K. M., & Kim, D. S. (2018). Removal of anionic dyes (Reactive Black 5 and Congo Red) from aqueous solutions using Banana Peel Powder as an adsorbent. *Ecotoxicology and Environmental Safety*, *148*, 601–607. https://doi.org/10.1016/j.ecoenv.2017.10.075

Naushad, M., Ahamad, T., Al-Maswari, B. M., Abdullah Alqadami, A., & Alshehri, S. M. (2017). Nickel ferrite bearing nitrogen-doped mesoporous carbon as efficient adsorbent for the removal of highly toxic metal ion from aqueous medium. *Chemical Engineering Journal*, *330*, 1351–1360. https://doi.org/10.1016/j.cej.2017.08.079

Ouyang, F., Liu, Y., Chen, J., Tang, C., Wang, A., Lu, Y., & Yuan, Y. (2023). Study on Preparation of Rabbit Manure Biochar and Activation of Peroxymonosulfate for Rhodamine B Degradation. *Water (Switzerland)*, *15*(11). https://doi.org/10.3390/w15112015

Patel, A., Soni, S., Mittal, J., Mittal, A., & Arora, C. (2021). Sequestration of crystal violet from aqueous solution using ash of black turmeric rhizome. *Desalination and Water Treatment*, *220*, 342–352. https://doi.org/10.5004/dwt.2021.26911

Piaskowski, K., Świderska-Dąbrowska, R., & Zarzycki, P. K. (2018). Dye Removal from Water and Wastewater Using Various Physical, Chemical, and Biological Processes. *Journal of AOAC INTERNATIONAL*, *101*(5), 1371–1384. https://doi.org/10.5740/jaoacint.18-0051

Qurrat-Ul-Ain, Khatoon, J., Shah, M. R., Malik, M. I., Khan, I. A. T., Khurshid, S., & Naz, R. (2019). Convenient pH-responsive removal of Acid Black 1 by green l-histidine/iron oxide magnetic nanoadsorbent from water: Performance and mechanistic studies. *RSC Advances*, *9*(6), 2978–2996. https://doi.org/10.1039/c8ra09279f

Qurrat-ul-Ain, Q.-A., Khatoon, J., Shah, M. R., Malik, M. I., Khan, I. A. T., Khurshid, S., & Naz, R. (2019). Convenient pH-responsive removal of Acid Black 1 by green <scp>l</scp> -histidine/iron oxide magnetic nanoadsorbent from water: performance and mechanistic studies. *RSC Advances*, *9*(6), 2978–2996. https://doi.org/10.1039/C8RA09279F

Ramesh, T. N., Kirana, D. V., Ashwini, A., & Manasa, T. R. (2017). Calcium hydroxide as low cost adsorbent for the effective removal of indigo carmine dye in water. *Journal of Saudi Chemical Society*, *21*(2), 165–171. https://doi.org/10.1016/j.jscs.2015.03.001

Sami, A. J., Butt, Y. N., & Nasar, S. (2018). Elimination of a Carcinogenic Anionic Dye Congo Red from Water Using Hydrogels Based on Chitosan, Acrylamide and Graphene Oxide. *Journal of Bioprocessing & Biotechniques*, *08*(05). https://doi.org/10.4172/2155-9821.1000334

Sánchez-Rodríguez, S., Trujillo-Reyes, J., Gutiérrez-Segura, E., Solache-Ríos, M., & Colín-Cruz, A. (2015). Removal of Indigo Carmine by a Ni Nanoscale Oxides/Schoenoplectus acutus Composite in Batch and Fixed Bed Column Systems. *Separation Science and Technology (Philadelphia)*, *50*(11), 1602–1610. https://doi.org/10.1080/01496395.2014.986579

Saravanan, P., Thillainayagam, B. P., Ravindiran, G., & Josephraj, J. (2020). Evaluation of the adsorption capacity of Cocos Nucifera shell derived biochar for basic dyes sequestration from aqueous solution. *Energy Sources, Part A: Recovery, Utilization and Environmental Effects*. https://doi.org/10.1080/15567036.2020.1800142

Shamsuddin, N. A., & Munajat, N. F. (2023). Characteristics of biochar from fish wastes pyrolysis in a fixed-bed reactor. *AIP Conference Proceedings*, *2484*. https://doi.org/10.1063/5.0110751

Shayesteh, H., Rahbar-Kelishami, A., & Norouzbeigi, R. (2016). Evaluation of natural and cationic surfactant modified pumice for congo red removal in batch mode: Kinetic, equilibrium, and thermodynamic studies. *Journal of Molecular Liquids*, *221*, 1–11. https://doi.org/10.1016/j.molliq.2016.05.053

Silveira Junior, E. G., Perez, V. H., de Paula, S. C. S. E., Silveira, T. da C., Olivares, F. L., & Justo, O. R. (2023). Coffee Husks Valorization for Levoglucosan Production and Other Pyrolytic Products through Thermochemical Conversion by Fast Pyrolysis. *Energies*, *16*(6). https://doi.org/10.3390/en16062835

Srivatsav, P., Bhargav, B. S., Shanmugasundaram, V., Arun, J., Gopinath, K. P., & Bhatnagar, A. (2020). Biochar as an eco-friendly and economical adsorbent for the removal of colorants (Dyes) from aqueous environment: A review. In *Water (Switzerland)* (Vol. 12, Issue 12). MDPI AG. https://doi.org/10.3390/w12123561

Sun, Y., Li, H., Li, G., Gao, B., Yue, Q., & Li, X. (2016). Characterization and ciprofloxacin adsorption properties of activated carbons prepared from biomass wastes by H3PO4 activation. *Bioresource Technology*, *217*, 239–244. https://doi.org/10.1016/j.biortech.2016.03.047

Tang, S., Zhao, Y., Wang, H., Wang, Y., Zhu, H., Chen, Y., Chen, S., Jin, S., Yang, Z., Li, P., & Li, S. (2018). Preparation of the sodium alginate-g-(polyacrylic acid-co-allyltrimethylammonium chloride) polyampholytic superabsorbent polymer and its dye adsorption property. *Marine Drugs*, *16*(12). https://doi.org/10.3390/md16120476

Thakur, S., & Arotiba, O. A. (2018). Synthesis, swelling and adsorption studies of a pH-responsive sodium alginate–poly(acrylic acid) superabsorbent hydrogel. *Polymer Bulletin*, *75*(10), 4587–4606. https://doi.org/10.1007/s00289-018-2287-0

Torabinejad, A., Nasirizadeh, N., Yazdanshenas, M. E., & Tayebi, H. A. (2017). Synthesis of conductive polymer-coated mesoporous MCM-41 for textile dye removal from aqueous media. *Journal of Nanostructure in Chemistry*, *7*(3), 217–229. https://doi.org/10.1007/s40097-017-0232-7

Tran, T. H., Le, H. H., Pham, T. H., Nguyen, D. T., La, D. D., Chang, S. W., Lee, S. M., Chung, W. J., & Nguyen, D. D. (2021). Comparative study on methylene blue adsorption behavior of coffee husk-derived activated carbon materials prepared using hydrothermal and soaking methods. *Journal of Environmental Chemical Engineering*, *9*(4). https://doi.org/10.1016/j.jece.2021.105362

Tsoutsa, E. K., Tolkou, A. K., Katsoyiannis, I. A., & Kyzas, G. Z. (2023). Composite Activated Carbon Modified with AlCl3 for the Effective Removal of Reactive Black 5 Dye from Wastewaters. *Journal of Composites Science*, *7*(6), 224. https://doi.org/10.3390/jcs7060224

Vijayaraghavan, K., & Ashokkumar, T. (2019). Characterization and evaluation of reactive dye adsorption onto Biochar Derived from Turbinaria conoides Biomass. *Environmental Progress and Sustainable Energy*, *38*(4). https://doi.org/10.1002/ep.13143

Wang, Z., Li, J., Zhang, G., Zhi, Y., Yang, D., Lai, X., & Ren, T. (2020). Characterization of acid-aged biochar and its ammonium adsorption in an aqueous solution. *Materials*, *13*(10). https://doi.org/10.3390/ma13102270

Wiśniewska, M., Nowicki, P., Nosal-Wiercińska, A., Pietrzak, R., Szewczuk-Karpisz, K., Ostolska, I., & Sternik, D. (2017). Adsorption of poly(acrylic acid) on the surface of microporous activated carbon obtained from cherry stones. *Colloids and Surfaces A: Physicochemical and Engineering Aspects*, *514*, 137–145. https://doi.org/10.1016/j.colsurfa.2016.11.053

Wong, S., Ghafar, N. A., Ngadi, N., Razmi, F. A., Inuwa, I. M., Mat, R., & Amin, N. A. S. (2020). Effective removal of anionic textile dyes using adsorbent synthesized from coffee waste. *Scientific Reports*, *10*(1). https://doi.org/10.1038/s41598-020-60021-6

Yang, H., Tejado, A., Alam, N., Antal, M., & van de Ven, T. G. M. (2012). Films Prepared from Electrosterically Stabilized Nanocrystalline Cellulose. *Langmuir*, *28*(20), 7834–7842. https://doi.org/10.1021/la2049663

Yang, T., Zhang, W., Liu, H., & Guo, Y. (2020). Enhanced removal of U(VI) from aqueous solution by chitosan-modified zeolite. *Journal of Radioanalytical and Nuclear Chemistry*, *323*(2), 1003–1012. https://doi.org/10.1007/s10967-019-06993-w

Yazdi, M. G., Ivanic, M., Mohamed, A., & Uheida, A. (2018). Surface modified composite nanofibers for the removal of indigo carmine dye from polluted water. *RSC Advances*, *8*(43), 24588–24598. https://doi.org/10.1039/c8ra02463d

Zeydouni, G., Kianizadeh, M., Omidi Khaniabadi, Y., Nourmoradi, H., Esmaeili, S., Mohammadi, M. J., & Rashidi, R. (2019). Eriochrme black-T removal from aqueous environment by surfactant modified clay: equilibrium, kinetic, isotherm, and thermodynamic studies. *Toxin Reviews*, *38*(4), 307–317. https://doi.org/10.1080/15569543.2018.1455214

Zhang, B., Wu, Y., & Cha, L. (2020). Removal of methyl orange dye using activated biochar derived from pomelo peel wastes: performance, isotherm, and kinetic studies. *Journal of Dispersion Science and Technology*, *41*(1), 125–136. https://doi.org/10.1080/01932691.2018.1561298

Zhang, S., Zhang, Y., Fu, L., & Jing, M. (2021). A chitosan fiber as green material for removing Cr(VI) ions and Cu(II) ions pollutants. *Scientific Reports*, *11*(1). https://doi.org/10.1038/s41598-021-02399-5

Zhao, D., & Shen, X. (2023). Preparation of Chitosan-Diatomite/Calcium Alginate Composite Hydrogel Beads for the Adsorption of Congo Red Dye. *Water*, *15*(12), 2254. https://doi.org/10.3390/w15122254

Zhao, J., Lu, Z., He, X., Zhang, X., Li, Q., Xia, T., Zhang, W., & Lu, C. (2017). Fabrication and Characterization of Highly Porous Fe(OH)3@Cellulose Hybrid Fibers for Effective Removal of Congo Red from Contaminated Water. *ACS Sustainable Chemistry and Engineering*, *5*(9), 7723–7732. https://doi.org/10.1021/acssuschemeng.7b01175

Zhu, Y., Yi, B., Yuan, Q., Wu, Y., Wang, M., & Yan, S. (2018). Removal of methylene blue from aqueous solution by cattle manure-derived low temperature biochar. *RSC Advances*, *8*(36), 19917–19929. https://doi.org/10.1039/c8ra03018a

Chapter 3: Harnessing of hydrogel beads and biochar composite to immobilize salinity, heavy metals and glyphosate and improvement of soil health

3.1 Introduction

The global agricultural landscape confronts significant challenges arising from the increase in global population and the growing impact of climate change. This has resulted in a rising need for innovative approaches to tackle the interconnected problems of water scarcity and soil degradation (Tomadoni et al., 2020). The productivity of agricultural food production is heavily dependent on soil quality and the availability of sufficient water. Human activities, such as unsustainable agricultural practices, deforestation, and soil pollution, can lead to soil mismanagement, erosion, and diminishing fertile land, which may negatively impact the production of food (Wantzen & Mol, 2013). Inadequate rainfall and ineffective utilization of accessible water substantially affect the quantity and quality of food produced. Consequently, crop productivity is declining annually, endangering the global food security. To ensure sufficient availability of food, it is crucial to rehabilitate deteriorating soils and optimize the utilization of limited natural resources, such as rainfall. A key research challenge involves devising innovative solutions to overcome existing limitations and enhance soil quality and yield to meet global demands (Bibi et al., 2019; Vundavalli et al., 2015).

Furthermore, soil salinization significantly threatens crop development and productivity, especially in arid and semiarid regions (Qadir et al., 2017). The overall extent of soil salinization affects approximately 1 billion hectares, accounting for about 7% of the Earth's continental area, nearly ten times the size of Venezuela or twenty times France (Metternicht & Zinck, 2003). Soil salinity represents a notable environmental stress caused by excessive salt concentrations or significant amounts of exchangeable sodium ions (Na) in soil contents (Shahid et al., 2018). The build-up of salts in soils results in the degradation of soil properties, leading to a decline in osmotic potential, which can restrict water availability to root cells, consequently hampering plant growth (Ahammed et al., 2020; Ashraf and Harris, 2004). Cevheri et al. (2022) and Leogrande and Vitti (2019) have illustrated the adverse effects of soil salinity on plant development, primarily ascribed to its detrimental impact on organic matter and nutrient cycling.

The solubility of chemical fertilizers is intimately tied to nutrient cycling processes and organic matter in the soil. Nutrient cycling involves the uptake of nutrients by plants, their release into the soil upon the breakdown of organic matter, and their subsequent availability for plant use (Grzyb et al., 2020). Organic matter is vital as it stores nutrients, supports microbial activity, and makes nutrients, including those in chemical fertilizers, more soluble and accessible to plants (Jamir et al., 2019; Rashid et al., 2016). High levels of organic matter enhance the soil's capacity to retain water and nutrients, facilitating the gradual release of nutrients from organic sources and chemical fertilizers. This improves overall nutrient availability to plants while reducing the risk of nutrient leaching (Malcolm et al., 2019). Additionally, organic matter contributes to soil aggregate stabilization, further impacting nutrient solubility and availability by influencing soil structure and porosity.

Conversely, nutrient cycling may not be as efficient in soil with low organic matter content, necessitating a greater reliance on soluble chemical fertilizers to meet plants' essential nutrient requirements. However, the effectiveness and solubility of these chemical fertilizers can be influenced by various factors, including pH level, electrical conductivity (EC), and the content of sodium (Na), potassium (K), magnesium (Mg), and calcium (Ca) (Fageria et al., 2014; Moreira et al., 2015). Moreover, metrics such as sodium absorption ratio (SAR) and exchangeable sodium percentage (ESP) provide valuable insights into establishing optimal chemical conditions within the soil component (Shirokova et al., 2000). Evaluating soil salinity and sodicity typically involves measuring EC, SAR, and ESP parameters. Soils containing lower values of EC (<4 mS/cm), SAR (<13), and ESP (<15%) are generally considered natural and non-sodic soil (Shrivastava & Kumar, 2015; Tanehgonbadi & Qaderi, 2023). EC values indicate soil salinity levels, while SAR and ESP values reflect the amount of sodium in the soil.

On the other hand, arsenic (As) and iron (Fe) contamination has received significant attention due to its greater mobility in soil than other metals. As is a metalloid which naturally occurs in the environment, often found at concentrations up to 40 mg/kg (Tchounwou et al., 2004). Furthermore, usually farmers used glyphosate to remove unwanted plant such as grass which cultivated around industrial activity. Nonetheless, uncontrolled application of glyphosate in agricultural area can cause serious damage to environmental ecosystems. As, Fe and Glyphosate enters the water system through several sources such as agricultural runoff from rainfall or irrigation and groundwater leakage from contaminated crop residues. These contamination can be washed into water bodies during rain events and then settled in surrounding soils leading to become saline condition. As a result, this highly poisonous As, Fe and glyphosate can contaminate clean water and food supplies, posing a risk of As, Fe, and glyphosate poisoning that may have fatal consequences to human health and plant life (Shankar et al., 2014).

Recently, hydrogel and biochar presented a promising alternative to counter the detrimental impacts of saline, As, Fe, and glyphosate contamination, with particular emphasis on immobilization techniques (Tefera et al., 2022). It absorbs water and gradually releases it to the surrounding soil (Z. Li & Zhang, 2023). These polymers are not only capable of soaking up and holding substantial quantities of water, but they also show potential as pollutant immobilization agents in soil. When immobilizing in solution, pollutant molecules captured by the hydrophilic functional groups within, such as the hydroxyl (-OH) groups.

Moreover, many studies have been reported to increase the porosity and surface properties of biochar through the use of additives during pyrolysis (H. Yang et al., 2024). For instance, (L. Yang et al., 2018) found that co-pyrolyzing sawdust with $Ca(H_2PO_4)_2$ at 600 °C significantly increased the surface area of the resulting biochar. Similarly, (H. Chen et al., 2019) demonstrated that adding H_3PO_4 during pyrolysis not only increased the surface area but also the concentration of oxygen-containing functional groups such as carboxyl and hydroxyl groups. (H. Zhang et al., 2022) showed that K_3PO_4 enhanced the pore structure and surface chemical properties of biochar, significantly boosting its capacity to adsorb cadmium (II). Further, (Crombie & Mašek, 2015) observed that adding MgO to biochar enhanced porosity and phosphorus removal (H. Liang et al., 2023) phosphorus removal and provided benefits as a slow-release phosphorus source due to the formation of Mg-P precipitates. With growing interest in improving biochar as for pollutant remediation, concerns about the stability of its carbon content have increased. The stability of biochar's carbon is crucial for its long-term effectiveness in carbon sequestration.

Increasing the stable carbon content in biochar is one method to enhance its carbon sequestration potential; this generally involves intensifying the pyrolysis conditions, such as higher temperatures and longer residence times, which, while reducing solid yield, increase carbon release as gas, leading to higher CO_2 emissions when these gases are burned (Crombie et al., 2013). In terms of carbon capture and storage, enhancing the stable carbon obtainable from a given amount of biomass is particularly relevant, as it effectively reduces the biomass required to sequester a unit of carbon.

The stability of biochar's carbon is linked to its condensed aromatic structure, which is influenced by the biomass composition and the pyrolysis conditions, especially the highest treatment temperature (HTT) (Ameloot et al., 2013). Some studies have shown increased carbon retention in biochar using additives (biomass-to-additive ratios), for example, (Ren et al., 2018) used $Ca(OH)_2$ in a 1:9 ratio, and (Zhao et al., 2017) used H_3PO_4 in ratios of 0.359:1 and 0.718:1. However, to the best author knowledge, no studies have reported the use of MgO-containing additives in biochar to assess carbon stability. We hypothesize that MgO additions significantly affect the structure and stability of biochar. Our extensive investigations into the effects of MgO on biochar's chemical composition, porosity, surface area, organic functional groups, and chemical stability can broaden the understanding of how MgO-containing additives impact biochar's capacity for carbon sequestration.

In this chapter, we employed various fabrication of hydrogel beads and biochar composites to remove saline, As, Fe, and glyphosate contamination. This study investigated a promising sustainable approach to managing mineral fertilizers' discharge and identified environmentally acceptable alternatives to enhance and mitigate soil quality in contamination areas.

3.2 Materials and method

3.2.1 Materials

Calcium chloride ($CaCl_2$, 99%), hydrochloric acid (HCl, 36.5-38%), sulfuric acid (H_2SO_4, 95%), potassium chloride (KCl, 99.5%), sodium carbonate (Na_2CO_3, >99.8%), sodium hydrogen phosphate ($NaHPO_4$, >99.95%), sodium bicarbonate ($NaHCO_3$, >99.5%), ammonium acetate (CH_3COONH_4, >97%), potassium dichromate ($K_2Cr_2O_7$, 99.5%) and sodium hydroxide (NaOH, 99.99%) were purchased from Kanto Chemical Co. Inc., Japan. Sodium alginate was purchased from Wako Chemicals, Tokyo, Japan. Poly (acrylic acid) (molecular weight: 100.000) was purchased from Scientific Polymer Products, INC., New York.

3.2.2 Preparation of samples

3.2.2.1 Effects of sodium alginate-poly (acrylic acid) cross-linked hydrogel beads on soil conditioner in the absence and presence of phosphate and carbonate ions

Hydrogel beads were formed by combining 6 mL of 1 wt% sodium alginate aqueous solution, 6 mL of 5 wt% poly (acrylic acid) aqueous solution, 1 mL of 3 M NaOH, and 1 mL of distilled water (DW) for the base S-Alg/P-Acc. To create functionalized variants, S-Alg/P-Acc@PO_4^{3-} and S-Alg/P-Acc@CO_3^{2-}, 1 mL of 2000 mg/L PO_4^{3-} and 1 mL of 2000 mg/L CO_3^{2-} were added, respectively, in place of DW. The samples were placed in bottle flasks and shaken on a rotary shaker (Rotator RT-50) for 1 h at room temperature (25°–30° C). Then, the solution was injected slowly using a 10 mL syringe, one drop at a time, into a pre-prepared 10 wt% $CaCl_2$ aqueous solution. Subsequently, the hydrogel beads were allowed to grow for 90 min to obtain the resultant hydrogel beads. The hydrogel beads were then washed with ethanol and DW, and then let to dry in an oven at 60 °C for 24 h.

3.2.2.2 Harnessing hydrogel beads for immobilization of arsenic

Sodium alginate and poly (acrylic acid) were mixed in DI water at concentrations of 2 and 5 wt%, respectively, and left to stand for 24 h at room temperature. PVA was fully dissolved in boiling water (100 °C) at a concentration of 5 wt%. Humic acid (HA) solution was prepared by mixing 0.2 g of HA with 20 mL of 1 M NaOH and allowing it to react at room temperature for 24 h, followed by filtration through filter paper. Hydrogel beads were formed in the presence (SPPG) and absence (SPP) of glutaraldehyde. SPPG was prepared by combining 5 mL of each solution containing SA, PAA, and PVA. Then, 2 mL of the HA extraction solution was added. Furthermore, 2 mL of a 10 g/L PO_4^{3-} solution and 0.1 mL of 25% glutaraldehyde were added in a flask and shaken with rotary shaker for 15 min at room temperature. The resultant solution was gradually injected into a 10 wt% $FeCl_3$ aqueous solution using a 10 mL syringe. The hydrogel beads were left for 90 min to ensure homogeneous formation before being rinsed with ethanol and DI and then dried in an oven at 60 °C for 24 h. SPP hydrogel bead samples were prepared using the same procedures as above without glutaraldehyde.

3.2.2.3 Evaluation of slow-release fertilizers derived from hydrogel beads: sodium alginate-poly (acrylic acid) and humic acid-encapsulated struvite for soil salinity amelioration

3.2.2.3.1 Preparation of struvite precipitation

Deionized water was used to prepare stock solutions of magnesium chloride, ammonium chloride, and sodium dihydrogen phosphate at room temperature. These solutions were mixed in a ratio of 1:1:1, with equal concentrations of Mg, NH_4-N, and P. The pH of the solution was adjusted to 8.0, 8.5, 9.0, 9.5, and 10.0 by gradually adding 0.1 M NaOH solution under magnetic stirring for 15 min. The solution was allowed to age overnight to ensure uniformity and was filtered to determine the Mg, NH_4-N, and P removal percentage (Removal, (%)) using Eq. (17) (Hidayat, Mohamad Sarbani, et al., 2023b). The resulting solid residue was dried in an oven at 60 °C for 48 hours for further analysis.

$$\text{Removal, (\%)} = \frac{C_i - C_e}{C_i} \times 100 \tag{17}$$

where *Removal, (*%) is the removal efficiency, and C_i and C_e are the initial and equilibrium phosphorus concentrations (mg/L), respectively.

3.2.2.3.2 The procedure to encapsulate struvite in hydrogel bead

This study utilized struvite obtained from a pH of 9.0 as the additional material to produce hydrogel beads encapsulation. Encapsulating struvite within hydrogel beads was carried out at room temperature. To prepare Sa@S, a combination of 6 mL of 2 wt% sodium alginate aqueous solution, 6 mL of 5 wt% poly (acrylic acid) aqueous solution, 1 mL of 3 M NaOH, and 0.1 g of struvite was mixed and agitated in bottle flasks for 1 hour. The mixture was then slowly injected into a 10 wt% $CaCl_2$ aqueous solution using a 10 mL syringe. The resulting hydrogel beads were left to grow overnight to facilitate crosslinking. Afterward, the hydrogel beads were washed with ethanol, deionized water, and dried in an oven at 25°C for 24 hours. The method for encapsulating Sa@SHa hydrogel beads involved substituting 3 M NaOH with HA solution. To prepare HA, a mixture of 3 M NaOH (20 mL) and 0.1 g of HA was allowed to react at room temperature for 24 hours, after which the solution was filtered through filter paper.

3.2.2.4 Co-pyrolysis MgO-Biochar under Difference Temperature Derived from Coffee Husk for glyphosate immobilization in soil: Evaluation of Biochar Characteristics and Carbon Stability

3.2.2.4.1 Production of biochar

Biochar was produced from coffee husk (CH) waste, sourced from Cooperative Solok Radjo in Solok, Indonesia. The CH was cut into small pieces, dried in an oven at 60 °C for three days, and then placed in a 50 mL crucible. During pyrolysis, magnesium oxide (MgO) was added in a 1:1 ratio to the CH. The mixture was then heated at a constant rate of 50 °C per minute to reach pyrolysis temperatures of 350 °C, 500 °C, and 650 °C, maintaining each temperature for three hours. Post-pyrolysis, all biochar samples were oven-dried at 60 °C for three days in preparation for further experiments. The samples were labelled as MgB-A, MgB-B, and MgB-C corresponding to the pyrolysis temperatures of 350 °C, 500 °C, and 650 °C, respectively.

3.2.3 Determination of the hydrogel beads porosity

Porosity was measured using the water displacement technique, following a previous study (Sornkamnerd et al., 2017). The hydrogel beads were immersed in ethanol for 24 h to to remove unreacted monomers and create pores. The weight of the hydrogel beads was then measured with an electronic balance, and the porosity was determined using the following Eq. (19).

$$V_s = V - \left(\frac{W_2 - W_1 - W_0}{\rho}\right) \tag{18}$$

$$\text{Porosity (\%)} = \frac{(W_s - W_d)/\rho}{V_s} \tag{19}$$

where V_s is the volume of the hydrogel beads (cm^3), V is the volume of the ethanol solution (mL), W_2 is the weighted sum of the empty beaker, ethanol, and hydrogel beads (g), W_1 is the weight of empty beaker (g), W_0 is the weight of dried beads (g). ρ is the density of ethanol (0.7892 g/cm^3). where W_d is the dry weight of the beads, and W_s is the weight of the beads filled with ethanol.

3.2.4 Carboxyl group analysis of hydrogel beads

The carboxyl content inside the cross-linked hydrogel beads was measured using conductometric titration (H. Yang et al., 2012). In brief, ~25 mg of dried hydrogel bead composite was mixed with a 20 mM NaCl solution (2.5 mL), and the mixture was agitated for 30 min to achieve a uniform distribution. Subsequently, HCl (100 mM) was gradually introduced into the mixture to reach a pH value of 3.0. The suspension was then incrementally adjusted using a 10 mM NaOH solution to attain a pH of 11.0. The content of carboxyl group in the crosslinked hydrogel beads was quantified using Eq. (20).

$$\text{COOH (mmol/g)} = \frac{V_{NaOH} \times M_{NaOH}}{W_d} \tag{20}$$

where COOH (mmol/g) is the carboxyl content of the cross-linked hydrogel beads. V_{NaOH} (mL) represents the volume of NaOH required to deprotonate COOH groups. M_{NaOH} (mol/L) represents the molarity of the NaOH. where W_d (g) is the weight of the initial dry hydrogel beads.

3.2.5 Swelling and degradation experiments

The swelling characteristics of the hydrogel beads and the influence of pH were assessed. In brief, dried hydrogel beads were immersed in a glass beaker containing 25 mL of aqueous solution. The experiments were conducted at 25 °C for 24 h and the swelling ratio was calculated using the following Eq. (21).

$$\text{SR}\ (\%) = \frac{W_s - W_d}{W_d} \times 100 \tag{21}$$

where W_s is the weights of swollen hydrogels and W_d is the weights of dried hydrogels.

The degradation of the hydrogel beads was conducted at 100 °C for 24 h. Subsequently, the dried hydrogel beads were immersed in 50 mL of solution. The resulting samples were filtered and dried in an oven at 60 °C for 24 hours. equation (22) was employed to calculate the degradation rate percentage.

$$\text{Degradation rate}\ (\%) = \frac{W_s - W_d}{W_s} \times 100 \tag{22}$$

where W_s is the weight of dried hydrogels before treatment, and W_d is the weight of dried hydrogels after treatment.

3.2.6 Determination of soil water loss (SWL)

We measured soil water loss (SWL) in the soil over a period of 14 days. Soils were purchased from a shop market in Shobara City. Initially, the soils were dried by placing in an oven at 60 °C for 48 h. Then, 100g of dried soil is placed into plastic container and subsequently, the dried hydrogel beads (1 g) were added. The soil was then watered with 100 ml of DW and weighed

(W_i). The containers were kept in the laboratory under ambient air and temperature conditions and were weighed for up to 14 days (W_t). The SWL was calculated using Eq. (23) (Rabat et al., 2016):

$$\text{SWL (\%)} = \frac{W_i\text{-}W_t}{\text{Soil Weight (g)}} \times 100 \tag{23}$$

3.2.7 Determination of mineral release

The quantities of Mg, Ca, P, and NH_4-N released from the hydrogel beads were assessed via batch water shaker experiments (BW101, Yamato, Japan). Each set of beads (0.5 g) was placed in 50 mL of deionized water and agitated at 25 °C with a speed of 100 rpm. Nutrient analysis (Mg, Ca, P, and NH_4-N) was performed at intervals of 3 hours, 3 days, 7 days, and 14 days.

3.2.8 Proximate analysis

Proximate analysis was done following the method D1762- 84, laid down by American Society for Testing and Materials (ASTM) (Nguyen et al., 2022). The biochar samples were analyzed for their moisture content (Eq. 24), volatile matter (Eq. 25), ash content (Eq. 26), and fixed carbon content (Eq. 27). For the analysis on moisture content, 1 g of sample was dried in a laboratory oven for 3 days at 60 °C. The moisture content was calculated using the formula below:

$$\text{Moisture content, \%=} \frac{\text{Initial weight of biochar-Dry weight of biochar}}{\text{Initial weight of biochar}} \times 100 \tag{24}$$

The sample volatile matter was analyzed by heating at 900 °C for 7 min.

$$\text{Volatile matter, \%=} \frac{\text{Initial weight of biochar-Dry weight of biochar}}{\text{Initial weight of biochar}} \times 100 \tag{25}$$

The sample ash content was determined by heating the sample used to analyze the volatile matter at 815 °C for 3 hours.

$$\text{Ash content, \%=} \frac{\text{Initial weight of biochar-Dry weight of biochar}}{\text{Initial weight of biochar}} \times 100 \tag{26}$$

Lastly, the fixed C content was calculated using the mathematical equation below:

$$\text{Fixed C, \%= } 100 - (\text{Moisture content (\%) + Volatile matter (\%) + Ash content (\%)}) \tag{27}$$

3.2.9 Spectral determination

Dissolved organic carbon (DOC) was analyzed using COD to DOC ratio (2.67) with mathematical calculation in (Eq. 28). This process involved preparation of biochar-DI water at a ratio of 1:40 (w/v), followed by shaking for 24 hours. COD was determined using pack test from Kyoritsu Chemical-Check Lab.,Corp. Kanagawa, Japan.

$$\text{DOC content, \%}=\frac{\text{COD (mg/L)}}{\text{COD to DOC ratio}} \times 100 \tag{28}$$

3.2.10 UV-Vis absorption

Using the same DOC extraction method, dissolved organic matter (DOM) can also be analysed to assess its aromaticity, hydrophobic component content, and degree of humification with a UV-Vis Spectrophotometer (JASCO V-530). This involves measuring the absorption at 254 nm, 260 nm, and 280 nm, which are then related to the DOC concentration as the ratio of the absorption coefficients at these wavelengths. This method follows the equations (29-31) as outlined by Huang et al. (2019).

$$UV_{254}=\frac{\alpha_{254}}{\text{DOC (mg/L)}} \times 100 \tag{29}$$

$$UV_{260}=\frac{\alpha_{260}}{\text{DOC (mg/L)}} \times 100 \tag{30}$$

$$UV_{280}=\frac{\alpha_{280}}{\text{DOC (mg/L)}} \times 100 \tag{31}$$

3.2.11 Biochar carbon stability

In this study, the resistance of biochar to environmental oxidation was evaluated using a H_2O_2 oxidation technique (Cross & Sohi, 2013b). This approach is benchmarked against charcoal that has naturally aged, equating to durations of 92 and 187 years at average annual temperatures of 17°C and 7°C, respectively (Mašek et al., 2019). Therefore, the stable carbon levels measured here represent the carbon sequestered in the soil, potentially eligible for carbon credits. Before testing, all biochar samples were finely ground using a mortar and sieved to a size less than 250 microns. Each char sample, containing 0.1g of carbon, was combined with 0.01 mol of hydrogen peroxide in a 7 mL solution in a test tube. These tubes were then heated to 80°C and maintained at that temperature with intermittent stirring for 48 hours until the liquid evaporated. Afterward, the residue was dried at 60°C over three days before analyzing the carbon content. Carbon analysis was conducted using the Walkley and Black wet oxidation method (Hidayat et al., 2024), and the percentage of stable carbon was calculated according to Equation 32.

$$\text{Stable carbon rate, \%} = \frac{\text{residual biochar carbon content (\%)}}{\text{initial biochar carbon content (\%)}} \times 100 \qquad (32)$$

3.2.12 Determination of biochar properties

The soil's pH and electrical conductivity (EC) were assessed using pH (LAQUAtwin, Horiba Co., Ltd.) and a conductivity meter (LAQUAtwin, Horiba Co., Ltd.). This process involved preparation of soil-water mixture at a ratio of 1:5, followed by shaking for 30 minutes. The 1 M HCl solution was utilized to extract exchangeable cations of the soil (Mg, Ca, K, and Na). 1 g of biochar combined with 20 mL of 1 M HCl was shaken for 2 hours and stood one night. The cation exchange capacity (CEC) of the biochar was determined using the method described by (Hien et al., 2021). Briefly, 1 gram of biochar was mixed with 40 mL of 1 M CH_3COONH_4 and shaken for 15 hours, then filtered through a membrane filter. The biochar was subsequently washed with 50 mL of 1 M CH_3COONH_4. After this, 30 mL of ethanol was used to remove any residual ammonium from the biochar. Finally, the biochar was washed with 90 mL of 2 M KCl, and the resulting filtrate was analyzed for NH_4 content to calculate the CEC of the biochar.

3.2.13 Soil arsenic incubation experimental design

First, 0.132 g of As_2O_3 was dissolved in an alkaline solution of 10 mL of 1 M NaOH, then 6 mL of 2 M HCl was added. The solution was then diluted to 100 mL with deionized water, and incorporated with 100 g of soil. The soil was incubated for 3 days, then filtered and dried in an oven at 60 °C for 5 days for subsequent experiments. The soil arsenic-contaminated experiment lasted 50 days with a 2 wt% dosage at a constant temperature of 25 °C. All experiments were conducted in plastic cups. Soil subsamples were collected after 7, 21, and 50 days. After each collection, 20 g of soil samples were dried in an oven at 60 °C for 3 days for further analysis.

3.2.14 Soil salinity incubation experimental design

A mixture of 1 kg of air-dried soil samples and 2 L of a 250 mM NaCl solution was prepared in a plastic container. The soil and solution were then incubated together for three days. Afterward, the soil was filtered and dried in an oven at 60 °C for three days. A soil salinity experiment was conducted over 20 days using an experimental design that included three conditions: a control group with only soil, a group with soil treated with 2 wt. % Sa@S, and a group with soil treated with 2 wt. % Sa@SHa. The temperature of the experimental environment was maintained at a constant 25 °C. Hydrogel bead samples were placed in plastic cups and soaked with deionized water to reach 25% of the soil's water-holding capacity. Around 30 g of soil samples were collected from each cup at intervals of 5, 10, and 20 days and dried in an oven at 60 °C for three days for further analysis.

3.2.15 Soil glyphosate incubation experimental design

First, 0.5 g of glyphosate was dissolved in 500 mL of DI water, then incorporated with 500 g of soil. The soil was incubated for 4 days, then filtered and dried in an oven at 60 °C for 5 days for subsequent experiments. The soil glyphosate-contaminated experiment lasted 7 days with a 2 wt% dosage under room temperature. Afterward, the soil samples were dried in an oven at 60 °C for 3 days for further analysis. During the incubation, a CO_2 sensor was used to measure soil CO_2 emissions using the Go Direct CO_2 Gas Sensor from Vernier Science Education.

3.2.16 Determination of soil properties

To determine the pH and electrical conductivity (EC) of the soil, laboratory equipments including pH and EC meters, were utilized. Before analyzing the pH and EC, the soil and water were mixed at a ratio of 1:5 (w/v) and shaken for 30 min (Hidayat et al., 2020). The C/N ratio was determined using a Macro-Corder JM1000 CN autosampler (JMA 1000). The Olsen technique (Iatrou et al., 2014) was used to quantify the available phosphorus (P) using a 0.5 M $NaHCO_3$ solution. Soil samples (1 g) were mixed with 20 mL $NaHCO_3$ and shaken for 30 min. Exchangeable cations (Ca^{2+}, K^+ and Mg^{2+}) were assessed using the 1 N CH_3COONH_4 extraction method, after which 10 wt% NaCl was added to the soil to determine its cation exchange capacity (CEC) (Hidayat & Harada, 2022). The soil available NH_4-N and NO_3-N were extracted using 2 M KCl. One gram of soil sample was shaken for 2 h at room temperature (Xi et al., 2023). Soil organic carbon (SOC) was determined using the Walkley and Black wet oxidation method. Soil samples (0.5 g) were placed in a 100 mL beaker. Then, 5 mL of 1 N $K_2Cr_2O_7$ (98.1 potassium dichromate + 900 mL distilled water + 100 mL H_2SO_4) was added, shaken for a while and then 7.5 mL H_2SO_4 was added, and the mixture was allowed to stand for 30 min. Subsequently, the solution was subjected to distilled water up to a volume of 100 mL. Then, it was allowed to stand overnight and measured using a UV-Vis Spectrophotometer (JASCO V-530) at $\lambda = 561$ nm. Glucose was used as the standard organic carbon source. To estimate exchangeable Fe, the soil was treated with 20 mM $CaCl_2$ at a 1:5 ratio. After 30 min of shaking, the mixture was centrifuged at 5000 rpm for 10 min before being filtered. The Fe content was determined by pack testing at Kyoritsu Chemical-Check Lab., Corp. Kanagawa, Japan, using the reduction and o-phenanthroline methods. To evaluate the available arsenic (As) levels, the soil underwent treatment with a 500 mM potassium dihydrogen phosphate (KH_2PO_4) solution at a 1:3 w/v ratio for two hours. To evaluate the available glyphosate levels, 2 g of the soil underwent treatment with a 15 mL of 0.1 M potassium hydroxide solution for 24 hours. The quantification of glyphosate was followed (Lita et al., 2023). The quantification of As was then performed using pack testing methods at Kyoritsu Chemical-Check Lab., Corp. in Kanagawa, Japan. Bulk density and soil porosity were measured using equation (33) and (34), respectively.

$$\text{Bulk density (g/cm}^3\text{)} = \left(\frac{\text{Mass dry soil}}{\text{Volume of dry soil}}\right) \times 100 \tag{33}$$

$$\text{Soil porosity (\%)} = \left(1 - \frac{\text{Bulk Density}}{\text{Soil Particle Density}}\right) \times 100 \tag{34}$$

3.2.17 Analysis of sodium adsorption ratio and exchangeable sodium percentage

The interaction between the sodium adsorption ratio (SAR) and exchangeable sodium percentage (ESP) and the concentration of Mg, Ca, and K in the water extract derived from saturated soil can be represented mathematically using equations (35) and (36) (Tefera et al., 2022).

$$\text{SAR} = \frac{\text{Na}}{\sqrt{\frac{1}{2}(\text{Mg} + \text{Ca})}} \tag{35}$$

$$\text{ESP} = \frac{\text{Na}}{\text{Na} + \text{K} + \text{Ca} + \text{Mg}} \times 100 \tag{36}$$

3.2.18 Characterization of hydrogel beads and biochar

The functional groups of samples were analyzed using a Thermo Scientific Nicolet iS10 FTIR instrument (Thermo Fisher Scientific Inc., Waltham, MA, USA). 2DCOS on the FTIR were performed using soil samples during the incubation period. Previous literature has also described the relevant principles in detail (Noda & Ozaki, 2005). Origin 2024 software was used to perform the COS computation and graphing functions. 2DCOS can improve the spectral resolution of the functional group to identify binding characteristics after treating the hydrogel beads under As-contaminated. In the 2DCOS map, the peak located on the main diagonal line of the synchronous correlation map is termed an auto peak. Peaks outside this diagonal line are referred to as cross peaks, which reveal the correlation between spectral peaks at two different wavenumbers. Positive cross peaks indicate that the corresponding spectral peaks change in the same direction, whereas negative cross peaks suggest that the peaks change in opposite directions. The asynchronous correlation map highlights the asynchronous nature of spectral intensity changes at two wavenumber positions. This map is asymmetrical about the main diagonal line and features only cross peaks, with no auto peaks present (Y. Huang et al., 2020). The structural images of the hydrogel beads were analyzed using a benchtop SEM Miniscope TM-4000PlusII (Hitachi-hitech, Tokyo, Japan). Thermogravimetric analysis (TGA) was carried out using a Rigaku Thermo Plus TG8120, Tokyo, Japan. The analysis was conducted in an inert N_2 atmosphere from 50 to 800 °C at a heating rate of 60 °C min^{-1}.

3.2.19 Statistical analysis

Data analyses were performed with MINITAB software (version 21.3.1). Mean values were subjected to one-way analysis of variance (ANOVA), and treatment comparisons were conducted using Tukey's test (P-value <0.05).

3.3 Results and discussion

3.3.1 Effects of sodium alginate-poly (acrylic acid) cross-linked hydrogel beads on soil conditioner in the absence and presence of phosphate and carbonate ions

3.3.1.1 Characteristics of hydrogel beads

Figure. 37 displays the photograph of the dried hydrogel beads and impact on the absence and presence of PO_4^{3-} and CO_3^{2-} ions on the surface morphology. Based on top surface view, the dried hydrogel beads exhibited a rough surface with angular components for all hydrogel bead samples. The surface of hydrogel beads S-Alg/P-Acc@PO_4^{3-} (Figure. 37c2) and S-Alg/P-

Acc@CO_3^{2-} (Figure. 37d2) have finer and smaller pore compared to S-Alg/P-Acc (Fig 37b2). In cross-section view of Figure. 37b3-37b4, the images show that S-Alg/P-acc has smooth and compact structure with less pore visibility. In contrast, hydrogel beads with the presence of PO_4^{3-} (Figure. 37c3-37c4) and CO_3^{2-} (Figure. 37d3-37d4) have rather coarse surface and visible image of pore with porosity opening up to 12 µm in size, with filamentous formations inside the hollow spaces of the hydrogel beads. Clearly, the presence of anionic ions influences the structure of hydrogel beads.

Table 13. Porosity and COOH value of hydrogel beads

Samples	Porosity (%)	COOH (mmol/g)
S-Alg/P-Acc	9.54	25.87 ± 10.18
S-Alg/P-Acc@PO_4^{3-}	10.90	25.02 ± 14.83
S-Alg/P-Acc@CO_3^{2-}	14.31	3.23 ± 0.98

Table 13 displays the percentage of porosity and the number of carboxyl groups in the hydrogel beads. Results show that the S-Alg/P-Acc@CO_3^{2-} and S-Alg/P-Acc@PO_4^{3-} composites had maximum porosities of 14.3% and 10.9%, respectively, while the S-Alg/P-Acc composite had a porosity of 9.5 %.

The presence of anionic ions increased the porosity by 14.7 to 50.5%, probably owing to the reinforcement of polymer networks resulting from the crosslinks between carboxylic acids bridged with calcium cations. The stiff polymer network retained the volume shrinkage of the beads during the drying process, maintaining a higher porosity. Meanwhile, the presence of anions may have led to a reduction in the carboxyl content of the S-Alg/P-Acc@CO_3^{2-} and S-Alg/P-Acc@PO_4^{3-} hydrogel beads because calcium ion capped some of the carboxyl groups, rendering them inactive for neutralization reactions. To confirm this hypothesis, the number of active carboxyl groups was quantitatively evaluated by titration method. The carboxyl groups possess a proton (H^+) that can be released by deprotonating the carboxyl group to form anions.

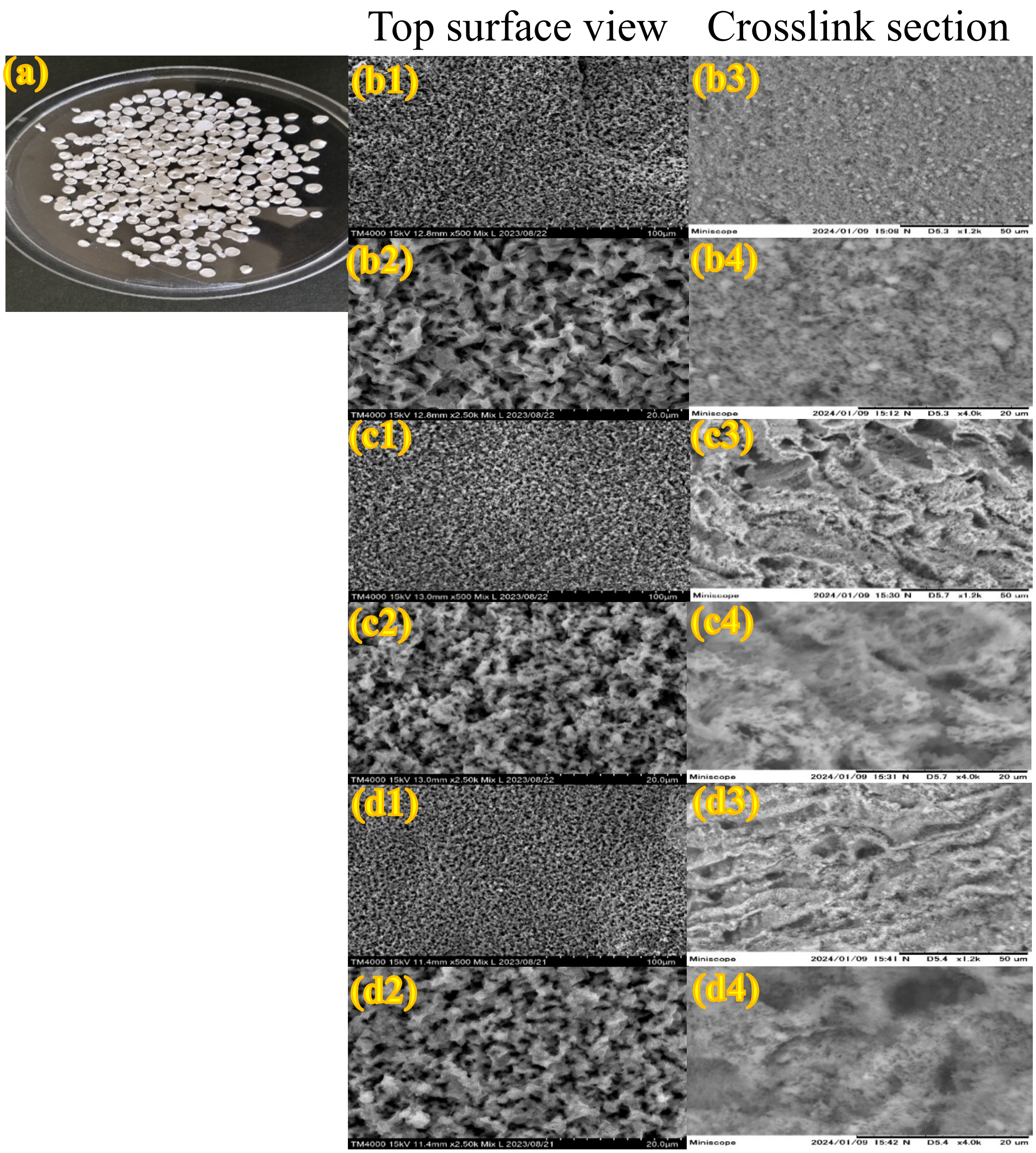

Figure. 37. (a) photograph of dried hydrogel beads. SEM images of morphology dried hydrogel beads (b1-b4) S-Alg/P-Acc (c1-c4) S-Alg/P-Acc@PO_4^{3-} (d1-d4) S-Alg/P-Acc@CO_3^{2-}.

This neutralization process decreases the concentration of carboxyl groups in the solution. Anions can be constituents of robust bases or other compounds that receive protons. For instance, the interaction between a carboxylic acid (RCOOH) and hydroxide ion (OH^-).

$$RCOOH + OH^- \rightarrow RCOO^- + H_2O \tag{37}$$

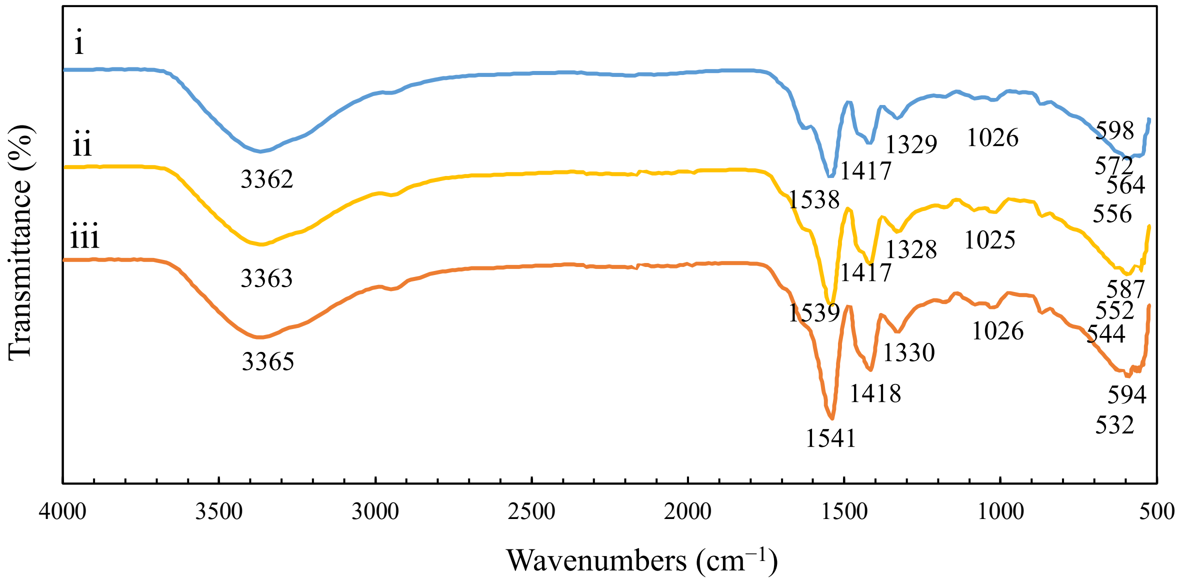

Figure. 38. FTIR spectra of hydrogel beads (i) S-Alg/P-Acc (ii) S-Alg/P-Acc@PO_4^{3-} (iii) S-Alg/P-Acc@CO_3^{2-}.

During this chemical reaction, carboxylic acid (COOH) transfers its proton to the hydroxide ion (OH^-), resulting in the formation of a carboxylate anion ($RCOO^-$) and water (H_2O). This decreases the concentration of the COOH groups in the solution. As indicated in Table 13, the increased porosity of S-Alg/P-Acc@CO_3^{2-} led to a reduction in free carboxylic groups, supporting the molecular model suggesting that the polymer network is reinforced by the bridging of calcium ion between carboxyl groups.

Figure. 38 shows the FTIR spectra of the hydrogel beads. The peaks at 3362 cm^{-1}, 3364 cm^{-1} and 3365 cm^{-1} are ascribed to O-H stretching (Das et al., 2023). The absorption peaks at 1541

cm^{-1} from S-Alg/P-Acc decreased to 1539 cm^{-1} and 1538 cm^{-1} for S-Alg/P-Acc@PO_4^{3-} and S-Alg/P-Acc@CO_3^{2-}, respectively, possibly due to interaction of anionic ions with the -COO- groups in S-Alg and P-Acc. The bands detected around 1418 cm^{-1}, 1329 cm^{-1}, and 1026 cm^{-1} are due to symmetric-COO-, O-H bending vibrations, and C-O-C, respectively (Hua et al., 2010).

3.3.1.2 Swelling behaviour

Hydrogel beads utilized for soil conditioner purposes must undergo water absorption during swelling (Di Martino et al., 2021). In this step, water is absorbed without hindrance, resulting in the dissociation of the ionic groups, charged groups repulsion, and swelling of the polymer chains to create volumes filled with water molecules (Kees de Kruif et al., 2015). The primary aim was to analyse the swelling characteristics of the hydrogel beads at pH 4, 7, and 9 (Figure. 39).

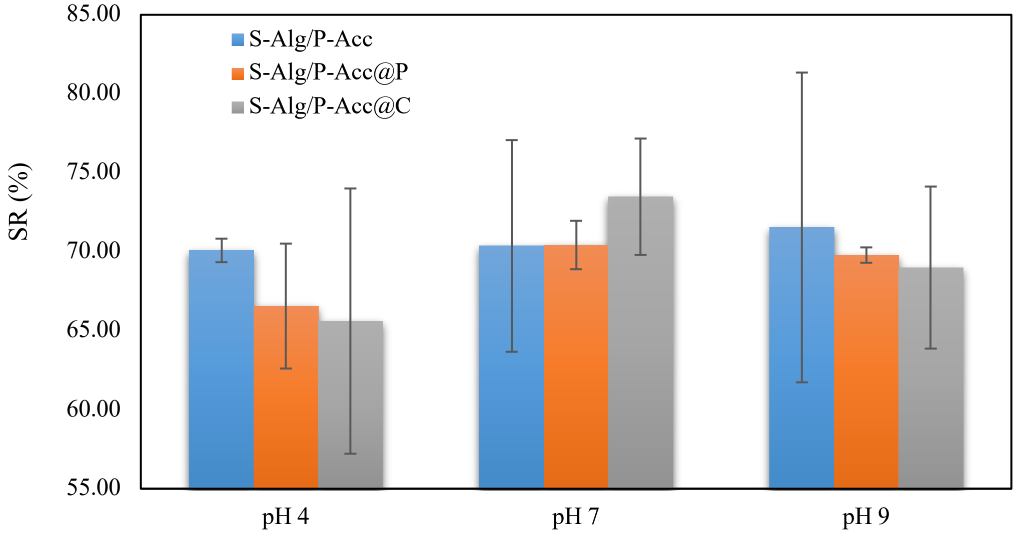

Figure. 39. Initial pH versus swelling properties of hydrogel beads.

The swelling percentage of S-Alg/P-Acc was higher under acidic conditions (pH 4) than that of S-Alg/P-Acc@PO_4^{3-} and S-Alg/P-Acc@CO_3^{2-}, but lower under neutral and basic conditions. The lowest swelling percentage observed was a consequence of the protonation of the COOH groups, lead to the formation of COOH and a reduction in the repulsion between PO_4^{3-} and CO_3^{2-}

anions. Simultaneously, this process strengthens the –OH-bonding contact between carboxylate groups, causing the shrinkage of the hydrogel (Lohmousavi et al., 2020; Tulain et al., 2018). The maximum swelling for S-Alg/P-Acc@CO_3^{2-} and S-Alg/P-Acc@PO_4^{3-} occurred at pH 7, likely due to steric hindrance or repulsion generated by the anions (CO_3^{2-} and PO_4^{3-}) near the hydrophobic part of the polymer chains. The hydrophobic portions of the hydrogel beads were transformed into hydrophilic elements through ionic effects, selectively interacting with nearby water molecules (Bibi et al., 2019). At a higher pH beyond 7 led to a reduction in the swelling percentage of S-Alg/P-Acc@PO_4^{3-} and S-Alg/P-Acc@CO_3^{2-}. This reaction may be due to the formation of a screening effect by the additional Na^+ cations, which shielded the charges on the COOH groups. Thus, the electrostatic repulsion between effective anions are weakened, leading to a decrease in water absorption (Lee & Lin, 2000).

3.3.1.3 Soil water loss studies

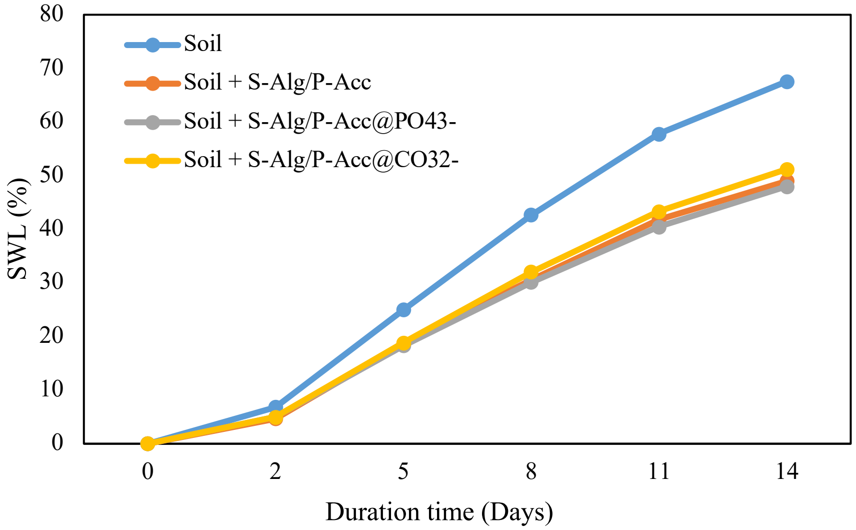

Figure. 40. Contact time effect of hydrogel beads versus soil water loss.

Figure. 40 shows the soil water loss (SWL) percentage over the 14-day period, including soils with hydrogel beads. The results indicated that S-Alg/P-Acc@PO_4^{3-} hydrogel beads exhibited great water retention capability and the lowest soil water loss, with a SWL value of 48%. The

SWLs of the S-Alg/P-Acc@CO_3^{2-} and S-Alg/P-Acc demonstrated values of 51% and 49%, respectively. In contrast, the SWL of soil was approximately 68%.

Initially, the incorporation of phosphate and carbonate ions into the hydrogel beads were expected to affect water retention via changing the distribution of pore sizes and improved the surface area and pore volume (Y. Chen et al., 2021; Han et al., 2023; H. Liu et al., 2012). This can be proven by the percentage of porosity of the hydrogel beads as shown in Table 13. These ions normally can form multidirectional crosslinking with polyacrylic acid and lead to a better network flexibility and water storage capacity (Jiao et al., 2023). However, based on the graph shown in Figure. 26, the effect of phosphate and carbonate ions does not seem to be significant. Furthermore, hydrogel beads with the highest porosity percentage (Table 13) showed lower efficiency in water absorption under the investigated soil conditions. These phenomena could be caused by the density of the hydrogel beads and environmental factors, such as humidity and air temperature, which may have influenced the beads` water-holding capacity (Rabat et al., 2016). Importantly, all the soils containing the hydrogel beads had significantly reduced water loss in soil by approximately a 30% smaller SWL compared to that of the intact soil.

3.3.1.4 Response of soil properties to hydrogel beads application

Figure. 41 and Figure. 42 demonstrated the effects of the hydrogel beads on the soil characteristics. The addition of hydrogel beads did not significantly impact the soil pH (Figure. 41a) and C/N ratio (Figure. 41b) (P-value <0.05). In contrast, there was a significant increase (P-value <0.05) in soil EC with the addition of hydrogel beads (Figure. 41c). The maximum EC of the soil was observed in the following order: S-Alg/P-Acc@CO_3^{2-}>S-Alg/P-Acc>S-Alg/P-Acc@PO_4^{3-}. The increase in soil EC is attributed to the release of salt ions as hydrogel beads react with soil water.

Phosphorus (P) is a crucial element of soil and plant growth and cannot be replaced by any other elements (Neset & Cordell, 2012). A significant increase (P-value <0.05) in available P (0.50 ± 0.03 mg/g) was confirmed by the use of hydrogel beads for S-Alg/P-Acc@PO_4^{3-}, whereas there was a reduction in the application of S-Alg/P-Acc and S-Alg/P-Acc@CO_3^{2-} compared to the intact soil (Figure. 41d). P is known to have low mobility because it tends to precipitate, adsorb, and convert into organic forms (Dixon et al., 2020). It is critical to consider the possible effects of nutrient leaching using hydrogel beads. In this study, the available P content was expected to decrease because of the adsorption of the hydrogel beads (S-Alg/P-Acc and S-Alg/P-Acc@CO_3^{2-}) since the soil pH is approximately 5.5, causing P to be present in the form of $H_2PO_4^-$. Electrostatic interactions may possibly form between the negatively charged $H_2PO_4^-$ and the hydrogel beads. Figure. 41e shows that the use of hydrogel beads significantly increased soil CEC compared with the intact soil, as the hydrogel beads may contain -OH and -COOH functional groups, which have the potential to enhance soil CEC (van Zwieten et al., 2010). The application of hydrogel beads substantially enhanced SOC compared to the intact soil (P-value <0.05) (Figure. 41f). The SOC of the soil was the highest in the following order: S-Alg/P-Acc > S-Alg/P-Acc@PO_4^{3-} > S-Alg/P-Acc@CO_3^{2-}. This may imply that the hydrogel beads retained water and able to help to maintain soil moisture at an appropriate level which might indirectly boost microbial activity by altering oxygen penetration into the soil, contributing to organic matter degradation and organic carbon production. Soil Fe availability decreased considerably (P-value <0.05) in the following order: control > S-Alg/P-Acc@PO_4^{3-} > S-Alg/P-Acc@ CO_3^{2-} > S-Alg/P-Acc, with a reduction of up to 89.86% (Figure. 41g). These findings suggest that hydrogel beads have a beneficial effect on Fe immobilization in soil.

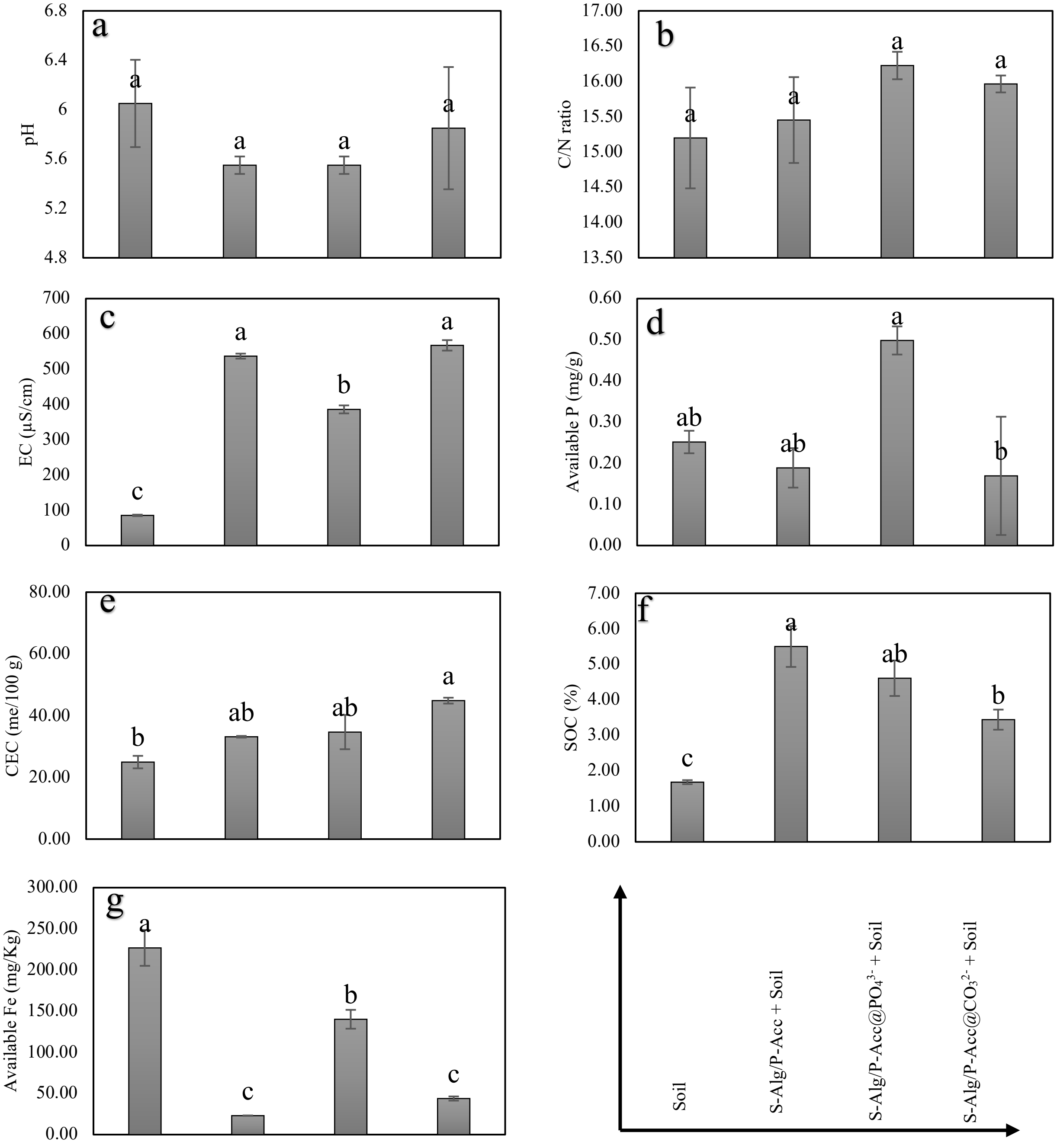

Figure. 41. Effect of hydrogel beads on soil pH, C/N ratio, electrical conductivity, available phosphorus, cation exchange capacity, soil organic carbon, and available Fe.

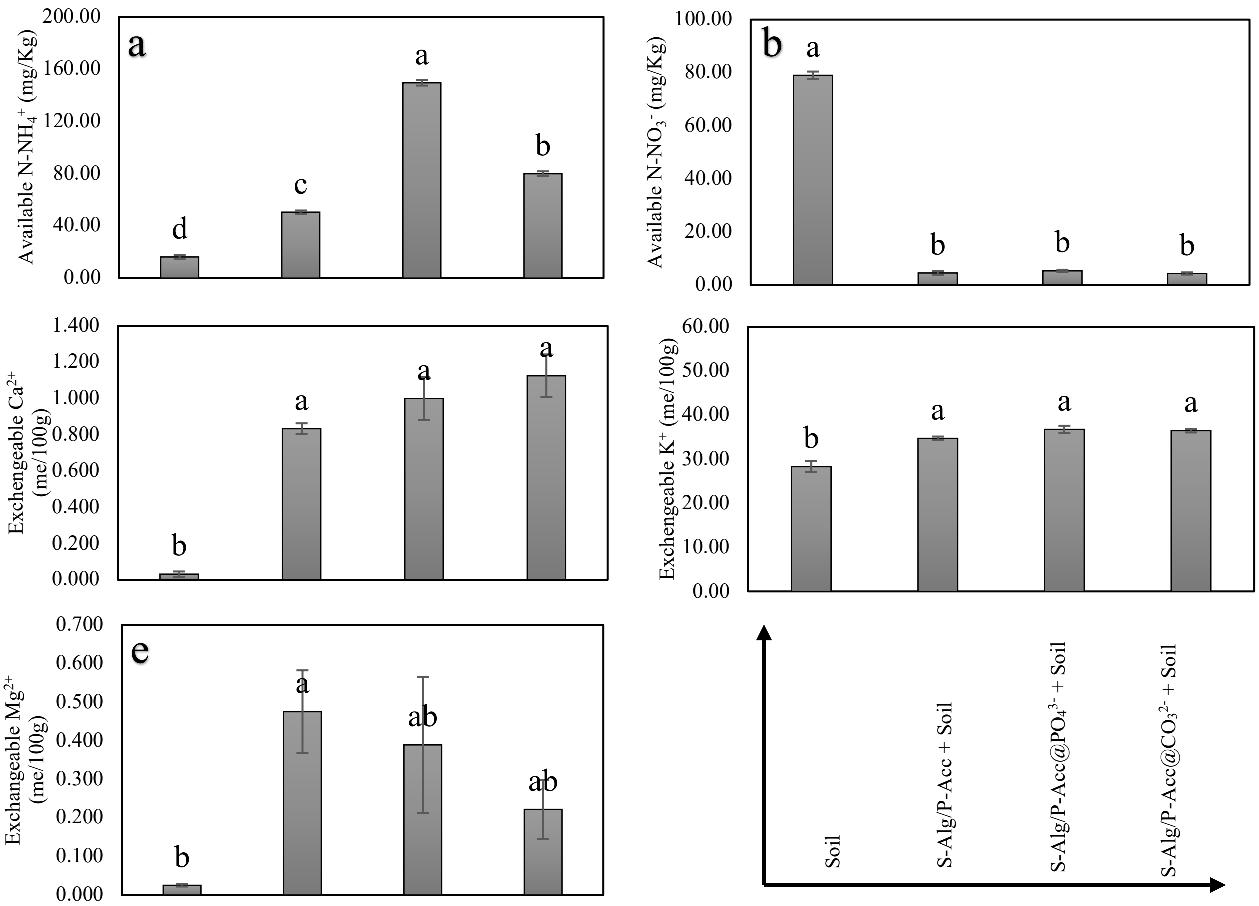

Figure. 42. Effect of hydrogel beads on soil available N-NH$_4^+$ and N-NO$_3^-$, and exchangeable Mg^{2+}, Ca^{2+} and K$^+$.

Furthermore, the addition of hydrogel beads considerably enhanced the available N-NH$_4^+$ level in the soil (P-value < 0.05) (Figure. 42a). S-Alg/P-Acc@PO$_4^{3-}$ had the highest concentration after treatment, up to 89.16% of the intact soil. This was followed by S-Alg/P-Acc@CO$_3^{2-}$ (79.72%) and S-Alg/P-Acc (67.92%). Moreover, the hydrogel bead applications significantly decreased the content of N-NO$_3^-$ in soils, and it decreased from 79.00 ± 1.41 mg/Kg (soil) to 4.30 ± 0.42 mg/Kg (S-Alg/P-Acc@CO$_3^{2-}$) (P-value < 0.05) (Figure. 42b). It might be indicated that hydrogel beads application inhibit the transformation of N-NH$_4^+$ from oxidized into N-NO$_3^-$ in soils. These results demonstrated similar trends with Zhang et al. (L. Zhang & Guan, 2022) who used hydrogel-biochar composites for simultaneous enhancement and immobilization of nitrogen use and heavy metals, respectively. The hydrogel bead treatment resulted in considerably higher exchangeable Ca^{2+}, K^{+}, and Mg^{2+} levels compared to the intact soil (P-value < 0.05) (Figure. 42c-e). Hydrogel beads may have the potential to absorb and retain water and assist in the transportation of ions in the soil, resulting in enhanced cations contents.

It is interesting to note that exchangeable Mg^{2+} has a greater value for S-Alg/P-Acc compared to S-Alg/P-Acc@PO_4^{3-}, and S-Alg/P-Acc@CO_3^{2-}. This might indicated that the presence of PO_4^{3-} and CO_3^{2-} anionic ions from hydrogel beads may compete with Mg^{2+} ion for binding sites on soil particles through cation exchange process.

3.3.2 Harnessing hydrogel beads for immobilization of arsenic

3.3.2.1 Characteristics of hydrogel beads

Table 14. Porosity and carboxyl group of hydrogel beads.

Samples	Porosity (%)	COOH (mmol/g)
SPPG	48.23 ± 13.17	25.87 ± 10.18
SPP	68.01 ± 35.92	3.23 ± 0.98

Figure. 43 shows the morphology of the dried hydrogel beads with and without glutaraldehyde, which were observed with SEM before and after As immobilized. The images visualized that synthesized SPP and SPPG had macro and microporous before treatment. SPP demonstrated a relatively uniform shape with fewer open pores compared to SPPG. These pores can benefit from the channelling and diffusion of components into their structure. Conversely, after treatment in soil, the hydrogel beads (SPPG and SPP) showed a slight change in their porous structure. This could be due to interaction with the soil components, deposition of As compounds on the hydrogel's structure, and decomposition of the hydrogel beads in the soil.

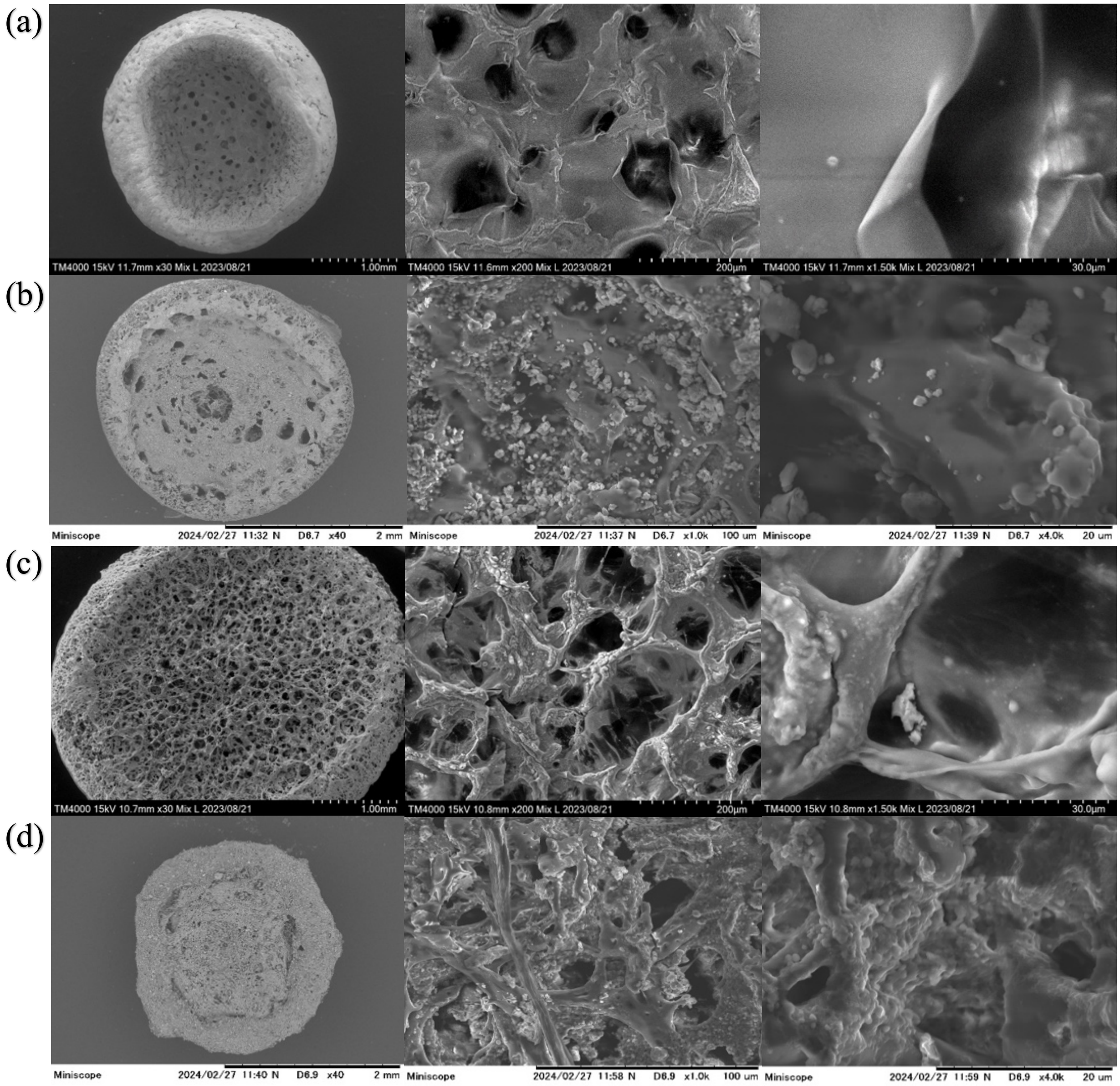

Figure. 43. SEM photograph of hydrogel beads (a) SPPG before As immobilization (b) SPPG after As immobilization (c) SPP before As immobilization (d) SPP after As immobilization.

Table 14 presents the percentage porosity and the amount of carboxyl groups within the hydrogel beads. The data indicate that SPP exhibited the highest porosity of 68.01%, whereas the SPPG demonstrated a lower porosity of 48.23 %. The introduction of glutaraldehyde led to a 29.08 % difference in porosity. This reduction is attributed to the reaction of reactive aldehyde groups in glutaraldehyde, which can form covalent bonds with functional groups like hydroxyl, amine, or carboxyl groups found in the hydrogel beads. Establishing these covalent bonds tightens the polymer chain network, culminating in a less porous structure as cross-linking increases. Conversely, the number of COOH groups in the SPPG hydrogel bead was higher than in the SPP sample. It might be due to glutaraldehyde reaction with other functional groups in the hydrogel beads, potentially forming cross-links that stabilize the structure of the hydrogel. This stabilization may prevent the loss or transformation of COOH groups during the preparation and washing of the beads, leading to an increases number of COOH groups.

This reduction is attributed to the two reactive aldehyde groups in glutaraldehyde, which can form covalent bonds with functional groups like hydroxyl, amine, or carboxyl groups found in the hydrogel beads. The establishment of these covalent bonds tightens the polymer chain network, culminating in a less porous structure as cross-linking increases. Conversely, the number of COOH groups in the SPPG hydrogel bead was higher in comparison to the SPP sample. It might be due to glutaraldehyde can react with other functional groups in the hydrogel beads, potentially forming cross-links that stabilize the structure of the hydrogel (In this case degradation rate (Figure. 44e). This stabilization may prevent the loss or transformation of COOH groups during the preparation and washing of the beads, leading to a increases number of COOH groups.

The functional groups of the hydrogel beads before and after soil incubation are depicted in Figure. 44a-b. The spectral at around 3524 cm^{-1} is attributed to the stretching vibrations of O-H bonds (Fajardo et al., 2012). A noticeable reduction in peak intensity from 1599 cm^{-1} to 1597 cm^{-1} for SPP and SPPG, respectively, is likely due to the interaction of the hydrogel bead composite with glutaraldehyde, which is associated with the carboxylate (-COO-) groups (Hua et al., 2010). The appearance of new peaks in the presence of glutaraldehyde (SPPG) at 1417 cm^{-1} and 1083 cm^{-}

^{1} can be attributed to the symmetric stretching of carboxylate (-COO-) and (C-O-C), respectively (Hua et al., 2010). The peak located at 845 cm^{-1} indicates the symmetric stretching of the PO_4 group, and the peak around 691 cm^{-1} is related to the stretching of the P-O-P bonds (Bogdan et al., 2021). Additionally, the peak at 598 cm^{-1} suggests the presence of the stretching vibration of the Fe-O (Chelike et al., 2020). Furthermore, after As immobilization, there are new peaks appeared at around 1922 and 1980 cm^{-1}, corresponding to the CN and CH_2 stretching (Mecozzi et al., 2012), and C=O stretching, respectively (Krivoshein et al., 2020). Peak at 1413 cm^{-1}, is attributed to -COO- (Hua et al., 2010). While peak at 1323 cm^{-1}, is related to OH stretching in-plane and C-H stretching in symmetric (Azniza et al., 2015). TGA curves of hydrogel beads is shown in Figure. 44c. It was observed that the initial temperature of polymeric decomposition started at 203 ºC and 222 ºC for SPPG and SPP, respectively. The final decomposition temperatures were observed at 434 ºC and 412 ºC for SPPG and SPP, respectively. Interestingly, SPP hydrogel bead continue to decompose at 758 ºC as can be seen by the sharp drop in weight loss (%), while SPPG maintains its gradual decomposition rate until 800 ºC. Finally, the residue left for SPPG and SPP were 34.36% and 45.11%, respectively. From the results, it could be concluded that the presence of glutaraldehyde reduced the thermal stability of hydrogel bead compared to without glutaraldehyde.

3.3.2.2 Swelling and degradation behaviour

Figure. 44d illustrates the swelling behavior of hydrogel beads when exposed to DI water, NaOH, and HCl solutions. The findings reveal that the swelling ratio of SPP exceeded that of SPPG across all tested conditions. This discrepancy is likely attributable to the reaction of glutaraldehyde with the hydrogel beads' functional groups, which promotes cross-linking.

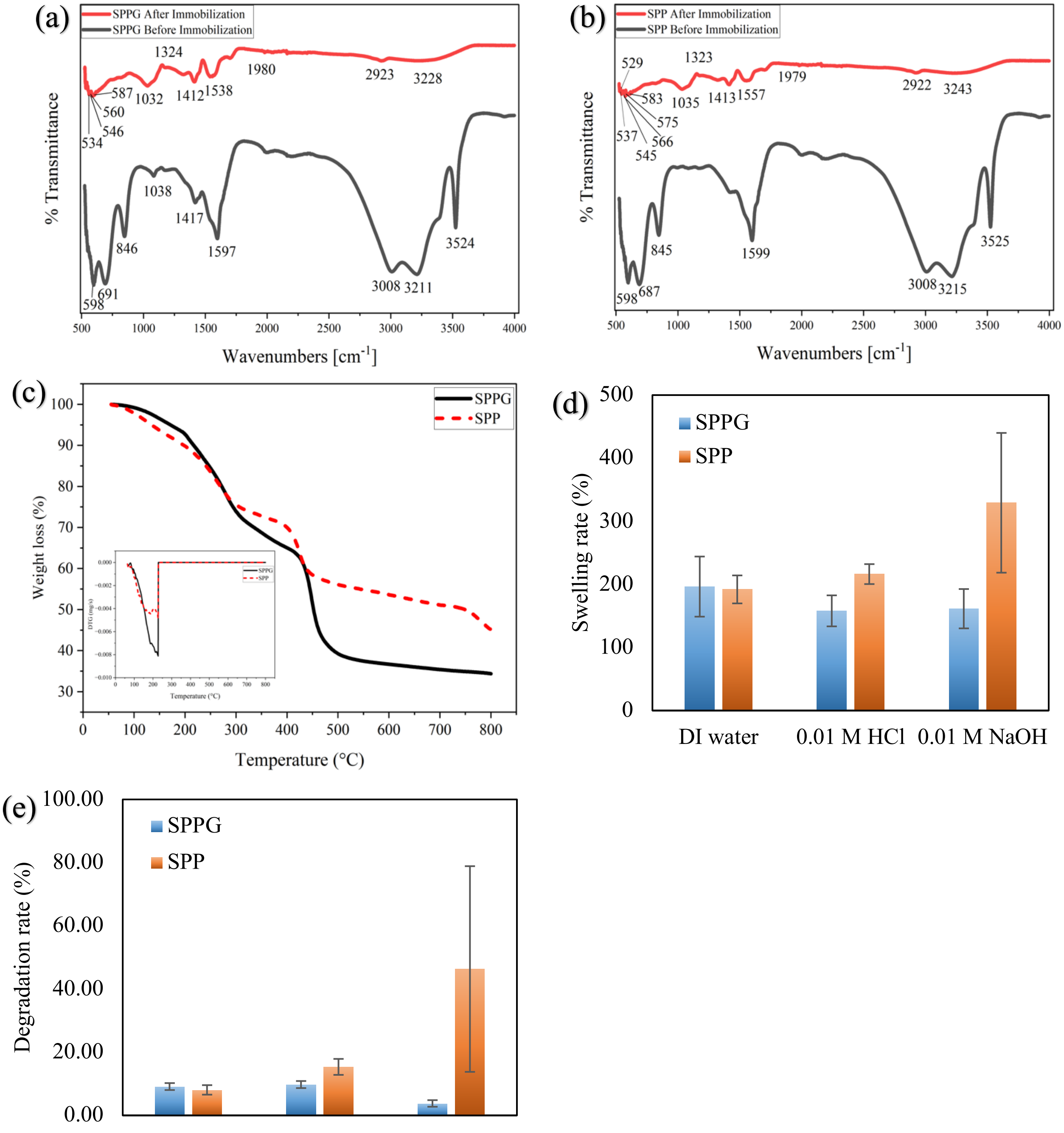

Figure. 44. FTIR spectra of the hydrogel beads before and after As immobilization (a) hydrogel bead composite (SPPG) (b) hydrogel bead composite (SPP) (c) TGA curves of hydrogel beads (d) Swelling percentage rate of the hydrogel beads (e) Degradation percentage rate of the hydrogel beads using liquid solution at 100 ºC for 24 h.

As a result, the beads become less prone to distortion, leading to a reduced swelling rate and an enhanced degradation rate (as depicted in Figure. 44e). Additionally, the SPP hydrogel bead exhibited a notably higher swelling value in alkaline (NaOH) condition (329%). This suggests that the hydrogel beads possess ionizable functionalities, such as carboxylic acid (-COOH) or its deprotonated form, carboxylate ($-COO^{-}$). In neutral (DI water) or acidic (HCl) media, these groups tend to remain protonated (COOH), fostering strong electrostatic forces within the hydrogel matrix. Such forces could hinder the hydrogel's capacity to absorb water, constraining its swelling capability (Al-qudah et al., 2014).

3.3.2.3 SEM images and properties of soil

The micrograph of SEM obtained from soil samples after application of SPPG and SPP were illustrated in Figure. 45. Based on the magnification of X400 and X3.0K, the structure of soil samples after SPPG and SPP treatments contain particles with the presence of pores, which were less dense and less compacted compared to the soil samples without any treatment. Furthermore, in contrast to the only soil sample, it can be noted that the soil aggregates after SPPG and SPP treatments exhibit larger spaces of pores, leading to lower bulk density of soil and making it ideal for agricultural activity. Therefore, it can be concluded that applying hydrogel beads can improve soil morphology and structure after 50 days of incubation.

Table 15 presents the soil's bulk density and porosity following a 50-day incubation period. The results indicate that incorporating hydrogel beads into the soil can decrease its bulk density. This reduction may occur because the hydrogel beads expand in volume when absorbing water and swelling. Such expansion displaces soil particles, which increases the soil's total volume without a corresponding increase in mass, thus lowering the bulk density. Additionally, the porosity of the soil increased after the hydrogel beads were increased. The presence of hydrogel beads promotes the formation of soil aggregates and clumps of soil particles that generate larger pore spaces between them, thereby enhancing the soil's overall porosity. This result is similar to (Guo et al., 2020) who used poly-γ-glutamic acid.

Table 15. Soil properties after 50 days of incubation.

Samples	Bulk density (g/cm^3)	Porosity (%)
Soil	0.86 ± 0.018	67.61 ± 0.69
Soil + SPPG	0.83 ± 0.070	68.78 ± 2.66
Soil + SPP	0.80 ± 0.067	69.71 ± 2.53

3.3.2.4 FTIR spectra and analysis of 2D correlation of soil

The FTIR spectra of the soil are shown in Figure. 46a. In the 7 days of incubation, an increase in peak intensity after treated hydrogel beads from 3286 cm^{-1} to 3293 cm^{-1} and 3289 cm^{-1} are attributed to the stretching vibrations of O-H and N-H bonds (Fajardo et al., 2012). This is a similar trend for up to 50 days of incubation. In addition, another peak around 1587 cm^{-1} also decreased after treatment of hydrogel beads for up to 50 days incubation, which corresponds to -COO- groups (Hua et al., 2010). Moreover, there are no peak changes around 1393 cm^{-1} for all soil samples, corresponding to the NO_3 band (Bantignies et al., 1998), which is a similar trend for N-NO_3 value that there is no significant effect (Figure. 49i). Peak from 1090 to 824 cm^{-1} typical metal hydroxyl (M-OH) stretching vibration, representing As-O-M stretching vibration (B. Chen et al., 2013; Min et al., 2017; Wu et al., 2014). Additionally, the peak at 594 cm^{-1} decreased to 591 cm^{-1} after the treated hydrogel bead, suggesting the presence of the Fe-O vibration peaks (Chelike et al., 2020) and indicating that these peaks were involved in stabilizing As.

Furthermore, 2DCOS FTIR data to clarify the dominant functional groups of hydrogel beads participating in the binding of As. The synchronous map (Figure. 46b) shows positive cross-peaks in the regions 937 cm^{-1}, 3280 $cm^{-1,}$ and 1587 cm^{-1} for up to the final incubations. It could be assigned to the O-H, N-H, and -COO- groups, respectively. In contrast, the asynchronous map (Figure. 46c) exhibits positive bands for all soil samples at 3280 cm^{-1} and 1587 cm^{-1}, 1393 cm^{-1}, while negative bands at 937 cm^{-1}. It could be confirmed that M-OH stretching plays an important role in As immobilization. The proposed As immobilization as shown in Figure. 47.

3.3.2.5 Impacts of amendments on As immobilization

Figure. 48 depicts the impact of treatment amendments on soil arsenic (As) levels, pH, and electrical conductivity (EC). As shown in Figure. 48a, the concentration of available As in soil decreased markedly following the application of treated hydrogel beads ($P<0.05$). After a 50-day incubation period, the As concentrations were reduced to 54.74 mg/L for the untreated soil and 6.93 and 6.68 mg/L for the SPPG and SPP-treated soils, respectively. This corresponds to immobilization rates of 87.34% for SPPG and 87.81% for SPP. Conversely, as indicated in Figure. 48b, the soil pH experienced a notable reduction post-treatment with hydrogel beads ($P<0.05$). After 7 days, the pH dropped from 5.80 in the untreated control soil to 5.05 and 4.65 for SPPG and SPP treated soils, respectively. The pH decreased over the incubation period, reaching values of 5.05 for untreated soil and 4.55 and 4.22 for SPPG and SPP-treated soils, respectively. This reduction in pH may be due to the protonation of COOH groups to form $COOH_2^+$, enhancing the electrostatic interactions between the positively charged hydrogel beads and the negatively charged As under acidic condition ($H_2ASO_4^-$) (Kumar & Jiang, 2017). Additionally, soil EC showed a significant increase after applying hydrogel beads ($P<0.05$), as demonstrated in Figure. 48c. The EC rose by 69.43% and 23.38% for SPP and SPPG treatments, respectively.

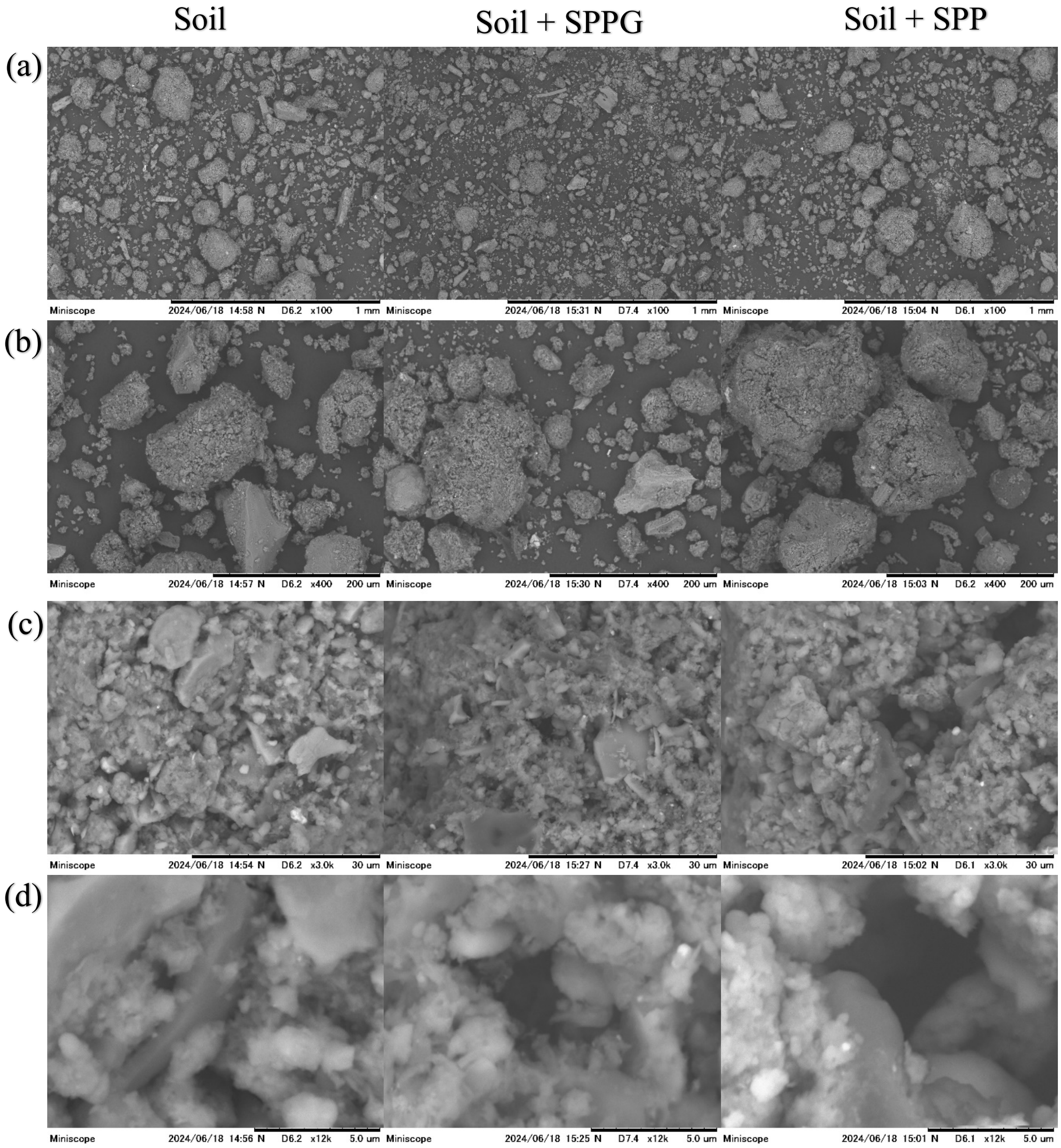

Figure. 45. SEM photograph of soil after 50 days of incubation (a) x100 magnification (b) x400 magnification (c) x3000 magnification (d) x12000 magnification.

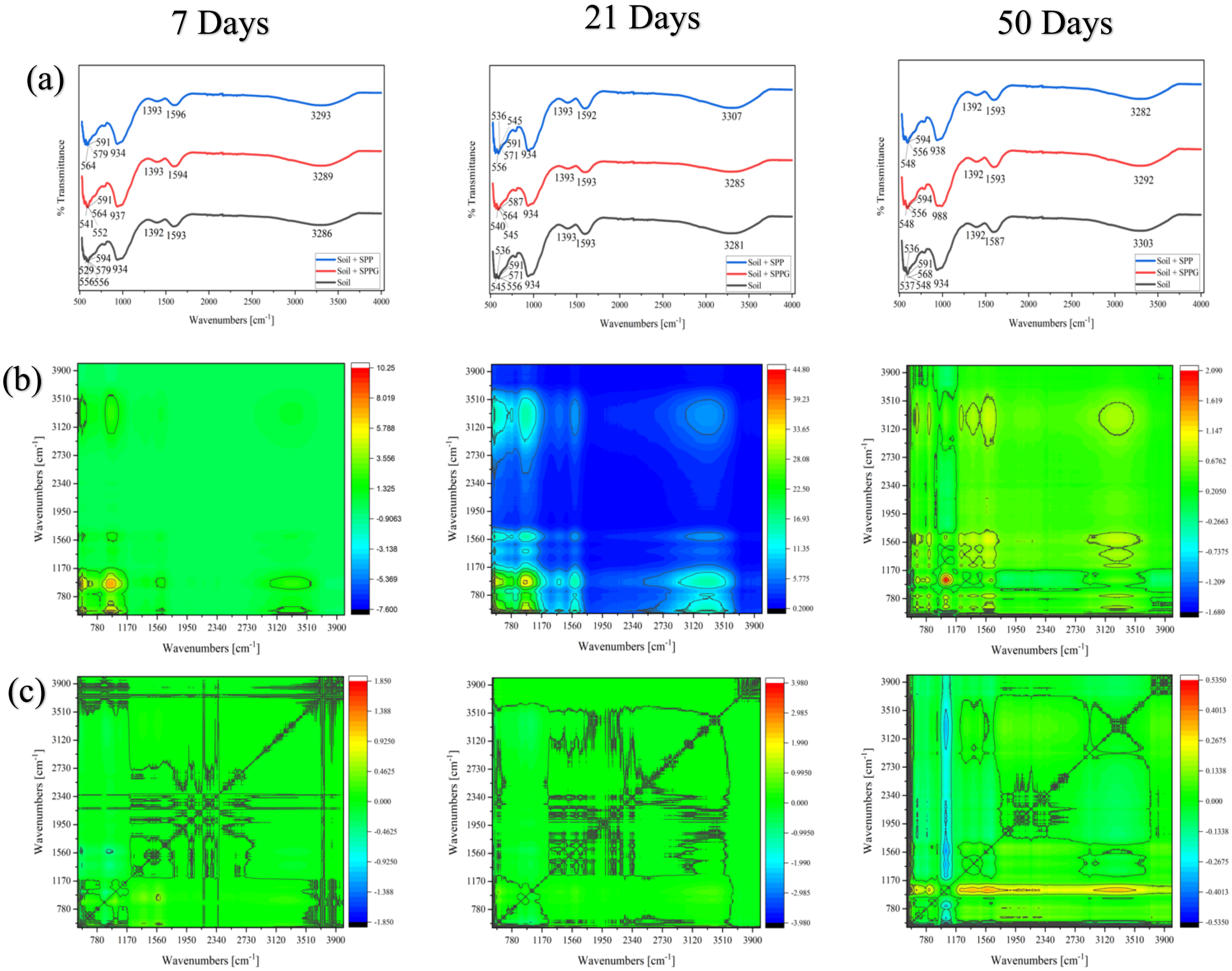

Figure. 46. (a) FTIR spectra of soil (b) 2DCOS FTIR synchronous of soil (c) 2DCOS FTIR asynchronous of soil.

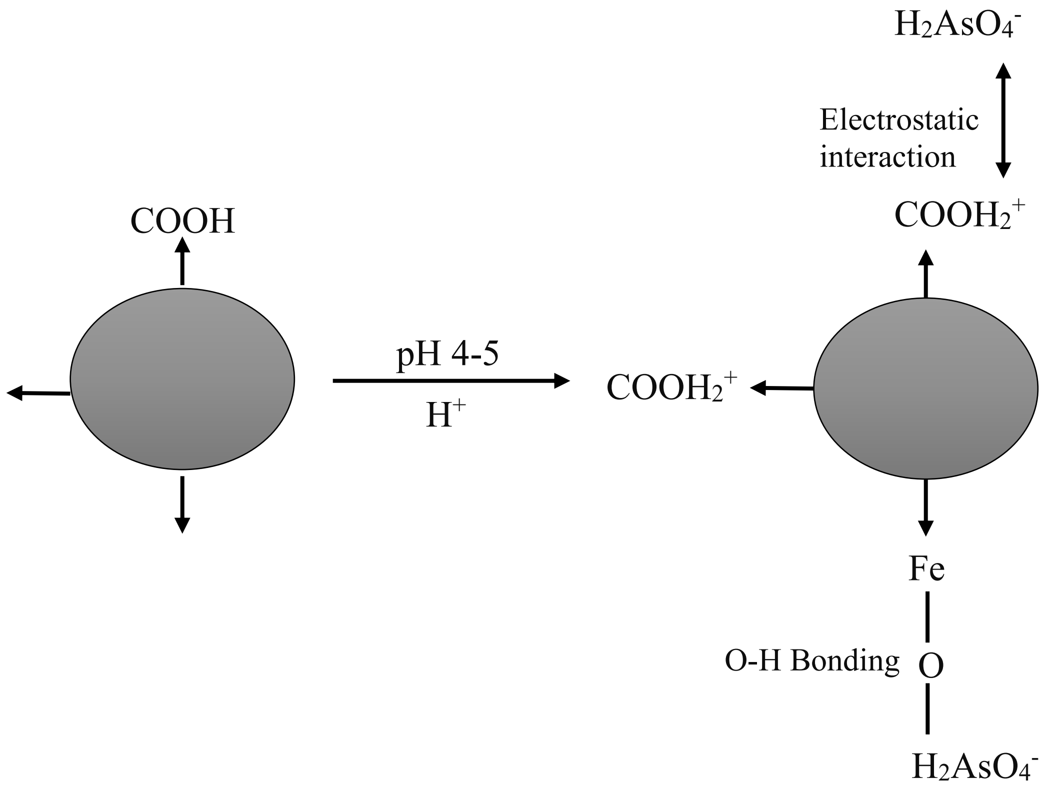

Figure. 47. Proposed As immobilization regarding hydrogel beads application.

3.3.2.6 Effects of amendments on nutrient availability

After 50 days of incubation, the level of available phosphorus (P) in the soil showed a significant increase ($P<0.05$) following treatment with hydrogel beads across all treatment groups, with the order of increase being SPP>SPPG>Soil, as illustrated in Figure. 49a. This enhancement in available P may be attributed to the mineralization of P during the incubation period. Within the soil matrix, As can lead to competitive adsorption, where As uptake by sorption sites causes P release into the soil. Moreover, changes in soil pH and the concentration of soluble ions could also contribute to the rise in available P. The soil organic carbon (SOC) value also showed a significant increase ($P<0.05$) with the addition of hydrogel bead amendments, as displayed in Figure. 49b. This suggests a correlation between the presence of SOC and the increased availability of P, which contributes to the reduction of As levels in the soil. These findings align with Ahmad et al. (2024), who documented similar effects using biochar to immobilize As in soil.

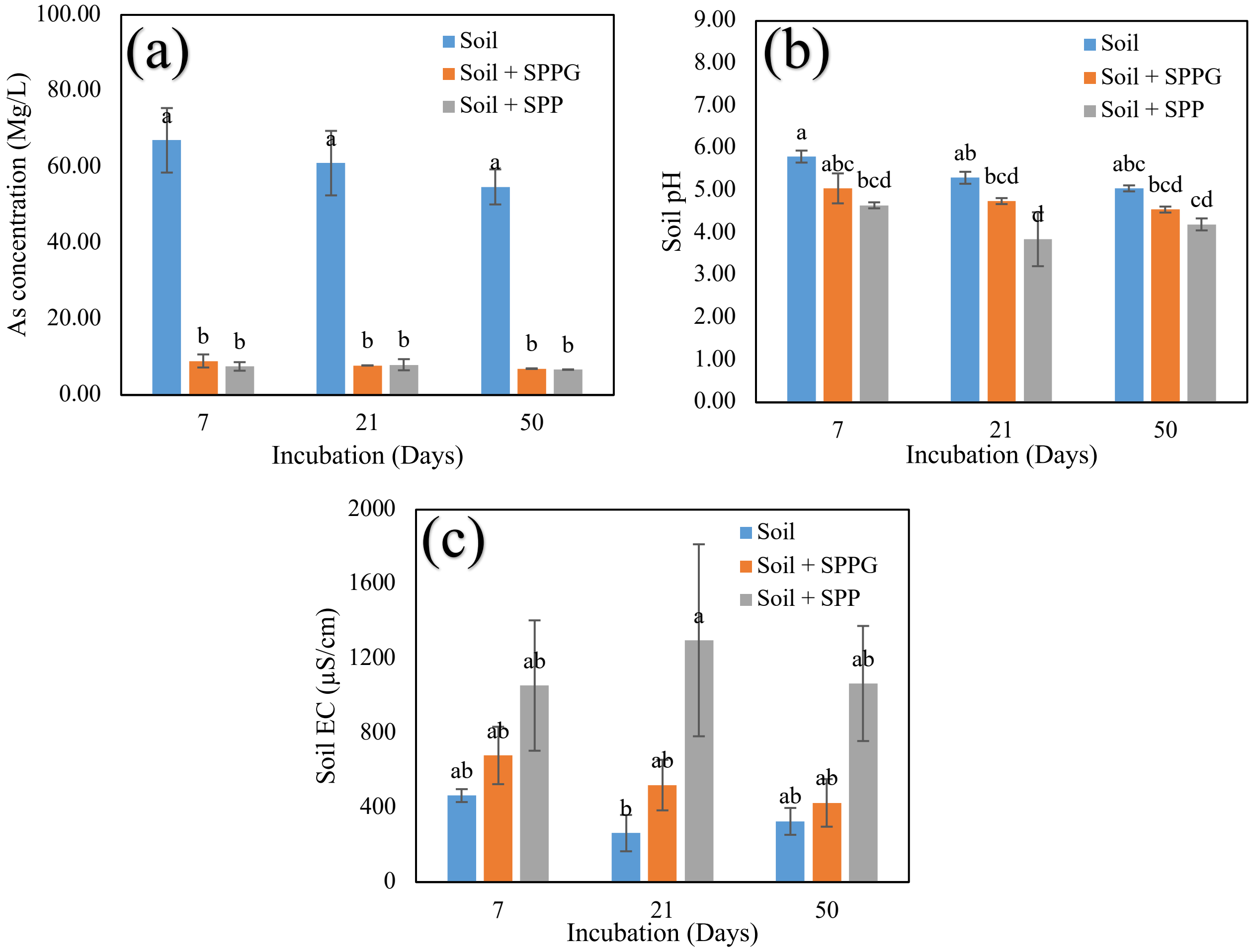

Figure. 48. Soil characteristics during incubation (a) soil Arsenic (b) soil pH (c) soil electrical conductivity.

Furthermore, the cation exchange capacity (CEC) of the soil was significantly increased ($P<0.05$) when compared to the control (soil only), as depicted in Figure. 49c. This increase is likely due to the -OH and -COOH functional groups from the hydrogel beads, which enhance the soil CEC (Hidayat et al., 2024). Notably, the CEC levels were higher in samples without glutaraldehyde (SPP) than those with glutaraldehyde (SPPG), suggesting that glutaraldehyde may engage in competitive ion interactions within the soil system.

The hydrogel bead treatment resulted in significantly higher levels of exchangeable Ca, K, and Na compared to the intact soil (P-value < 0.05) (Figure. 49d-f). This suggests that hydrogel beads can absorb and retain water, facilitating the transport of ions in the soil and thereby enhancing the content of these cations. However, there was no significant effect on the levels of Mg, N-NH_4, and N-NO_3 in the soil (Figure. 49g-i). This may be due to the low soil pH, which increases competition between hydrogen (H^+) ions and Mg and N-NH_4. These cations can be displaced from cation exchange sites by H^+, leading to their leaching. Additionally, low pH conditions can also lead to increased leaching of N-NO_3. However, this effect might be less pronounced in soils contaminated with As due to the inhibition of nitrate production.

Figure. 50 illustrates the Pearson correlation in general soil parameters after 50 days of incubation. The results showed a strongest positive relationship between pH and As ($r = 0.90$). It might be since As immobilization depends on pH conditions. Moreover, the available P had a positive correlation with SOC ($r = 0.92$) and CEC ($r = 0.89$), whereas a strong and negative relationship for As ($r = -0.97$). It might be because there is competition between As and P for adsorption sites in the soil matrix, leading to decreased As (Figure. 48a) and increased P value (Figure. 49a).

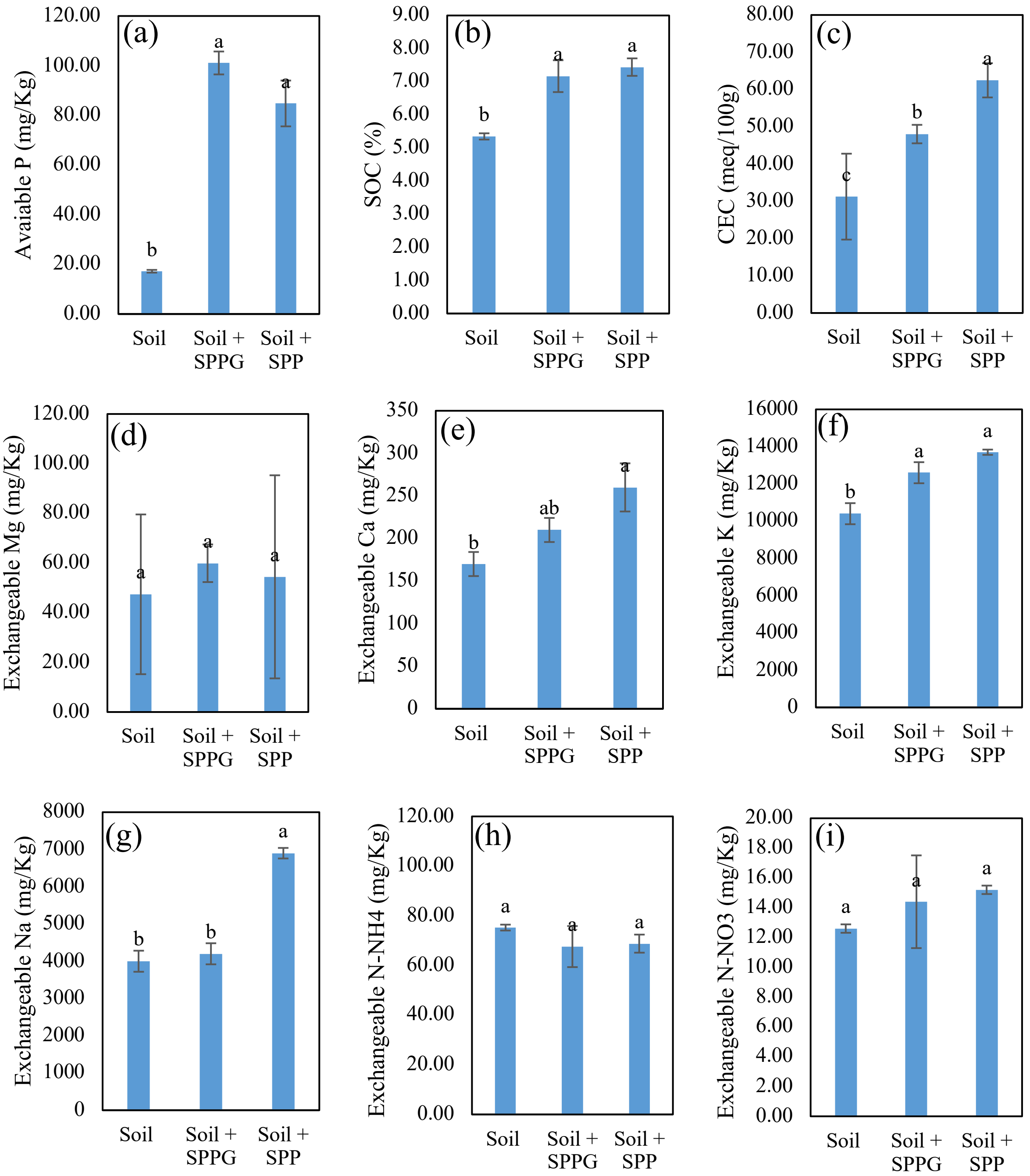

Figure. 49. Soil nutrient characteristics after 50 days of incubation in As contaminated regarding hydrogel beads application.

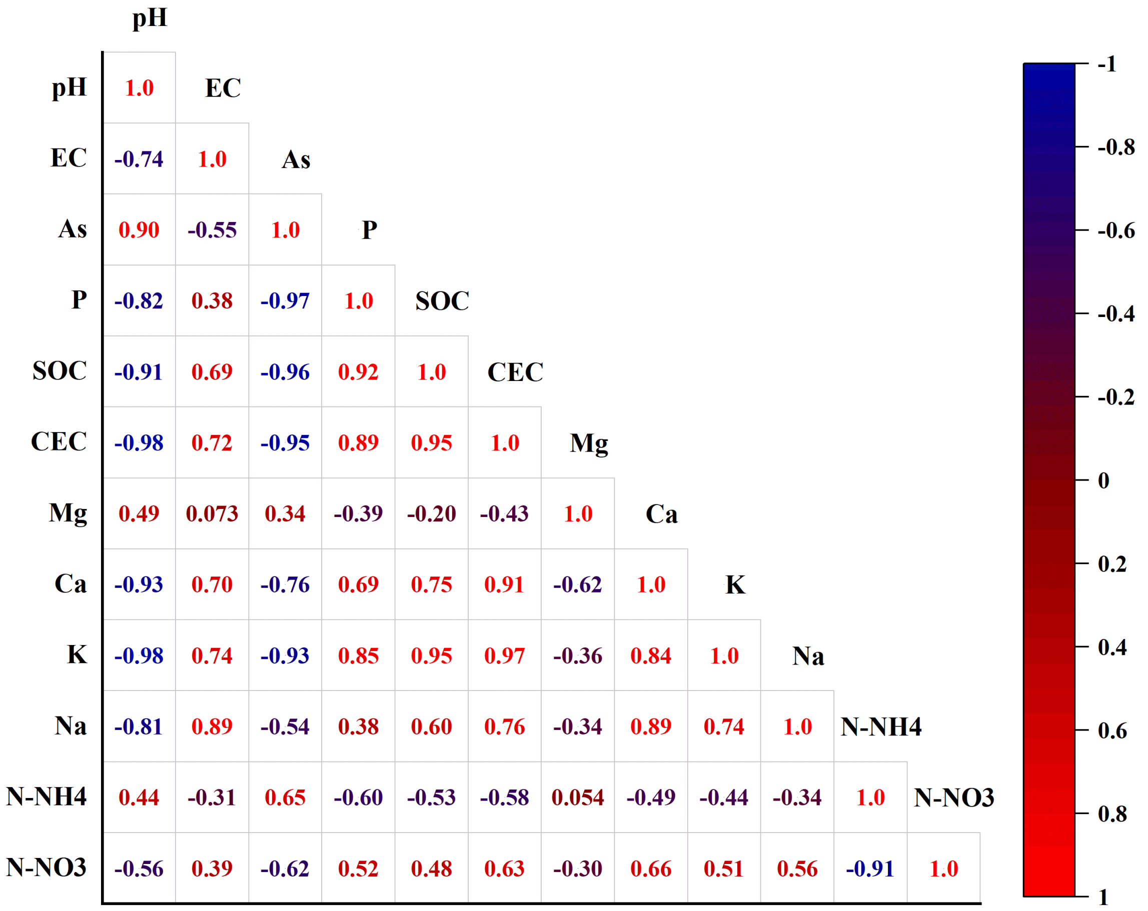

	pH	EC	As	P	SOC	CEC	Mg	Ca	K	Na	N-NH4	N-NO3
pH	1.0											
EC	-0.74	1.0										
As	0.90	-0.55	1.0									
P	-0.82	0.38	-0.97	1.0								
SOC	-0.91	0.69	-0.96	0.92	1.0							
CEC	-0.98	0.72	-0.95	0.89	0.95	1.0						
Mg	0.49	0.073	0.34	-0.39	-0.20	-0.43	1.0					
Ca	-0.93	0.70	-0.76	0.69	0.75	0.91	-0.62	1.0				
K	-0.98	0.74	-0.93	0.85	0.95	0.97	-0.36	0.84	1.0			
Na	-0.81	0.89	-0.54	0.38	0.60	0.76	-0.34	0.89	0.74	1.0		
N-NH4	0.44	-0.31	0.65	-0.60	-0.53	-0.58	0.054	-0.49	-0.44	-0.34	1.0	
N-NO3	-0.56	0.39	-0.62	0.52	0.48	0.63	-0.30	0.66	0.51	0.56	-0.91	1.0

Figure. 50. Pearson correlation coefficient matrix (r) of the soil nutrient characteristics after 50 days of incubation.

Moreover, changes in soil pH and the concentration of soluble ions could also contribute to the rise in available P. The soil organic carbon (SOC) value also showed a significantly increased ($P<0.05$) with the addition of hydrogel bead amendments, as displayed in Figure. 49b. This suggests a correlation between the presence of SOC and the increased availability of P, which contributes to the reduction of As levels in the soil. These findings are in line with those of Ahmad et al. (2024), who documented similar effects using biochar to immobilize As in soil. Furthermore, the cation exchange capacity (CEC) of the soil was significantly increased ($P<0.05$) when compared to the control (unamended soil), as depicted in Figure. 49c. This increase is likely due to the -OH and -COOH functional groups from the hydrogel beads, which enhance the soil CEC (Hidayat et al, 2024). Notably, the CEC levels were higher in samples without glutaraldehyde (SPP) than in those with glutaraldehyde (SPPG), suggesting that glutaraldehyde may engage in competitive ion interactions within the soil system.

3.3.3 Evaluation of slow-release fertilizers derived from hydrogel beads: Sodium alginate-poly (acrylic acid) and humic acid-encapsulated struvite for soil salinity amelioration

3.3.3.1 Characterization of precipitation

The experiment was conducted by mixing equal volumes and concentrations of Mg, NH_4-N, and P solutions at various pH levels ranging from 8-10. The results showed that the highest Mg, NH_4-N and P removal percentage at pH 9.0 with value of 73.21%, 98.74%, and 99.20%, respectively. However, as the pH increased to 10.0, the removal percentage decreased (Figure. 51). This suggests that there may have been additional compounds that precipitated alongside the struvite. These results are consistent with the study conducted by (X. Zhou & Chen, 2019) which used electrochemical techniques to produce struvite precipitates. Figure. 52 shows SEM micrographs of the residues obtained from different pH conditions. Regardless of pH, each crystal possessed a needle-shaped structure. Moreover, pH has a particular influence on the size of the crystal. Due to increased nucleation density, crystals will typically be smaller at higher pH. The largest crystal size was recorded at pH 8.0, while the smallest size was observed at pH 8.5. In addition, Figure. 52a-e presents the SEM images and assemblies of the C, O, N, P, and Mg maps, respectively. Notably, the samples contain significant amounts of N, P, K grains, which are prominent characteristics. Although the elemental maps of C, O, N, P, and Mg appear similar, the grains exhibit varying signal intensities (Table 16).

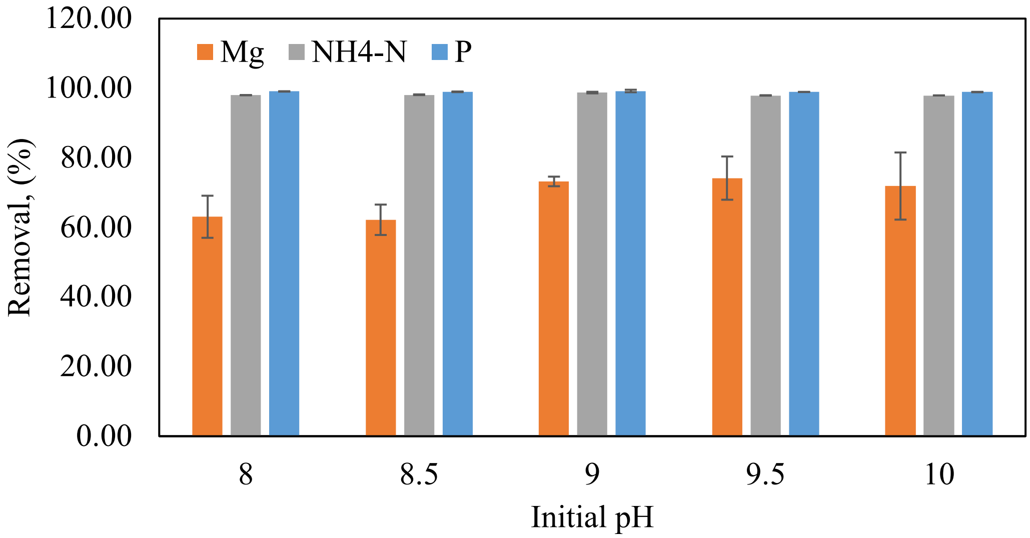

Figure. 51. Initial pH precipitation solution versus removal percentage.

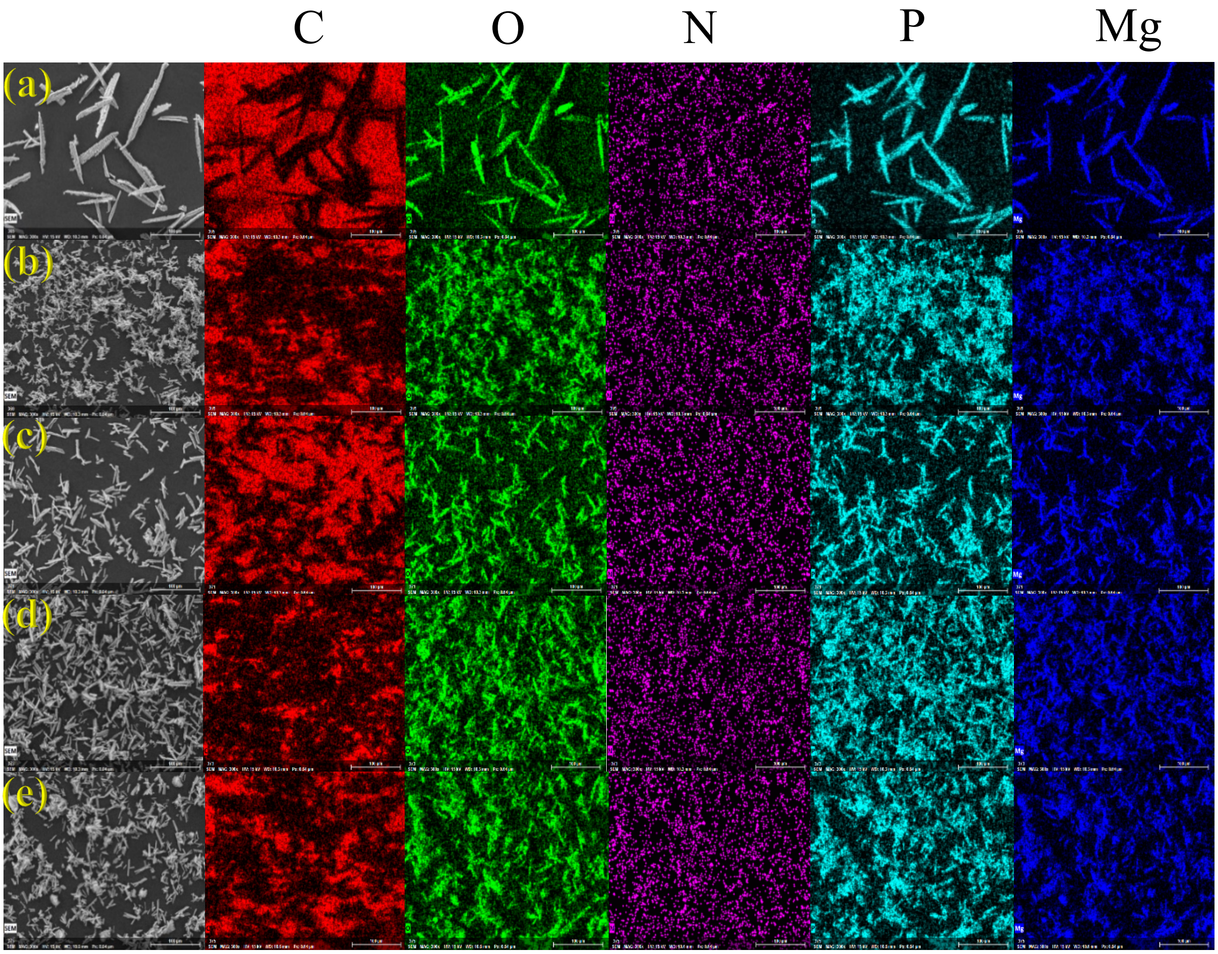

Figure. 52. SEM images and EDS mapping of solid residue in different pH conditions.

The XRD spectrum of the precipitate shown in Figure. 53 matched that of the struvite registered in the Powder Diffraction File (PDF) database (JCPDS 00-015-0762). The EDS data were used to examine the composition of the precipitation surface. The findings in Table 16 indicate that at pH 9.0, the maximum atom percentages of N, P, and Mg were obtained. This discovery corresponds to the formation of struvite precipitates (as seen in Eq. 38) and is consistent with the study reported by (González-Morales et al., 2021).

$$Mg^{2+} + NH_4^{+} + HPO_4^{2-} + 6H_2O \rightarrow MgNH_4PO_4 \cdot 6H_2O \quad (38)$$

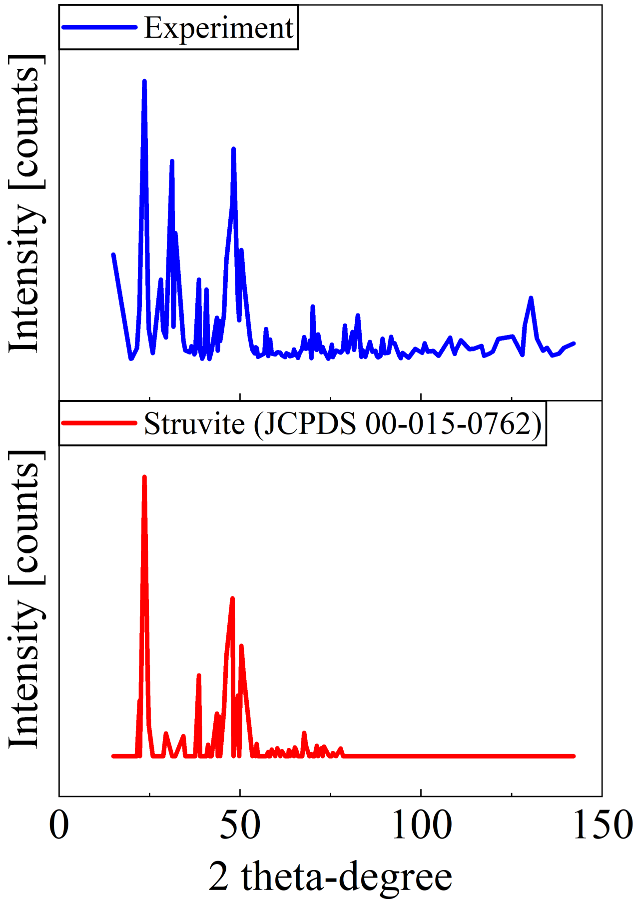

Figure. 53. XRD spectra of struvite collected at pH 9.0 condition and struvite (JCPDS 00-015-0762).

Table 16. EDS data composition of struvite precipitation in different pH conditions.

pH	Composition (Atom %)				
	C	O	N	P	Mg
8.0	61.75	31.42	3.82	1.27	1.74
8.5	56.90	35.00	3.97	1.84	2.29
9.0	39.28	47.41	3.86	5.01	4.43
9.5	51.45	38.81	3.89	2.40	3.45
10.0	54.94	36.65	3.40	2.09	2.92

3.3.3.2 Characteristics of encapsulation

The structure of the struvite encapsulated within hydrogel beads was analyzed using scanning electron microscopy (SEM). Figure. 54 and Figure. 55 corresponds to Sa@S and Sa@SHa, respectively. The hydrogel beads were microscopically tiny, exhibiting a sponge-like structure with interconnected pores (Figure. 54a and Figure. 55a). The size of the pores gradually increased from the surface to the interior of the Sa@S hydrogel beads (Figure. 54b). The addition of HA was found to enhance the formation of hydrogel networks. The introduction of HA resulted in a change in the structure of the hydrogel beads, producing a smooth surface (Figure. 55a). Figure. 55c illustrates the fibrous morphology of the hydrogel beads, which have interconnected pores on both the inside and outside of the beads. Upon closer examination, struvite crystals were observed on the surfaces of both the Sa@S (Figure. 54f) and Sa@SHa (Figure. 55f) hydrogel beads encapsulation. The fabrication process successfully encapsulated the struvite within the hydrogel beads, effectively regulating the release of minerals from the beads.

FTIR spectroscopy was utilized to investigate the functional groups within a molecule. The FTIR results for struvite, Sa@S, and Sa@SHa are depicted in Figure. 56a. Peaks detected between 3227 cm^{-1} and 3346 cm^{-1} were attributed to the elongation of O-H bonds, as described by researchers (Das et al., 2023). Peaks identified between 2896 cm^{-1} and 2924 cm^{-1} indicated the stretching of N-H bonds (Valle et al., 2022). The bending frequency of water molecules was verified to be approximately 1650 cm^{-1} (Valle et al., 2022). The peak at around 1541 cm^{-1} suggested the presence of COO groups formed by the combination of sodium alginate and poly (acrylic acid) (S. Hua et al., 2010). The wavenumbers 1328 cm^{-1} and 1028 cm^{-1} corresponded to the bending vibrations of O-H bonds and C-O-C bond stretching, respectively (S. Hua et al., 2010). The peak at 971 cm^{-1} corresponded to the symmetric stretching of the phosphate group, while a peak at 754 cm^{-1} was correlated to the elongation of P-O-P bonds (Bogdan et al., 2021). The peak at 884 cm^{-1} may have been responsible for cubic MgO (Chinthakuntla et al., 2016; Y. Ding et al., 2001). Research conducted by (Chinthakuntla et al., 2016) revealed that the stretching vibration of Mg-O occurred within the spectral region 550-670 cm^{-1}.

3.3.3.3 Mineralization release rate, swelling and soil water loss study

This present study investigated the mineral release profiles of struvite, Sa@S, and Sa@SHa hydrogel bead composites using distilled water at a controlled temperature of 25 °C for duration ranging from 3 hours to 14 days. The findings demonstrate that struvite exhibits a greater ease of dissolution, leading to a significantly higher release of all nutrients, including Mg, NH_4-N, and P, compared to the encapsulated formulations of Sa@S and Sa@SHa, as shown in Figure. 56b. The average release rates of struvite were 47.11 mg/L, 10.96 mg/L, and 16.95 mg/L for Mg, NH_4-N, and P, respectively, whereas for Sa@S, they were 7.81 mg/L, 0.49 mg/L, and 1.64 mg/L.

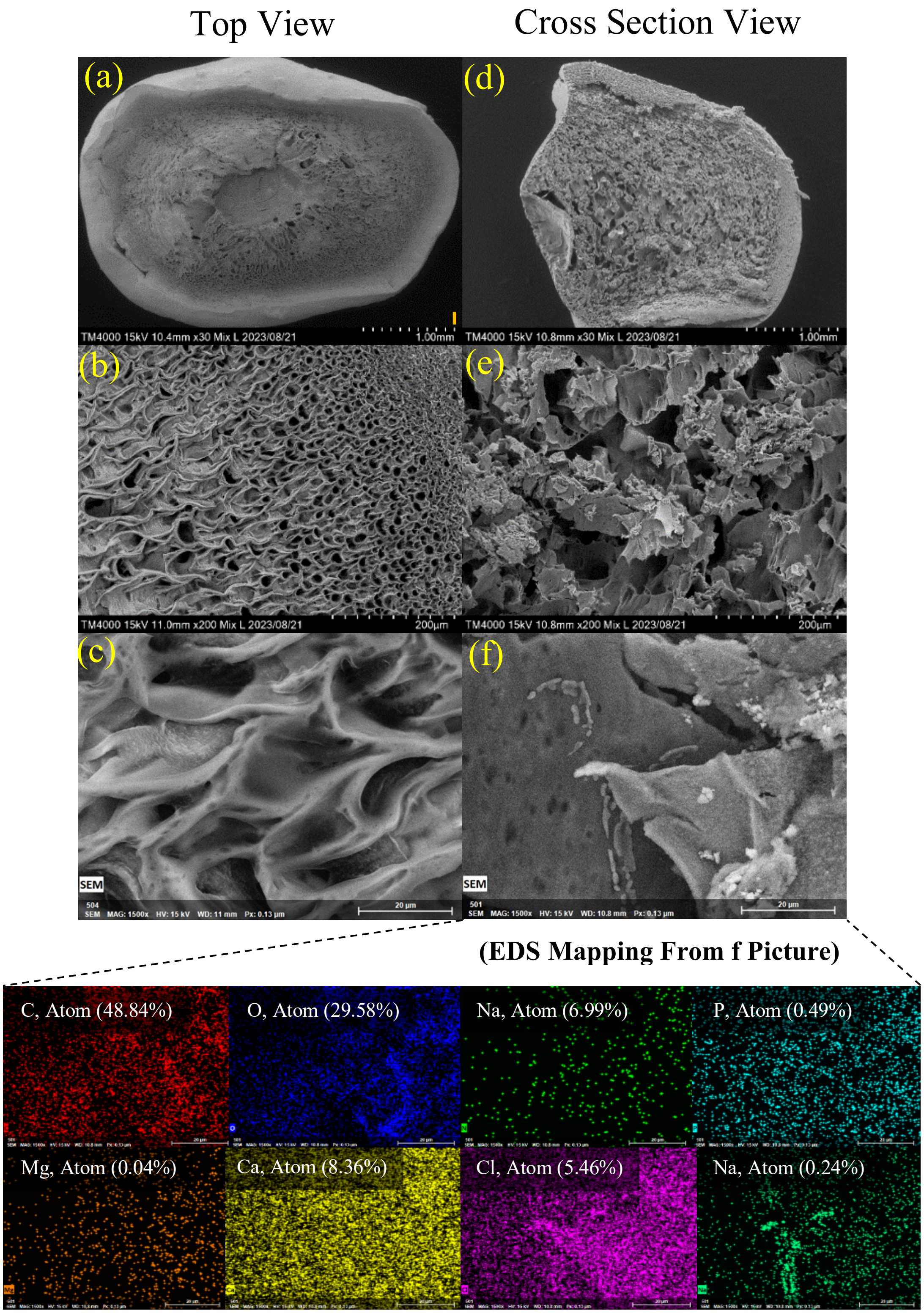

Figure. 54. SEM picture and EDS mapping of Sa@S hydrogel bead.

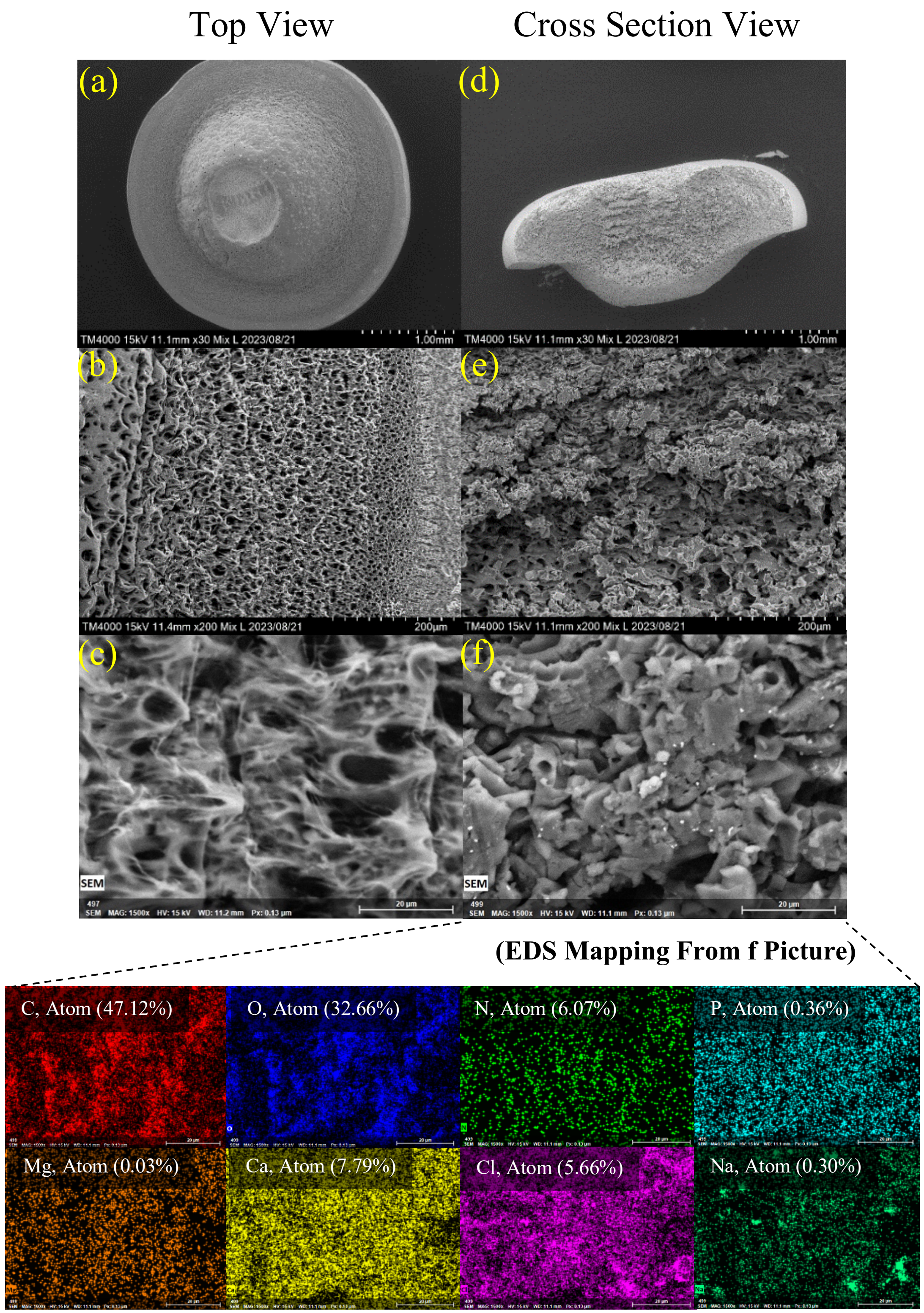

Figure. 55. SEM picture and EDS mapping of Sa@SHa hydrogel bead.

This indicates a difference of approximately 83.43%, 90.35%, and 95.54% in nutrient release. Similarly, for Sa@SHa, the average release rates were 7.81 mg/L, 0.49 mg/L, and 1.64 mg/L for Mg, NH_4-N, and P with percentage difference of 88.14%, 98.56%, and 93.55%. These percentage differences may be attributed to the barrier effect of the polymer hydrogels, hindering nutrient release. Furthermore, Sa@SHa showed higher percentage difference for struvite compared to Sa@S. This is due to the complex and intricate structure formed by the layers of HA, which obstructs the movement of minerals through the polymer network and into the surrounding environment.

Additionally, the concentration of Ca showed a higher rate of release during the initial 3-hour period but then decreased significantly over 14 days for both hydrogel bead encapsulations (Figure. 56c). This decline may be due to the higher concentration of Ca observed on the surface of the hydrogel beads, which act as cross-linkers and allow for the faster dissociation of Ca from the hydrogel beads. The process by which minerals are released from hydrogel beads can be described as follows: the struvite utilized in the formulations is in the form of hydrogel beads. Upon adding the sample into water, the hydrogel undergoes water absorption and swelling, resulting in the dissolution of the mineral. The dissolved mineral is gradually released into the water thorugh the polymeric shell due to the kinetic movement of water in the hydrogel and release medium. The difference in the concentration of soluble material between the internal and external conditions of the hydrogel bead primarily determines the rate of mineral release. However, the release rate slows down as the difference decreases over time.

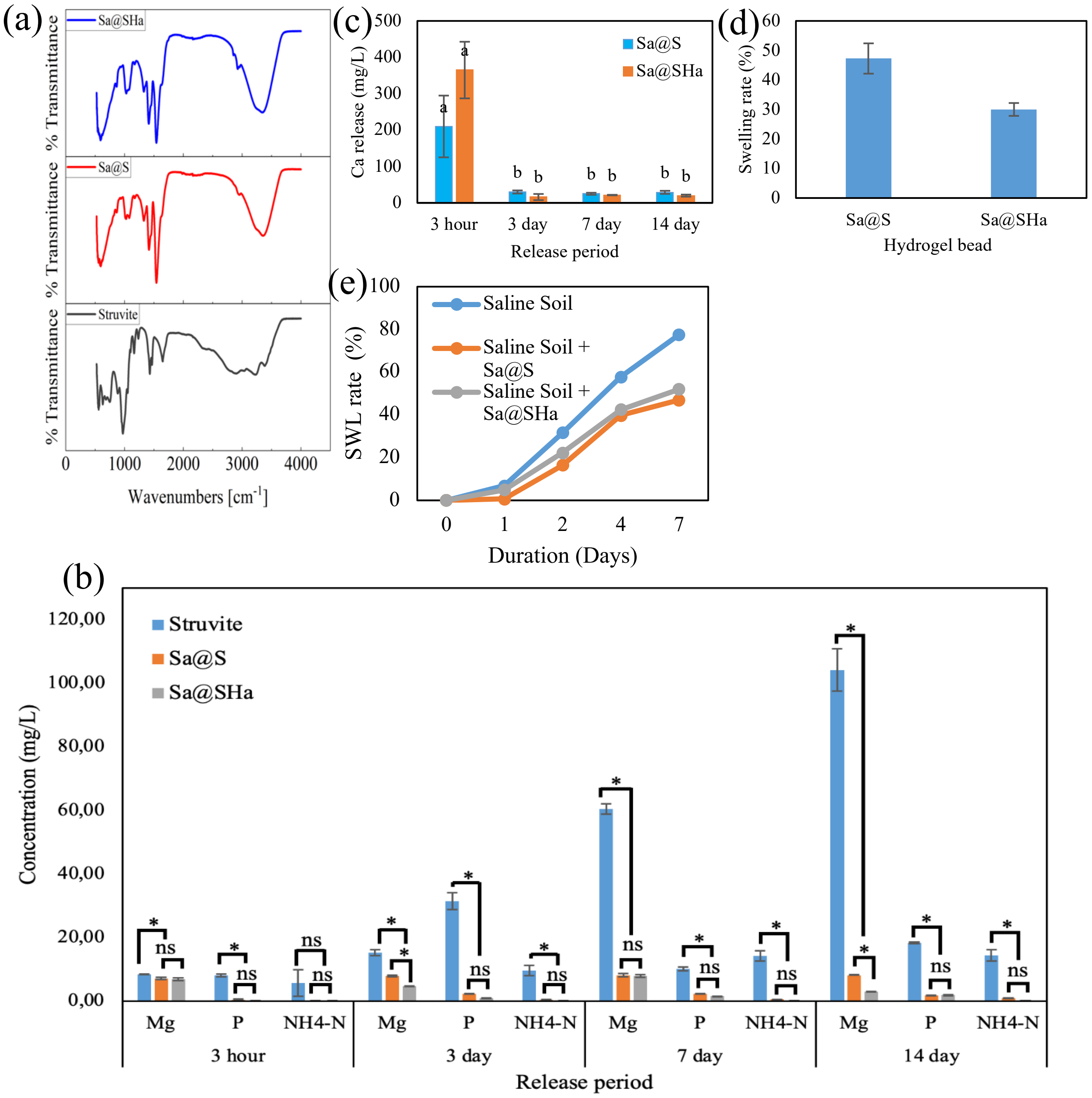

Figure. 56. (a) FTIR spectra of struvite pH 9.0, Sa@S, and Sa@SHa (b) Comparison nutrient release from struvite pH 9.0, Sa@S, and Sa@SHa (c) Ca release from hydrogel beads (Sa@S and Sa@SHa) (d) Swelling rate of Sa@S and Sa@SHa (e) Soil water loss of Sa@S and Sa@SHa under salinity. *Indicates statistically significant at a significance level of $P<0.05$; ns denotes no significant difference in Tukey's test.

Figure. 56d illustrates the swelling percentage of the hydrogel beads encapsulation. The data regarding swelling percentage indicate that Sa@S exhibits a higher rate of swelling than Sa@SHa. This is most likely due to the crosslinks formed by HA, which can constrain the movement of polymer chains and diminish the overall flexibility of the hydrogel network. Consequently, the hydrogel beads may reduce capacity to swell in response to water absorption. Figure. 56e presents the percentage of soil water loss (SWL rate) for up to 7 days. The findings suggest that Sa@S hydrogel beads demonstrate significant water retention capability, with the lowest SWL rate recorded at 47%. Conversely, Sa@SHa exhibits a value of 52%. This showed that inclusion of HA into hydrogel beads has an unfavourable effect on swelling and soil water loss. In contrast, the SWL rate of intact saline soil was observed to be 78%. It can be concluded that the introduction of hydrogel beads into the soil has a positive effect on water retention in the soil, as indicated by a reduction in soil water loss.

3.3.3.4 Assessment of soil quality

3.3.3.4.1 Soil pH, EC, SAR, and ESP

Table 17. Effect of hydrogel bead on SAR and ESP value

Treatment	SAR			ESP		
	Incubation time (days)					
	5	10	20	5	10	20
Soil (Control)	41.86	41.52	27.73	8.30	11.87	9.01
Soil + Sa@S	17.49	22.58	12.73	5.92	6.85	2.63
Soil + Sa@SHa	14.69	22.15	10.93	4.68	6.16	2.65

Soil pH is vital in detecting soil quality because low and high pH levels can affect nutrient availability, soil structure, and microbial activity, impacting plant growth (Y.-Y. Zhang et al., 2019). The saline soil incubation experiment was conducted for 20 days. The results showed that the soil pH remained stable and unaffected by the treatment and incubation conditions ($p<0.05$) (Figure. 57a).

Similarly, high EC levels can hinder plant water uptake and lead to osmotic stress (X. Ding et al., 2018). The results show that there was a significant interaction between the treatments on EC ($p<0.05$) (Figure. 57b), which showed a substantial decline over the incubation period. After 5 days of incubation, using Sa@SHa in saline soil reduced EC from 6.09 mS/cm in the control treatment to 4.88 mS/cm and 5.41 mS/cm for Sa@S, respectively. After the incubation period (20 days), the control treatment (soil) was 6.61 mS/cm, while Sa@S and Sa@SHa treatment reached 3.83 and 3.52 mS/cm, respectively. These values indicate that the soil is normal (Negacz et al., 2022), and suggest that the encapsulation of hydrogel beads served as a barrier, effectively inhibiting excessive nutrient leaching and promoting water retention, resulting in decreased soil electrical conductivity.

The SAR and ESP are essential indicators of soil salinity and sodicity, respectively, significantly impacting crop growth (Andrade Foronda & Colinet, 2023; Gharaibeh et al., 2021). SAR measures the ratio of Na ions to Ca and Mg ions in the soil solution, and elevated SAR values indicate higher Na levels that can harm soil structure, reduce water infiltration, impede nutrient retention, and restrict root development. As shown in Table 17, all treatments exhibited varying SAR values. The application of hydrogel bead encapsulation, particularly the use of Sa@SHa, resulted in the most significant reduction in SAR levels, with a decrease of 60.58% from 27.73 to 10.93, followed by Sa@S with a reduction of 54.09% compared to the soil only.

The ESP represents the proportion of exchangeable sodium concerning the total exchangeable cations (including Na, Mg, Ca and K) in the soil. High ESP values suggest a greater Na concentration than other cations, leading to soil dispersion and reduced permeability. This can negatively impact root penetration and nutrient absorption in crops. The ESP values after incubation are presented in Table 17, which indicates that all treatments had ESP values below 12 following the incubation period. However, after 20 days of incubation, the application of hydrogel bead encapsulation resulted in the lowest values, measuring 2.65 and 2.63 for Sa@S and Sa@SHa, respect (Tanehgonbadi & Qaderi, 2023). These findings align with (Abdeen and Saeed, 2019), who used hydrogels derived from poly (vinyl alcohol) borate to remediate saline and sodic conditions and restore soil to its normal state.

3.3.3.4.2 Phosphorus and organic carbon

P is an indispensable nutrient for the development and growth of plants, performing a vital function in photosynthesis, energy transfer, and root formation. Adequate P levels in the soil are essential for optimal plant growth and (Al-Tohamy et al., 2022; J. Liu et al., 2011). The majority of the results of the study demonstrated that the amount of available P in the saline soil increased significantly over time in all treatments compared to the soil (control) treatment (Figure. 57c). Statistical analysis showed a remarkable relationship between treatment and incubation period ($P<0.05$). After five days of incubation, the soil treatment showed the lowest concentration of available P. However, the soil treated with Sa@S exhibited the most significant increase in available P content after incubation. The available P concentration in the study was primarily 2.18, 4.14, and 10.40 mg/Kg for soil, Sa@S, and Sa@SHa, respectively. After 20 days of incubation, the values for soil, Sa@S, and Sa@SHa increased to 9.23, 31.96, and 24.85 mg/Kg, respectively. In contrast, SOC value revealed there was no notable difference for all treatments and incubation periods ($P<0.05$) (Figure. 57d). This may be attributed to the presence of struvite-encapsulated hydrogel beads, which can exacerbate stress and further limit the activity of soil organisms involved in the decomposition of organic matter.

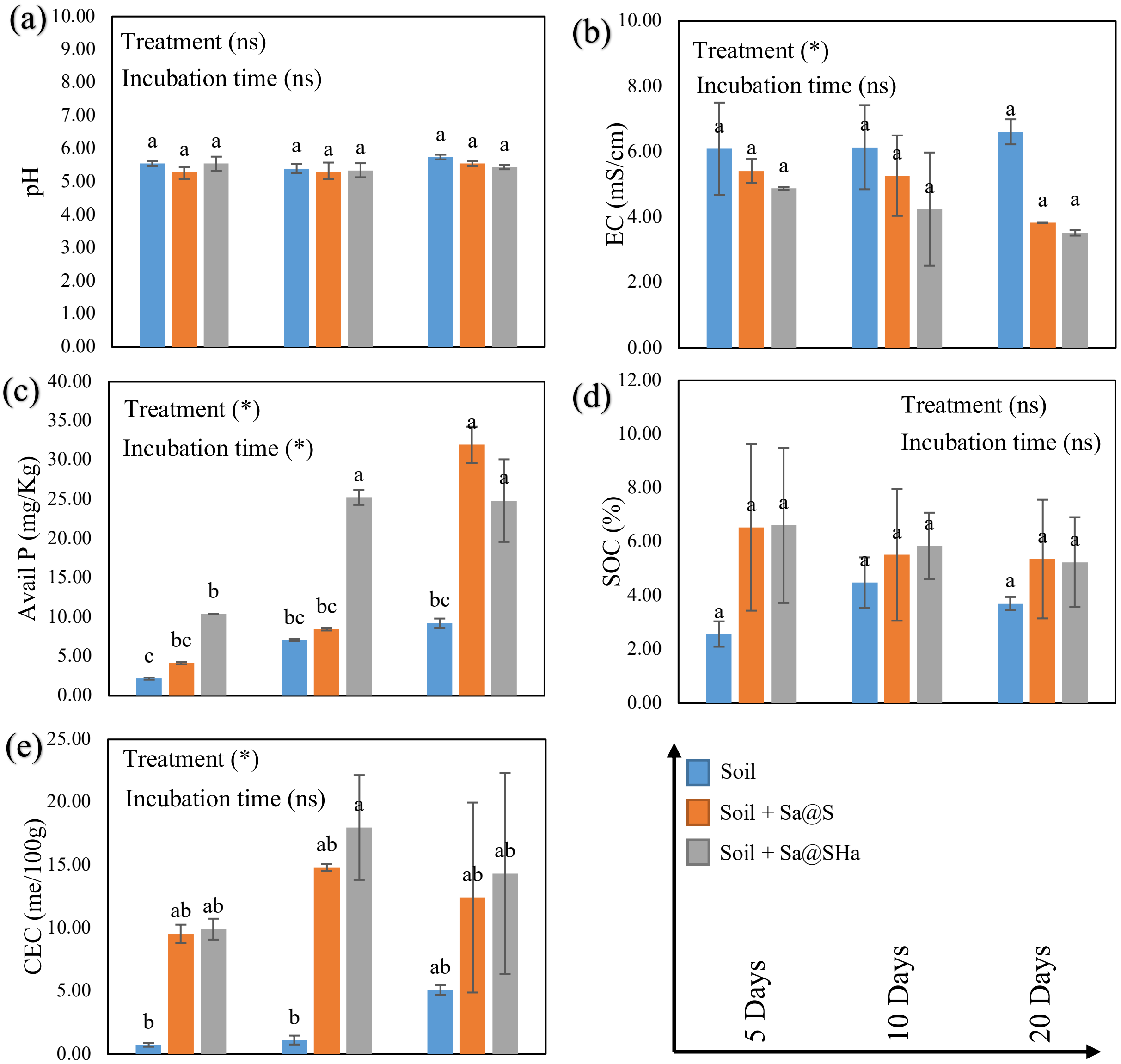

Figure. 57. Soil characteristics (pH, EC, available P, SOC, and CEC) in saline soil regarding hydrogel beads application at different incubation times.

3.3.3.4.3 Cation exchange capacity and exchangeable cations

CEC refers to the capacity of soil to retain and exchange cations such as Ca, Mg, K, and Na. Higher CEC soil content can retain more nutrients, making them more fertile (Razzaghi et al., 2021). The difference in the soil CEC was significant ($P<0.05$) throughout all treatments, as shown in Figure. 57e. Overall, the application of both hydrogel beads showed a substantial increase in

CEC ($P<0.05$) compared to soil (control) with the following order: Sa@SHa > Sa@S > soil. This is because carboxyl (-COOH) and aromatic rings from polymer composites can attract and bind to positively charged cations. When these functional groups interact with soil particles, they create additional sites for cation adsorption, increasing CEC.

Figure. 58a-c depicts the exchangeable Mg, K, and Ca values for all treatments. The data shows that hydrogel beads encapsulated-struvite treatment leads to a significant increase in Mg, K and Ca ($P<0.05$) compared to the control. After 20 days of incubation, the Sa@S treatment exhibited the highest concentration of Mg, with a 99.31% increase compared to the control, followed by the Sa@SHa treatment, with a 97.31% increase. The Sa@SHa treatment also showed the highest concentration of K and Ca after 20 days of incubation, with 49.07% and 46.87% increases, respectively. These findings were due to the presence of struvite, a mineral complex of Mg and Ca ions, in the hydrogel beads. When these beads disintegrate into the soil, they release ions contributing to the soil's exchangeable Mg and Ca pools. Because of its porous nature, the hydrogel absorbed and retained significant water and nutrients such as K ion. Consequently, when these beads are added to the soil, they function as containers for K ion, thereby avoiding the leaching process and subsequent loss of nutrients.

In contrast, the decrease in exchangeable Na was substantial ($P<0.05$) after treatment with hydrogel beads encapsulated (Figure. 58d). Specifically, there was a reduction of up to 48.93% for Sa@S and 46.09% for Sa@SHa. Lowering the Na concentration in soil can positively impact plant growth (Almeida et al., 2017; Kronzucker et al., 2013). This finding agrees with the results of (Costa et al., 2022), who used a hydrogel composed of potassium acrylate and acrylamide to recover saline soil.

3.3.3.4.4 Available NH_4-N and NO_3-N

NH_4-N and NO_3-N are essential forms of nitrogen in soil that are vital for plant growth and soil fertility (Xu et al., 2012). These forms of nitrogen are used by plants through their roots and utilized for various physiological processes (Hachiya et al., 2012; Zayed et al., 2023). The study showed a significant increase ($P<0.05$) in NH_4-N levels in the soil with treatment (Figure. 58e). After 20 days of incubation, the highest concentration of NH_4-N was observed in Sa@S with a 26.57% increase, followed by Sa@SHa with an 18.52% increase compared to the control. The increase observed over incubation time suggests the conversion of readily convertible nutrients to minerals.

Additionally, the study discovered a significant increase ($P<0.05$) in NO_3-N concentration in soil samples incubated after the hydrogel beads encapsulated application (Figure. 58f). After 20 days of incubation, NO_3-N concentration increased by 92.15% and 80.68% for Sa@S and Sa@SHa, respectively. This result is similar to the findings of (Tefera et al., 2022), who reported that liquefied biomass hydrogel increased NH_4-N and NO_3-N values under saline soil conditions.

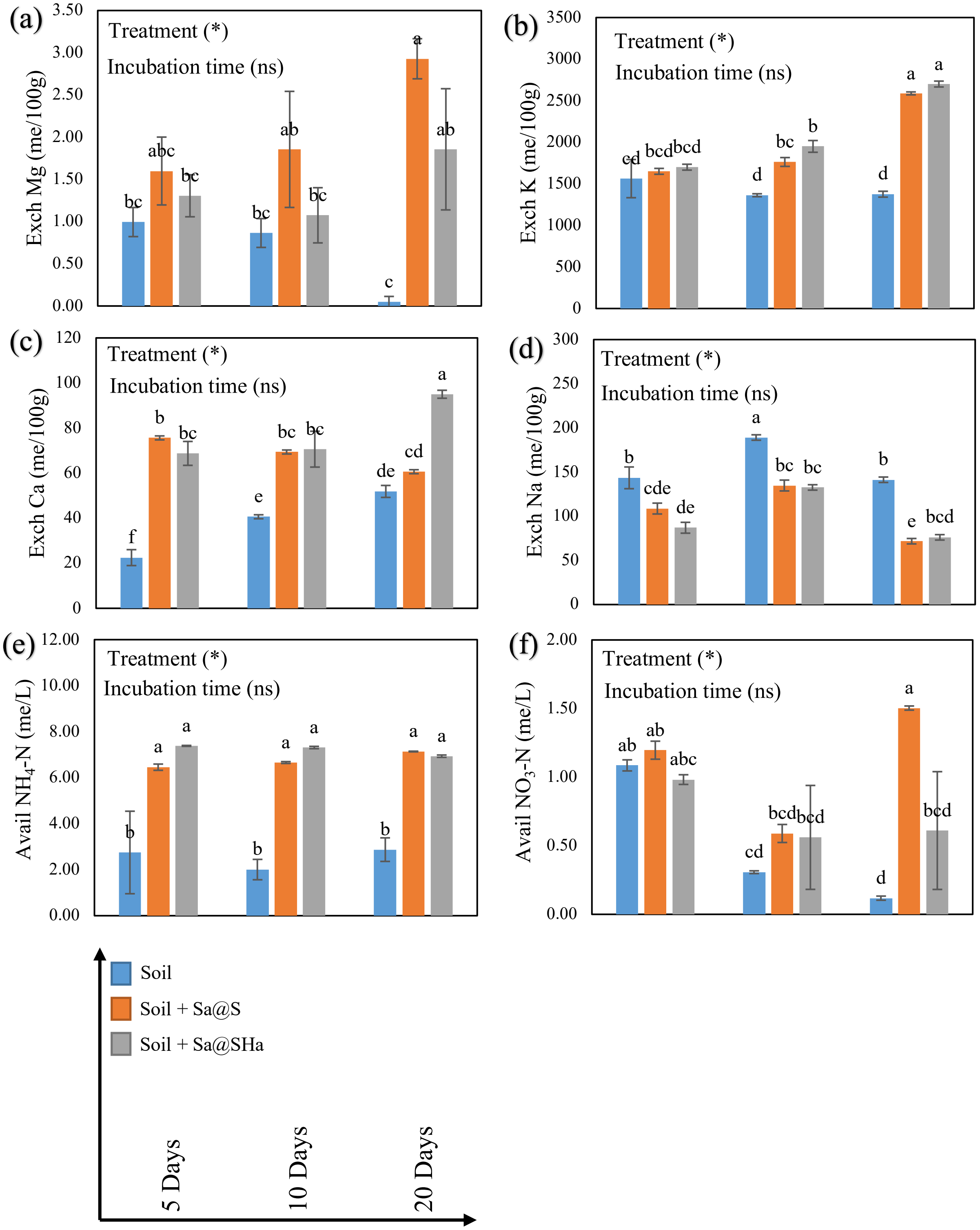

Figure. 58. Soil characteristics (Exchangeable Mg, K, Ca, Na, Available NH_4-N, and NO_3-N) in saline soil regarding hydrogel beads application at different incubation times.

3.3.4 Co-pyrolysis MgO-Biochar under Difference Temperature Derived from Coffee Husk for glyphosate immobilization in soil: Evaluation of Biochar Characteristics and Carbon Stability

3.3.4.1 Biochar characterization

The morphology of the biochar samples was analysed using scanning electron microscopy (SEM) and is presented in Figure. 59. The surfaces of all samples were uniformly coated with some substances, although MgB-C exhibited a relatively smooth surface. Figure. 60a displays the N_2 adsorption/desorption isotherms, and Table 18 provides a summary of the Brunauer-Emmett-Teller (BET) specific surface area (S_{BET}), total pore volume (V_{total}), and average pore size (D_{meso}) of the biochar. The results indicate that an increase in temperature leads to an increase in S_{BET} and V_{total}, but a decrease in D_{meso} content. From these findings, it can be concluded that the biochar exhibits a mesoporous structure.

Table 18. Physical characteristics of biochar composite.

Sample	S_{BET} [m^2 g^{-1}]	V_{total} [cm^3 g^{-1}]	D_{nano} [nm]
MgB-A	10.566	0.026	9.997
MgB-B	30.853	0.044	5.733
MgB-C	54.937	0.048	3.520

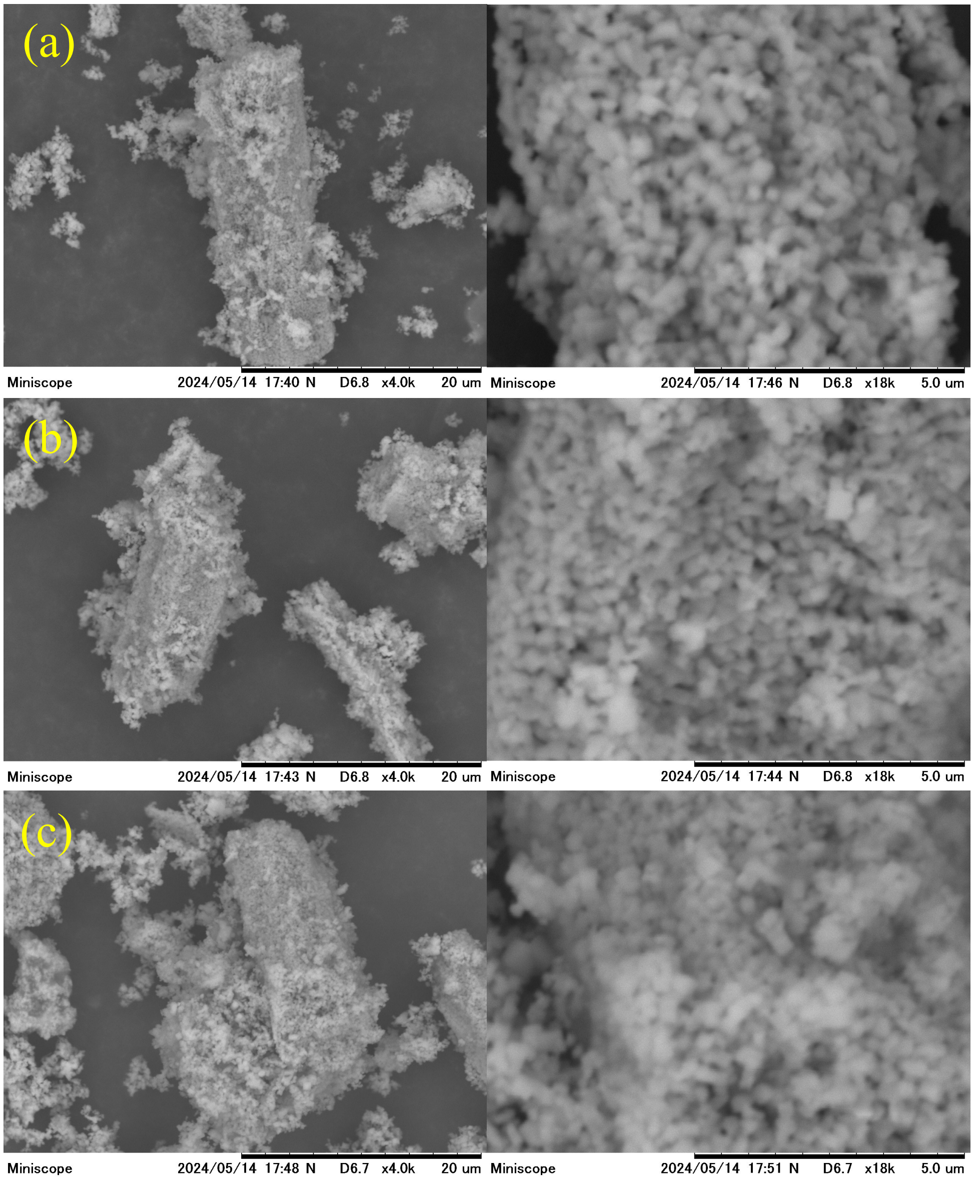

Figure. 59. SEM images of biochar composite (a) MgB-A (b) MgB-B (c) MgB-C.

Table 19. Moisture, volatile matter, ash, and fixed carbon content of biochar composite.

Sample	Moisture content (%)	Volatile matter (%)	Ash content (%)	Fixed carbon (%)
MgB-A	0.51 ± 0.40	25.58 ± 0.20	0.17 ± 0.13	73.74 ± 0.47
MgB-B	0.70 ± 0.27	0.22 ± 0.04	0.25 ± 0.21	98.83 ± 0.33
MgB-C	0.85 ± 0.12	0.12 ± 0.04	0.39 ± 0.39	98.64 ± 0.45

The chemical functional groups of the biochar as shown in Figure. 60b. The spectral at 3364 cm^{-1} is attributed to the stretching vibrations of O-H bonds. A new appearance peak for MgB-C at 2161 cm^{-1} is characteristics of C≡C (Ashby et al., 2014). A peak at 1582 cm^{-1} is associated with the carboxylate (-COO-) groups (Hua et al., 2010). The peaks around 1434 cm^{-1} can be attributed to the symmetric stretching of -COO- (Hua et al., 2010). The peak spectral from 525-2583 cm^{-1} revealed that the stretching vibration of Mg-O (Chinthakuntla et al., 2016).

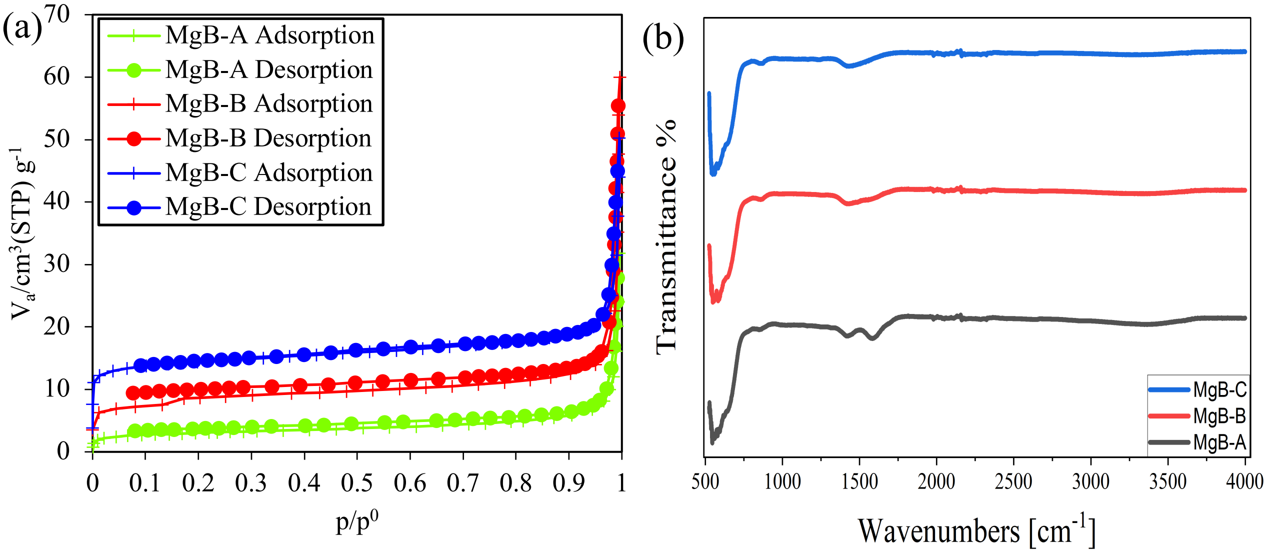

Figure. 60. (a) N_2 adsorption/desorption of biochar composite (b) FTIR spectra of biochar composite.

3.3.4.2 Biochar stability

The content of stable carbon is a key parameter in evaluating the efficiency of biochar in sequestering carbon (Mašek et al., 2019). In this study, the stable carbon content was measured using an H_2O_2 oxidation method, calibrated to simulate approximately 100 years of soil aging (Crombie et al., 2013), as depicted in Figure. 61a.

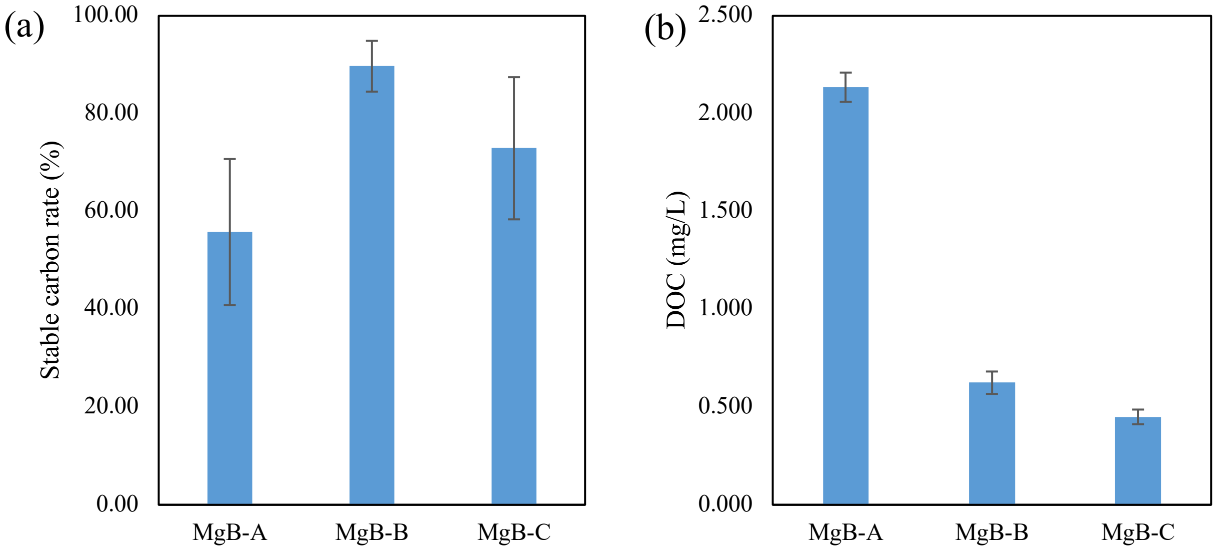

Figure 61. (a) Biochar carbon stability (b) DOC concentration from biochar composite.

The results indicate that as the pyrolysis temperature increased from 350 °C to 500 °C, the stable carbon content rose from 55.76% to 89.69%. However, when the temperature reached 650 °C, the stable carbon content dropped to 72.92%, suggesting an increase in the biochar's reactivity at higher temperatures. This increase in reactivity could be attributed to the collapse of the biochar's pore structure at elevated temperatures, which exposes more active sites, and to the enhanced electron transfer capabilities of the graphitized structure formed at these high temperatures, facilitating the oxidation of biochar by oxidants such as H_2O_2 (H. Yang et al., 2024). The impact of H_2O_2 oxidation on biochar can be described by the following formula:

$$H_2O_2 \rightarrow 2\cdot OH \tag{39}$$

$$OH + C \rightarrow CO_2\uparrow + H_2O \tag{40}$$

This observation was corroborated by varying the pyrolysis temperature. The highest stable carbon content was recorded at 500°C for MgB-B. This indicates that the impact of MgO doping on the stability of carbon is influenced by the pyrolysis conditions.

3.3.4.3 Proximate analysis

The quality of the biochar products was assessed using proximate analysis, as detailed in Table 19. The moisture content of the biochar samples, measured at room temperature, indicates the amount of water they contain. The volatile matter content refers to the quantity and state (liquid, gas, or solid) of compounds and molecules that can be released from the biochar. The ash content represents the mineral and incombustible material present, while the fixed carbon content shows the amount of solid carbon remaining after excluding moisture, volatile matter, and ash (Kasantikul et al., 2020).

Generally, the moisture content in all samples was below 1%, with the highest being 0.85 ± 0.12 in the MgB-C sample. Significant differences were observed in the volatile matter content across all samples, with increasing pyrolysis temperatures leading to a reduction in volatile matter. This reduction is likely due to higher temperatures promoting the breakdown of organic material, resulting in the release of water vapor and organic molecules through reactions such as dehydrogenation, isomerization, and condensation (Hassan et al., 2023). The decrease in volatile matter might also be linked to the volatilization of hydrogen and oxygen (Park et al., 2019).

The ash content in the biochar samples increased with higher carbonization temperatures. The observed ash content in MgB-C was 0.39 ± 0.39. The ash consists of alkaline metals such as potassium (K), magnesium (Mg), calcium (Ca), and sodium (Na), as well as transition metals like zinc (Zn), copper (Cu), and manganese (Mn) (Sadaka et al., 2014; Werner et al., 2014). These non-combustible elements form oxides or carbonates, referred to as ash, as they do not volatilize during the analysis (Bakshi et al., 2020). The fixed C content showed as the pyrolysis temperature increased from 350 °C to 500 °C, the fixed C content rose from 73.74 ± 0.47 to 98.83 ± 0.33. However, when the temperature reached 650 °C, the stable carbon content was consistent above

98%. According to (Crombie et al., 2013) that the higher fixed C content is associated with the higher release of volatile matter during the pyrolysis process.

3.3.4.4 DOC concentration

Figure. 61b illustrates the impact of pyrolysis temperature on the dissolved organic carbon (DOC) concentrations released from the prepared biochar. The results indicate that DOC concentrations decline sharply as the pyrolysis temperature increases. This decrease in DOC concentration could be attributed to the reduction in volatile substance content in the biochar, which occurs as the pyrolysis temperature rises. At higher temperatures, the chemical bonds of some organic components are broken and rearranged, leading to a series of reactions including decomposition, condensation, cyclization, and polymerization (Liu et al., 2019). This process results in the formation of stable polyaromatic hydrocarbons (Huang et al., 2024).

Table 20. DOM characteristics of biochar composite.

Sample	SUV_{254}	SUV_{260}	SUV_{280}
MgB-A	0.992 ± 0.03	0.885 ± 0.027	0.614 ± 0.02
MgB-B	0.025 ± 0.001	0.027 ± 0.003	0.023 ± 0.003
MgB-C	0.031 ± 0.003	0.040 ± 0.01	0.022 ± 0.004

3.3.4.5 UV-Vis parameters

Table 20 displays the UV-Vis parameters of biochar produced at various pyrolysis temperatures. UV_{254} is commonly utilized to assess the aromaticity of dissolved organic matter (DOM), while UV_{260} measures the content of the hydrophobic components of DOM. The trends observed show that UV_{254} and UV_{260} decreased and increased with pyrolysis temperature, both peaking at 350 °C. However, 650 °C served as the inflection point for changes in these spectral parameters of DOM. This suggests that secondary reactions may occur at a pyrolysis temperature of 650 °C, leading to the ongoing degradation and removal of aromatic dissolved organic components, and the transformation of larger molecules into smaller ones within the DOM (He et al., 2021). The values of UV_{254} and UV_{260} were significantly higher at lower temperatures compared to higher temperatures, indicating that lower pyrolysis temperatures better preserve the aromatic and hydrophobic components in DOM. Since the aromatic structure is closely linked to the reactivity of DOM (Dittman et al., 2009), it can be inferred that DOM produced at lower pyrolysis temperatures has a more pronounced impact on the environmental behaviour of pollutants. UV_{280}, which serves as an indicator of the molecular weight of organic matter and reflects the degree of humification of DOM (WANG et al., 2009), showed a gradual decrease with increasing pyrolysis temperature, reaching its highest values at 350 °C. This indicates that DOM produced at lower temperatures has a higher degree of humification.

3.3.4.6 Biochar pH, EC, P, and CEC

Results for biochar pH, electrical conductivity (EC), available P, and cation exchange capacity (CEC) are presented in Figure. 62a-d. The pH measurements indicate that all samples were alkaline, ranging from 11.23 to 11.30. These high pH values in the WH biochar correlate with its respective ash content, produced at specific temperatures as shown in Table 19. The increase in biochar pH with temperature is likely due to the accumulation of alkali salts (Ding et al., 2014), and the replacement of acidic functional groups with alkaline ones during pyrolysis (Al-Wabel et al., 2013). Consequently, biochar with a high pH may be beneficial for ameliorating soil acidity (Windeatt et al., 2014), a trend similarly reported by (F. Zhang et al., 2015). Regarding EC, the mean values varied with temperature, with the highest recorded at 600 mS/cm for MgB-C. These EC values align with the ash content of the respective biochar samples, suggesting that higher pyrolysis temperatures lead to greater loss of volatile matter, thereby increasing the mineral content in the ash and subsequently the EC values (Cantrell et al., 2012). Similar result for available P in biochar. CEC, which indicates the biochar's capacity to bind cations, was found to increase with higher pyrolysis temperatures (Hmid et al., 2014). The EC results are consistent with both the UV-Vis analysis and the ash content of the biochar samples.

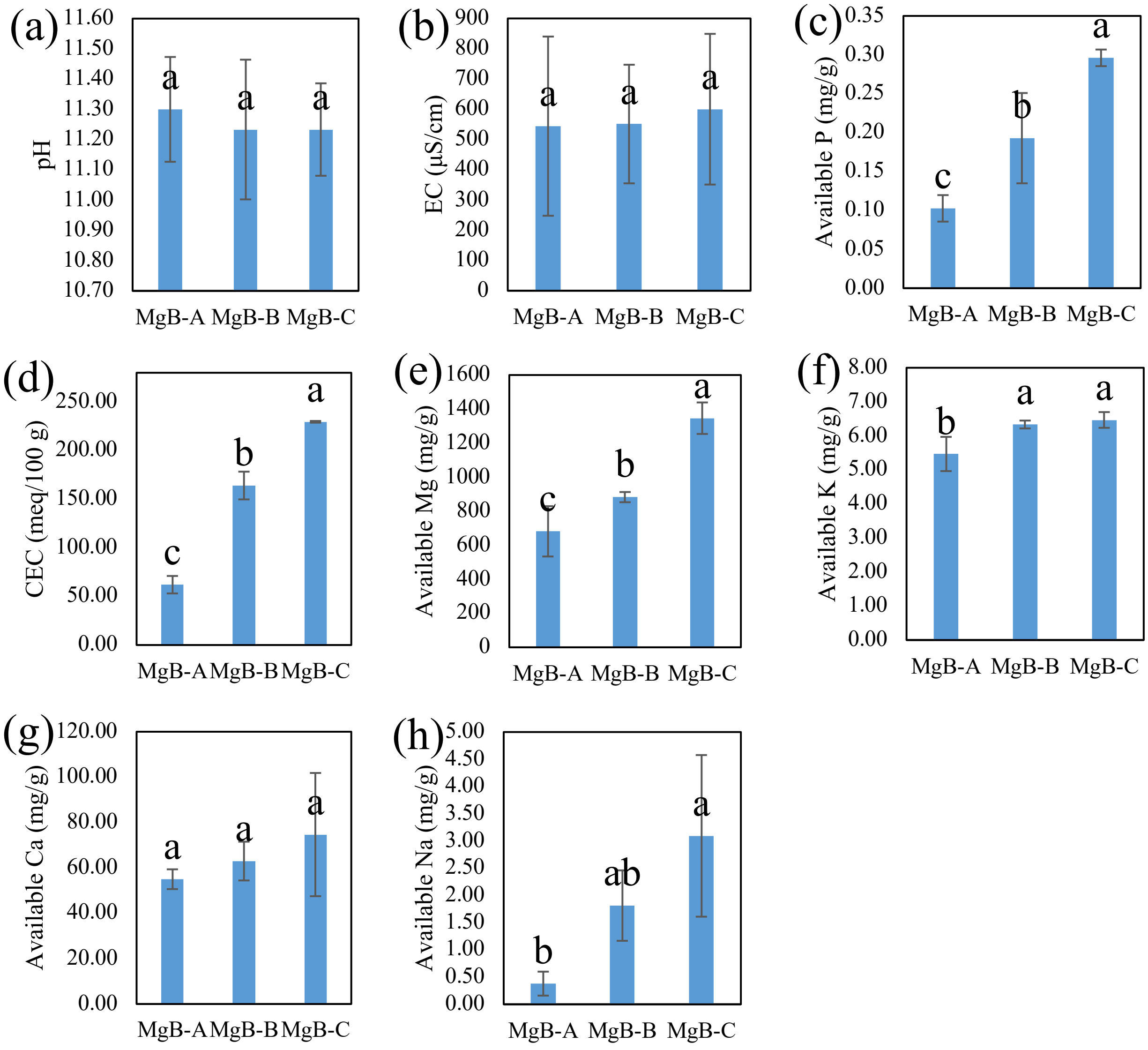

Figure. 62. Nutrient characteristics of biochar composite.

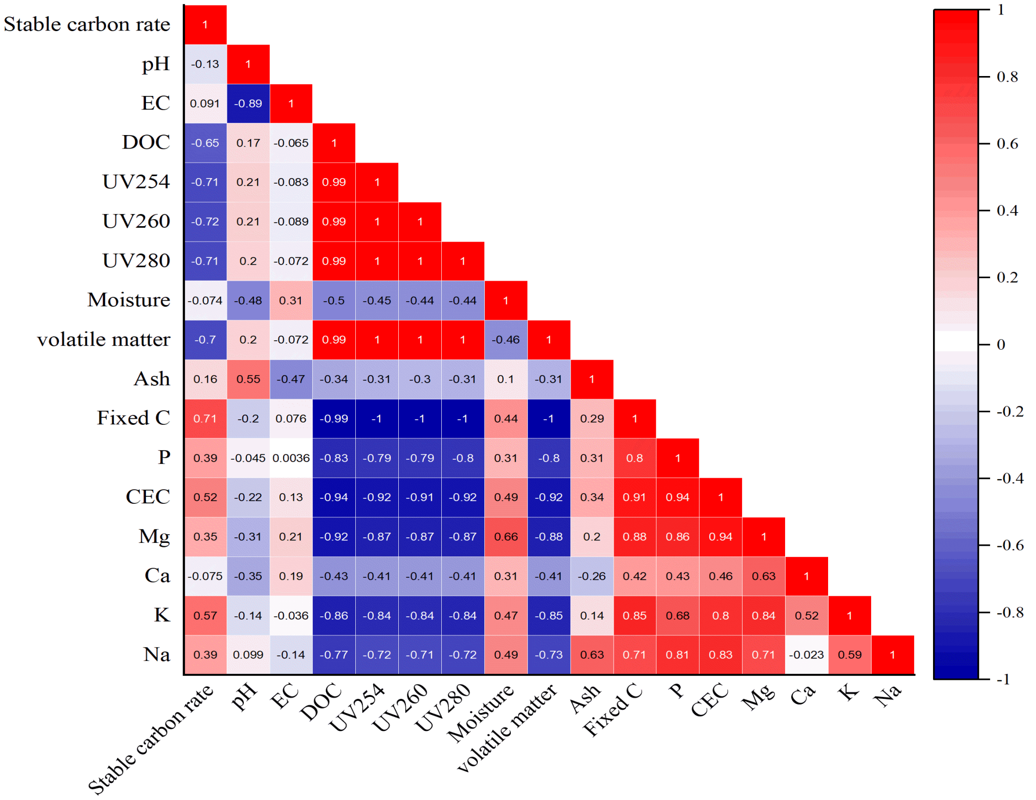

	Stable carbon rate	pH	EC	DOC	UV254	UV260	UV280	Moisture	volatile matter	Ash	Fixed C	P	CEC	Mg	Ca	K	Na
Stable carbon rate	1																
pH	-0.13	1															
EC	0.091	-0.89	1														
DOC	-0.65	0.17	-0.065	1													
UV254	-0.71	0.21	-0.083	0.99	1												
UV260	-0.72	0.21	-0.089	0.99	1	1											
UV280	-0.71	0.2	-0.072	0.99	1	1	1										
Moisture	-0.074	-0.48	0.31	-0.5	-0.45	-0.44	-0.44	1									
volatile matter	-0.7	0.2	-0.072	0.99	1	1	1	-0.46	1								
Ash	0.16	0.55	-0.47	-0.34	-0.31	-0.3	-0.31	0.1	-0.31	1							
Fixed C	0.71	-0.2	0.076	-0.99	-1	-1	-1	0.44	-1	0.29	1						
P	0.39	-0.045	0.0036	-0.83	-0.79	-0.79	-0.8	0.31	-0.8	0.31	0.8	1					
CEC	0.52	-0.22	0.13	-0.94	-0.92	-0.91	-0.92	0.49	-0.92	0.34	0.91	0.94	1				
Mg	0.35	-0.31	0.21	-0.92	-0.87	-0.87	-0.87	0.66	-0.88	0.2	0.88	0.86	0.94	1			
Ca	-0.075	-0.35	0.19	-0.43	-0.41	-0.41	-0.41	0.31	-0.41	-0.26	0.42	0.43	0.46	0.63	1		
K	0.57	-0.14	-0.036	-0.86	-0.84	-0.84	-0.84	0.47	-0.85	0.14	0.85	0.68	0.8	0.84	0.52	1	
Na	0.39	0.099	-0.14	-0.77	-0.72	-0.71	-0.72	0.49	-0.73	0.63	0.71	0.81	0.83	0.71	-0.023	0.59	1

Figure. 63. Pearson correlation of biochar composite.

3.3.4.7 Biochar available nutrients

Figure 62e-h display the levels of available nutrients (Mg, K, Ca, and Na) in biochar produced at different temperatures. The highest concentrations of available Mg, K, and Na were observed in MgB-C, whereas the highest level of available Ca was noted in MgB-B. These results align with the findings of (J. W. Gaskin et al., 2008; K. Wang et al., 2020) who reported increases in Mg and K levels with rising pyrolysis temperatures. Figure. 63 illustrates the Pearson correlation in biochar characteristics. The results showed a strongest positive relationship between UV254, UV260, UV260, UV280 and volatile matter (r = 1). Furthermore, between DOC and volatile matter (r = 0.99) and stable carbon rate and fixed C (r = 0.71). It can be suggest that stable carbon have correlation with proximate analysis.

3.3.4.8 Impacts of biochar on soil CO_2 emissions

Effect of MgO-biochar on carbon dioxide emission rate is presented in Figure. 64. CO_2 emission results were statistically significant at all the studied durations. The data shows that untreated sample (control) was the highest CO_2 concentration compared to treated sample. Soil CO2 release peaked at 7 days (sample A, 553 mg/L ± 29), 1 day (sample B, 492 mg/L ± 60, and C, 352 mg/L ± 60), and 6 days (sample C, 401 mg/L ± 32), then it decreased and increased during incubation period. The total average difference percentage were 11.70%, 39.84 %, and 26.52%, respectively, compared to control. It might be indicates that temperature conditions influences capability to hold or sequester CO_2 emission from soil.

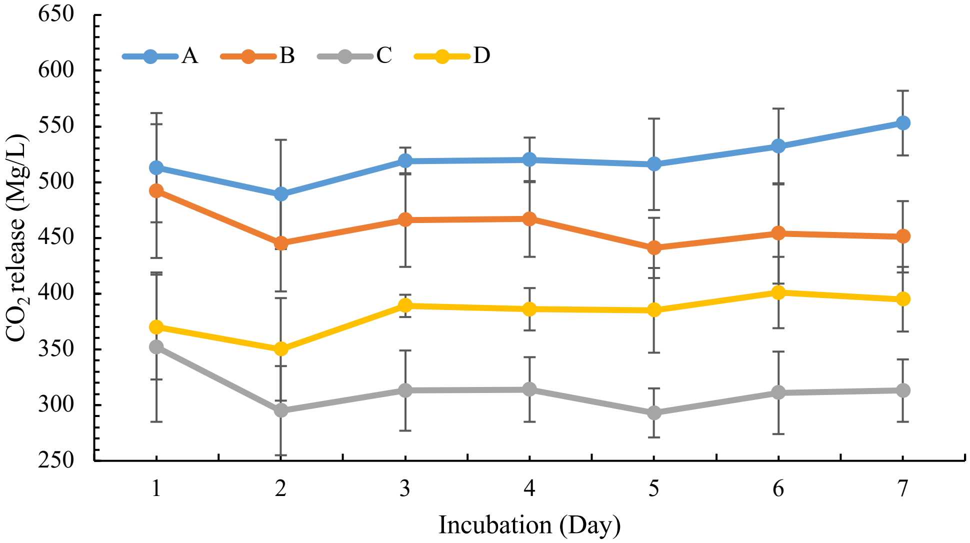

Figure. 64. Soil CO_2 emission during incubation. A; soil, B; soil + MgB-A, C; soil + MgB-B, D; soil + MgB-C.

3.3.4.9 Impacts of biochar amendments on glyphosate immobilization

Figure. 65 depicts the impact of treatment amendments on soil glyphosate levels such as pH, P, SOC, available $N\text{-}NH_4$ and $N\text{-}NO_3$. As shown in Figure. 65a, the concentration of available glyphosate in soil decreased markedly following the application of treated hydrogel beads ($P<0.05$). After 7-day incubation period, the glyphosate concentrations were reduced to 0.69 mg/g, 0.74 mg/g, and 0.58 mg/g for B, C, and D, respectively, from 1.18 mg/g (untreated soil). This corresponds to immobilization rates of 40.79% for B, 37.68% for C, and 50.42% for D. Moreover, Figure. 65b, the soil pH experienced a notable increased significantly post-treatment with biochar ($P<0.05$). Soil pH increased by 3.8, 3.9, and 3.93 units. This increased in pH may be due to release of exchangeable base cations into soil which increases the net basic cations in the soil. Additionally, soil EC showed a significant increase after applying hydrogel beads ($P<0.05$), as demonstrated in Figure. 65c. The EC rose by 56.20%, 56.88%, 57.54% for sample B, C, and D, respectively.

3.3.4.10 Effects of biochar amendments on soil nutrient availability

After 7 days of incubation, the level of available phosphorus (P) in the soil showed a reduction, however there is no significant results based on statistics (Figure. 65d). This reduction in available P may be attributed to the immobilization of P during the incubation period with MgO-Biochar. This is due to electrostatic attraction between negative charge of P ions and MgO in biochar surface. The SOC value showed a significant increase ($P<0.05$) with the addition of biochar amendments, as displayed in Figure. 65e. This suggests a correlation between the presence of SOC, biochar stable rate (Figure. 61a) and soil CO_2 release (Figure. 64), which contributes to the reduction of glyphosate levels in the soil. Furthermore, there was significant decreased on the levels of N-NH_4 ($P<0.05$) (Figure. 65f). This is might be due to that under alkaline conditions, the equilibrium between ammonium (NH_4) and ammonia (NH_3) shifts towards the formation of ammonia gas. Biochar, with its porous structure can enhance the volatilization of ammonia by providing more surface sites for NH_3 to escape into the atmosphere. This leads to a decrease in soil NH_4 concentrations. In contrast, the levels of N-NO_3 increased after treated biochar ($P<0.05$) (Figure. 65g). This is probably due to nitrification process accelerated conversion of NH_4 to NO_3.

The biochar treatment resulted in significantly higher levels of exchangeable Ca, Na, and Mg compared to the intact soil ($P<0.05$) (Figure. 66a-c).

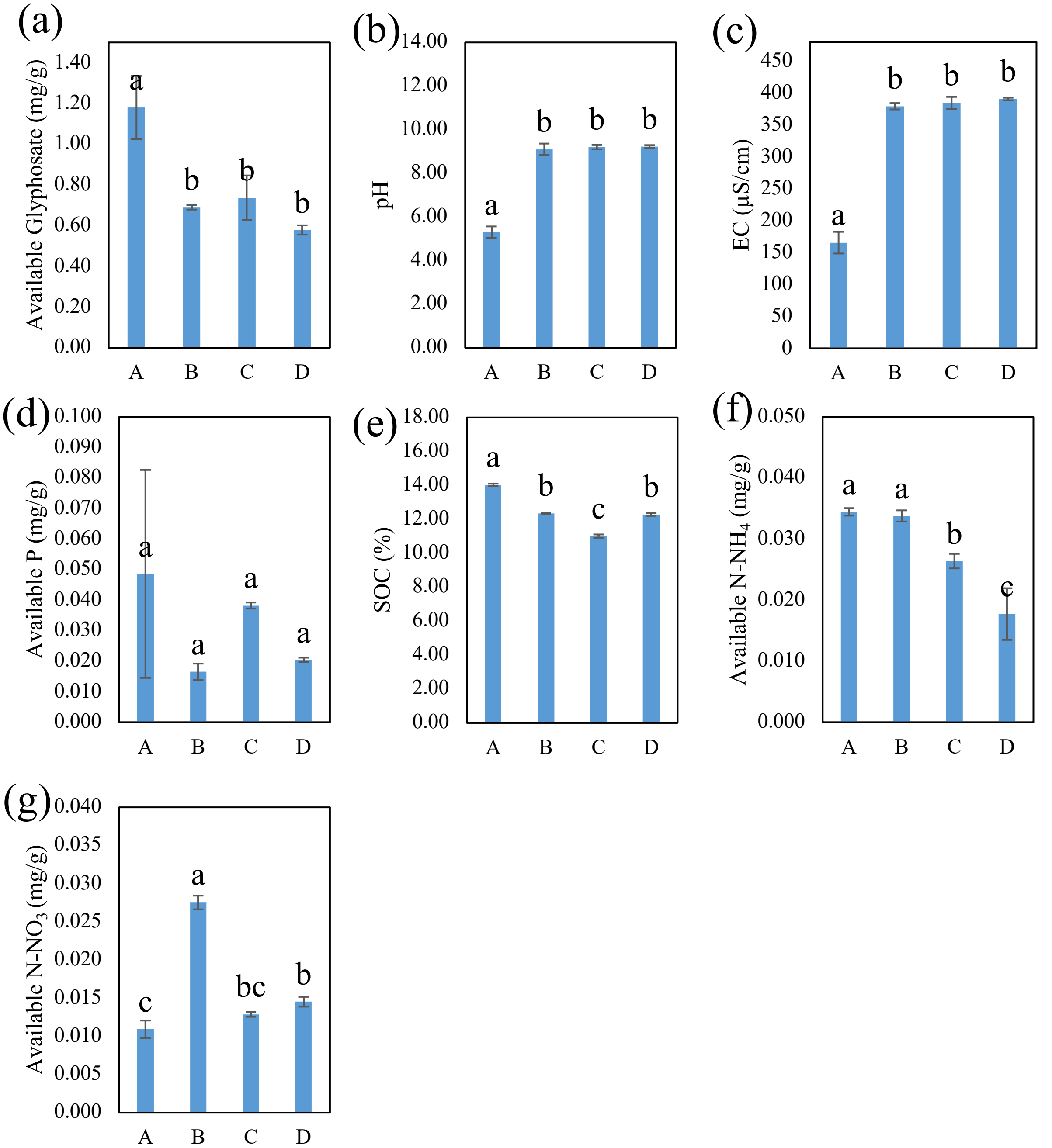

Figure. 65. Soil nutrient characteristics after treated biochar composite. A; soil, B; soil + MgB-A, C; soil + MgB-B, D; soil + MgB-C.

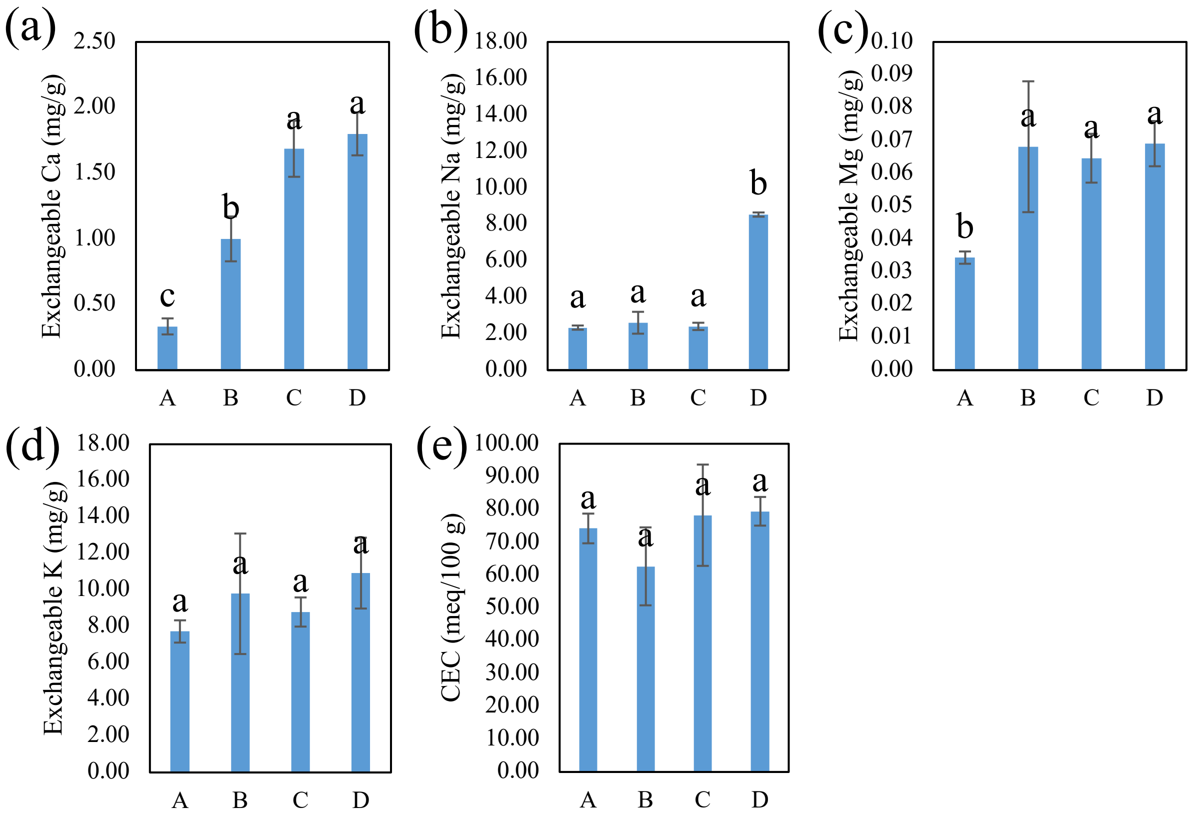

Figure. 66. Soil nutrient characteristics after treated biochar composite. A; soil, B; soil + MgB-A, C; soil + MgB-B, D; soil + MgB-C.

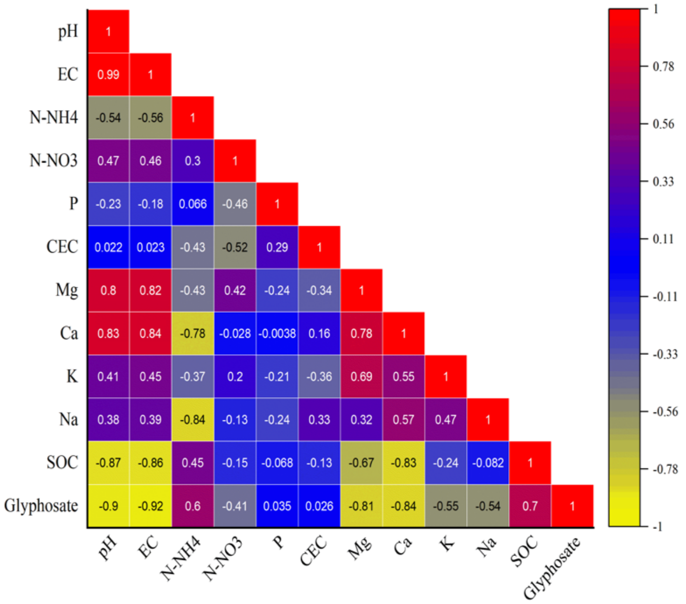

	pH	EC	N-NH4	N-NO3	P	CEC	Mg	Ca	K	Na	SOC	Glyphosate
pH	1											
EC	0.99	1										
N-NH4	-0.54	-0.56	1									
N-NO3	0.47	0.46	0.3	1								
P	-0.23	-0.18	0.066	-0.46	1							
CEC	0.022	0.023	-0.43	-0.52	0.29	1						
Mg	0.8	0.82	-0.43	0.42	-0.24	-0.34	1					
Ca	0.83	0.84	-0.78	-0.028	-0.0038	0.16	0.78	1				
K	0.41	0.45	-0.37	0.2	-0.21	-0.36	0.69	0.55	1			
Na	0.38	0.39	-0.84	-0.13	-0.24	0.33	0.32	0.57	0.47	1		
SOC	-0.87	-0.86	0.45	-0.15	-0.068	-0.13	-0.67	-0.83	-0.24	-0.082	1	
Glyphosate	-0.9	-0.92	0.6	-0.41	0.035	0.026	-0.81	-0.84	-0.55	-0.54	0.7	1

Figure. 67. Pearson correlation of soil nutrient characteristics after treated biochar composite.

While there is no significant effect for exchangeable K and CEC ($P<0.05$) (Figure. 66d-e). Figure. 67 illustrates the Pearson correlation in general soil parameters after incubation. The results showed a strongest negative relationship between pH and glyphosate ($r = -0.90$), pH and SOC ($r = -0.87$). Moreover, pH had a positive correlation with Mg ($r = 0.8$) and Ca ($r = 0.83$).

3.4 Conclusion

3.4.1 Effects of sodium alginate-poly (acrylic acid) cross-linked hydrogel beads on soil conditioner in the absence and presence of phosphate and carbonate ions

This study demonstrated the synthesis of hydrogel beads using sodium alginate (S-Alg) and poly (acrylic acid) (P-Acc) as the major components, with Ca^{2+} ions serving as an effective cross-linking agent. Hydrogel beads, both in the absence (S-Alg/P-Acc) and presence of PO_4^{3-} (S-Alg/P-Acc@PO_4^{3-}) and CO_3^{2-} (S-Alg/P-Acc@CO_3^{2-}) were examined in terms of swelling behavior, soil water loss (SWL), and soil properties. Hydrogel beads showed better water absorption properties and 30% suppression of SWL capabilities compared with the control (intact soil). There were no significant changes in the soil pH and C/N ratio after the application of hydrogel beads. Nevertheless, the N-NH_4^+ concentration increased while N-NO_3^- decreased. Hydrogel bead treatment may hinder the conversion of N-NH_4^+ to N-NO_3^- via nitrification in soils. In addition, there was a simultaneous improvement in the levels of available phosphorus (P), cation exchange capacity (CEC), soil organic carbon (SOC), exchangeable cations (Ca^{2+}, K^+, and Mg^{2+}), and immobilization of Fe by up to 89.86%. The presence of hydroxyl (-OH) and carboxyl (-COOH) groups is essential for improving soil characteristics and facilitating water retention.

3.4.2 Harnessing hydrogel beads for immobilization of arsenic

This study entailed the successful formulation of hydrogel bead composites using sodium alginate (SA), polyvinyl alcohol (PVA), poly (acrylic acid) (PAA), humic acid (HA), and phosphate (PO_4) ions, both with (SPPG) and without (SPP) the addition of glutaraldehyde. The primary goals of the research were to immobilize arsenic (As) and to improve soil properties. The soil incubation experiments were carried out over 50 days at room temperature, ranging from 20 to 25 °C. The findings indicated that including glutaraldehyde decreased the porosity by 29.08% and the degradation rate by 37.78% in 0.01 M HCl. While TGA analysis show that the presence of glutaraldehyde reduced the thermal stability of hydrogel bead composite. At the same time, it increases the levels of carboxyl (COOH) groups and enhances the swelling capacity, enabling the beads to absorb water up to 329% in alkaline solution. The rates at which As was immobilized were notable, with SPPG achieving 87.34% and SPP reaching 87.81%. The introduction of the hydrogel beads into the soil resulted in a marked reduction in pH, while there was a significant rise ($P<0.05$) in electrical conductivity (EC), available phosphorus (P), and soil organic carbon (SOC), cation exchange capacity (CEC) and exchangeable cations (Ca, K, and Na) contents. The application of hydrogel beads influences reduced soil bulk density and increase soil porosity. Pearson correlation analysis showed that pH plays an essential influence on soil characteristics in As contaminated. It could be attributed to this technique's effective removal of As value and improvement of soil health.

3.4.3 Evaluation of slow-release fertilizers derived from hydrogel beads: Sodium alginate-poly (acrylic acid) and humic acid-encapsulated struvite for soil salinity amelioration

Soil salinity exerts a negative impact on crop productivity due to excessive nutrient levels in the soil. To address this issue, the efficacy of slow-release mineral fertilizers struvite encapsulated in hydrogel beads was investigated. In this study, a two-step process was employed to synthesize the hydrogel beads. Firstly, struvite was synthesized by mixing magnesium, ammonium-nitrogen, and phosphate in equal proportions. Secondly, hydrogel beads were formed using sodium alginate-poly (acrylic acid) and humic acid. Subsequently, the struvite was combined with the hydrogel beads to create Sa@S (without humic acid) and Sa@SHa (with humic acid).

The findings revealed that the optimal conditions for struvite formation occurred at pH 9.0. The study on slow-release mineral fertilizers indicated a significant release of struvite compared to hydrogel beads encapsulated ($P<0.05$). Swelling experiments demonstrated that Sa@S exhibited higher water retention capacities compared to Sa@SHa. Additionally, experiments on soil water loss rate (SWL rate) confirmed the ability of hydrogel beads to retain water in the soil, reducing soil water loss by up to 33.33% compared to intact soil. Furthermore, the soil salinity incubation experiment reveals a significant reduction in soil EC and Na after treatment with the hydrogel bead encapsulation. However, there is no considerable variation in pH and SOC. Additionally, there was a significant increase ($P<0.05$) in the available NH_4-N, NO_3-N, P, CEC, and exchangeable Ca, Mg and K levels. These experiments suggest that the encapsulated struvite hydrogel beads efficiently reduce salts and improve soil properties.

3.4.4 Co-pyrolysis MgO-Biochar under Difference Temperature Derived from Coffee Husk for glyphosate immobilization in soil: Evaluation of Biochar Characteristics and Carbon Stability

To investigate the effects of MgO-containing additives on the evolution of carbon structure and the enhancement of biochar stability, coffee husk was selected as the biomass, and MgO was used as the magnesium-containing additive. A series of pyrolysis experiments were conducted in a muffle furnace at temperatures ranging from 350°C to 650°C. The influence of temperature on the biochar's chemical composition, porosity, surface area, organic functional groups, and chemical stability was examined. It was found that temperature increases led to a rise in S_{BET} (specific surface area) and V_{total} (total pore volume), but a decrease in D_{meso} (pore size). The stability of the biochar's carbon content showed an increase as the pyrolysis temperature was raised from 350 °C to 500 °C, with stable carbon content climbing from 55.76% to 89.69%. However, at 650 °C, the stable carbon content decreased to 72.92%. The fixed carbon content was observed to increase with higher pyrolysis temperatures. Additionally, the aromaticity of the biochar increased with temperature, and the nutrient characteristics of the biochar showed optimal results at higher temperatures. The rates at which glyphosate was immobilized were notable, with soil + biochar (350 °C) achieving 40.79%, soil + biochar (500 °C) of 37.68%, and soil + biochar (650 °C) of 50.42%. The introduction of the biochar into the soil resulted increased in pH, while there was a significant rise ($P<0.05$) in electrical conductivity (EC), and exchangeable cations (Mg, Ca, and Na) contents.

References:

Abdeen, Z. U., & Saeed, R. (2019). Soil Desalination via Poly(vinyl alcohol) Borate Hydrogel. *Theoretical Foundations of Chemical Engineering*, *53*(6), 1094–1098. https://doi.org/10.1134/S0040579519060010

Abdel-Fattah, M. K. (2012). Role of gypsum and compost in reclaiming saline-sodic soils. *IOSR Journal of Agriculture and Veterinary Science*, *1*(3), 30–38. https://doi.org/10.9790/2380-0133038

Ahammed, G. J., Li, X., Liu, A., & Chen, S. (2020). Brassinosteroids in Plant Tolerance to Abiotic Stress. *Journal of Plant Growth Regulation*, *39*(4), 1451–1464. https://doi.org/10.1007/s00344-020-10098-0

Ahmad, J., Al-Farraj, A. S., Ahmad, M., Al-Swadi, H. A., & Al-Wabel, M. I. (2024). Functionalized organo-mineral composites of biochar for the effectual immobilization of arsenic in contaminated soil. *Journal of Soils and Sediments*. https://doi.org/10.1007/s11368-024-03730-z

Almeida, D. M., Oliveira, M. M., & Saibo, N. J. M. (2017). Regulation of Na+ and K+ homeostasis in plants: towards improved salt stress tolerance in crop plants. *Genetics and Molecular Biology*, *40*(1 suppl 1), 326–345. https://doi.org/10.1590/1678-4685-gmb-2016-0106

Al-qudah, Y. H. F., Mahmoud, G. A., & Abdel Khalek, M. A. (2014). Radiation crosslinked poly (vinyl alcohol)/acrylic acid copolymer for removal of heavy metal ions from aqueous solutions. *Journal of Radiation Research and Applied Sciences*, *7*(2), 135–145. https://doi.org/10.1016/j.jrras.2013.12.008

Al-Tohamy, R., Ali, S. S., Li, F., Okasha, K. M., Mahmoud, Y. A. G., Elsamahy, T., Jiao, H., Fu, Y., & Sun, J. (2022). A critical review on the treatment of dye-containing wastewater: Ecotoxicological and health concerns of textile dyes and possible remediation approaches for environmental safety. In *Ecotoxicology and Environmental Safety* (Vol. 231). Academic Press. https://doi.org/10.1016/j.ecoenv.2021.113160

Al-Wabel, M. I., Al-Omran, A., El-Naggar, A. H., Nadeem, M., & Usman, A. R. A. (2013). Pyrolysis temperature induced changes in characteristics and chemical composition of biochar produced from conocarpus wastes. *Bioresource Technology*, *131*, 374–379. https://doi.org/10.1016/j.biortech.2012.12.165

Ameloot, N., Graber, E. R., Verheijen, F. G. A., & De Neve, S. (2013). Interactions between biochar stability and soil organisms: review and research needs. *European Journal of Soil Science*, *64*(4), 379–390. https://doi.org/10.1111/ejss.12064

Andrade Foronda, D., & Colinet, G. (2023). Prediction of Soil Salinity/Sodicity and Salt-Affected Soil Classes from Soluble Salt Ions Using Machine Learning Algorithms. *Soil Systems*, *7*(2), 47. https://doi.org/10.3390/soilsystems7020047

Ashby, S. P., Thomas, J. A., García-Cañadas, J., Min, G., Corps, J., Powell, A. V., Xu, H., Shen, W., & Chao, Y. (2014). Bridging silicon nanoparticles and thermoelectrics: phenylacetylene functionalization. *Faraday Discuss.*, *176*, 349–361. https://doi.org/10.1039/C4FD00109E

Ashraf, M., & Harris, P. J. C. (2004). Potential biochemical indicators of salinity tolerance in plants. *Plant Science*, *166*(1), 3–16. https://doi.org/10.1016/j.plantsci.2003.10.024

Azniza, N., Noor, M., Nizam, M. I., & Isa, M. (2015). Structural and Conduction Studies of Solid Biopolymer Electrolytes System Based on Carboxymethyl Cellulose. In *Article in American-Eurasian Journal of Sustainable Agriculture*. http://www.aensiweb.com/AEJSA

Bakshi, S., Banik, C., & Laird, D. A. (2020). Estimating the organic oxygen content of biochar. *Scientific Reports*, *10*(1), 13082. https://doi.org/10.1038/s41598-020-69798-y

Bantignies, J.-L., Carr, L., Dumas, P., Miller, L., & Williams, G. P. (1998). Applications of infrared microspectroscopy to geology, biology and cosmetics. *Synchrotron Radiation News*, *11*(4), 31–37. https://doi.org/10.1080/08940889808260939

Bibi, A., Rehman, S. U., Faiz, R., Akhtar, T., Nawaz, M., & Bibi, S. (2019). Effect of surfactants on swelling capacity and kinetics of alginate-chitosan/CNTs hydrogel. *Materials Research Express*, *6*(8). https://doi.org/10.1088/2053-1591/ab0697

Bogdan, A., O' Donnell, C., Robles Aguilar, A. A., Sigurnjak, I., Power, N., Michels, E., Harrington, J., & Meers, E. (2021). Impact of time and phosphorus application rate on phosphorus bioavailability and efficiency of secondary fertilizers recovered from municipal wastewater. *Chemosphere*, *282*, 131017. https://doi.org/10.1016/j.chemosphere.2021.131017

Cantrell, K. B., Hunt, P. G., Uchimiya, M., Novak, J. M., & Ro, K. S. (2012). Impact of pyrolysis temperature and manure source on physicochemical characteristics of biochar. *Bioresource Technology*, *107*, 419–428. https://doi.org/10.1016/j.biortech.2011.11.084

Cevheri, C. İ., Sakin, E., & Ramazanoglu, E. (2022). Effects of different fertilizers on some soil enzymes activity and chlorophyll contents of two cotton (*G. hirsutum* L.) varieties grown in a saline and non-saline soil. *Journal of Plant Nutrition*, *45*(1), 95–106. https://doi.org/10.1080/01904167.2021.1949467

Chelike, D. K., Alagumalai, A., Acharya, J., Kumar, P., Sarkar, K., Gurusamy Thangavelu, S. A., & Chandrasekhar, V. (2020). Functionalized iron oxide nanoparticles conjugate of multi-anchored Schiff's base inorganic heterocyclic pendant groups: Cytotoxicity studies. *Applied Surface Science*, *501*, 143963. https://doi.org/10.1016/j.apsusc.2019.143963

Chen, B., Zhu, Z., Guo, Y., Qiu, Y., & Zhao, J. (2013). Facile synthesis of mesoporous Ce–Fe bimetal oxide and its enhanced adsorption of arsenate from aqueous solutions. *Journal of Colloid and Interface Science*, *398*, 142–151. https://doi.org/10.1016/j.jcis.2013.02.004

Chen, H., Li, W., Wang, J., Xu, H., Liu, Y., Zhang, Z., Li, Y., & Zhang, Y. (2019). Adsorption of cadmium and lead ions by phosphoric acid-modified biochar generated from chicken feather: Selective adsorption and influence of dissolved organic matter. *Bioresource Technology*, *292*, 121948. https://doi.org/10.1016/j.biortech.2019.121948

Chen, Y., Gao, Y., Ng, C. W. W., & Guo, H. (2021). Bio-improved hydraulic properties of sand treated by soybean urease induced carbonate precipitation and its application Part 1: Water retention ability. *Transportation Geotechnics*, *27*, 100489. https://doi.org/10.1016/j.trgeo.2020.100489

Chinthakuntla, A., Venkateswara Rao, K., & Rao Kandregula, G. (2016). *MgO Nanoparticles Prepared By Microwave-Irradiation Technique and Its Seed Germination Application*. https://www.researchgate.net/publication/301658376

Costa, M. C. G., Freire, A. G., Lourenço, D. V., Sousa, R. R. de, Feitosa, J. P. de A., & Mota, J. C. A. (2022). Hydrogel composed of potassium acrylate, acrylamide, and mineral as soil conditioner under saline conditions. *Scientia Agricola*, *79*(4). https://doi.org/10.1590/1678-992x-2020-0235

Crombie, K., & Mašek, O. (2015). Pyrolysis biochar systems, balance between bioenergy and carbon sequestration. *GCB Bioenergy*, *7*(2), 349–361. https://doi.org/10.1111/gcbb.12137

Crombie, K., Mašek, O., Sohi, S. P., Brownsort, P., & Cross, A. (2013). The effect of pyrolysis conditions on biochar stability as determined by three methods. *GCB Bioenergy*, *5*(2), 122–131. https://doi.org/10.1111/gcbb.12030

Cross, A., & Sohi, S. P. (2013). A method for screening the relative long-term stability of biochar. *GCB Bioenergy*, *5*(2), 215–220. https://doi.org/10.1111/gcbb.12035

Das, D., Bhattacharjee, S., & Bhaladhare, S. (2023). Preparation of Cellulose Hydrogels and Hydrogel Nanocomposites Reinforced by Crystalline Cellulose Nanofibers (CNFs) as a Water Reservoir for Agriculture Use. *ACS Applied Polymer Materials*, *5*(4), 2895–2904. https://doi.org/10.1021/acsapm.3c00109

Di Martino, A., Khan, Y. A., Durpekova, S., Sedlarik, V., Elich, O., & Cechmankova, J. (2021). Ecofriendly renewable hydrogels based on whey protein and for slow release of fertilizers and soil conditioning. *Journal of Cleaner Production*, *285*. https://doi.org/10.1016/j.jclepro.2020.124848

Ding, W., Dong, X., Ime, I. M., Gao, B., & Ma, L. Q. (2014). Pyrolytic temperatures impact lead sorption mechanisms by bagasse biochars. *Chemosphere*, *105*, 68–74. https://doi.org/10.1016/j.chemosphere.2013.12.042

Ding, X., Jiang, Y., Zhao, H., Guo, D., He, L., Liu, F., Zhou, Q., Nandwani, D., Hui, D., & Yu, J. (2018). Electrical conductivity of nutrient solution influenced photosynthesis, quality, and antioxidant enzyme activity of pakchoi (Brassica campestris L. ssp. Chinensis) in a hydroponic system. *PLOS ONE*, *13*(8), e0202090. https://doi.org/10.1371/journal.pone.0202090

Ding, Y., Zhang, G., Wu, H., Hai, B., Wang, L., & Qian, Y. (2001). Nanoscale Magnesium Hydroxide and Magnesium Oxide Powders: Control over Size, Shape, and Structure via Hydrothermal Synthesis. *Chemistry of Materials*, *13*(2), 435–440. https://doi.org/10.1021/cm000607e

Dittman, J. A., Shanley, J. B., Driscoll, C. T., Aiken, G. R., Chalmers, A. T., & Towse, J. E. (2009). Ultraviolet absorbance as a proxy for total dissolved mercury in streams. *Environmental Pollution*, *157*(6), 1953–1956. https://doi.org/10.1016/j.envpol.2009.01.031

Dixon, M., Simonne, E., Obreza, T., & Liu, G. (2020). Crop Response to Low Phosphorus Bioavailability with a Focus on Tomato. *Agronomy*, *10*(5), 617. https://doi.org/10.3390/agronomy10050617

Elrashidi, M. A., West, L. T., Seybold, C. A., Benham, E. C., Schoeneberger, P. J., & Ferguson, R. (2010). Effects of Gypsum Addition on Solubility of Nutrients in Soil Amended With Peat. *Soil Science*, *175*(4), 162–172. https://doi.org/10.1097/SS.0b013e3181dd51d0

Fageria, N. K., Moreira, A., Moraes, L. A. C., & Moraes, M. F. (2014). Influence of Lime and Gypsum on Yield and Yield Components of Soybean and Changes in Soil Chemical Properties. *Communications in Soil Science and Plant Analysis*, *45*(3), 271–283. https://doi.org/10.1080/00103624.2013.861906

Fajardo, A. R., Lopes, L. C., Pereira, A. G. B., Rubira, A. F., & Muniz, E. C. (2012). Polyelectrolyte complexes based on pectin–NH2 and chondroitin sulfate. *Carbohydrate Polymers*, *87*(3), 1950–1955. https://doi.org/10.1016/j.carbpol.2011.09.096

Gharaibeh, M. A., Albalasmeh, A. A., Pratt, C., & El Hanandeh, A. (2021). Estimation of exchangeable sodium percentage from sodium adsorption ratio of salt-affected soils using traditional and dilution extracts, saturation percentage, electrical conductivity, and generalized regression neural networks. *CATENA*, *205*, 105466. https://doi.org/10.1016/j.catena.2021.105466

González-Morales, C., Fernández, B., Molina, F. J., Naranjo-Fernández, D., Matamoros-Veloza, A., & Camargo-Valero, M. A. (2021). Influence of pH and Temperature on Struvite Purity and Recovery from Anaerobic Digestate. *Sustainability*, *13*(19), 10730. https://doi.org/10.3390/su131910730

Grzyb, A., Wolna-Maruwka, A., & Niewiadomska, A. (2020). Environmental Factors Affecting the Mineralization of Crop Residues. *Agronomy*, *10*(12), 1951. https://doi.org/10.3390/agronomy10121951

Guo, J., Shi, W., Wen, L., Shi, X., & Li, J. (2020). Effects of a super-absorbent polymer derived from poly-γ-glutamic acid on water infiltration, field water capacity, soil evaporation, and soil water-stable aggregates. *Archives of Agronomy and Soil Science*, *66*(12), 1627–1638. https://doi.org/10.1080/03650340.2019.1686137

Gusiatin, Z. M., Kulikowska, D., & Klik, B. (2020). New-Generation Washing Agents in Remediation of Metal-Polluted Soils and Methods for Washing Effluent Treatment: A Review. *International Journal of Environmental Research and Public Health*, *17*(17), 6220. https://doi.org/10.3390/ijerph17176220

Hachiya, T., Watanabe, C. K., Fujimoto, M., Ishikawa, T., Takahara, K., Kawai-Yamada, M., Uchimiya, H., Uesono, Y., Terashima, I., & Noguchi, K. (2012). Nitrate Addition Alleviates Ammonium Toxicity Without Lessening Ammonium Accumulation, Organic Acid Depletion and Inorganic Cation Depletion in Arabidopsis thaliana Shoots. *Plant and Cell Physiology*, *53*(3), 577–591. https://doi.org/10.1093/pcp/pcs012

Han, F., An, S., Liu, L., Ma, L., Wang, Y., & Yang, L. (2023). Simultaneous enhancement of soil properties along with water-holding and restriction of Pb–Cd mobility in a soil-plant system by the addition of a phosphorus-modified biochar to the soil. *Journal of Environmental Management*, *345*, 118827. https://doi.org/10.1016/j.jenvman.2023.118827

Hassan, N., Abdullah, R., Khadiran, T., Elham, P., & Vejan, P. (2023). Biochar derived from oil palm trunk as a potential precursor in the production of high-performance activated carbon. *Biomass Conversion and Biorefinery*, *13*(17), 15687–15703. https://doi.org/10.1007/s13399-021-01797-z

He, C., He, X., Li, J., Luo, Y., Li, J., Pei, Y., & Jiang, J. (2021). The spectral characteristics of biochar-derived dissolved organic matter at different pyrolysis temperatures. *Journal of Environmental Chemical Engineering*, *9*(5), 106075. https://doi.org/10.1016/j.jece.2021.106075

Hidayat, E., Afriliana, A., Gusmini, G., Taizo, M., & Harada, H. (2020). Evaluate of Coffee Husk Compost. *International Journal on Food, Agriculture and Natural Resources*, *1*(1), 37–43. https://doi.org/10.46676/ij-fanres.v1i1.8

Hidayat, E., & Harada, H. (2022). Simultaneously Recovery of Phosphorus and Potassium Using Bubble Column Reactor as Struvite-K and Implementation on Crop Growth. In *Crystallization and Applications*. IntechOpen. https://doi.org/10.5772/intechopen.100103

Hidayat, E., Mohamad Sarbani, N. M. B., Yonemura, S., Mitoma, Y., & Harada, H. (2023). Application of Box–Behnken Design to Optimize Phosphate Adsorption Conditions from Water onto Novel Adsorbent CS-ZL/ZrO/Fe3O4: Characterization, Equilibrium, Isotherm, Kinetic, and Desorption Studies. *International Journal of Molecular Sciences*, *24*(11). https://doi.org/10.3390/ijms24119754

Hidayat, E., Sarbani, N. M. M., Lahiri, S. K., Samitsu, S., Yonemura, S., Mitoma, Y., & Harada, H. (2024). Effects of sodium alginate-poly(acrylic acid) cross-linked hydrogel beads on soil conditioner in the absence and presence of phosphate and carbonate ions. *Case Studies in Chemical and Environmental Engineering*, *9*, 100642. https://doi.org/10.1016/j.cscee.2024.100642

Hien, T. T. T., Tsubota, T., Taniguchi, T., & Shinogi, Y. (2021). Enhancing soil water holding capacity and provision of a potassium source via optimization of the pyrolysis of bamboo biochar. *Biochar*, *3*(1), 51–61. https://doi.org/10.1007/s42773-020-00071-1

Hmid, A., Mondelli, D., Fiore, S., Fanizzi, F. P., Al Chami, Z., & Dumontet, S. (2014). Production and characterization of biochar from three-phase olive mill waste through slow pyrolysis. *Biomass and Bioenergy*, *71*, 330–339. https://doi.org/10.1016/j.biombioe.2014.09.024

Hua, S., Ma, H., Li, X., Yang, H., & Wang, A. (2010). pH-sensitive sodium alginate/poly(vinyl alcohol) hydrogel beads prepared by combined Ca2+ crosslinking and freeze-thawing cycles for controlled release of diclofenac sodium. *International Journal of Biological Macromolecules*, *46*(5), 517–523. https://doi.org/10.1016/j.ijbiomac.2010.03.004

Huang, S., Chen, M., Lu, H., Eitssayeam, S., Min, Y., & Shi, P. (2024). Effect of pyrolysis temperature on the binding characteristics of DOM derived from livestock manure biochar with Cu(II). *Environmental Science and Pollution Research*, *31*(16), 24250–24262. https://doi.org/10.1007/s11356-024-32646-x

Huang, Y., Tian, Y., Xie, L., Liu, Y., Dai, B., Guo, X., & Yang, Y. (2020). The application of two-dimensional correlation spectroscopy for the binding properties of heavy metals onto digestate-derived DOM from anaerobic digestion of chicken manure. *Ecotoxicology and Environmental Safety*, *204*, 111129. https://doi.org/10.1016/j.ecoenv.2020.111129

Iatrou, M., Papadopoulos, A., Papadopoulos, F., Dichala, O., Psoma, P., & Bountla, A. (2014). Determination of Soil Available Phosphorus using the Olsen and Mehlich 3 Methods for Greek Soils Having Variable Amounts of Calcium Carbonate. *Communications in Soil Science and Plant Analysis*, *45*(16), 2207–2214. https://doi.org/10.1080/00103624.2014.911304

J. W. Gaskin, C. Steiner, K. Harris, K. C. Das, & B. Bibens. (2008). Effect of Low-Temperature Pyrolysis Conditions on Biochar for Agricultural Use. *Transactions of the ASABE*, *51*(6), 2061–2069. https://doi.org/10.13031/2013.25409

Jamir, E., Kangabam, R. Das, Borah, K., Tamuly, A., Deka Boruah, H. P., & Silla, Y. (2019). *Role of Soil Microbiome and Enzyme Activities in Plant Growth Nutrition and Ecological Restoration of Soil Health* (pp. 99–132). https://doi.org/10.1007/978-981-13-9117-0_5

Jiao, Y., Su, T., Chen, Y., Long, M., Luo, X., Xie, X., & Qin, Z. (2023). Enhanced Water Absorbency and Water Retention Rate for Superabsorbent Polymer via Porous Calcium Carbonate Crosslinking. *Nanomaterials*, *13*(18), 2575. https://doi.org/10.3390/nano13182575

Kasantikul, B., Auttaranakon, R., & Kongkeaw, A. (2020). Bamboo scraps and hardwood chips biochar derived from a cone-truncated open fire kiln for use as a nutrition medium for agricultural purpose. *E3S Web of Conferences*, *187*, 03003. https://doi.org/10.1051/e3sconf/202018703003

Kees de Kruif, C. G., Anema, S. G., Zhu, C., Havea, P., & Coker, C. (2015). Water holding capacity and swelling of casein hydrogels. *Food Hydrocolloids*, *44*, 372–379. https://doi.org/10.1016/j.foodhyd.2014.10.007

Krivoshein, P. K., Volkov, D. S., Rogova, O. B., & Proskurnin, M. A. (2020). FTIR photoacoustic spectroscopy for identification and assessment of soil components: Chernozems and their size fractions. *Photoacoustics*, *18*, 100162. https://doi.org/10.1016/j.pacs.2020.100162

Kronzucker, H. J., Coskun, D., Schulze, L. M., Wong, J. R., & Britto, D. T. (2013). Sodium as nutrient and toxicant. *Plant and Soil*, *369*(1–2), 1–23. https://doi.org/10.1007/s11104-013-1801-2

Kumar, A. S. K., & Jiang, S.-J. (2017). Synthesis of magnetically separable and recyclable magnetic nanoparticles decorated with β-cyclodextrin functionalized graphene oxide an excellent adsorption of As(V)/(III). *Journal of Molecular Liquids*, *237*, 387–401. https://doi.org/10.1016/j.molliq.2017.04.093

Lee, W.-F., & Lin, G.-H. (2000). *Superabsorbent Polymeric Materials VIII: Swelling Behavior of Crosslinked Poly[Sodium Acrylate-co-Trimethyl Methacryloyloxyethyl Ammonium Iodide] in Aqueous Salt Solutions*.

Leogrande, R., & Vitti, C. (2019). Use of organic amendments to reclaim saline and sodic soils: a review. *Arid Land Research and Management*, *33*(1), 1–21. https://doi.org/10.1080/15324982.2018.1498038

Li, Z., & Zhang, M. (2023). Progress in the Preparation of Stimulus-Responsive Cellulose Hydrogels and Their Application in Slow-Release Fertilizers. *Polymers*, *15*(17), 3643. https://doi.org/10.3390/polym15173643

Liang, H., Wang, W., Liu, H., Deng, X., Zhang, D., Zou, Y., & Ruan, X. (2023). Porous MgO-modified biochar adsorbents fabricated by the activation of Mg(NO3)2 for phosphate removal: Synergistic enhancement of porosity and active sites. *Chemosphere*, *324*, 138320. https://doi.org/10.1016/j.chemosphere.2023.138320

Liang, J., Li, Y., Si, B., Wang, Y., Chen, X., Wang, X., Chen, H., Wang, H., Zhang, F., Bai, Y., & Biswas, A. (2021). Optimizing biochar application to improve soil physical and hydraulic properties in saline-alkali soils. *Science of The Total Environment*, *771*, 144802. https://doi.org/10.1016/j.scitotenv.2020.144802

Liang, X. Q., Chen, Y. X., Li, H., Tian, G. M., Ni, W. Z., He, M. M., & Zhang, Z. J. (2007). Modeling transport and fate of nitrogen from urea applied to a near-trench paddy field. *Environmental Pollution*, *150*(3), 313–320. https://doi.org/10.1016/j.envpol.2007.02.003

Lita, A. L., Hidayat, E., Mohamad Sarbani, N. M., Harada, H., Yonemura, S., Mitoma, Y., Herviyanti, & Gusmini. (2023). Glyphosate Removal from Water Using Biochar Based Coffee Husk Loaded Fe3O4. *Water*, *15*(16), 2945. https://doi.org/10.3390/w15162945

Liu, C.-H., Chu, W., Li, H., Boyd, S. A., Teppen, B. J., Mao, J., Lehmann, J., & Zhang, W. (2019). Quantification and characterization of dissolved organic carbon from biochars. *Geoderma*, *335*, 161–169. https://doi.org/10.1016/j.geoderma.2018.08.019

Liu, H., Zhang, J., Bao, N., Cheng, C., Ren, L., & Zhang, C. (2012). Textural properties and surface chemistry of lotus stalk-derived activated carbons prepared using different phosphorus oxyacids: Adsorption of trimethoprim. *Journal of Hazardous Materials*, *235–236*, 367–375. https://doi.org/10.1016/j.jhazmat.2012.08.015

Liu, J., Guo, D., Zhou, Y., Wu, Z., Li, W., Zhao, F., & Zheng, X. (2011). Identification of ancient textiles from Yingpan, Xinjiang, by multiple analytical techniques. *Journal of Archaeological Science*, *38*(7), 1763–1770. https://doi.org/10.1016/j.jas.2011.03.017

Lohmousavi, S. M., Abad, H. H. S., Noormohammadi, G., & Delkhosh, B. (2020). Synthesis and characterization of a novel controlled release nitrogen-phosphorus fertilizer hybrid nanocomposite based on banana peel cellulose and layered double hydroxides nanosheets. *Arabian Journal of Chemistry*, *13*(9), 6977–6985. https://doi.org/10.1016/j.arabjc.2020.06.042

Mahimairaja, S., Bolan, N. S., Adriano, D. C., & Robinson, B. (2005). *Arsenic Contamination and its Risk Management in Complex Environmental Settings* (pp. 1–82). https://doi.org/10.1016/S0065-2113(05)86001-8

Malcolm, B. J., Cameron, K. C., Curtin, D., Di, H. J., Beare, M. H., Johnstone, P. R., & Edwards, G. R. (2019). Organic matter amendments to soil can reduce nitrate leaching losses from livestock urine under simulated fodder beet grazing. *Agriculture, Ecosystems & Environment*, *272*, 10–18. https://doi.org/10.1016/j.agee.2018.11.003

Mašek, O., Buss, W., Brownsort, P., Rovere, M., Tagliaferro, A., Zhao, L., Cao, X., & Xu, G. (2019). Potassium doping increases biochar carbon sequestration potential by 45%, facilitating decoupling of carbon sequestration from soil improvement. *Scientific Reports*, *9*(1), 5514. https://doi.org/10.1038/s41598-019-41953-0

Mecozzi, M., Pietroletti, M., Scarpiniti, M., Acquistucci, R., & Conti, M. E. (2012). Monitoring of marine mucilage formation in Italian seas investigated by infrared spectroscopy and independent component analysis. *Environmental Monitoring and Assessment*, *184*(10), 6025–6036. https://doi.org/10.1007/s10661-011-2400-4

Metternicht, G. I., & Zinck, J. A. (2003). Remote sensing of soil salinity: potentials and constraints. *Remote Sensing of Environment*, *85*(1), 1–20. https://doi.org/10.1016/S0034-4257(02)00188-8

Min, X., Li, Y., Ke, Y., Shi, M., Chai, L., & Xue, K. (2017). Fe-FeS2 adsorbent prepared with iron powder and pyrite by facile ball milling and its application for arsenic removal. *Water Science and Technology*, *76*(1), 192–200. https://doi.org/10.2166/wst.2017.204

Moreira, A., Sfredo, G. J., Moraes, L. A. C., & Fageria, N. K. (2015). Lime and Cattle Manure in Soil Fertility and Soybean Grain Yield Cultivated in Tropical Soil. *Communications in Soil Science and Plant Analysis*, *46*(9), 1157–1169. https://doi.org/10.1080/00103624.2015.1033542

Munns, R., Passioura, J. B., Colmer, T. D., & Byrt, C. S. (2020). Osmotic adjustment and energy limitations to plant growth in saline soil. *New Phytologist*, *225*(3), 1091–1096. https://doi.org/10.1111/nph.15862

Negacz, K., Malek, Ž., de Vos, A., & Vellinga, P. (2022). Saline soils worldwide: Identifying the most promising areas for saline agriculture. *Journal of Arid Environments*, *203*. https://doi.org/10.1016/j.jaridenv.2022.104775

Neset, T. S. S., & Cordell, D. (2012). Global phosphorus scarcity: Identifying synergies for a sustainable future. *Journal of the Science of Food and Agriculture*, *92*(1), 2–6. https://doi.org/10.1002/jsfa.4650

Nguyen, B. T., Dinh, G. D., Dong, H. P., & Le, L. B. (2022). Sodium adsorption isotherm and characterization of biochars produced from various agricultural biomass wastes. *Journal of Cleaner Production*, *346*, 131250. https://doi.org/10.1016/j.jclepro.2022.131250

Noda, I., & Ozaki, Y. (2005). *Two-Dimensional Correlation Spectroscopy: Applications in Vibrational and Optical Spectroscopy*. John Wiley & Sons.

Park, S. H., Jang, J. H., Wistara, N. J., Febrianto, F., & Lee, M. (2019). Fuel properties of Indonesian bamboo carbonized at different temperatures. *BioResources*, *14*(2), 4224–4235. https://doi.org/10.15376/biores.14.2.4224-4235

Qadir, A., Khan, S. A., Ahmad, R., Masood, S., Irshad, M., Kaleem, F., Kumar, S., & Shahzad, M. (2017). Exogenous Ca 2 SiO 4 enrichment reduces the leaf apoplastic Na + and increases the growth of okra (Abelmoschus esculentus L.) under salt stress. *Scientia Horticulturae*, *214*, 1–8. https://doi.org/10.1016/j.scienta.2016.11.008

Qiao, D., Liu, H., Yu, L., Bao, X., Simon, G. P., Petinakis, E., & Chen, L. (2016). Preparation and characterization of slow-release fertilizer encapsulated by starch-based superabsorbent polymer. *Carbohydrate Polymers*, *147*, 146–154. https://doi.org/10.1016/j.carbpol.2016.04.010

Rabat, N. E., Hashim, S., & Majid, R. A. (2016). Effect of Different Monomers on Water Retention Properties of Slow Release Fertilizer Hydrogel. *Procedia Engineering*, *148*, 201–207. https://doi.org/10.1016/j.proeng.2016.06.573

Rashid, M. I., Mujawar, L. H., Shahzad, T., Almeelbi, T., Ismail, I. M. I., & Oves, M. (2016). Bacteria and fungi can contribute to nutrients bioavailability and aggregate formation in degraded soils. *Microbiological Research*, *183*, 26–41. https://doi.org/10.1016/j.micres.2015.11.007

Razzaghi, F., Arthur, E., & Moosavi, A. A. (2021). Evaluating models to estimate cation exchange capacity of calcareous soils. *Geoderma*, *400*, 115221. https://doi.org/10.1016/j.geoderma.2021.115221

Rech, I., Withers, P., Jones, D., & Pavinato, P. (2018). Solubility, Diffusion and Crop Uptake of Phosphorus in Three Different Struvites. *Sustainability*, *11*(1), 134. https://doi.org/10.3390/su11010134

Ren, N., Tang, Y., & Li, M. (2018). Mineral additive enhanced carbon retention and stabilization in sewage sludge-derived biochar. *Process Safety and Environmental Protection*, *115*, 70–78. https://doi.org/10.1016/j.psep.2017.11.006

Sadaka, S., Sharara, M., Ashworth, A., Keyser, P., Allen, F., & Wright, A. (2014). Characterization of Biochar from Switchgrass Carbonization. *Energies*, *7*(2), 548–567. https://doi.org/10.3390/en7020548

Shahid, S. A., Zaman, M., & Heng, L. (2018). Introduction to Soil Salinity, Sodicity and Diagnostics Techniques. In *Guideline for Salinity Assessment, Mitigation and Adaptation Using Nuclear and Related Techniques* (pp. 1–42). Springer International Publishing. https://doi.org/10.1007/978-3-319-96190-3_1

Shankar, S., Shanker, U., & Shikha. (2014). Arsenic Contamination of Groundwater: A Review of Sources, Prevalence, Health Risks, and Strategies for Mitigation. *The Scientific World Journal*, *2014*, 1–18. https://doi.org/10.1155/2014/304524

Shirokova, Y., Forkutsa, I., & Sharafutdinova, N. (2000). Use of Electrical Conductivity Instead of Soluble Salts for Soil Salinity Monitoring in Central Asia. Irrigation and Drainage Systems. *Irrigation and Drainage Systems*, *14*(3), 199–206. https://doi.org/10.1023/A:1026560204665

Shrivastava, P., & Kumar, R. (2015). Soil salinity: A serious environmental issue and plant growth promoting bacteria as one of the tools for its alleviation. *Saudi Journal of Biological Sciences*, *22*(2), 123–131. https://doi.org/10.1016/j.sjbs.2014.12.001

Sornkamnerd, S., Okajima, M. K., & Kaneko, T. (2017). Tough and Porous Hydrogels Prepared by Simple Lyophilization of LC Gels. *ACS Omega*, *2*(8), 5304–5314. https://doi.org/10.1021/acsomega.7b00602

Taleei, M. M., Karbalaei Ghomi, N., & Jozi, S. A. (2019). Arsenic Removal of Contaminated Soils by Phytoremediation of Vetiver Grass, Chara Algae and Water Hyacinth. *Bulletin of Environmental Contamination and Toxicology*, *102*(1), 134–139. https://doi.org/10.1007/s00128-018-2495-1

Tanehgonbadi, M., & Qaderi, F. (2023). Investigation of the effect of initial composition of soil on the efficiency of desalination by polyvinyl alcohol borate hydrogel. *Environmental Earth Sciences*, *82*(13), 340. https://doi.org/10.1007/s12665-023-11009-8

Tchounwou, P. B., Centeno, J. A., & Patlolla, A. K. (2004). Arsenic toxicity, mutagenesis, and carcinogenesis – a health risk assessment and management approach. *Molecular and*

Cellular Biochemistry, *255*(1/2), 47–55. https://doi.org/10.1023/B:MCBI.0000007260.32981.b9

Tefera, B. B., Bayabil, H. K., Tong, Z., Teshome, F. T., Wenbo, P., Li, Y. C., Hailegnaw, N. S., & Gao, B. (2022a). Using liquefied biomass hydrogel to mitigate salinity in salt-affected soils. *Chemosphere*, *309*, 136480. https://doi.org/10.1016/j.chemosphere.2022.136480

Tefera, B. B., Bayabil, H. K., Tong, Z., Teshome, F. T., Wenbo, P., Li, Y. C., Hailegnaw, N. S., & Gao, B. (2022b). Using liquefied biomass hydrogel to mitigate salinity in salt-affected soils. *Chemosphere*, *309*, 136480. https://doi.org/10.1016/j.chemosphere.2022.136480

Tomadoni, B., Salcedo, M. F., Mansilla, A. Y., Casalongué, C. A., & Alvarez, V. A. (2020). Macroporous alginate-based hydrogels to control soil substrate moisture: Effect on lettuce plants under drought stress. *European Polymer Journal*, *137*. https://doi.org/10.1016/j.eurpolymj.2020.109953

Tulain, U. R., Ahmad, M., Rashid, A., Malik, M. Z., & Iqbal, F. M. (2018). Fabrication of pH-Responsive Hydrogel and Its In Vitro and In Vivo Evaluation. *Advances in Polymer Technology*, *37*(1), 290–304. https://doi.org/10.1002/adv.21668

Valle, S. F., Giroto, A. S., Dombinov, V., Robles-Aguilar, A. A., Jablonowski, N. D., & Ribeiro, C. (2022). Struvite-based composites for slow-release fertilization: a case study in sand. *Scientific Reports*, *12*(1). https://doi.org/10.1038/s41598-022-18214-8

van Zwieten, L., Kimber, S., Morris, S., Chan, K. Y., Downie, A., Rust, J., Joseph, S., & Cowie, A. (2010). Effects of biochar from slow pyrolysis of papermill waste on agronomic performance and soil fertility. *Plant and Soil*, *327*(1), 235–246. https://doi.org/10.1007/s11104-009-0050-x

Vundavalli, R., Vundavalli, S., Nakka, M., & Rao, D. S. (2015). Biodegradable Nano-Hydrogels in Agricultural Farming - Alternative Source For Water Resources. *Procedia Materials Science*, *10*, 548–554. https://doi.org/10.1016/j.mspro.2015.06.005

Wang, K., Peng, N., Lu, G., & Dang, Z. (2020). Effects of Pyrolysis Temperature and Holding Time on Physicochemical Properties of Swine-Manure-Derived Biochar. *Waste and Biomass Valorization*, *11*(2), 613–624. https://doi.org/10.1007/s12649-018-0435-2

WANG, L., WU, F., ZHANG, R., LI, W., & LIAO, H. (2009). Characterization of dissolved organic matter fractions from Lake Hongfeng, Southwestern China Plateau. *Journal of Environmental Sciences*, *21*(5), 581–588. https://doi.org/10.1016/S1001-0742(08)62311-6

Wang, L., Ye, C., Gao, B., Wang, X., Li, Y., Ding, K., Li, H., Ren, K., Chen, S., Wang, W., & Ye, X. (2023). Applying struvite as a N-fertilizer to mitigate N2O emissions in agriculture: Feasibility and mechanism. *Journal of Environmental Management*, *330*, 117143. https://doi.org/10.1016/j.jenvman.2022.117143

Wantzen, K., & Mol, J. (2013). Soil Erosion from Agriculture and Mining: A Threat to Tropical Stream Ecosystems. *Agriculture*, *3*(4), 660–683. https://doi.org/10.3390/agriculture3040660

Werner, K., Pommer, L., & Broström, M. (2014). Thermal decomposition of hemicelluloses. *Journal of Analytical and Applied Pyrolysis*, *110*, 130–137. https://doi.org/10.1016/j.jaap.2014.08.013

Windeatt, J. H., Ross, A. B., Williams, P. T., Forster, P. M., Nahil, M. A., & Singh, S. (2014). Characteristics of biochars from crop residues: Potential for carbon sequestration and soil amendment. *Journal of Environmental Management*, *146*, 189–197. https://doi.org/10.1016/j.jenvman.2014.08.003

Wu, P.-Y., Jia, Y., Jiang, Y.-P., Zhang, Q.-Y., Zhou, S.-S., Fang, F., & Peng, D.-Y. (2014). Enhanced arsenate removal performance of nanostructured goethite with high content of surface hydroxyl groups. *Journal of Environmental Chemical Engineering*, *2*(4), 2312–2320. https://doi.org/10.1016/j.jece.2014.10.010

Xi, H., Jia, M., Kuzyakov, Y., Peng, Z., Zhang, Y., Han, J., Ali, G., Mao, L., Zhang, J., Fan, T., & Liu, Y. (2023). Key decomposers of straw depending on tillage and fertilization. *Agriculture, Ecosystems & Environment*, *358*, 108717. https://doi.org/10.1016/j.agee.2023.108717

Xu, G., Fan, X., & Miller, A. J. (2012). Plant Nitrogen Assimilation and Use Efficiency. *Annual Review of Plant Biology*, *63*(1), 153–182. https://doi.org/10.1146/annurev-arplant-042811-105532

Yang, H., Tejado, A., Alam, N., Antal, M., & van de Ven, T. G. M. (2012). Films Prepared from Electrosterically Stabilized Nanocrystalline Cellulose. *Langmuir*, *28*(20), 7834–7842. https://doi.org/10.1021/la2049663

Yang, H., Yu, Y., Zhang, H., Wang, W., Zhu, J., Chen, Y., Zhang, S., & Chen, H. (2024). Effect mechanism of phosphorous-containing additives on carbon structure evolution and biochar stability enhancement. *Biochar*, *6*(1), 39. https://doi.org/10.1007/s42773-024-00330-5

Yang, L., Tan, W., Mumford, K., Ding, L., Lv, J., Zhang, X., & Wang, H. (2018). Effects of phosphorus-rich sawdust biochar sorption on heavy metals. *Separation Science and Technology*, *53*(17), 2704–2716. https://doi.org/10.1080/01496395.2018.1470641

Zahedifar, M. (2020). Effect of Biochar on Cadmium Fractions in Some Polluted Saline and Sodic Soils. *Environmental Management*, *66*(6), 1133–1141. https://doi.org/10.1007/s00267-020-01371-9

Zayed, O., Hewedy, O. A., Abdelmoteleb, A., Ali, M., Youssef, M. S., Roumia, A. F., Seymour, D., & Yuan, Z.-C. (2023). Nitrogen Journey in Plants: From Uptake to Metabolism, Stress Response, and Microbe Interaction. *Biomolecules*, *13*(10), 1443. https://doi.org/10.3390/biom13101443

Zhang, F., Wang, X., Yin, D., Peng, B., Tan, C., Liu, Y., Tan, X., & Wu, S. (2015). Efficiency and mechanisms of Cd removal from aqueous solution by biochar derived from water hyacinth (Eichornia crassipes). *Journal of Environmental Management*, *153*, 68–73. https://doi.org/10.1016/j.jenvman.2015.01.043

Zhang, H., Liao, W., Zhou, X., Shao, J., Chen, Y., Zhang, S., & Chen, H. (2022). Coeffect of pyrolysis temperature and potassium phosphate impregnation on characteristics, stability, and adsorption mechanism of phosphorus-enriched biochar. *Bioresource Technology*, *344*, 126273. https://doi.org/10.1016/j.biortech.2021.126273

Zhang, L., & Guan, Y. (2022). Microbial investigations of new hydrogel-biochar composites as soil amendments for simultaneous nitrogen-use improvement and heavy metal immobilization. *Journal of Hazardous Materials*, *424*. https://doi.org/10.1016/j.jhazmat.2021.127154

ZHANG, Y., YANG, J., YAO, R., WANG, X., & XIE, W. (2020). Short-term effects of biochar and gypsum on soil hydraulic properties and sodicity in a saline-alkali soil. *Pedosphere*, *30*(5), 694–702. https://doi.org/10.1016/S1002-0160(18)60051-7

Zhang, Y.-Y., Wu, W., & Liu, H. (2019). Factors affecting variations of soil pH in different horizons in hilly regions. *PLOS ONE*, *14*(6), e0218563. https://doi.org/10.1371/journal.pone.0218563

Zhao, L., Zheng, W., Mašek, O., Chen, X., Gu, B., Sharma, B. K., & Cao, X. (2017). Roles of Phosphoric Acid in Biochar Formation: Synchronously Improving Carbon Retention and Sorption Capacity. *Journal of Environmental Quality*, *46*(2), 393–401. https://doi.org/10.2134/jeq2016.09.0344

Zheng, X.-J., Li, Q., Peng, H., Zhang, J.-X., Chen, W.-J., Zhou, B.-C., & Chen, M. (2022). Remediation of Heavy Metal-Contaminated Soils with Soil Washing: A Review. *Sustainability*, *14*(20), 13058. https://doi.org/10.3390/su142013058

Zhou, W., Hui, D., & Shen, W. (2014). Effects of Soil Moisture on the Temperature Sensitivity of Soil Heterotrophic Respiration: A Laboratory Incubation Study. *PLoS ONE*, *9*(3), e92531. https://doi.org/10.1371/journal.pone.0092531

Zhou, X., & Chen, Y. (2019). An integrated process for struvite electrochemical precipitation and ammonia oxidation of sludge alkaline hydrolysis supernatant. *Environmental Science and Pollution Research*, *26*(3), 2435–2444. https://doi.org/10.1007/s11356-018-3667-6

Chapter 4: Fabrication of hydrogel beads and biochar composites as soil acidity amelioration

4.1 Introduction

Ammonium (NH_4) and phosphate (PO_4) represent key macronutrients essential for plant growth and development. These elements are commonly used as agricultural fertilizers to sustain the world's growing population (Jing et al., 2019). The commercial manufacturing of chemical fertilizers heavily relies on energy sources that are not renewable, such as natural gas and finite mineral reserves (i.e., phosphate rock). If the demand for fertilizers continues to rise annually at a rate of 3%, the remaining accessible phosphate mineral sources will be diminished within 50 years (Nancharaiah et al., 2016). There is a need to recover resources that can be used as fertilizer. On the other hand, the recent escalating demand for food production has resulted in the excessive use of fertilizers, leading to potential water contamination, eutrophication, and an increase in harmful algal blooms. These algal blooms adversely impact aquatic ecosystems, reduce oxygen levels (Chen et al., 2018), and negatively affect the taste and odor of drinking water (Pawar et al., 2016). Moreover, NH_4 could give rise to carcinogenic nitrates through the activity of nitrifying bacteria, posing a potential hazard to the general population (Nguyen et al., 2019). Potential water pollutants other than NH_4 and PO_4 are phenolic compounds in effluent from industries such as chemicals, petrochemicals, coke factories, and refineries (Kim et al., 2008). Phenolic substances considered to be hazardous and mutagenic at elevated levels, and the human body can absorb them through the skin (Abdelwahab and Amin, 2013; Al Bsoul et al., 2021). On the other hand, small amounts of phenolic compounds play a beneficial role as a vital nutrient cycling process for soil and plant life (Kraus et al., 2003). Therefore, if excess NH_4, PO_4, and phenol can be recovered from wastewater and supplied to the soil in optimal amounts as fertilizer, this can improve water quality and also conserve valuable NH_4, PO_4, and phenol resources, resulting in significant environmental and socioeconomic advantages (Shakoor et al., 2021).

Various effective techniques have been identified for removing water contaminants from liquid solutions, such as encompassing biological methods (Cai et al., 2013), precipitation (Y. Chen et al., 2021; González-Morales et al., 2021; Zhou & Chen, 2019), electrochemical methods (F. Wang et al., 2019; Z. Wang & He, 2022), ion exchange (Tarpeh et al., 2018), and adsorption (Harada et al., 2021; Wang et al., 2016; Xie et al., 2020). Each of these approaches possesses distinct advantages and limitations. Biological methods offer greater cost efficiency; nevertheless, the drawback lies in the residual dead bacteria post-treatment (Matei & Racoviteanu, 2021). While the precipitation process proves simple and effective in chemical treatment, it falters in managing sewage sludge, waste disposal, and organic compounds (Huang et al., 2017). Despite being costly, electrochemical techniques exhibit lower efficacy in ion removal (Rodrigues & da Silva, 2009). Ion exchange presents an alternative for removing anions by substituting sulfates (SO_4) with PO_4 ions (Blaney et al., 2007). However, this approach worsens solution corrosiveness and necessitates expensive clean-up procedures. Adsorption, considered an efficient and widely employed method for water contaminant removal, is characterized by ecological sustainability, a straightforward and swift procedure, and high technological effectiveness. In particular, environmentally compatible adsorbents such as biochar and chitosan are promising because of their potential to convert adsorbed compounds into fertilizer.

Biochar has garnered great attention as a prospective adsorbent due to its cost-effectiveness, environmental friendliness, abundance, and high carbon content (Srivatsav et al., 2020). Produced through pyrolysis in the temperature range of 350-800°C under a restricted oxygen supply (Chatterjee et al., 2020), biochar's suitability for adsorption applications is attributed to its high porosity and extensive surface area (Lita et al., 2023; Suliman et al., 2017). Numerous experiments have been conducted to remove N-NH_4, PO_4, and phenol. For instance, Hu et al. (2020) utilized biochar derived from pineapple, orange peel, and dragon fruit, reporting maximum adsorption capacities for N-NH_4 of 5.60 mg/g, 4.71 mg/g, and 2.65 mg/g, respectively. In another study, Begum et al. (2021) observed an N-NH_4 adsorption capacity of 0.96 mg/g. Emenike et al. (2022) reported that Delonix regia biochar has a limited phenol adsorption capacity, reaching a maximum of 2.59 mg/g. In one study, Lawal et al. (2021) showed a phenol adsorption capability of 62.89 mg/g using oil palm frond in the biochar. The use of coffee husks as a biochar source is currently in high demand and increasingly recognized as a viable alternative (Silveira Junior et al., 2023). Global coffee production in the 2021/2022 recorded 0.3 billion metric tons, based on 6% coffee husks obtained from 48% of coffee trees (Hidayat et al., 2020). However, the substantial quantities may pose serious issues if not properly managed. There is little studies on the simultaneous removal of NH_4, PO_4, and phenol from water. Still, this combination is being actively studied for use as a soil amendment, and the integration of adsorbents and agricultural applications could be promising.

Enhancing the adsorption capacity via modifying biochar increases its surface characteristics and structure (Wu et al., 2020). Chitosan is becoming a promising polymer to be used as an efficient adsorbent for water pollutants due to its abundant hydroxyl (–OH) and amino (–NH_2) functional groups, facilitating easy interactions with other substances, along with its environmentally friendly characteristics (W. Li et al., 2021). However, due to its low tensile strength and susceptibility to dissolution in acidic environments (Aranaz et al., 2021), it is not desirable to directly employ chitosan in wastewater treatment. Therefore, it is crucial to enhance chitosan`s chemical stability and adsorption capability through modification. Chitosan-metal oxide composites have been synthesized as an interesting approach due to their advantageous properties, including chemical stability, a substantial surface area, and effective adsorptive capabilities (Nga et al., 2020; Spoială et al., 2022). In particular, magnetic materials have attracted much focus in recent years for their efficient and rapid separation of adsorbents from wastewater (Cordova Estrada et al., 2021; P. Wang et al., 2020). With the chemical formula Fe_3O_4, magnetites are highly magnetic particles widely utilized for their compact dimensions and extensive surface area (Fu et al., 2015). However, simple Fe_3O_4 magnetic particles generally form aggregates, reducing stability and limiting available functional groups (Zhao et al., 2023).Therefore, zirconium oxide (ZrO) was additionally incorporated to increase the porosity of chitosan (L. Zhang et al., 2022) and to increase the potential to adsorb PO_4 ions, which is difficult with biochar alone. To improve the stability and physicochemical quality of the composite, cross-linking, a chemical procedure that creates strong covalent bonds between two or more molecules and results in their linkage was performed, which would improve the physicochemical qualities of chitosan (Jawad et al., 2023). Employing a crosslinking process to combine biochar, chitosan, ZrO, and Fe_3O_4 proves to be a successful method for increasing the surface-active sites and assisting easy separation. Thus, the integrating coffee husk biochar-loaded chitosan, ZrO, and magnetite ($CBCZrOFe_3O_4$) composite materials hold promise with diverse components.

When the composites are used as soil modifiers, the NH_4, PO_4, and phenol supplied to the soil exist in three forms: dissolved molecules freely moving within the soil solution, sorbed molecules capable of reversible binding to soil particles or proteins, and polymerized molecules forming part of humic substances (Min et al., 2015). The compounds would be useful in mitigating soil acidification. Soil acidification significantly influences the soil environment, leading to deterioration of soil quality (Geng et al., 2022). This issue negatively impacts agricultural output and food safety. Soil acidification occurs naturally and relatively slowly for hundreds to millions of years. However in recent decades, this process has accelerated dramatically due to acid deposition (Driscoll et al., 2016) and overuse of N-based fertilizers (Tian & Niu, 2015). When nitrogen (N) is applied to farmland soils, it undergoes a process called hydrolysis, which involves ammonification ($R–NH_2 + H^+ + H_2O \rightarrow R–OH + NH_4^+ + OH^–$) and followed by nitrification ($NH_4^+ + 2O_2 \rightarrow 2H^+ + H_2O + NO_3^–$). Ammonification increases the soil pH, whereas nitrification decreases it. Several scientists have used biochar to regulate soil acidification (Fidel et al., 2017) via decarboxylation and chitosan, which releases -OH groups to elevate soil pH. Phosphorus (P) is a macronutrient essential to soil health and plant development. It affects soil acidity by releasing hydrogen (H^+) ions through PO_4^{3-} molecules. Besides macronutrients, a micronutrient such as iron is needed by plants for regulation of plant growth and development and is involved in the metabolism processes of photosynthesis and dark respiration. A study performed by Kreslavski et al. (2023) has stated that treating plants with Fe_3O_4 nanoparticles could enhance plant growth and photosynthesis by minimizing the negative impact of soil salinity. In addition, Liu et al. (2023) have used a polymer- Fe_3O_4 interaction to increase soil's pH effectively. Contrastingly, the presence of phenol in soil may be observed to lower the rate of organic matter's decomposition by reducing soil pH. However, other studies (Hättenschwiler & Vitousek, 2000; Misra et al., 2023) have highlighted the addition of phenol able to improve nutrient cycling, help with chemical stabilization of soil N, and enhance the mobilization of nutrients such as P in soil. Since few works are reported regarding these compounds` effect on soil acidity, further research is needed to investigate the possible interactions. We hypothesize that a combination of biochar, chitosan, magnetite, and ZrO ($CBCZrOFe_3O_4$) could be useful to alleviate soil acidity with loaded NH_4, PO_4, and phenol via adsorption.

Furthermore, the utilization of polymer hydrogel to control mineral release represents a promising approach. The shift towards sustainable and green resources has prompted the exploration and adoption of biodegradable polymers like sodium alginate (SA), poly (acrylic acid) (PA), and carboxymethyl cellulose (CMC), which offer solutions to the cost, environmental, and manufacturing challenges associated with synthetic polymers. SA is a bio-based hydrogel known for its hydrophilic nature and non-toxicity, boasting a high capacity for swelling (Satheesh Kumar et al., 2023). However, the stability of SA hydrogel can be compromised by excessive ionic interactions or the presence of certain ions. The incorporation of PA, CMC and oleic acid (OA) by cross-linking method can improve the stability (Abd El-Aziz et al., 2022; Alam & Christopher, 2018) and mechanical strength of the hydrogel composites (Enoch & Somasundaram, 2023; Faturechi et al., 2015). Nonetheless, when applied to soil, bulk hydrogel may not distribute evenly, potentially leading to irregular water distribution around the hydrogel material. In contrast, hydrogel beads, with their higher surface area to volume ratio compared to bulk hydrogels, facilitate more effective water and soil interactions, thus enabling a more uniform, and controlled release of minerals.

This chapter aimed to develop (1) a novel adsorbent ($CBCZrOFe_3O_4$) to remove NH_4, PO_4, and phenol from water simultaneously in a single-step process. Subsequently, the adsorbent, enriched with NH_4, PO_4, and phenol, was employed as an alternative fertilizer to enhance soil acidity properties. (2) Develop a controlled-release fertilizer using hydrogel beads derived from SA, PA, CMC and OA, with ammonium chloride (NH_4Cl) as the primary nitrogen source. The absence of OA was also investigated to evaluate the slow release mineral and immobilization effects. Additionally, the study examines CO_2 emissions during the incubation of soil contaminated.

4.2 Materials and methods

4.2.1 Materials

Ferric chloride ($FeCl_3$, 98%), hydrochloric acid (HCl, 36.5-38%), sulfuric acid (H_2SO_4, 95%), potassium chloride (KCl, 99.5%), Iron sulfate ($FeSO_4$, >95%), sodium carbonate (Na_2CO_3, >99.8%), sodium hydrogen phosphate ($NaHPO_4$, >99.95%), sodium bicarbonate ($NaHCO_3$, >99.5%), ammonium acetate (CH_3COONH_4, >97%), potassium dichromate ($K_2Cr_2O_7$, 99.5%), oleic acid ($C_{18}H_{34}O_2$, 90%), and sodium hydroxide (NaOH, 99.99%) were purchased from Kanto Chemical Co. Inc., Japan. Sodium alginate, humic acid and glutaraldehyde was purchased from Wako Chemicals, Tokyo, Japan. Poly (acrylic acid), (molecular weight: 100.000) and polyvinyl alcohol was purchased from Scientific Polymer Products, INC., New York.

4.2.2 Preparation of samples

4.2.2.1 Simultaneous removal of ammonium, phosphate, and phenol via self-assembled biochar composites CBCZrOFe$_3$O$_4$ and its utilization as soil acidity amelioration

Coffee husk biochar (CB) was generated by heating a muffle furnace at 600 °C for 3 h. The preparation of CB + chitosan (CBC) involved mixing 0.5 g of CB with 25 mL of chitosan solution (1 g of chitosan dissolved in 100 mL of 1% acetic acid for 24 h), followed by stirring the mixture for 1 h at 60°C. The resulting solution was filtered and washed with deionized water (DW) and ethanol. In addition, CBCZrO was produced by incorporating ZrClO (0.5 M) into the CBC solution. Finally, CBCZrOFe$_3$O$_4$ was prepared by adding the magnetic materials to the mixture. The production process for the samples was similar to that for the CBCZrO. Chitosan solution (25 mL) was mixed with CB (0.5 g), 1 M $FeCl_3$, 0.5 M Fe_2SO_4, and ZrClO (20 mL). The mixture was subsequently heated until 60°C while agitated for 1 h. The pH of the mixture was raised to 10 by adding 3 M NaOH and stirred magnetically at room temperature for 24 h. The solution was subsequently passed through filter and washed with distilled water and ethanol for multiple times to remove residual NaOH. All of the adsorbent samples were then dried in an oven for three days at 60°C for further experiments.

4.2.2.2 Evaluation of Hydrogel Beads Composites Derived from Alginate-Poly (Acrylic Acid)-Carboxylmethyl Cellulose-Oleic Acid as Slow Release NH_4 Fertilizer and Soil Acidity Conditioner with S and Fe Contaminated

Hydrogel beads were formed by combining 6 mL of 2 wt% sodium alginate aqueous solution, 6 mL of 5 wt% poly (acrylic acid) aqueous solution, 6 mL of 1 wt% carboxylmethyl cellulose, 1 mL of 3 M NaOH, and 0.25 g NH_4Cl for the SPC-A. While, SPC-B, 0.05 mL oleic acid was added. The samples were placed in bottle flasks and shaken for 1 h at constant temperature of 50 ºC. After cooled down, the solution was injected slowly into 10 wt% $CaCl_2$ aqueous solution. Subsequently, the hydrogel beads were allowed to grow for one night to obtain the resultant hydrogel beads. The hydrogel beads were then washed with ethanol and deionized (DI) water, and then let to dry in an oven at 60 °C for 24 h.

4.2.3 Batch adsorption and desorption experiments

In a sequence of experiments, the simultaneous removal of NH_4, PO_4, and phenol was examined, considering various experimental factors such as initial pH (ranging from 6 to 10), concentrations of NH_4, PO_4, and phenol solutions (ranging from 10 to 250 mg/L), and adsorption duration (ranging from 30 to 90 min). Batch adsorption tests were carried out by immersing the adsorbent in 50 mL. The mathematical calculations for calculating the percentage of removal and adsorption equilibrium amount are outlined in Eq. (41) and (42), respectively.

$$\text{Removal, \%} = \frac{C_o - C_e}{C_o} \times 100 \tag{41}$$

$$q_e = \frac{C_o - C_e}{W} \times V \tag{42}$$

where *Removal, %* is the removal efficiency, and C_o and C_e are the initial and equilibrium NH_4, PO_4, and phenol concentrations (mg/L), respectively, q_e is the equilibrium adsorption capacity of the adsorbent (mg/g), W is the amount of adsorbent (g), and V is the volume of ion solution (L).

In desorption studies, we used adsorption conditions such as contact time: 90 min and ions concentration: 250 mg/L. Then, we soaked in 1 M (HCl and H_2SO_4) solution for 24 h at 30 °C. The desorption equation is calculated using in Eq. (43)

$$\text{Desorption, \%} = \frac{q_e des}{q_e} \times 100 \tag{43}$$

where, *Desorption, %,* represented by Desorption, is calculated as the ratio of the equilibrium ions concentration after desorption ($q_e des$, mg/g) to the initial ions concentration after adsorption (q_e, mg/g), multiplied by 100.

4.2.4 Soil acidity incubation experimental design

One kilogram of air-dried soil samples was mixed with 1 litter of deionized water in a plastic container, and the pH was adjusted with 10 mM H_2SO_4 until the pH reached 2.5 and 4.0. Subsequently, the soil was incubated for 24 h, filtered, and dried in an oven at 60°C for 3 days for subsequent experiments. The soil acidity experiment spanned 30 days with the following experimental design: control (soil only at pH 2.5 and 4.0), $CBCZrOFe_3O_4$ loaded with NH_4, PO_4, and phenol ($CBCZrOFe_3O_4$-APP) (1 wt% of soil at pH 2.5 and 4.0), all conducted under a constant temperature of 25°C. All experiments were conducted in plastic cups, with 40% of the soil's field water-holding capacity. Soil subsamples were collected after 3, 7, 15, 30, and 60 days. Following each day of incubation, 30 g of soil samples were taken out and dried in an oven at 60°C for 3 days for further analysis.

4.2.5 Soil incubation contaminated S and Fe experimental design

Soil was sourced from a store in Shobara City and used to create artificial contaminated-soil. A mixture consisting of 1 kg of air-dried soil and 1 L of a 0.5 M $FeSO_4$ solution was prepared in a plastic container. This mixture was incubated for three days, after which the soil was filtered and dried at 60 °C for another three days. An experiment involving contaminated S and Fe was conducted over 30 days, employing two experimental conditions: one group of soil was treated with 1 wt.% SPC-A, and another with 1 wt.% SPC-B. The experiments were placed in plastic cups at room temperature. After 30 days, the soil samples were collected and oven-dried at 60 °C for three days for subsequent analysis. During the incubation, a CO_2 sensor was used to measure soil CO_2 emissions using the Go Direct CO_2 Gas Sensor from Vernier Science Education.

4.2.6 Determination of mineral release

The quantities of NH_4 released from the hydrogel beads were assessed via batch water shaker experiments (BW101, Yamato, Japan). Each set of beads (0.5 g) was placed in 50 mL of DI water, 0.01 M NaOH, 0.01 M HCl, 0.01 M NaCl, 0.01 M $MgCl_2$ and agitated at 25 °C with a speed of 100 rpm. The NH_4 analysis was performed at intervals of 1 day, 3 days, 7 days, and 14 days.

4.2.7 Determination of soil properties

The assessment of soil pH and electrical conductivity (EC) was carried out using laboratory instruments such as pH meters and EC meters. Prior to the measurement of pH and EC, a mixture was prepared with soil and water at a 1:5 (w/v) ratio and agitated for 30 min. The available phosphorus (P) content in the soil was measured using the Olsen method, which involves a 0.5 M sodium bicarbonate ($NaHCO_3$) solution. The exchangeable cations, specifically calcium (Ca), potassium (K), and magnesium (Mg), were evaluated using an ammonium acetate (CH_3COONH_4)

extraction method at a normality of 1 N. Additionally, to ascertain the soil's cation exchange capacity (CEC), 10 wt% sodium chloride (NaCl) was integrated with the soil. For the extraction of soil-available nitrogen-ammonium (N-NH_4) and nitrogen-nitrate (N-NO_3), a 2 M potassium chloride (KCl) solution was utilized. Soil organic carbon (SOC) levels were determined utilizing the Walkley-Black wet oxidation technique and the subsequent measurements were conducted using a UV-Visible Spectrophotometer (JASCO V-530) at a wavelength of 561 nm. To evaluate the levels of available S and Fe, the soil underwent treatment with a 20 mM solution of $CaCl_2$ at a 1:5 w/v ratio for a period of 30 min. The quantification of S was analysed using $BaCl_2$-tween 80 solution using a UV-Visible Spectrophotometer (JASCO V-530) at a wavelength of 432 nm. While Fe amount was then performed using pack testing methods at Kyoritsu Chemical-Check Lab., Corp. in Kanagawa, Japan.

4.2.8 Analytical measurements

The physical characteristics of CBCZrOFe_3O_4 were determined using the BET (Brunauer-Emmett-Teller) technique (MicroActive AutoPore V 9600 2.03.00, Shimadzu Techno-Research Incorporation, Japan). The crystalline configuration of CBCZrOFe_3O_4 was examine using powder X-ray diffraction (XRD) with Cu/Kα radiation (Rigaku, SmartLab 9kW, Japan). The Fourier transform infrared spectroscopy (FTIR) analysis was accessed using a Thermo Scientific Nicolet iS10 instrument (Thermo Fisher Scientific Inc., Waltham, MA, USA). The surface morphology of the adsorbent was observed by scanning electron microscopy (SEM) (Miniscope TM3000, Hitachi-hitech, Tokyo, Japan). The pH_{zpc} value, representing the neutral surface charge, was calculated using the equation $\Delta pH = pH\text{-final} - pH\text{-initial}$.

4.2.9 Statistical analysis

Data analyses were performed with MINITAB software (version 21.3.1). Mean values were subjected to one-way analysis of variance (ANOVA), and treatment comparisons were conducted using Tukey's test (P-value <0.05).

4.3 Results and discussion

4.3.1 Simultaneous removal of ammonium, phosphate, and phenol via self-assembled biochar composites CBCZrOFe$_3$O$_4$ and its utilization as soil acidity amelioration

4.3.1.1 Characterization

The four types of porous composite adsorbents were first prepared using coffee husk biochar alone, and then subsequently combined with chitosan, magnetite, and ZrO, respectively. The photograph and morphological structures of all the adsorbents in as-synthesized state and after adsorption test are depicted in Figure. 68. It is evident that the CHB sample (Figure. 68b) exhibited porous structures, with an increase in porosity observed after the incorporation of chitosan (Figure. 68c) and chitosan-ZrO (Figure. 68d).

Furthermore, the structure underwent a significant transformation with CBCZrOFe$_3$O$_4$ (Figure. 63e), displaying a heterogeneous, uneven, and rough groove structure, attributed to the possible iron oxide layer covering the surface. However, following the adsorption process, the surface underwent noticeable changes, with a reduced number of rough grooves that appeared relatively flatter and smoother (Figure. 68f). This alteration was likely due to the presence and deposition of adsorbed NH$_4$, PO$_4$, and phenol on the surface.

All the four types of composite adsorbents prepared were tested for their adsorption performance on NH$_4$, PO$_4$, and phenol. The adsorption of NH$_4$, PO$_4$, and phenol onto various adsorbents was conducted at pH 6 and a contact time of 30 min at room temperature (Figure. 69a).

Statistical analysis revealed that CBCZrOFe$_3$O$_4$ demonstrated the highest removal efficiency for NH$_4$, PO$_4$, and phenol ($P<0.05$), whereas CB exhibited the lowest removal efficiency ($P<0.05$). This indicates that the combination of chitosan and metal oxides are effective for concurrently removing ions from water. Consequently, this adsorbent was selected for subsequent experiments.

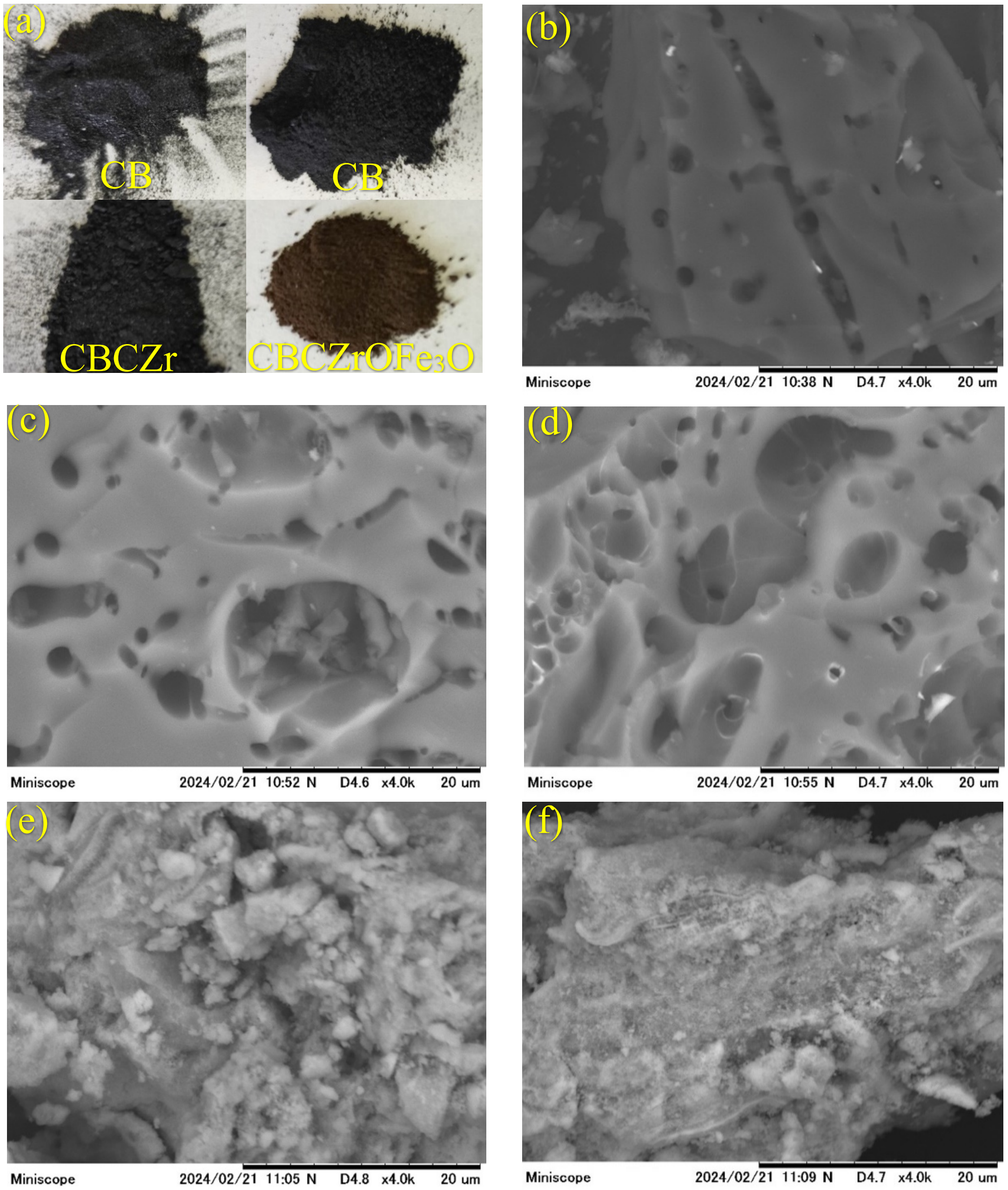

Figure. 68. (a) Photograph of adsorbent. SEM photograph of the adsorbent (b) CB (c) CBC (d) CBCZrO (e) CBCZrOFe$_3$O$_4$ (before adsorption) (f) CBCZrOFe$_3$O$_4$-APP (after adsorption).

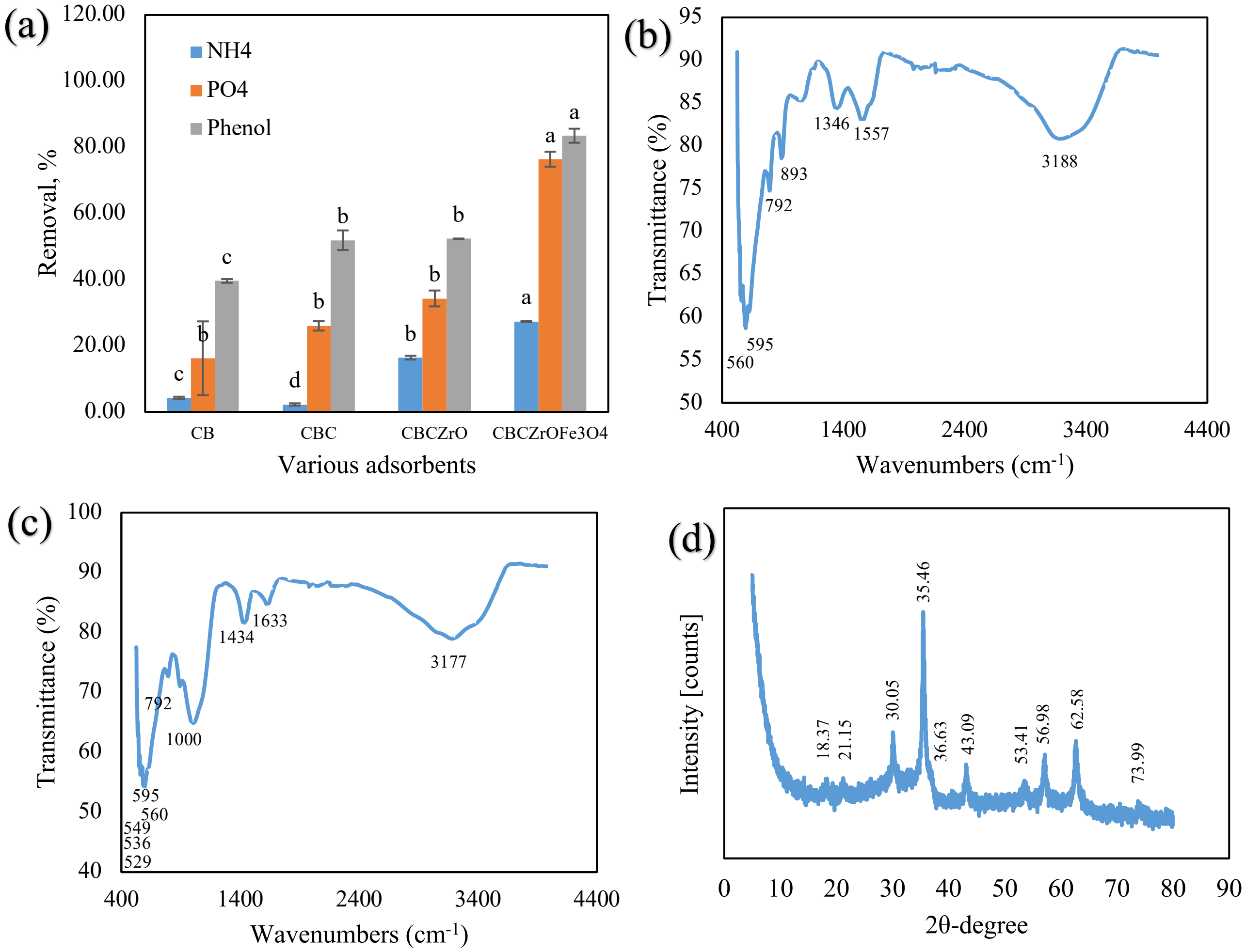

Figure. 69. (a) Comparison of various adsorbents for simultaneous removal percentage of NH_4, PO_4, and phenol. FTIR spectra of adsorbent (b) $CBCZrOFe_3O_4$ (before adsorption) (c) $CBCZrOFe_3O_4$ (after adsorption) (d) XRD of $CBCZrOFe_3O_4$. Statistical analytical by Tukey test ($P<0.05$).

Table 21. Physical characteristics of $CBCZrOFe_3O_4$.

Adsorbent	SSA_{BET} [m^2/g]	Pore Volume [mL/g]	Average pore diameter [nm]	Porosity (%)
$CBCZrOFe_3O_4$	73.6	1.041	56.58	72

The chemical functional groups of the $CBCZrOFe_3O_4$ (Figure. 69b) and post-adsorption $CBCZrOFe_3O_4$ (Figure. 69c) samples were analyzed using FTIR. The decrease in peak intensity observed from 3188 cm^{-1} to 3177 cm^{-1} is likely due to the adsorption process involving functional groups engaged in intermolecular bonding interactions, such as van der Waals forces and -OH bonding, along with the C-H peak of phenol (Allahkarami et al., 2023; Modrzejewska, 2013; Zheng et al., 2020). Additionally, a shift in the peak from 1557 cm^{-1} to 1633 cm^{-1} corresponds to the asymmetric stretching of COO- and C=O, respectively (Qurrat-Ul-Ain et al., 2019; Ravikumar et al., 2013). These changes were attributed to the electrostatic interactions that occur between NH_4 (positive charge) and carboxylate (negative charge). Another distinct shift was observed between 1346 cm^{-1} and 1434 cm^{-1}, indicating the symmetric bending vibrations of N-H, which confirmed the existence of chitosan. Furthermore, the shift of the bands from 893 cm^{-1} to 1000 cm^{-1} after adsorption, typical of the aromatic C-H bending region, suggests the adsorption of phenol onto the adsorbent. The presence of peaks in the range of 560 cm^{-1} to 595 cm^{-1} indicated the existence of Fe-O and Zr-O bonds (Azizi, 2020), serving as distinctive markers for identifying phosphate adsorption from a solution by the adsorbent. The appearance of new peaks after adsorption at 549 cm^{-1}, 536 cm^{-1}, and 529 cm^{-1} confirms the success of the adsorption process.

Figure. 69d presents the XRD spectrum aimed at validating the crystalline structure of $CBCZrOFe_3O_4$. The broad diffraction peak observed within the angle range of $2\theta = 10°$ to 20° is likely attributed to chitosan. Peaks identified at 30.05°, 35.45°, and 36.63° correspond to mineral quartz and hematite. Peaks indicating the presence of iron (Fe) are observed at 43.08°, 53.41°, 56.98°, 62.58°, and 73.99° (L. Liu et al., 2023; M. Zhang et al., 2020). According to mercury intrusion analysis, the $CBCZrOFe_3O_4$ adsorbent exhibits a specific surface area (SSA-BET) of 73.6 m^2/g, a pore volume of 1.041 mL/g, an average pore diameter of 56.58 nm, and a porosity of

72% (see Table 21). The high porosity of the adsorbents facilitates the transfer of NH_4, PO_4, and phenol molecules within the adsorbent matrix.

4.3.1.2 Initial pH effect and surface charge of adsorbent (pH_{zpc})

The influence of pH on the adsorption capacity of adsorbents has been demonstrated to be significant, as indicated by (Abdellaoui et al., 2021; R. Li et al., 2017). As depicted in Figure. 70a, the concurrent adsorption of NH_4, PO_4, and phenol is subjected to variations in solution's pH conditions. Notably, the findings reveal a pH of 8.0, representing the optimal condition for NH_4 and PO_4 adsorption, with removal percentages of 37.50% and 77.40%, respectively. The highest removal percentage of phenol was examined to be 83.50% at pH condition of 6. Similar findings have been reported by Liu et al. (2021), who employed Rhizoma Typhonium Gigantei and Radix Glycyrrhizae Preparata to remove NH_4 and PO_4 at pH 8 .

At pH levels below 8, the increased release of H^+ ions leading to competitive interaction between NH_4 ions and H^+ for exchange site, impeding NH_4 adsorption. Conversely, at pH levels above 8, NH_4 predominantly exists in the NH_3 form, resulting in a reduction in the proportion of NH_4 removal due to the volatilization of NH_4 as NH_3. The formation of NH_4 above pH 8 can be described by the following equation (44):

$$NH_4^+ + OH^- \leftrightarrow NH_3 + H_2O \tag{44}$$

Under acidic conditions, hydroxyl (-OH) and carboxyl (-COOH) groups present on the adsorbent's surface undergo protonation. This protonation process facilitates PO_4 adsorption through ligand exchange with -OH groups. Furthermore, at a pH of 8.0, amino groups (-NH) exist in a free amine state, creating a favourable environment for PO_4 adsorption in the form of $H_2PO_4^-$. However, as pH levels increase, the concentration of $H_2PO_4^-$ decreases, resulting in the prevalence of HPO_4^{2-} in the solution and consequently reducing PO_4 uptake. As for phenol, raising the initial pH level led to a decline in the percentage removal of phenol (Figure. 70a). This observation aligns with those reported by Gundogdu et al. (2012), who utilized activated carbon derived from waste generated in the tea industry to adsorb phenol. This decrease is attributed to phenol's nature as a weak acid, which reacts with NaOH to form sodium phenoxide, as depicted in Eq. (45). At higher pH levels, repulsion occurs between the adsorbent surface and phenolate anions due to the negative charge on the surface of adsorbent (Figure. 70b), resulting in decreased removal efficiency.

$$C_6H_6O + NaOH \rightarrow C_6H_5NaO + H_2O \qquad (45)$$

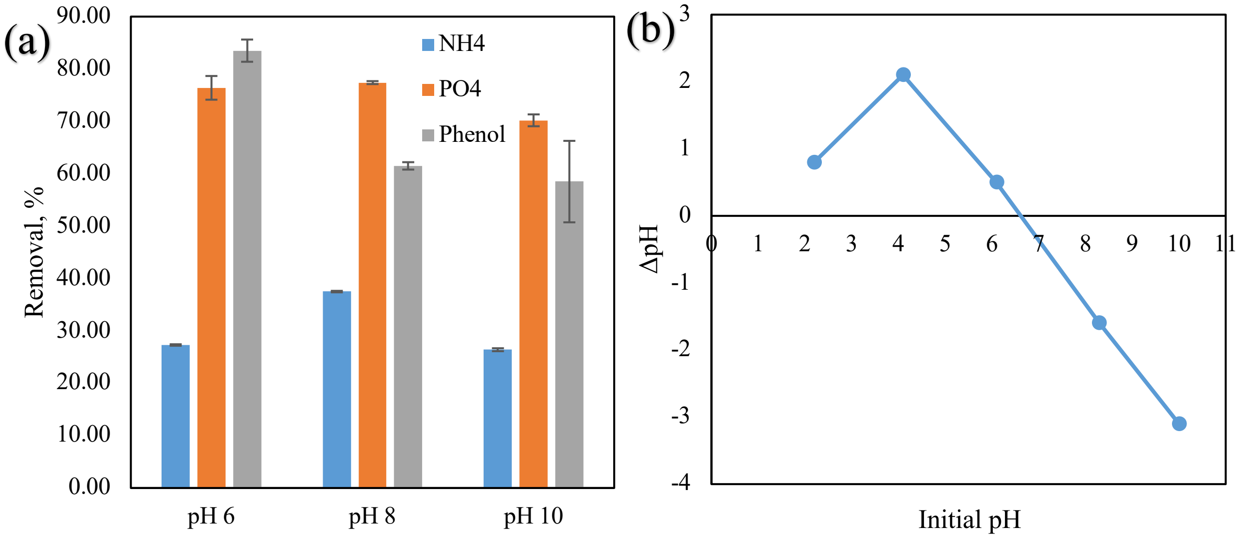

Figure. 70. (a) Initial pH effect versus percentage removal (b) Surface charge (pH_{zpc}) of the $CBCZrOFe_3O_4$.

4.3.1.3 Kinetic of the adsorption process

The kinetic information provide valuable insights into the adsorption process. The graphs in Figure. 71 visualize the fluctuation trends in the adsorption capacity (q_e) of NH_4, PO_4, and phenol over time (min). Certain study has shown an inconsistent trend of adsorption of PO_4 as described by Tomin and Yazdani (2022) due to undesired desorption of the ions. Generally, at the beginning of adsorption process, adsorbate rapidly diffuses into the adsorbent since there are plenty of adsorption sites that are accessible to ions. Eventually after some time, there are fewer active sites left throughout the adsorption process, causing the uptake of ions slows down and fluctuates.

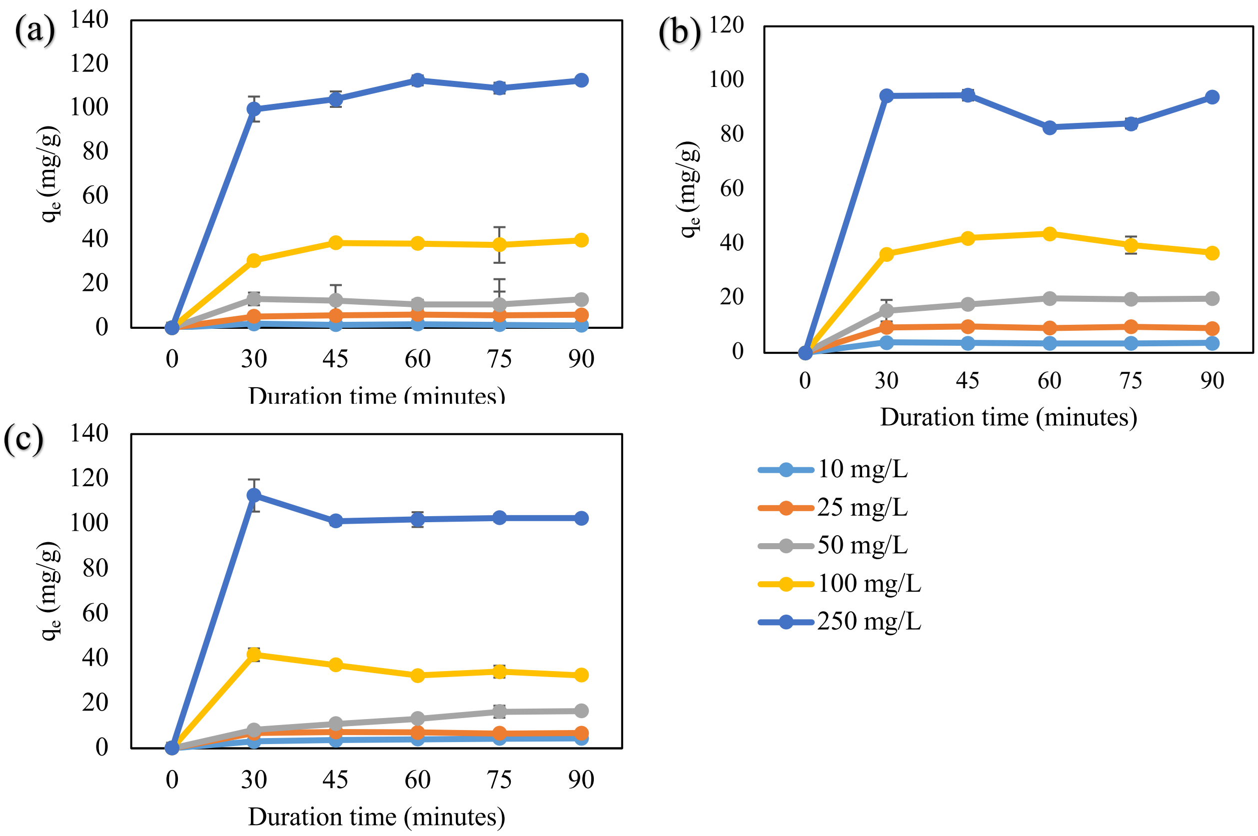

Figure. 71. Effect of various initial ion concentrations and contact time (min) versus adsorption capacity (q_e) (a) NH_4 (b) PO_4 (c) phenol.

To further the analysis on kinetic studies, data derived from the adsorption of NH_4, PO_4, and phenol onto the adsorbent surface were evaluated using two distinct kinetic models: the pseudo-first-order model linear and non-linear in Eq. (46-47), respectively and the pseudo-second-order models linear and non-linear in Eq. (48-49), respectively.

$$\ln(q_e - q_t) = \ln q_e - k_1 t \quad (46)$$

$$q_t = q_e(1 - e^{-k_1 t}) \quad (47)$$

$$t/q_t=1/(k_2q_e^2)+t/q_e \quad (48)$$

$$q_t=\frac{k_2q_e^2t}{1+k_2q_et} \quad (49)$$

where k_1 (min^{-1}) represents the rate constant of the pseudo-first-order model, t (min) denotes the time. Linear plots of ln$(q_e$-$q_t)$ against ln t and t/q_t against t were created and used to determine k_1 and k_2 from the slopes of the linear plots corresponding to the pseudo-first-order and pseudo-second-order models, respectively.

Figure. 72-73 and Table 22-23 show the linear and non-linear correlation coefficients and kinetic factors associated with NH_4, PO_4, and phenol adsorption, respectively. The results observed that the correlation coefficient R^2 of the second-order models in linear equation was higher than others in all analyses, and were mostly greater than 0.99. These high correlation coefficient values of pseudo-second-order reaction demonstrating that chemisorption was the main adsorption process involved in this experiment. This finding is comparable with those of the previous studies conducted by Mohamad Sarbani et al. (2023) utilized carboxyl methyl cellulose-chitosan magnetite for Cr (VI) and Pb (II) adsorption, respectively. The reaction constant (k_2) was determined by identifying the point of intersection on the t/q_e plot against t. According to the Table 22, the rate constant values indicated that the adsorbents accelerate the absorption kinetics for NH_4, PO_4, and phenol at initial concentrations of 250, 50, and 50 mg/L, respectively after 90 minutes of adsorption experiments.

4.3.1.4 Adsorption isotherm analysis

This experiment focused on the impact of varying the initial concentrations of NH_4, PO_4, and phenol on the adsorption capacity of the adsorbent, ranging from 10 to 250 mg/L, as depicted in Figure. 71. The adsorption capacity exhibited a clear correlation with the initial ion concentration. The increase in ion adsorption is directly associated with the higher concentration of the initial ions, resulting in an augmented driving force for mass transfer. Consequently, a steeper concentration gradient is established between the ions in the solution and those in the adsorbent (Al Bsoul et al., 2021; Yeliz Ozudogru & Ecem Tekne, 2023).

From the adsorption data, the adsorption isotherms of adsorbent were analyzed using Langmuir, Freundlich, Temkin, and Redlich-Peterson models. The Langmuir model implies single-layer adsorption on a homogenous surface, wherein adsorption taking place at specified places on the adsorbent surface. This model suggests that no further adsorption can happen once an adsorbate molecule occupies a spot on a surface. By contrast, the Freundlich model is an empirical equation that explains multilayer adsorption on heterogeneous surfaces. This model signify that the adsorption process take place at a surface with uneven energy distribution, resulting in a heterogeneous surface. Temkin model posits that the heat of adsorption for all molecules within the layer diminishes proportionally with coverage because of interactions between the adsorbent and the adsorbate (NH_4, PO_4 and phenol). While, the Redlich-Peterson isotherm extends beyond the Langmuir model, which presupposes monolayer adsorption on a uniform surface. The linear mathematical representations of the Langmuir, Freundlich, Temkin, and Redlich-Peterson models are provided in Eq. (50), (51), (52), and (53), respectively.

$$\frac{C_e}{q_e} = \frac{C_e}{q_{max}} + \frac{1}{K_L q_{max}} \quad (50)$$

$$\log q_e = \log K_F + \frac{1}{n} \log C_e \quad (51)$$

$$q_e = RT\ln K_T + RT\ln C_e \quad (52)$$

$$\ln\left(\frac{C_e}{q_e}\right) = \beta \ln C_e - \ln A \quad (53)$$

where q_e (mg/g) is the amount of solute adsorbed per unit mass of adsorbent at equilibrium (adsorption capacity), C_e (mg/L) is the equilibrium concentration of the solute in solution, q_{max}

(mg/g) is the maximum adsorption capacity (related to the number of adsorption sites on the surface), C_o (mg/L) is the initial concentration. K_f (mg/g) is the Freundlich equilibrium constant (related to the adsorption capacity of the adsorbent) and $1/n$ is the Freundlich constant. R is the gas constants of the model (differential surface capacity for the ions sorption per unit binding energy), K_T is the equilibrium binding constant corresponding to maximum binding energy were obtained from the slope and intercept of the graph of the q_e versus lnC_e, respectively. β is an empirical constant.

Table 24 presents the linear regression coefficient (R_2) values extracted from Figure. 74 and 75, alongside additional parameters pertaining to the adsorption isotherm. The Freundlich model demonstrated superior accuracy in fitting the NH_4, PO_4, and phenol adsorption data compared to the Langmuir, Temkin, and Redlich-Peterson models, as indicated by higher R_2 values across all initial concentrations. This study suggests that NH_4, PO_4, and phenol molecules adhere to the heterogeneous surface through multilayer adsorption.

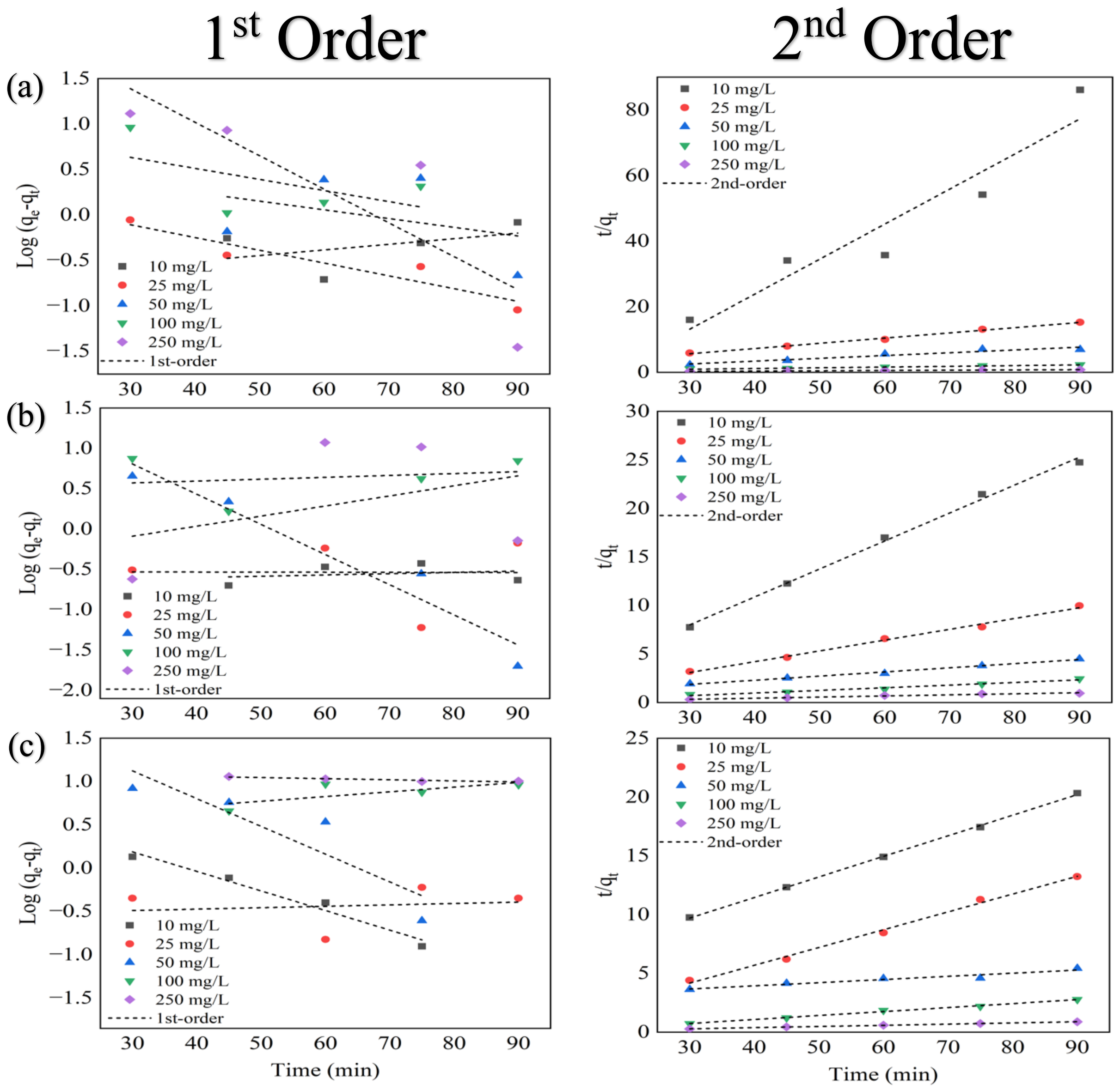

Figure. 72. Linear curve of adsorption kinetic models (a) NH_4 (b) PO_4 (c) phenol.

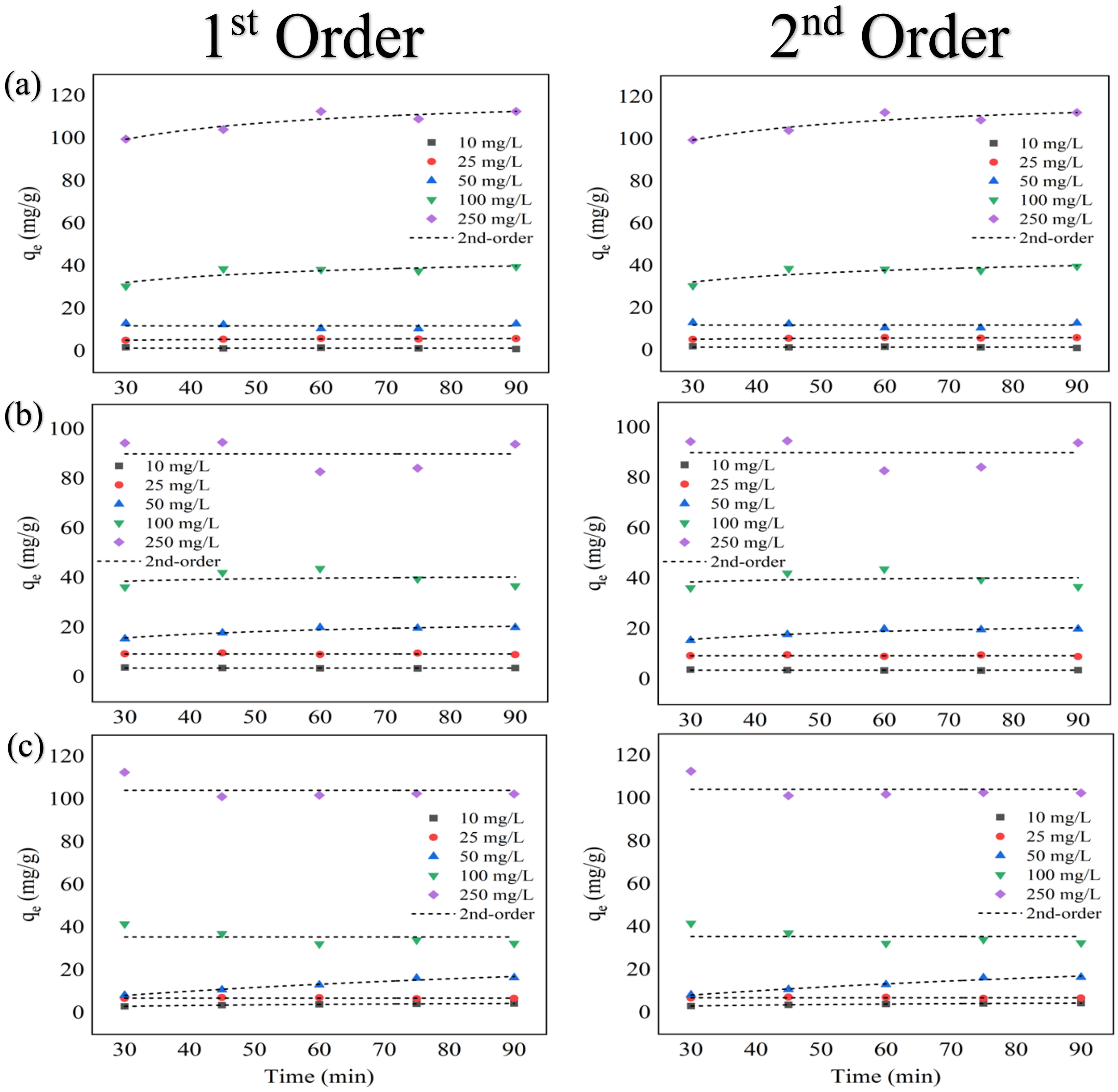

Figure. 73. Non-linear curve of adsorption kinetic models (a) NH_4 (b) PO_4 (c) phenol.

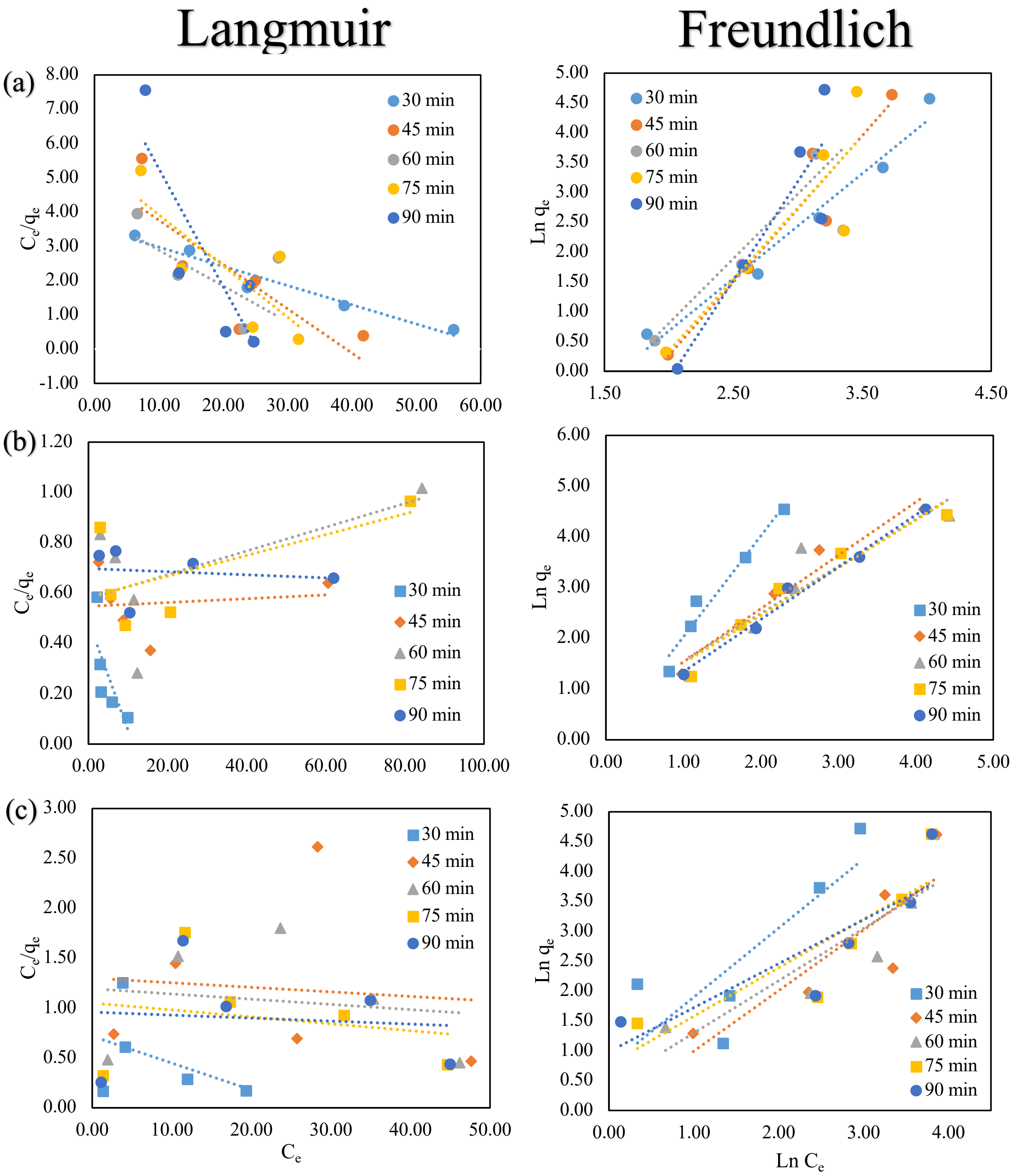

Figure. 74. Linear curve of adsorption isotherm models (a) NH_4 (b) PO_4 (c) phenol (Langmuir and Freundlich).

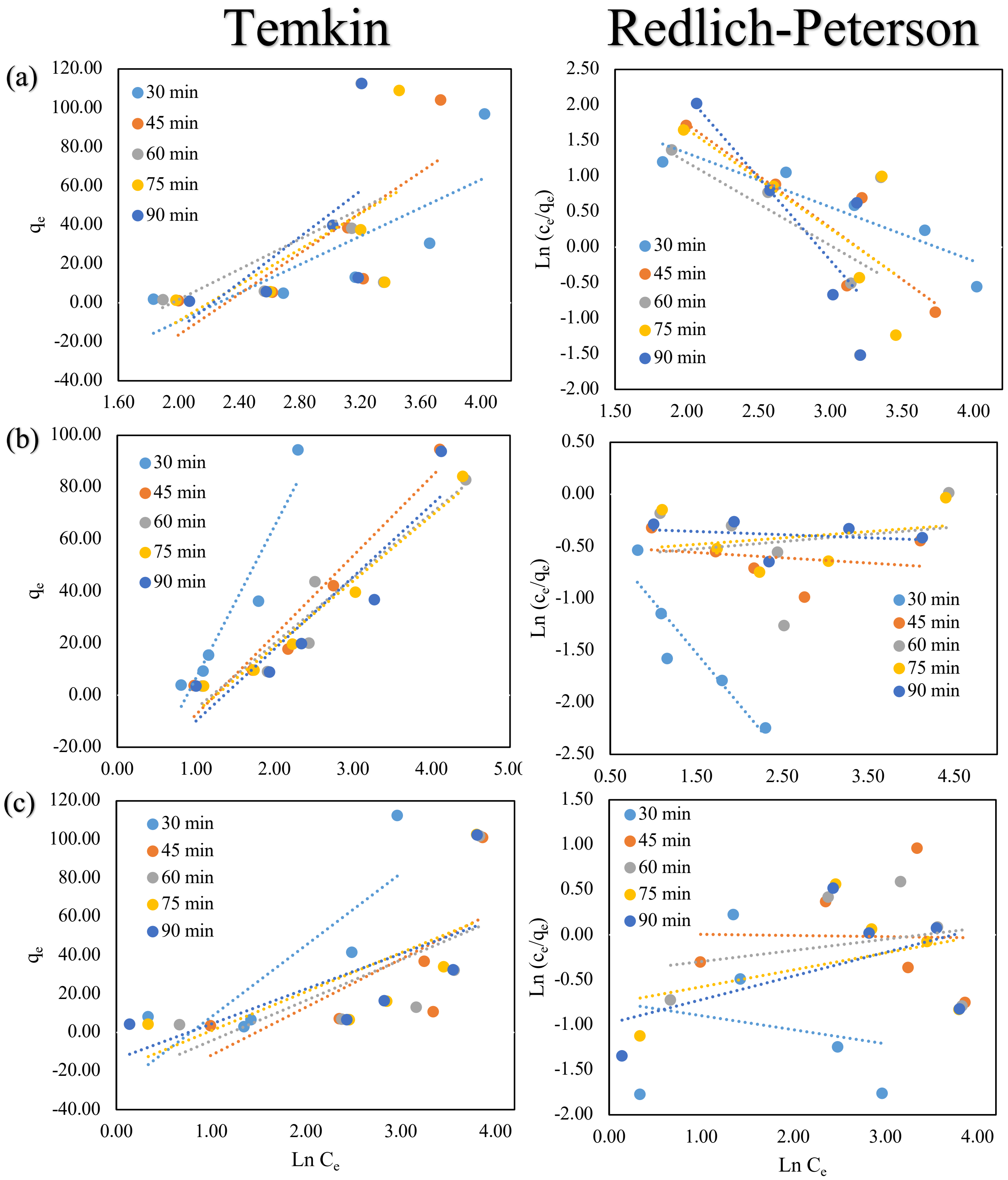

Figure. 75. Linear curve of adsorption isotherm models (a) NH_4 (b) PO_4 (c) phenol (Temkin and Redlich Peterson).

Table 22. Linear kinetic model parameters for adsorption NH_4, PO_4, and phenol.

Isotherm models	Parameters	Initial concentration (mg/L)	Value		
			NH_4	PO_4	Phenol
1st-order	R^2	10	0.2016	0.2426	0.9681
		25	0.8864	0.0030	0.0244
		50	0.1299	0.9068	0.8074
		100	0.3159	0.0071	0.5267
		250	0.7264	0.2376	0.8257
2nd-order		10	0.9110	0.9961	0.9994
		25	0.9947	0.9933	0.9948
		50	0.9251	0.9920	0.9231
		100	0.9854	0.9691	0.9938
		250	0.9968	0.9700	0.9980
2nd-order	q_e (mg/g)	10	4.6795	17.3611	28.5714
		25	31.4465	45.0450	33.0033
		50	58.4795	117.6471	185.1852
		100	222.2222	185.1852	147.0588
		250	588.2353	434.7826	500
	k_2 (g/mg min^{-1})	10	0.0121	0.0263	0.0013
		25	0.0056	0.0102	0.0123
		50	0.0573	0.0006	0.00005
		100	0.0004	0.0013	0.0008
		250	0.0003	0.0053	0.0009

Table 23. Non-linear kinetic model parameters for adsorption NH_4, PO_4, and phenol.

Isotherm models	Parameters	Initial concentration (mg/L)	Value		
			NH_4	PO_4	Phenol
1st-order	R^2	10	<0.0001	<0.0001	0.9960
		25	0.8794	<0.0001	<0.0001
		50	<0.0001	0.95879	0.9769
		100	0.8206	0.19912	<0.0001
		250	0.8298	<0.0001	<0.0001
2nd-order		10	<0.0001	<0.0001	0.9980
		25	0.7911	<0.0001	<0.0001
		50	<0.0001	0.91905	0.9757
		100	0.73963	0.0475	<0.0001
		250	0.8482	<0.0001	<0.0001

4.3.1.5 Desorption studies

The desorption percentages of NH_4, PO_4, and phenol using different desorbing agent solutions are depicted in Figure. 76. The findings indicate that HCl exhibits the highest efficacy for NH_4 and phenol, with values of 85.31% and 92.12%, respectively, while H_2SO_4 shows the highest desorption percentage for PO_4, at 79.87%. This suggests that each desorbing agent may influence the simultaneous release of ions from the adsorbent.

Table 24. Linear isotherm model parameters for adsorption NH_4, PO_4, and phenol.

Isotherm models	Parameters	Time (min)	Value		
			NH_4	PO_4	Phenol
Langmuir	R^2	30	0.9520	0.0559	0.1905
		45	0.6592	<0.0001	0.0082
		60	0.3859	0.9389	0.0240
		75	0.6275	0.0442	0.0426
		90	0.7223	0.1428	0.0090
Freundlich		30	0.9680	0.9585	0.6644
		45	0.9137	0.9607	0.7380
		60	0.6468	0.8473	0.7628
		75	0.7853	0.9399	0.7496
		90	0.8106	0.9854	0.7317
Temkin		30	0.5826	0.9085	0.6874
		45	0.6484	0.9378	0.4723
		60	0.2550	0.9139	0.4272
		75	0.4010	0.9674	0.4524
		90	0.3837	0.8409	0.4246
Redlich-Peterson		30	0.7994	0.8512	0.0349
		45	0.7883	0.0531	0.0005
		60	0.3474	0.0304	0.0602
		75	0.5550	0.0628	0.1384
		90	0.6765	0.0554	0.2584
Freundlich	K_f $(g/mg\ min^{-1})^n$	30	1.9534	1.0905	5.5187
		45	0.8257	3.050	0.9585
		60	1.005	4.2598	2.6342
		75	0.3350	3.7447	5.8339
		90	0.00000017	2.0504	9.6511
	1/n	30	0.0848	1.9910	1.1564
		45	0.1199	1.0503	1.0129
		60	0.1356	0.9301	0.8763
		75	0.1429	0.9385	0.8119
		90	3.3209	1.0304	0.7367

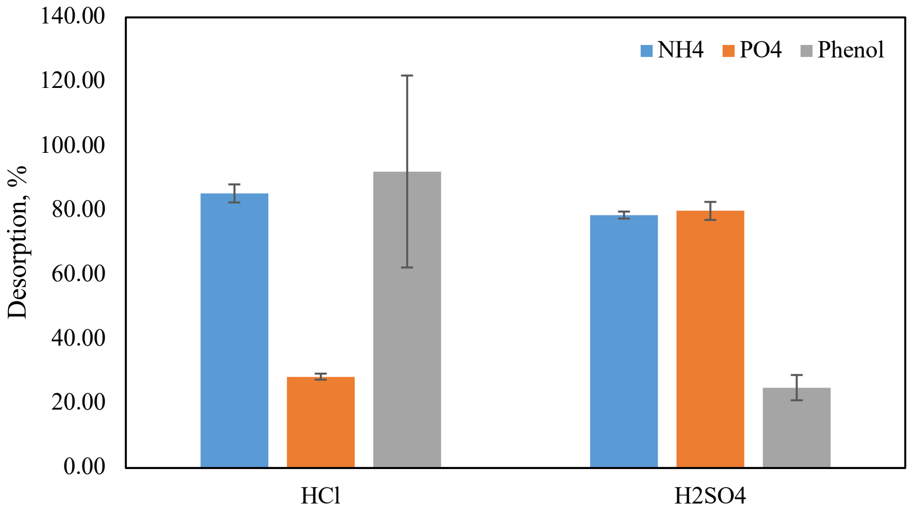

Figure. 76. Desorption studies with different agent solutions.

4.3.1.6 Soil response to the effect of adsorbent loaded adsorbate (NH_4, PO_4, and phenol)

Figure. 77 and Figure. 78 show the results of applying CBCZrOFe$_3$O$_4$-APP on soil acidity characteristics at pH levels of 2.5 and 4.0. The results revealed that the application of CBCZrOFe$_3$O$_4$-APP did not significantly ($P<0.05$) altered the exchangeable acidity (Figure. 77a) and H^+ (Figure. 77b). However, a notable decrease (P-value <0.05) was evident in soil exchangeable Al (Figure. 77c). This reduction may be ascribed to the reduced solubility of Al ions in soil water at pH levels above 5.20, thus leading to a decrease in the Al value. In addition, Al may compete with other cations for binding sites on soil particles, further contributing to the reduction in soil exchangeable Al. Furthermore, there was a significant (P-value<0.05) improvement in the soil pH (Figure. 77d) and EC (Figure. 77e) after treated with CBCZrOFe$_3$O$_4$-APP under both initial soil pH conditions. Findings from a study by Geng et al. (2022) showed similar outcome of improved soil pH after biochar addition. This increase is attributed to various metals and polymers especially coffee husk biochar in CBCZrOFe$_3$O$_4$-APP, which interact with soil and water to influence soil pH and EC.

P is one of the major plant nutrients in the soil (Bechtaoui et al., 2021). The findings indicated that there was a substantial increase in available P content in the soil containing adsorbent (P-value<0.05) compared to intact soil (pH 2.5 and 4.0) (Figure. 77f). After three days of incubation, the control sample (soil only) resulted in the lowest concentration of available P for both pH conditions. However, the soil treated with CBCZrOFe$_3$O$_4$-APP showed the most significant increase in available P content after 60 days of incubation. This is because soil P becomes more soluble at pH levels above 5.20 (after treatment) (Figure. 77d), making more P available to the soil which simultaneously explained the decrease in the Al content (Figure. 77c).

The soil CEC is shown in Figure. 77g. The results demonstrated a significant increase ($P<0.05$) in soil CEC following treatment with BCZrO@Fe$_3$O$_4$-APP compared with the control soil with the pH levels of 2.5 and 4.0. Interestingly, CEC exhibited a large increase after 15 days of incubation, followed by a significant decrease up to 60 days. This fluctuation may be attributed to the increased microbial activity during the initial incubation period, fuelled by the availability of fresh organic matter (Domingues et al., 2020). However, as decomposition progresses and organic matter content diminishes, microbial activity may decline, leading to a gradual decrease in CEC over time. Additionally, CBCZrOFe$_3$O$_4$-APP comprises carboxyl, hydroxyl, and phenolic groups on its surface, capable of attracting and retaining positively charged cations, thereby effectively enhancing the CEC of the soil.

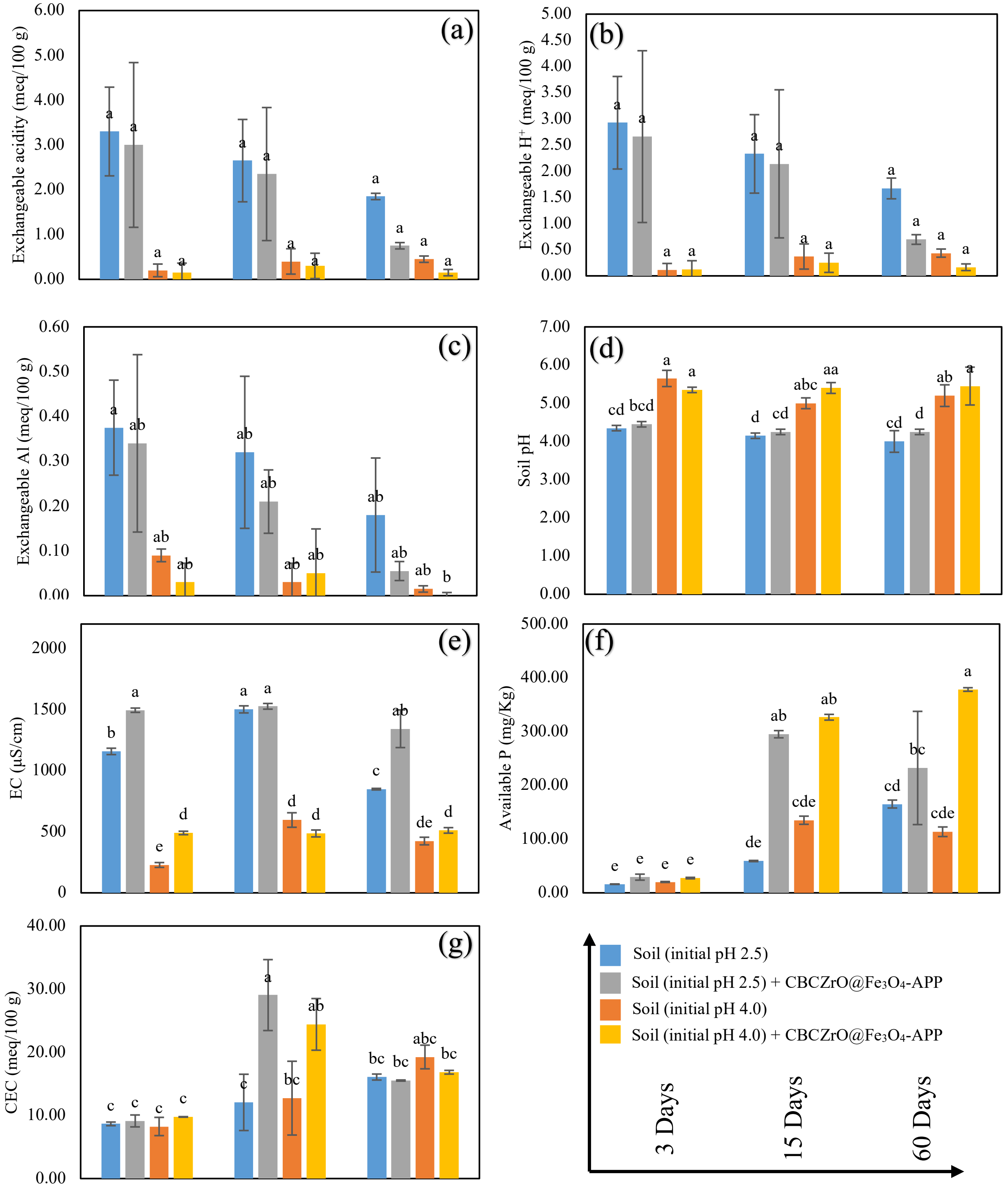

Figure. 77. Effect of CBCZrOFe$_3$O$_4$-APP on soil exchangeable acidity, exchangeable H$^+$, exchangeable Al, pH, EC, available P, and CEC. Statistical analytical by Tukey test ($P<0.05$).

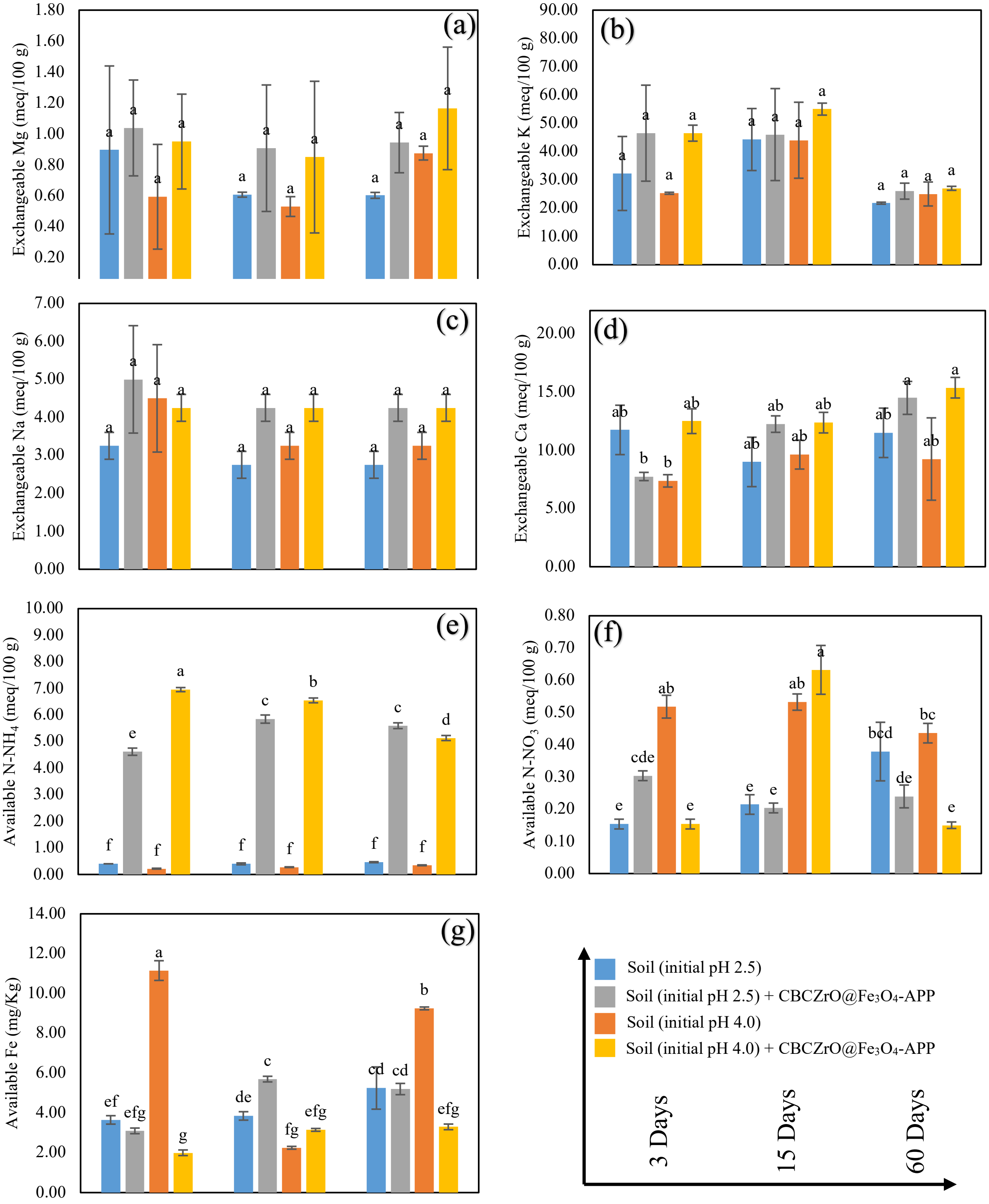

Figure. 78. Effect of CBCZrOFe$_3$O$_4$-APP on soil exchangeable Mg, K, Na and Ca, available N-NH$_4$, N-NO$_3$ and Fe. Statistical analytical by Tukey test (P<0.05).

Figure. 78a-d depict the exchangeable values of Mg, K, Na, and Ca across all treatments. The data highlight no significant difference ($P<0.05$) in soil's Mg, K, and Na values after 60 days of incubation. Conversely, Ca values increased significantly ($P<0.05$) following the treatment with CBCZrOFe$_3$O$_4$-APP. This suggests that CBCZrOFe$_3$O$_4$-APP may have a high binding preference for Ca compared to Mg, K and Na, potentially resulting in an increase in soil Ca levels. Additionally, the introduction of CBCZrOFe$_3$O$_4$-APP significantly increased available N-NH$_4$ levels in the soil ($P< 0.05$) (Figure. 78e). Specifically, CBCZrOFe$_3$O$_4$-APP + soil at an initial pH of 4.0 displayed the maximum concentration of N-NH$_4$ after a 60-day incubation period, reaching up to 93.17% of the control soil content, followed by CBCZrOFe$_3$O$_4$-APP + soil at an initial pH of 2.5 (91.78%). Moreover, the application of CBCZrOFe$_3$O$_4$-APP resulted in a substantial reduction of the N-NO$_3$ content in the soils, with a decrease of up to 65.91% after 60 days of incubation (Figure. 78f). This reduction implies that the application of CBCZrOFe$_3$O$_4$-APP, particularly at pH levels above 5.20, created conditions for Fe oxide to partially inhibited nitrification, thereby allowing more N-NH$_4$, to persist in the soil. Numerous studies have supported the role of iron oxide in forming organo-Fe precipitates (flocs) in soil which can delay the process of nitrification in soil (Jiang et al., 2015; Slimani et al., 2024).

As previously mentioned, iron oxides are likely to coprecipitate and form flocs, therefore we anticipated a decrease in the soil Fe value after treatment with CBCZrOFe$_3$O$_4$-APP. The results show a reduction in available soil Fe ($P<0.05$) (Figure. 78g). The available soil Fe content decreased by 64.32% after a 60-day incubation period with CBCZrOFe$_3$O$_4$-APP. This phenomenon could also be attributed to carboxyl and amine groups, which may acquire negative charges at pH levels of 5.2 or higher. In contrast, phenolic and hydroxyl groups from CBCZrOFe$_3$O$_4$-APP may remain neutral or negatively charged. These disparities in surface charge can influence the electrostatic interactions between the soil particles and Fe ions, consequently affecting their sorption and immobilization.

4.3.2 Evaluation of Hydrogel Beads Composites Derived from Alginate-Poly (Acrylic Acid)-Carboxylmethyl Cellulose-Oleic Acid as Slow Release NH_4 Fertilizer and Soil Acidity Conditioner with S and Fe Contaminated

4.3.2.1 Characteristics of hydrogel beads

Table 25. Porosity and carboxyl group of hydrogel beads.

Samples	Porosity (%)	COOH (mmol/g)
SPC-A	43.30 ± 7.36	21.33 ± 5.83
SPC-B	57.91 ± 32.43	38.53 ± 10.04

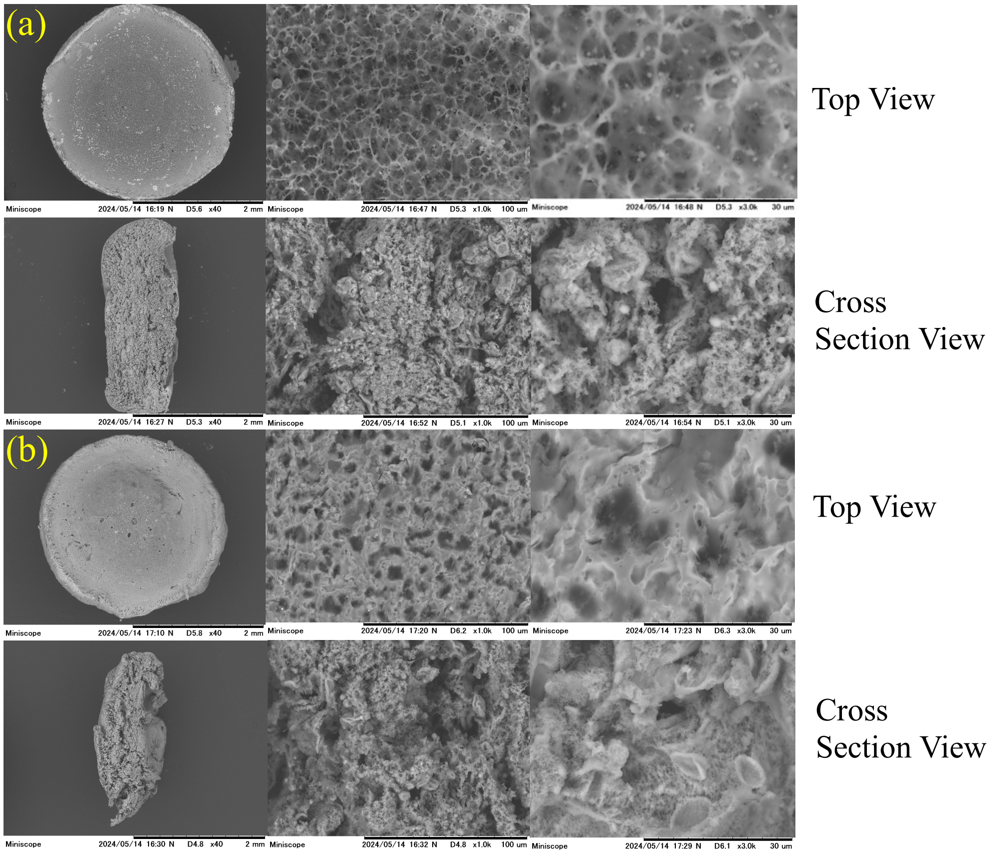

Figure. 79. SEM photograph of hydrogel beads (a) SPC-A (b) SPC-B.

Figure. 79 displays the SEM morphology images of the dried hydrogel beads. The images reveal that both SPC-A and SPC-B exhibit a 3D interconnected porous structure with macro- and micropores. SPC-B shows a more uniform bead shape with fewer open pores compared to SPC-A. These pores are beneficial for the channelling and diffusion of components into the structure.

Table 25 presents the porosity percentages and the amount of COOH groups within the hydrogel beads. The data indicate that SPC-B exhibited the highest porosity with a value of 57.91 ± 32.43, whereas the SPC-A composite demonstrated a lower porosity of 43.30 ± 7.36. The introduction of oleic acid led to a 25.22% difference. Similarly, the number of COOH groups in the SPC-B hydrogel bead was higher in comparison to the SPC-B sample with 44.64% difference.

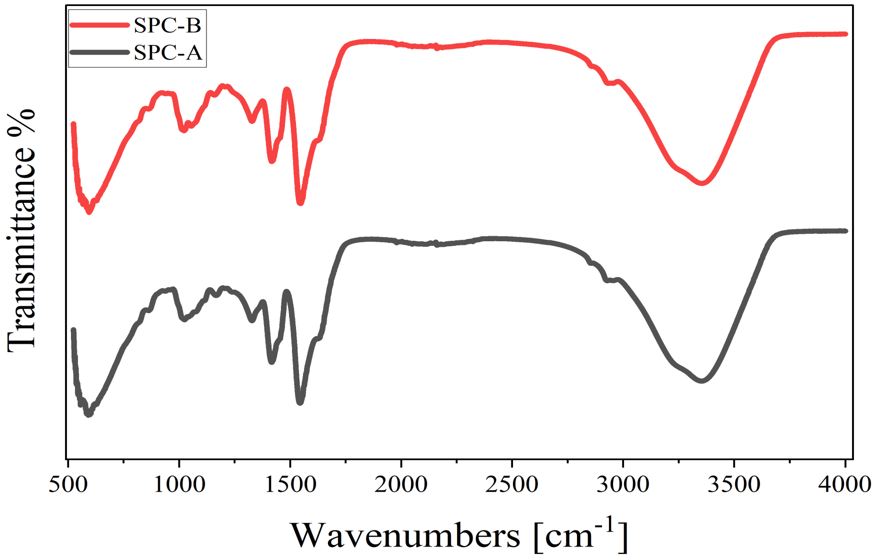

Figure. 80. FTIR spectra of hydrogel beads.

The surface functional groups of the hydrogel beads, are depicted in Figure. 80. The spectral range from 3008 cm^{-1} to 3524 cm^{-1} is attributed to the stretching vibrations of O-H bonds. A new appearance peak for SPC-B at 2161 cm^{-1} is characteristics of C≡C (Ashby et al., 2014). A increase in peak intensity from 1544 cm^{-1} to 1547 cm^{-1} for SPC-A and SPC-B, respectively, it might be due to the interaction of the hydrogel bead composite with oleic acid, which is associated with the carboxylate (-COO-) groups (Hua et al., 2010). The peaks around 1417 cm^{-1}, 1328 cm^{-1} and 1083 cm^{-1} can be attributed to the symmetric stretching of carboxylate (-COO-), (C-O), and (C-O-C), respectively (Hua et al., 2010). Additionally, the peak at 594 cm^{-1} suggests the presence of the stretching vibration of the Ca-O bond.

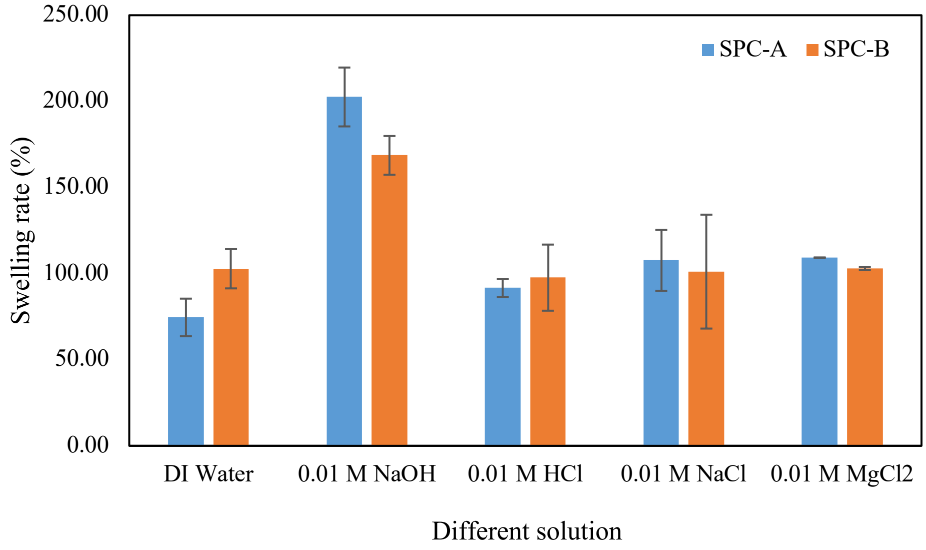

Figure. 81. Swelling rate of hydrogel beads under different solution.

4.3.2.2 Swelling behaviour

Figure. 81 illustrates the swelling behaviour of hydrogel beads when exposed to DI water, NaOH, HCl, NaCl and $MgCl_2$ solutions. The findings revealed that the swelling rate under NaOH solution was achieved higher result for both samples compared to others solution. This suggests that the hydrogel beads possess ionizable functionalities, such as carboxylic acid (-COOH) or its deprotonated form, carboxylate ($-COO^-$). In neutral, acidic and salt conditions, these groups tend to remain protonated (COOH), fostering strong electrostatic forces within the hydrogel matrix. Such forces could hinder the hydrogel's capacity to absorb water, thereby constraining its swelling capability (Al-qudah et al., 2014). Therefore, SPC-A was higher result compared to SPC-B, this is due to that the oleate ion are more hydrophobic compared to the non-ionized form of oleic acid. This means they have a lower affinity for water molecules.

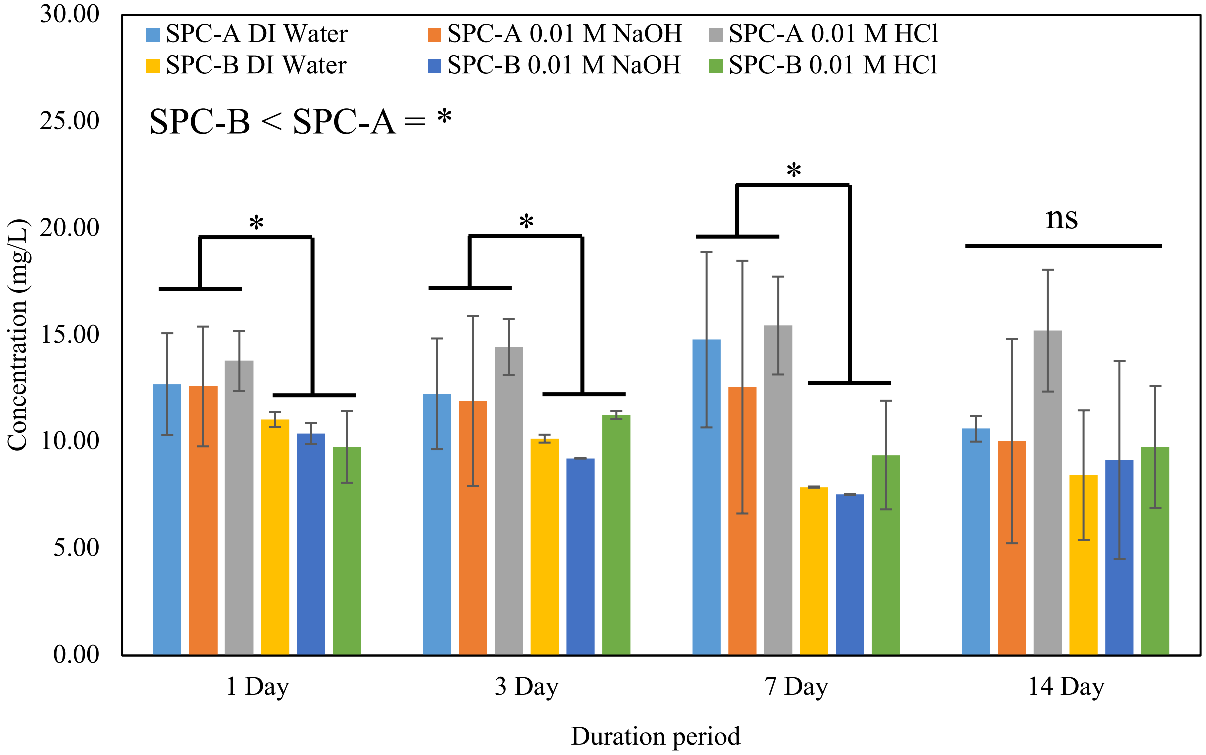

Figure. 82. Slow release NH_4 rate from hydrogel beads. (*) Indicates statistically significant at a significance level of $P \leq 0.05$; (ns) denotes no significant difference in Tukey's test.

4.3.2.3 NH_4 release rate

This present study investigated the NH_4 release profiles of hydrogel bead composites using DI water, NaOH and HCl. The findings demonstrate that SPC-A exhibits a greater ease of dissolution, leading to a higher release of NH_4 compared to the SPC-B, as shown in Figure. 82. The average release rates of SPC-A were 12.59 mg/L, 11.78 mg/L, and 14.73 mg/L for DI water, NaOH, and HCl, respectively, whereas for SPC-B, they were 9.39 mg/L, 9.08 mg/L, and 10.05 mg/L. This indicates a difference of approximately 25.45%, 22.91%, and 31.77% in NH_4 release. These percentage differences may be attributed to the complex and intricate structure formed by the layers of oleic acid, which obstructs the movement of minerals through the polymer network and into the surrounding environment.

4.3.2.4 Impacts of amendments on soil CO_2 emissions

Effect of hydrogel beads on carbon dioxide emission rate is presented in Figure. 83. Carbon dioxide emission results were statistically significant at all the studied durations. Maximum carbon dioxide emissions (869 for intact soil (control), 714 mg/L for SPC-A and 583 mg/L for SPC-B) was found at 9 days after incubation, then it decreased and increased with the increase of time. However, SPC-B show the lowest value compared to the SPC-A, and control, it might be indicates that oleate ion have capability to hold or sequester CO_2 emission from soil.

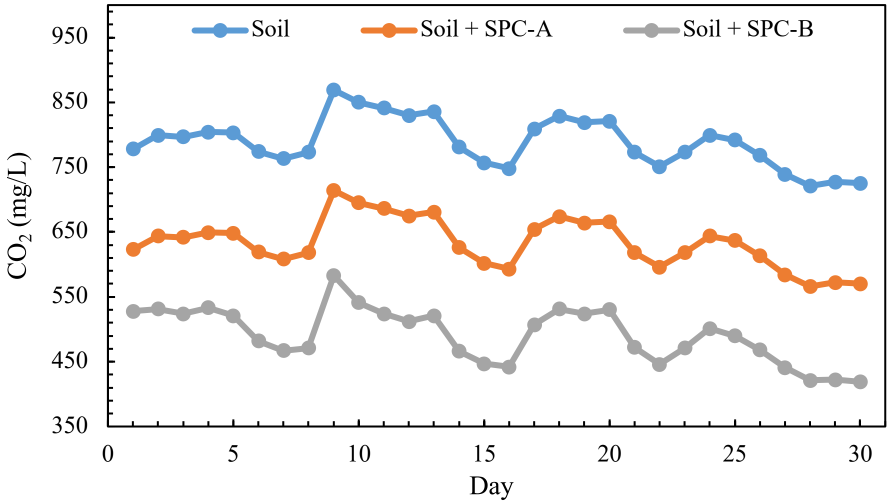

Figure. 83. CO_2 release from soil regarding hydrogel beads application.

4.3.2.5 Impacts of amendments on soil characteristics

Figure. 84 depicts the impact of treatment amendments on soil pH, EC, available P, CEC, SOC, available S, available Fe and immobilization rate of S and Fe under high contaminated S and Fe. As shown in Figure. 84a and 84b, the soil pH and EC show there is no significant difference for all samples. Conversely, the level of available phosphorus (P) in the soil showed a significant increase ($P<0.05$) following treatment with the order of increase being SPC-B>SPC-A>soil, as illustrated in Figure. 84c. This enhancement in available P may be attributed that oleate ion promotes to the mineralization of P during the incubation period. Furthermore, the cation exchange capacity (CEC) of the soil was significantly difference ($P<0.05$) when compared to the soil (control) (Figure. 84d). This increase is likely duo the presence of -OH and -COOH groups from polymer materials in hydrogel beads. Figure. 84e-h displayed the exchangeable cation (Mg, Ca, K and Na). The results show that there is no significant difference for Mg, and K, by contrast for Ca and Na value. It might be indicated that the presence of Ca from hydrogel beads enhance soil Ca, whereas Na ions was adsorb into the hydrogel beads which decreased after treated hydrogel beads. Moreover, the soil organic carbon (SOC) value showed a significantly difference ($P<0.05$) with the addition of hydrogel bead amendments following treatment SPC-B>SPC-A>soil, as displayed in Figure. 84i. This is might be due to that oleate ion can interact with soil minerals and organic matter to form more stable organo-mineral complexes. These complexes can protect organic carbon from rapid decomposition, thereby increasing the SOC. It can be suggest that a correlation between SOC and CO_2 emission (Figure. 83) which contributes long-term carbon sequestration in the soil.

Figure. 85a-b show the available $N–NH_4$ and $N-NO_3$ level in the soil. The results show that there is significant difference for $N-NH_4$ value, in contrast to $N-NO_3$. Moreover, SPC-B applications show the highest $N-NH_4$ and lowest the content of $N–NO_3$. It might be indicated that the presence of oleate ion inhibit the transformation of $N–NH_4$ from oxidized into $N–NO_3$, which correlate with SOC value and CO_2 emission in soil. Figure. 85c-d show the concentration of available S in soil decreased markedly following the application of treated hydrogel beads ($P<0.05$). After a 30-day incubation period, the As concentrations were reduced to 3514 mg/Kg and 450 mg/Kg for SPC-A and SPC-B, respectively, from control concentration of 6770 mg/Kg. This corresponds to immobilization rates of 48.10% for SPC-A and 93.36% for SPC-B. Similarly, the Fe concentrations were also reduced with immobilization rates of 87.03% for SPC-A and 88.33% for SPC-B.

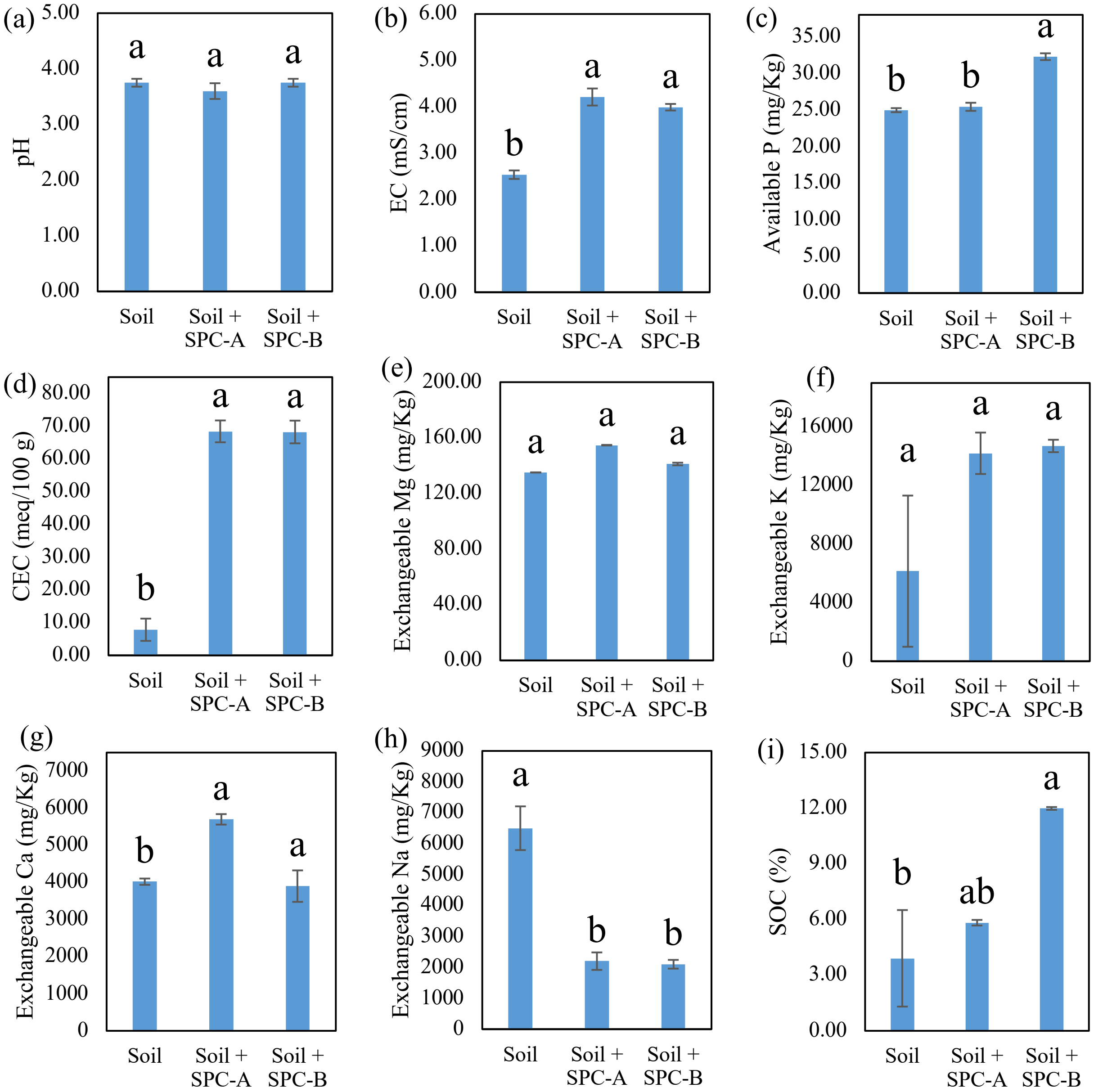

Figure. 84. Effect of hydrogel beads on soil characteristics. Statistically significant at a significance level of $P \leq 0.05$ in Tukey's test.

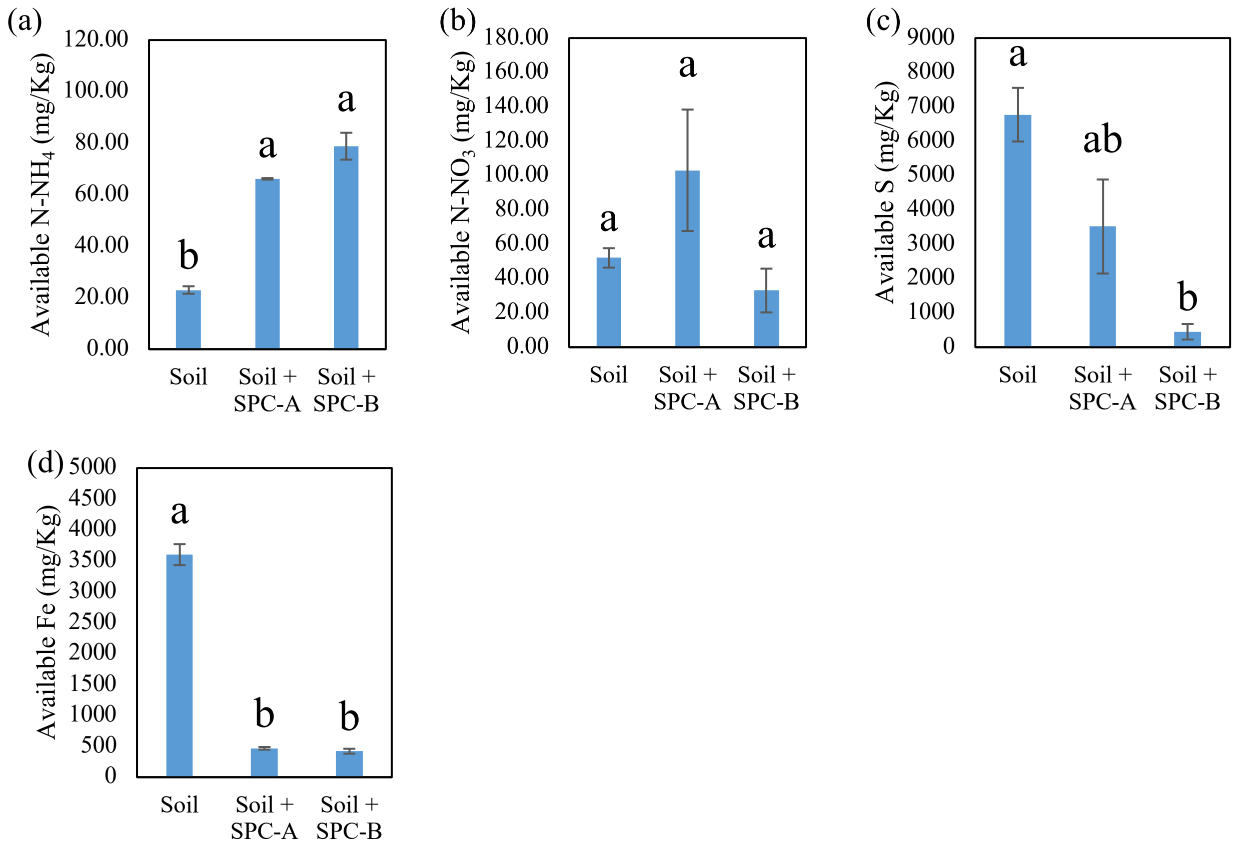

Figure. 85. Effect of hydrogel beads on soil characteristics. Statistically significant at a significance level of P ≤ 0.05 in Tukey's test.

4.4 Conclusion

4.4.1 Simultaneous removal of ammonium, phosphate, and phenol via self-assembled biochar composites CBCZrOFe_3O_4 and its utilization as soil acidity amelioration

In this study, biochar composite materials were prepared and utilized to remove water pollutants, such as NH_4, PO_4, and phenol, followed by their application to improve soil acidity. Initially, comparative studies on the simultaneous removal of NH_4, PO_4, and phenol using CB (biochar), CBC (biochar + chitosan), CBCZrO (biochar + chitosan + ZrO), and CBCZrOFe_3O_4 (biochar + chitosan + ZrO + Fe_3O_4) were conducted. The results discovered that CBCZrOFe_3O_4 exhibited the highest removal percentage among the adsorbents ($P<0.05$). The adsorption kinetics followed a second-order model, whereas the isotherms adapted to the Freundlich model.

Desorption studies revealed that HCl is more effective at desorbing NH_4 and phenol, whereas H_2SO_4 is more efficient for PO_4. In our hypothesis suggests that the treated adsorbent, containing ammonium, phosphate, and phenol, can be reused for soil acidity treatment, enhancing soil characteristics and reducing nitrification. The $CBCZrOFe_3O_4$ sample was chosen for soil experiments due to its highest removal percentage. Results from soil acidity incubation experiments demonstrated a significant increase in soil pH, electrical conductivity (EC), available phosphorus (P), cation exchange capacity (CEC), ammonium nitrogen ($N\text{-}NH_4$), and nitrate nitrogen ($N\text{-}NO_3$). However, no significant changes ($P<0.05$) were observed in soil exchangeable acidity, hydrogen ions (H^+), magnesium (Mg), potassium (K), or sodium (Na). Additionally, a notable decrease was observed in available soil exchangeable aluminum (Al) and iron (Fe) ($P<0.05$). Overall, this innovative adsorbent exhibits promising potential for soil applications. Despite that, further studies and improvement are necessary to maximize the efficiency of this material, particularly in addressing exchangeable acidity and nitrogen fixation processes to improve overall soil's properties.

4.4.2 Evaluation of Hydrogel Beads Composites Derived from Alginate-Poly (Acrylic Acid)-Carboxylmethyl Cellulose-Oleic Acid as Slow Release NH_4 Fertilizer and Soil Acidity Conditioner with S and Fe Contaminated

In this study, a slow-release mineral fertilizer was prepared from sodium alginate, poly (acrylic acid) and carboxylmethyl cellulose and NH_4, which has rich N source. The absence (SPC-A) and presence (SPC-B) of oleic acid were investigated. The results show that SPC-B has high porosity and the amount of COOH groups. Swelling behaviour indicates that the highest results was obtained under NaOH solution for all samples. Slow release fertilizer studies indicated that the presence of oleic acid has a low amount of NH_4 release with difference percentage of 25.45%, 22.91%, and 31.77%, for DI water, NaOH and HCl, respectively. The CO_2 data obtained that oleic acid have capability to sequester CO_2 emission from soil which is similar trends with soil organic carbon results. The immobilization rate show satisfactory up to 84.26% for S and 99.76% for Fe.

References:

Abd El-Aziz, M. E., Salama, D. M., Morsi, S. M. M., Youssef, A. M., & El-Sakhawy, M. (2022). Development of polymer composites and encapsulation technology for slow-release fertilizers. Reviews in Chemical Engineering, 38(5), 603–616. https://doi.org/10.1515/revce-2020-0044

Abdellaoui, Y., Abou Oualid, H., Hsini, A., El Ibrahimi, B., Laabd, M., El Ouardi, M., Giácoman-Vallejos, G., & Gamero-Melo, P. (2021). Synthesis of zirconium-modified Merlinoite from fly ash for enhanced removal of phosphate in aqueous medium: Experimental studies supported by Monte Carlo/SA simulations. Chemical Engineering Journal, 404, 126600. https://doi.org/10.1016/j.cej.2020.126600

Abdelwahab, O., & Amin, N. K. (2013). Adsorption of phenol from aqueous solutions by Luffa cylindrica fibers: Kinetics, isotherm and thermodynamic studies. Egyptian Journal of Aquatic Research, 39(4), 215–223. https://doi.org/10.1016/j.ejar.2013.12.011

Al Bsoul, A., Hailat, M., Abdelhay, A., Tawalbeh, M., Al-Othman, A., Al-kharabsheh, I. N., & Al-Taani, A. A. (2021). Efficient removal of phenol compounds from water environment using Ziziphus leaves adsorbent. Science of the Total Environment, 761. https://doi.org/10.1016/j.scitotenv.2020.143229

Alam, M. N., & Christopher, L. P. (2018). Natural Cellulose-Chitosan Cross-Linked Superabsorbent Hydrogels with Superior Swelling Properties. ACS Sustainable Chemistry & Engineering, 6(7), 8736–8742. https://doi.org/10.1021/acssuschemeng.8b01062

Allahkarami, E., Dehghan Monfared, A., Silva, L. F. O., & Dotto, G. L. (2023). Toward a mechanistic understanding of adsorption behavior of phenol onto a novel activated carbon composite. Scientific Reports, 13(1). https://doi.org/10.1038/s41598-023-27507-5

Al-qudah, Y. H. F., Mahmoud, G. A., & Abdel Khalek, M. A. (2014). Radiation crosslinked poly (vinyl alcohol)/acrylic acid copolymer for removal of heavy metal ions from aqueous solutions. Journal of Radiation Research and Applied Sciences, 7(2), 135–145. https://doi.org/10.1016/j.jrras.2013.12.008

Aranaz, I., Alcántara, A. R., Civera, M. C., Arias, C., Elorza, B., Heras Caballero, A., & Acosta, N. (2021). Chitosan: An Overview of Its Properties and Applications. Polymers, 13(19), 3256. https://doi.org/10.3390/polym13193256

Ashby, S. P., Thomas, J. A., García-Cañadas, J., Min, G., Corps, J., Powell, A. V., Xu, H., Shen, W., & Chao, Y. (2014). Bridging silicon nanoparticles and thermoelectrics: phenylacetylene functionalization. Faraday Discuss., 176, 349–361. https://doi.org/10.1039/C4FD00109E

Azizi, A. (2020). Green Synthesis of Fe3O4 Nanoparticles and Its Application in Preparation of Fe3O4/Cellulose Magnetic Nanocomposite: A Suitable Proposal for Drug Delivery Systems. Journal of Inorganic and Organometallic Polymers and Materials, 30(9), 3552–3561. https://doi.org/10.1007/s10904-020-01500-1

Bechtaoui, N., Rabiu, M. K., Raklami, A., Oufdou, K., Hafidi, M., & Jemo, M. (2021). Phosphate-Dependent Regulation of Growth and Stresses Management in Plants. Frontiers in Plant Science, 12. https://doi.org/10.3389/fpls.2021.679916

Begum, S. A., Golam Hyder, A. H. M., Hicklen, Q., Crocker, T., & Oni, B. (2021). Adsorption characteristics of ammonium onto biochar from an aqueous solution. Journal of Water

Supply: Research and Technology-Aqua, 70(1), 113–122. https://doi.org/10.2166/aqua.2020.062

Blaney, L., Cinar, S., & Sengupta, A. (2007). Hybrid anion exchanger for trace phosphate removal from water and wastewater. Water Research, 41(7), 1603–1613. https://doi.org/10.1016/j.watres.2007.01.008

Cai, T., Park, S. Y., & Li, Y. (2013). Nutrient recovery from wastewater streams by microalgae: Status and prospects. Renewable and Sustainable Energy Reviews, 19, 360–369. https://doi.org/10.1016/j.rser.2012.11.030

Chatterjee, R., Sajjadi, B., Chen, W. Y., Mattern, D. L., Hammer, N., Raman, V., & Dorris, A. (2020). Effect of Pyrolysis Temperature on PhysicoChemical Properties and Acoustic-Based Amination of Biochar for Efficient CO2 Adsorption. Frontiers in Energy Research, 8. https://doi.org/10.3389/fenrg.2020.00085

Chen, M., Ding, S., Chen, X., Sun, Q., Fan, X., Lin, J., Ren, M., Yang, L., & Zhang, C. (2018). Mechanisms driving phosphorus release during algal blooms based on hourly changes in iron and phosphorus concentrations in sediments. Water Research, 133, 153–164. https://doi.org/10.1016/j.watres.2018.01.040

Chen, Y., Gao, Y., Ng, C. W. W., & Guo, H. (2021). Bio-improved hydraulic properties of sand treated by soybean urease induced carbonate precipitation and its application Part 1: Water retention ability. Transportation Geotechnics, 27, 100489. https://doi.org/10.1016/j.trgeo.2020.100489

Cordova Estrada, A. K., Cordova Lozano, F., & Lara Díaz, R. A. (2021). Thermodynamics and Kinetic Studies for the Adsorption Process of Methyl Orange by Magnetic Activated Carbons. Air, Soil and Water Research, 14. https://doi.org/10.1177/11786221211013336

Domingues, R. R., Sánchez-Monedero, M. A., Spokas, K. A., Melo, L. C. A., Trugilho, P. F., Valenciano, M. N., & Silva, C. A. (2020). Enhancing Cation Exchange Capacity of Weathered Soils Using Biochar: Feedstock, Pyrolysis Conditions and Addition Rate. Agronomy, 10(6), 824. https://doi.org/10.3390/agronomy10060824

Driscoll, C. T., Driscoll, K. M., Fakhraei, H., & Civerolo, K. (2016). Long-term temporal trends and spatial patterns in the acid-base chemistry of lakes in the Adirondack region of New York in response to decreases in acidic deposition. Atmospheric Environment, 146, 5–14. https://doi.org/10.1016/j.atmosenv.2016.08.034

Emenike, E. C., Ogunniyi, S., Ighalo, J. O., Iwuozor, K. O., Okoro, H. K., & Adeniyi, A. G. (2022). Delonix regia biochar potential in removing phenol from industrial wastewater. Bioresource Technology Reports, 19, 101195. https://doi.org/10.1016/j.biteb.2022.101195

Enoch, K., & Somasundaram, A. A. (2023). Rheological insights on Carboxymethyl cellulose hydrogels. International Journal of Biological Macromolecules, 253, 127481. https://doi.org/10.1016/j.ijbiomac.2023.127481

Faturechi, R., Karimi, A., Hashemi, A., Yousefi, H., & Navidbakhsh, M. (2015). Influence of Poly(acrylic acid) on the mechanical properties of composite hydrogels. Advances in Polymer Technology, 34(2). https://doi.org/10.1002/adv.21487

Fidel, R. B., Laird, D. A., Thompson, M. L., & Lawrinenko, M. (2017). Characterization and quantification of biochar alkalinity. Chemosphere, 167, 367–373. https://doi.org/10.1016/j.chemosphere.2016.09.151

Fu, Z., Li, H., Yang, L., Yuan, H., Jiao, Z., Chen, L., Huang, J., & Liu, Y.-N. (2015). Magnetic polar post-cross-linked resin and its adsorption towards salicylic acid from aqueous solution. Chemical Engineering Journal, 273, 240–246. https://doi.org/10.1016/j.cej.2015.03.005

Geng, N., Kang, X., Yan, X., Yin, N., Wang, H., Pan, H., Yang, Q., Lou, Y., & Zhuge, Y. (2022). Biochar mitigation of soil acidification and carbon sequestration is influenced by materials and temperature. Ecotoxicology and Environmental Safety, 232, 113241. https://doi.org/10.1016/j.ecoenv.2022.113241

González-Morales, C., Fernández, B., Molina, F. J., Naranjo-Fernández, D., Matamoros-Veloza, A., & Camargo-Valero, M. A. (2021). Influence of pH and Temperature on Struvite Purity and Recovery from Anaerobic Digestate. Sustainability, 13(19), 10730. https://doi.org/10.3390/su131910730

Gundogdu, A., Duran, C., Senturk, H. B., Soylak, M., Ozdes, D., Serencam, H., & Imamoglu, M. (2012). Adsorption of phenol from aqueous solution on a low-cost activated carbon produced from tea industry waste: Equilibrium, kinetic, and thermodynamic study. Journal of Chemical and Engineering Data, 57(10), 2733–2743. https://doi.org/10.1021/je300597u

Harada, H., Hidayat, E., Uemoto, S., & Fujita, K. (2021). Extraction of phosphorous from thermally treated sludge and separation of aluminum by adsorption. Journal of Material Cycles and Waste Management, 23(6), 2112–2119. https://doi.org/10.1007/s10163-021-01273-w

Hättenschwiler, S., & Vitousek, P. M. (2000). The role of polyphenols in terrestrial ecosystem nutrient cycling. Trends in Ecology & Evolution, 15(6), 238–243. https://doi.org/10.1016/S0169-5347(00)01861-9

Hidayat, E., Afriliana, A., Gusmini, G., Taizo, M., & Harada, H. (2020). Evaluate of Coffee Husk Compost. International Journal on Food, Agriculture and Natural Resources, 1(1), 37–43. https://doi.org/10.46676/ij-fanres.v1i1.8

Hu, X., Zhang, X., Ngo, H. H., Guo, W., Wen, H., Li, C., Zhang, Y., & Ma, C. (2020). Comparison study on the ammonium adsorption of the biochars derived from different kinds of fruit peel. Science of The Total Environment, 707, 135544. https://doi.org/10.1016/j.scitotenv.2019.135544

Hua, S., Ma, H., Li, X., Yang, H., & Wang, A. (2010). pH-sensitive sodium alginate/poly(vinyl alcohol) hydrogel beads prepared by combined Ca2+ crosslinking and freeze-thawing cycles for controlled release of diclofenac sodium. International Journal of Biological Macromolecules, 46(5), 517–523. https://doi.org/10.1016/j.ijbiomac.2010.03.004

Huang, W., Zhang, Y., & Li, D. (2017). Adsorptive removal of phosphate from water using mesoporous materials: A review. Journal of Environmental Management, 193, 470–482. https://doi.org/10.1016/j.jenvman.2017.02.030

Jawad, A. H., Hameed, B. H., & Abdulhameed, A. S. (2023). Synthesis of biohybrid magnetic chitosan-polyvinyl alcohol/MgO nanocomposite blend for remazol brilliant blue R dye adsorption: solo and collective parametric optimization. Polymer Bulletin, 80(5), 4927–4947. https://doi.org/10.1007/s00289-022-04294-z

Jiang, X., Xin, X., Li, S., Zhou, J., Zhu, T., Müller, C., Cai, Z., & Wright, A. L. (2015). Effects of Fe oxide on N transformations in subtropical acid soils. Scientific Reports, 5(1), 8615. https://doi.org/10.1038/srep08615

Jing, H. P., Li, Y., Wang, X., Zhao, J., & Xia, S. (2019). Simultaneous recovery of phosphate, ammonium and humic acid from wastewater using a biochar supported Mg(OH)2/bentonite composite. Environmental Science: Water Research and Technology, 5(5), 931–943. https://doi.org/10.1039/c8ew00952j

Kim, Y. M., Park, D., Lee, D. S., & Park, J. M. (2008). Inhibitory effects of toxic compounds on nitrification process for cokes wastewater treatment. Journal of Hazardous Materials, 152(3), 915–921. https://doi.org/10.1016/j.jhazmat.2007.07.065

Kraus, T. E. C., Dahlgren, R. A., & Zasoski, R. J. (2003). Tannins in nutrient dynamics of forest ecosystems - a review. Plant and Soil, 256(1), 41–66. https://doi.org/10.1023/A:1026206511084

Kreslavski, V. D., Shmarev, A. N., Ivanov, A. A., Zharmukhamedov, S. K., Strokina, V., Kosobryukhov, A., Yu, M., Allakhverdiev, S. I., & Shabala, S. (2023). Effects of iron oxide nanoparticles (Fe3O4) and salinity on growth, photosynthesis, antioxidant activity and distribution of mineral elements in wheat (Triticum aestivum). Functional Plant Biology, 50(11), 932–940. https://doi.org/10.1071/FP23085

Lawal, A. A., Hassan, M. A., Ahmad Farid, M. A., Tengku Yasim-Anuar, T. A., Samsudin, M. H., Mohd Yusoff, M. Z., Zakaria, M. R., Mokhtar, M. N., & Shirai, Y. (2021). Adsorption mechanism and effectiveness of phenol and tannic acid removal by biochar produced from oil palm frond using steam pyrolysis. Environmental Pollution, 269, 116197. https://doi.org/10.1016/j.envpol.2020.116197

Li, R., Wang, J. J., Zhou, B., Zhang, Z., Liu, S., Lei, S., & Xiao, R. (2017). Simultaneous capture removal of phosphate, ammonium and organic substances by MgO impregnated biochar and its potential use in swine wastewater treatment. Journal of Cleaner Production, 147, 96–107. https://doi.org/10.1016/j.jclepro.2017.01.069

Li, W., Zhang, L., Hu, D., Yang, R., Zhang, J., Guan, Y., Lv, F., & Gao, H. (2021). A mesoporous nanocellulose/sodium alginate/carboxymethyl-chitosan gel beads for efficient adsorption of

Cu2+ and Pb2+. International Journal of Biological Macromolecules, 187, 922–930. https://doi.org/10.1016/j.ijbiomac.2021.07.181

Lita, A. L., Hidayat, E., Mohamad Sarbani, N. M., Harada, H., Yonemura, S., Mitoma, Y., Herviyanti, & Gusmini. (2023). Glyphosate Removal from Water Using Biochar Based Coffee Husk Loaded Fe3O4. Water, 15(16), 2945. https://doi.org/10.3390/w15162945

Liu, L., Sun, P., Chen, Y., Li, X., & Zheng, X. (2023). Distinct chromium removal mechanisms by iron-modified biochar under varying pH: Role of iron and chromium speciation. Chemosphere, 331, 138796. https://doi.org/10.1016/j.chemosphere.2023.138796

Liu, R., Yang, Z., Wang, G., Xian, J., Li, T., Pu, Y., Jia, Y., Zhou, W., Cheng, Z., Zhang, S., Xiang, G., & Xu, X. (2021). Simultaneous removal of ammonium and phosphate in aqueous solution using Chinese herbal medicine residues: Mechanism and practical performance. Journal of Cleaner Production, 313. https://doi.org/10.1016/j.jclepro.2021.127945

Matei, A., & Racoviteanu, G. (2021). Review of the technologies for nitrates removal from water intended for human consumption. IOP Conference Series: Earth and Environmental Science, 664(1), 012024. https://doi.org/10.1088/1755-1315/664/1/012024

Min, K., Freeman, C., Kang, H., & Choi, S.-U. (2015). The Regulation by Phenolic Compounds of Soil Organic Matter Dynamics under a Changing Environment. BioMed Research International, 2015, 1–11. https://doi.org/10.1155/2015/825098

Misra, D., Dutta, W., Jha, G., & Ray, P. (2023). Interactions and Regulatory Functions of Phenolics in Soil-Plant-Climate Nexus. Agronomy, 13(2), 280. https://doi.org/10.3390/agronomy13020280

Modrzejewska, Z. (2013). Sorption mechanism of copper in chitosan hydrogel. Reactive and Functional Polymers, 73(5), 719–729. https://doi.org/10.1016/j.reactfunctpolym.2013.02.014

Mohamad Sarbani, N. M., Hidayat, E., Naito, K., Mitoma, Y., & Harada, H. (2023). Cr (VI) and Pb (II) Removal Using Crosslinking Magnetite-Carboxymethyl Cellulose-Chitosan Hydrogel Beads. Gels, 9(8), 612. https://doi.org/10.3390/gels9080612

Nancharaiah, Y. V., Venkata Mohan, S., & Lens, P. N. L. (2016). Recent advances in nutrient removal and recovery in biological and bioelectrochemical systems. Bioresource Technology, 215, 173–185. https://doi.org/10.1016/j.biortech.2016.03.129

Nga, N. K., Thuy Chau, N. T., & Viet, P. H. (2020). Preparation and characterization of a chitosan/MgO composite for the effective removal of reactive blue 19 dye from aqueous solution. Journal of Science: Advanced Materials and Devices, 5(1), 65–72. https://doi.org/10.1016/j.jsamd.2020.01.009

Nguyen, T. T. N., Némery, J., Gratiot, N., Strady, E., Tran, V. Q., Nguyen, A. T., Aimé, J., & Peyne, A. (2019). Nutrient dynamics and eutrophication assessment in the tropical river system of Saigon – Dongnai (southern Vietnam). Science of The Total Environment, 653, 370–383. https://doi.org/10.1016/j.scitotenv.2018.10.319

Pawar, R. R., Gupta, P., Lalhmunsiama, Bajaj, H. C., & Lee, S.-M. (2016). Al-intercalated acid activated bentonite beads for the removal of aqueous phosphate. Science of The Total Environment, 572, 1222–1230. https://doi.org/10.1016/j.scitotenv.2016.08.040

Qurrat-Ul-Ain, Khatoon, J., Shah, M. R., Malik, M. I., Khan, I. A. T., Khurshid, S., & Naz, R. (2019). Convenient pH-responsive removal of Acid Black 1 by green l-histidine/iron oxide magnetic nanoadsorbent from water: Performance and mechanistic studies. RSC Advances, 9(6), 2978–2996. https://doi.org/10.1039/c8ra09279f

Ravikumar, N., Gaddamanugu, G., & Anand Solomon, K. (2013). Structural, spectroscopic (FT-IR, FT-Raman) and theoretical studies of the 1:1 cocrystal of isoniazid with p-coumaric acid. Journal of Molecular Structure, 1033, 272–279. https://doi.org/10.1016/j.molstruc.2012.10.029

Rodrigues, L. A., & da Silva, M. L. C. P. (2009). An investigation of phosphate adsorption from aqueous solution onto hydrous niobium oxide prepared by co-precipitation method. Colloids and Surfaces A: Physicochemical and Engineering Aspects, 334(1–3), 191–196. https://doi.org/10.1016/j.colsurfa.2008.10.023

Satheesh Kumar, K. V., Bindu, M., Suresh, S., Anil, A., Sujoy, S., Mohanan, A., & Periyat, P. (2023). Investigation on swelling behavior of sodium alginate/black titania nanocomposite hydrogels and effect of synthesis conditions on water uptake. Results in Engineering, 20, 101460. https://doi.org/10.1016/j.rineng.2023.101460

Shakoor, M. B., Ye, Z.-L., & Chen, S. (2021). Engineered biochars for recovering phosphate and ammonium from wastewater: A review. Science of The Total Environment, 779, 146240. https://doi.org/10.1016/j.scitotenv.2021.146240

Silveira Junior, E. G., Perez, V. H., de Paula, S. C. S. E., Silveira, T. da C., Olivares, F. L., & Justo, O. R. (2023). Coffee Husks Valorization for Levoglucosan Production and Other Pyrolytic Products through Thermochemical Conversion by Fast Pyrolysis. Energies, 16(6). https://doi.org/10.3390/en16062835

Slimani, I., Doane, T., Zhu-Barker, X., Lazicki, P., Lybrand, R. A., Zaharescu, D. G., & Horwath, W. (2024). Iron-organic carbon coprecipitates reduce nitrification by restricting molybdenum in agricultural soils. Frontiers in Materials, 11. https://doi.org/10.3389/fmats.2024.1346112

Spoială, A., Ilie, C. I., Dolete, G., Croitoru, A. M., Surdu, V. A., Trușcă, R. D., Motelica, L., Oprea, O. C., Ficai, D., Ficai, A., Andronescu, E., & Dițu, L. M. (2022). Preparation and Characterization of Chitosan/TiO2 Composite Membranes as Adsorbent Materials for Water Purification. Membranes, 12(8). https://doi.org/10.3390/membranes12080804

Srivatsav, P., Bhargav, B. S., Shanmugasundaram, V., Arun, J., Gopinath, K. P., & Bhatnagar, A. (2020). Biochar as an eco-friendly and economical adsorbent for the removal of colorants (Dyes) from aqueous environment: A review. In Water (Switzerland) (Vol. 12, Issue 12). MDPI AG. https://doi.org/10.3390/w12123561

Suliman, W., Harsh, J. B., Abu-Lail, N. I., Fortuna, A. M., Dallmeyer, I., & Garcia-Pérez, M. (2017). The role of biochar porosity and surface functionality in augmenting hydrologic properties of a sandy soil. Science of the Total Environment, 574, 139–147. https://doi.org/10.1016/j.scitotenv.2016.09.025

Tarpeh, W. A., Wald, I., Wiprächtiger, M., & Nelson, K. L. (2018). Effects of operating and design parameters on ion exchange columns for nutrient recovery from urine. Environmental Science: Water Research & Technology, 4(6), 828–838. https://doi.org/10.1039/C7EW00478H

Tian, D., & Niu, S. (2015). A global analysis of soil acidification caused by nitrogen addition. Environmental Research Letters, 10(2). https://doi.org/10.1088/1748-9326/10/2/024019

Tomin, O., & Yazdani, M. R. (2022). Production and characterization of porous magnetic biochar: before and after phosphate adsorption insights. Journal of Porous Materials, 29(3), 849–859. https://doi.org/10.1007/s10934-022-01217-1

Wang, F., Wei, J., Zou, X., Fu, R., Li, J., Wu, D., Lv, H., Zhu, G., Wu, X., & Chen, H. (2019). Enhanced electrochemical phosphate recovery from livestock wastewater by adjusting pH with plant ash. Journal of Environmental Management, 250. https://doi.org/10.1016/j.jenvman.2019.109473

Wang, P., Shen, T., Li, X., Tang, Y., & Li, Y. (2020). Magnetic Mesoporous Calcium Carbonate-Based Nanocomposites for the Removal of Toxic Pb(II) and Cd(II) Ions from Water. ACS Applied Nano Materials, 3(2), 1272–1281. https://doi.org/10.1021/acsanm.9b02036

Wang, Y., Chen, H., Liu, Y. X., Ren, R. P., & Lv, Y. K. (2016). An adsorption-release-biodegradation system for simultaneous biodegradation of phenol and ammonium in phenol-rich wastewater. Bioresource Technology, 211, 711–719. https://doi.org/10.1016/j.biortech.2016.03.149

Wang, Z., & He, Z. (2022). Electrochemical phosphorus leaching from digested anaerobic sludge and subsequent nutrient recovery. Water Research, 223, 118996. https://doi.org/10.1016/j.watres.2022.118996

Wu, P., Wang, Z., Wang, H., Bolan, N. S., Wang, Y., & Chen, W. (2020). Visualizing the emerging trends of biochar research and applications in 2019: a scientometric analysis and review. Biochar, 2(2), 135–150. https://doi.org/10.1007/s42773-020-00055-1

Xie, B., Qin, J., Wang, S., Li, X., Sun, H., & Chen, W. (2020). Adsorption of Phenol on Commercial Activated Carbons: Modelling and Interpretation. International Journal of Environmental Research and Public Health, 17(3). https://doi.org/10.3390/ijerph17030789

Yeliz Ozudogru, & Ecem Tekne. (2023). Adsorption of Methylene Blue from Aqueous Solution Using Spent Coffee/Chitosan Composite. Journal of Water Chemistry and Technology, 45(3), 234–245. https://doi.org/10.3103/s1063455x23030086

Zhang, L., Lou, S., Hao, X., Zhang, H., Zhang, W., Liu, X., & Huang, J. (2022). Highly-porous and excellent-capacity zirconium-chitosan composite with superior Sb(III)/Sb(V) removal performance. Separation and Purification Technology, 303, 122253. https://doi.org/10.1016/j.seppur.2022.122253

Zhang, M., Zhang, Z., Peng, Y., Feng, L., Li, X., Zhao, C., & Sarfaraz, K. (2020). Novel cationic polymer modified magnetic chitosan beads for efficient adsorption of heavy metals and dyes over a wide pH range. International Journal of Biological Macromolecules, 156, 289–301. https://doi.org/10.1016/j.ijbiomac.2020.04.020

Zhao, Y., Shi, H., Du, Z., Zhou, J., & Yang, F. (2023). Removal of As(V) from aqueous solution using modified Fe3O4 nanoparticles. Royal Society Open Science, 10(1). https://doi.org/10.1098/rsos.220988

Zheng, Q., Yang, L., Song, D., Zhang, S., Wu, H., Li, S., & Wang, X. (2020). High adsorption capacity of Mg–Al-modified biochar for phosphate and its potential for phosphate interception in soil. Chemosphere, 259, 127469. https://doi.org/10.1016/j.chemosphere.2020.127469

Zhou, X., & Chen, Y. (2019). An integrated process for struvite electrochemical precipitation and ammonia oxidation of sludge alkaline hydrolysis supernatant. Environmental Science and Pollution Research, 26(3), 2435–2444. https://doi.org/10.1007/s11356-018-3667-6

Chapter 5: Conclusion and future work

5.1 Importance of polymer and biochar characterization

Polymer and biochar have great potential as adsorbent to remove water and soil pollutant and improve soils as well as sequester carbon. Polymer and biochar characterization research has shown that biochar properties and their effectiveness in different applications can vary widely. Several recent polymer and biochar research reviews have identified the ability to understand raw materials and production condition relations to polymer and biochar properties and their effects as a key knowledge gap and research need. Indeed, one of the most pressing challenges faced by the fledging polymer and biochar industry is the inability to define and measure polymer and biochar quality.

5.2 General conclusion

The results in this dissertation demonstrate that polymers derived from sodium alginate composites and biochar from coffee husk successfully removed dyes from aqueous solutions. Furthermore, to tackle issues such as water scarcity and soil degradation (including salinity, heavy metals, and glyphosate contamination) that negatively affect food production, we developed hydrogel beads and biochar composites derived from sodium alginate and coffee husk, respectively. The hydrogel bead composite materials were able to retain up to 30% more water in the soil than untreated soil, significantly enhancing soil nutrients and reducing levels of heavy metals such as iron and arsenic by up to 89.6% and 87.81%, respectively. Additionally, we created hydrogel bead composites encapsulating struvite ($MgNH_4PO_4 \cdot 6H_2O$) as slow-release fertilizers to improve salt-affected soils. These materials significantly released Mg, P, and $N\text{-}NH_4$ ($P<0.05$) and were effective in reducing soil salinity to normal levels while also enhancing soil nutrients. Furthermore, glyphosate removal using biochar-MgO was notable, achieving up to 50.42% removal after one week of soil incubation. The introduction of biochar-MgO into the soil resulted in an increased pH, while there was a significant rise ($P<0.05$) in electrical conductivity (EC) and exchangeable cations (Mg, Ca, and Na) contents.

Lastly, we developed (1) porous biochar composites via an in-situ technique using a combination of materials: ZrO, chitosan, and Fe_3O_4 to remove NH_4, PO_4, and phenol from water through adsorption techniques, and (2) hydrogel bead composites with oleic acid-loaded NH_4 ions as slow-release NH_4 fertilizers for application in soil acidity amelioration. The biochar application showed that this combination could enhance the simultaneous removal of NH_4, P, and phenol. The hydrogel bead composites demonstrated that the presence of oleic acid could maintain NH_4 ion release and reduce CO_2 emissions from soil. Both materials showed enhanced soil acidity properties.

5.3 Challenges and future progress development to applying polymer and biochar

5.3.1 Chapter 2

1. **Regeneration and reusability:** Polymers and biochar used for adsorption in wastewater treatment often require regeneration after use. This process can be energy-intensive and may involve chemical treatments, which raises concerns about secondary pollution and environmental impact. Developing cost-effective and environmentally friendly regeneration methods without compromising polymers and biochar properties is a significant challenge.
2. **Adsorption capacity and efficiency:** While biochar has a high surface area and porosity, its adsorption capacity can vary depending on production conditions, and surface functional groups. Optimizing biochar properties to enhance adsorption efficiency for a wide range of contaminants remains a challenge.

5.3.2 Chapter 3

Hydrogel beads have the ability to retain water and can be utilized within soil matrices to immobilize heavy metal pollutants. However, the polymer binding tends to weaken during soil incubation. Therefore, future studies should focus on enhancing the stability, swelling capacity, and mechanical strength of hydrogel beads to improve their long-term water retention and pollutant immobilization capabilities. Similarly, while biochar is effective at immobilizing pollutants like glyphosate, it does not retain water as effectively as hydrogel beads due to its lower hydrophilic properties.

5.3.3 Chapter 4

The use of hydrogel beads and biochar for ameliorating soil acidity is promising. Biochar can enhance soil pH and other nutrient characteristics, whereas hydrogel beads primarily improve soil nutrients with less effect on soil pH. Combining hydrogel beads and biochar offers a promising strategy for retaining water in the soil and enhancing soil nutrients under acidic conditions.

5.4 Prospect of future work

In this dissertation, we developed hydrogel beads and biochar composite materials to address water and soil pollutant remediation while enhancing soil quality. The limitations of this study included the weaker polymer binding in the soil matrix for long-term application and gas release during biochar pyrolysis. A promising strategy is to develop hydrogel beads with high mechanical strength and swelling capacity. Additionally, our investigation revealed a correlation between stable carbon rates, soil CO2 emissions, and soil characteristics. It is important to develop biochar with a high stable carbon rate and yield while minimizing carbon loss during pyrolysis.

List of publications

Main Research:

1. Endar Hidayat; Nur Maisarah Mohamad Sarbani, Sadaki Samitsu, Ferry Anggoro Ardy Nugroho, Sudip Kumar Lahiri, Mitsuru Aoyagi, Seichiro Yonemura, Hiroyuki Harada. Evaluation of slow-release fertilizers derived from hydrogel beads: Sodium alginate-poly (acrylic acid) and humic acid-encapsulated struvite for soil salinity amelioration. *Arabian Journal of Chemistry*. 2024, 17(9), 105877. https://doi.org/10.1016/j.arabjc.2024.105877. IF 6.0 (2023)
2. Endar Hidayat; Nur Maisarah Mohamad Sarbani, Sadaki Samitsu, Yaressa Vaskah Situngkir, Sudip Kumar Lahiri, Seichiro Yonemura, Yoshiharu Mitoma, Hiroyuki Harada. Simultaneous removal of ammonium, phosphate, and phenol via self-assembled biochar composites CBCZrOFe$_3$O$_4$ and its utilization as soil acidity amelioration. *Environmental Technology*. 2024, 1-20. https://doi.org/10.1080/09593330.2024.2362993. IF 2.8 (2023)
3. Endar, Hidayat; Nur Maisarah Mohamad Sarbani, Sadaki Samitsu, Yoshiharu Mitoma, Mitsuru Aoyagi, Seiichiro Yonemura, Hiroyuki Harada. Porous sodium alginate/poly (acrylic acid) composites cross-linked with FeCl$_3$ for acid black 1 dye removal from aqueous solution. *Desalination and Wastewater Treatment*. 2024, 319, 100407. https://doi.org/10.1016/j.dwt.2024.100313. https://doi.org/10.1016/j.dwt.2024.100407. IF 1.0 (2023)
4. Endar, Hidayat; Nur Maisarah Mohamad Sarbani, Helmi, Baharuddin Susanto, Yaressa Vaskah Situngkir, Marchanda Wahyu Chrisandi, Sadaki Samitsu, Yoshiharu Mitoma, Seiichiro Yonemura, Hiroyuki Harada. Performance of hydrogel beads composites derived from sodium alginate-cetyltrimethylammonium bromide toward congo red dye adsorption

from aqueous solution. *Desalination and Wastewater Treatment*. 2024, 318, 100313, 1-11. https://doi.org/10.1016/j.dwt.2024.100313. IF 1.0 (2023)

5. Endar, Hidayat; Nur Maisarah Mohamad Sarbani, Sudip Kumar Lahiri, Sadaki Samitsu, Seiichiro Yonemura, Yoshiharu Mitoma, Hiroyuki Harada, Effects of sodium alginate-poly (acrylic acid) cross-linked hydrogel beads on soil conditioner in the absence and presence of phosphate and carbonate ions. *Case Studies in Chemical and Environmental Engineering*. 2024, 9, 100642, 1-8. https://doi.org/10.1016/j.cscee.2024.100642. IF 1.28 (2023)
6. Endar, Hidayat; Nur Maisarah Binti Mohamad Sarbani, Seiichiro Yonemura, Yoshiharu Mitoma, Hiroyuki Harada. Application of Box-Behken Design to Optimize Phosphate Adsorption Conditions from Water onto Novel Adsorbent CS-ZL/ZrO/Fe_3O_4: Characterization, Equilibrium, Isotherm, Kinetic, and Desorption Studies. *International Journal of Molecular Sciences*. 2023, 24(11), 9754, 1-19. https://doi.org/10.3390/ijms24119754. IF 5.6 (2023)
7. Endar, Hidayat; Tomoyuki Yoshino, Seiichiro Yonemura, Yoshiharu Mitoma, Hiroyuki Harada. A Carbonized Zeolite/Chitosan Composite as an Adsorbent for Copper (II) and Chromium (VI) Removal from Water. *Materials*. 2023, 16(6), 2532, 1-13. https://doi.org/10.3390/ma16062532. IF 3.4 (2023)
8. Endar, Hidayat; Tomoyuki Yoshino, Seiichiro Yonemura, Yoshiharu Mitoma, Hiroyuki Harada, Synthesis. Adsorption Isotherm and Kinetic Study of Alkaline-Treated Zeolite/Chitosan Fe^{3+} Composites for Nitrate Removal from Aqueous Solution-Anion and Dye Effects. *Gels*. 2022, 8(12), 782, 1-15. https://doi.org/10.3390/gels8120782. IF 4.6 (2023)
9. Endar, Hidayat; Seiichiro Yonemura, Yoshiharu Mitoma, Hiroyuki Harada, Synthesis. Methylene Blue Removal By Chitosan Cross-linked Zeolite from Aqueous Solution and Other

ion Effects: Isotherm, Kinetic, and Desorption Studies. *Adsorption Science & Technology*, 2022, 2022, 1-10. https://doi.org/10.1155/2022/1853758. IF 2.9 (2023)

10. Endar, Hidayat; Saranya Khaekhum, Seiichiro Yonemura, Yoshiharu Mitoma, Hiroyuki Harada. Biosorption of Eriochrome Black T Using *Exserohilum rostratum* NMS1.5 Mycelia Biomass. *J*. 2022, 5(4), 427-434. https://doi.org/10.3390/j5040029. EBSCO Indexed.
11. Endar, Hidayat; Hiroyuki Harada, Yoshiharu Mitoma, Seiichiro Yonemura, Hadi Imran A Halem. Rapid Removal of Acid Red 88 by Zeolite/Chitosan Hydrogel in Aqueous Solution. *Polymers*. 2022, 14(5), 893, 1-18. https://doi.org/10.3390/polym14050893. IF 5.0 (2023).

Sub Research:

1. Arestha, Leo, Lita; Endar Hidayat, Nur Maisarah Mohamad Sarbani, Hiroyuki Harada, Seiichiro Yonemura, Yoshiharu Mitoma, Herviyanti, Gusmini. Glyphosate Removal from Water Using Biochar Based Coffee Husk Loaded Fe_3O_4. *Water*. 2023, 15(16), 2945, 1-12. https://doi.org/10.3390/w15162945. IF 3.4 (2023)
2. Asmak, Afriliana; Feby Erawantini, Endar Hidayat, Hiroyuki Harada, Achmad Subagio, Assessing the Beneficial Effect of Spent Coffee Ground Compost under Mustard Plants (*Brassica juncea L*). *Asian Journal of Agricultural and Horticultural Research*. 2023, 10(4), 310-321. https://doi.org/10.9734/ajahr/2023/v10i4272. Google Scholar Indexed.
3. Nur, Maisarah, Binti, Mohamad, Sarbani; Endar Hidayat, Kanako Naito, Yoshiharu Mitoma, Hiroyuki Harada. Cr (VI) and Pb (II) Removal Using Crosslinking Magnetite-Carboxymethyl Cellulose-Chitosan Hydrogel Beads. *Gels*. 2023, 9(8), 612. https://doi.org/10.3390/gels9080612. IF 4.6 (2023)

4. Hiroyuki, Harada; Akagi Kotaro, Endar Hidayat. Ammonium Removal from Ammonium Rich Solution by Bio Char, *Journal of Environmental Protection*. 2022, 13, 171-182. https://doi.org/10.4236/jep.2022.131011. Google Scholar Indexed

Acknowledgment

1. I would like to thank Prof Hiroyuki Harada, Prof Seiichiro Yonemura, Assoc Prof Mitsuru Aoyagi, Prof Sadaki Samitsu and Prof Yoshiharu Mitoma for guidance during my study at the Prefectural University of Hiroshima.
2. I wish to express thank to the MEXT Scholarship for providing sponsorship during studies at the Prefectural University of Hiroshima.
3. I would like to express gratitude to the National Institute for Materials Science (NIMS), Japan, for accepting the research internship.